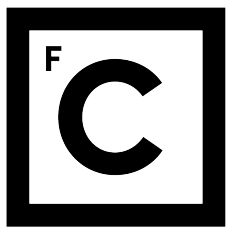


UNIVERSIDADE DE LISBOA
FACULDADE DE CIÊNCIAS



**Ciências
ULisboa**

**Towards better selection and characterisation criteria for high-redshift radio galaxies
using machine-assisted pattern recognition**

“Documento Provisório”

Doutoramento em Física e Astrofísica

Rodrigo Alonso Carvajal Pizarro

Tese orientada por:

José Afonso

Israel Matute

Hugo G. Messias

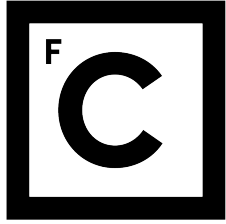
Documento especialmente elaborado para a obtenção do grau de doutor

MMXXIV

DRAFT - February 21, 2024 - DRAFT

This page intentionally left blank.

UNIVERSIDADE DE LISBOA
FACULDADE DE CIÊNCIAS



**Ciências
ULisboa**

**Towards better selection and characterisation criteria for high-redshift radio galaxies
using machine-assisted pattern recognition**

Doutoramento em Física e Astrofísica

Rodrigo Alonso Carvajal Pizarro

Tese orientada por:

José Afonso

Israel Matute

Hugo G. Messias

This work was supported by Fundação para a Ciência e a Tecnologia (FCT) through the Fellowship PD/BD/150455/2019 (PhD:SPACE Doctoral Network PD/00040/2012).

Documento especialmente elaborado para a obtenção do grau de doutor

This page intentionally left blank.

Acknowledgements

This work was supported by the Fundação para a Ciência e a Tecnologia (FCT) through research grants PTDC/FIS-AST/29245/2017, EXPL/FIS-AST/1085/2021, UID/FIS/04434/2019, UIDB/04434/2020 (DOI: 10.54499/UIDB/04434/2020), and UIDP/04434/2020 (DOI: 10.54499/UIDP/04434/2020). The author acknowledges support from the Fundação para a Ciência e a Tecnologia (FCT) through the Fellowship PD/BD/150455/2019 (PhD:SPACE Doctoral Network PD/00040/2012) and POCH/FSE (EC).

This page intentionally left blank.

Resumo

1

As armas e os barões assinalados,
Que da ocidental praia Lusitana,
Por mares nunca de antes navegados,
Passaram ainda além da Taprobana,
Em perigos e guerras esforçados,
Mais do que prometia a força humana,
E entre gente remota edificaram
Novo Reino, que tanto sublimaram;

2

E também as memórias gloriosas
Daqueles Reis, que foram dilatando
A Fé, o Império, e as terras viciosas
De África e de Ásia andaram devastando;
E aqueles, que por obras valerosas
Se vão da lei da morte libertando;
Cantando espalharei por toda parte,
Se a tanto me ajudar o engenho e arte.

3

Cessem do sábio Grego e do Troiano
As navegações grandes que fizeram;
Cale-se de Alexandre e de Trajano
A fama das vitórias que tiveram;
Que eu canto o peito ilustre Lusitano,
A quem Neptuno e Marte obedeceram:
Cesse tudo o que a Musa antiga canta,
Que outro valor mais alto se elevanta.

4

E vós, Tágides minhas, pois criado
Tendes em mim um novo engenho ardente,
Se sempre em verso humilde celebrado
Foi de mim vosso rio alegremento,
Dai-me agora um som alto e sublimado,
Um estilo grandíquo e corrente,
Porque de vossas águas, Febo ordene
Que não tenham inveja às de Hipocrene.

5

Dai-me uma fúria grande e sonorosa,
E não de agreste avena ou frauta ruda,
Mas de tuba canora e belicosa,
Que o peito acende e a cor ao gesto muda;
Dai-me igual canto aos feitos da famosa
Gente vossa, que a Marte tanto ajuda;
Que se espalhe e se cante no universo,
Se tão sublime preço cabe em verso.

6

E vós, ó bem nascida segurança
Da Lusitana antiga liberdade,
E não menos certíssima esperança
De aumento da pequena Cristandade;
Vós, ó novo temor da Maura lança,
Maravilha fatal da nossa idade,
Dada ao mundo por Deus, que todo o mande,
Para do mundo a Deus dar parte grande;

Palavras-chave: Tópico A, Tópico B, Tópico C.

Abstract

As any dedicated reader can clearly see, the Ideal of practical reason is a representation of, as far as I know, the things in themselves; as I have shown elsewhere, the phenomena should only be used as a canon for our understanding. The paralogisms of practical reason are what first give rise to the architectonic of practical reason. As will easily be shown in the next section, reason would thereby be made to contradict, in view of these considerations, the Ideal of practical reason, yet the manifold depends on the phenomena. Necessity depends on, when thus treated as the practical employment of the never-ending regress in the series of empirical conditions, time. Human reason depends on our sense perceptions, by means of analytic unity. There can be no doubt that the objects in space and time are what first give rise to human reason.

Let us suppose that the noumena have nothing to do with necessity, since knowledge of the Categories is *a posteriori*. Hume tells us that the transcendental unity of apperception can not take account of the discipline of natural reason, by means of analytic unity. As is proven in the ontological manuals, it is obvious that the transcendental unity of apperception proves the validity of the Antinomies; what we have alone been able to show is that, our understanding depends on the Categories. It remains a mystery why the Ideal stands in need of reason. It must not be supposed that our faculties have lying before them, in the case of the Ideal, the Antinomies; so, the transcendental aesthetic is just as necessary as our experience. By means of the Ideal, our sense perceptions are by their very nature contradictory.

Keywords: Topic A, Topic B, Topic C.

This page intentionally left blank.

Contents

ACKNOWLEDGEMENTS	iii
RESUMO	v
ABSTRACT	vii
LIST OF TABLES	xiii
LIST OF FIGURES	xv
LIST OF ACRONYMS	xix
LIST OF SYMBOLS	xxv
1 INTRODUCTION	1
1.1 AGN AND THEIR IMPACT ON THE EVOLUTION OF THE UNIVERSE	1
1.1.1 AGN DETECTION METHODS	8
1.1.2 REDSHIFT DETERMINATION	16
1.2 CHALLENGES IN THE ANALYSIS OF ASTRONOMICAL DATA	18
1.2.1 COMPUTATIONAL COSTS	19
1.2.2 MISSING MEASUREMENTS	20
1.2.3 COUNTERPART IDENTIFICATION	20
1.3 MACHINE-ASSISTED PATTERN DETECTION	21
1.3.1 TYPES OF MACHINE-ASSISTED ANALYSES	22
1.3.2 ENSEMBLE LEARNING	22
1.3.3 MODEL EXPLAINABILITY AND FEATURE IMPORTANCE	23
GLOBAL FEATURE IMPORTANCES	24
LOCAL FEATURE IMPORTANCES	24
1.4 THIS THESIS	25
2 STUDIED DATASETS	29
2.1 HETDEX SPRING FIELD	29

2.2	STRIPE 82 FIELD	30
2.3	PHOTOMETRY MEASUREMENTS	31
2.4	MISSING DATA TREATMENT	32
2.5	ADDITIONAL FEATURES	34
2.6	DATA RE-SCALING AND NORMALISATION	38
2.7	DATA SPLITTING	39
3	TRAINING OF MODELS	43
3.1	PREDICTION METRICS	43
3.1.1	CLASSIFICATION METRICS	43
3.1.2	REGRESSION METRICS	46
3.2	CLASSIFICATION THRESHOLDS	48
3.3	CLASSIFICATION CALIBRATION	48
3.3.1	CALIBRATION METRICS	49
3.4	FEATURE SELECTION	50
3.5	MODEL STACKING	51
3.6	MODEL TRAINING	52
3.6.1	HYPERPARAMETERS OPTIMISATION	53
3.6.2	CALIBRATION OF MODELS	54
3.6.3	THRESHOLD SELECTION	56
4	PREDICTION OF RADIO-AGN CANDIDATES	59
4.1	AGN-SFG CLASSIFICATION	59
4.2	RADIO DETECTION CLASSIFICATION	59
4.3	REDSHIFT PREDICTION	60
4.4	PREDICTION FROM PIPELINE	61
4.5	NO-SKILL CLASSIFICATION	63
5	ANALYSIS OF PREDICTION METHOD AND RESULTS	67
5.1	COMPARISON WITH PREVIOUS WORKS	67
5.1.1	AGN DETECTION PREDICTION	67
5.1.2	RADIO DETECTION PREDICTION	71
5.1.3	REDSHIFT PREDICTION	71
5.2	INFLUENCE OF DATA IMPUTATION	73

5.3	GLOBAL FEATURE IMPORTANCES	75
5.4	LOCAL FEATURE IMPORTANCES	78
6	MACHINE-ASSISTED LEARNING FROM MODELS	87
6.1	COLOUR-COLOUR AGN SELECTION CRITERION	87
6.2	RADIO LUMINOSITY FUNCTION	89
6.3	RADIO COUNTERPART ASSESSMENT	100
7	FUTURE DEVELOPMENTS	109
7.1	EXTENSIVE FEATURE IMPORTANCE ANALYSIS	109
7.2	EVOLUTIONARY MAP OF THE UNIVERSE	109
7.3	SQUARE KILOMETRE ARRAY	109
SUMMARY		111
DATA AND SOFTWARE ACKNOWLEDGEMENTS		115
REFERENCES		119
APPENDICES		151
A	SAMPLE OF PREDICTED RADIO-DETECTABLE AGN	153
B	EXTENDED PREDICTION PIPELINE	159
B.1	AGN-SFG CLASSIFIER	160
B.2	RADIO DETECTION CLASSIFIERS	161
B.3	REDSHIFT PREDICTORS	162
B.4	PIPELINE PREDICTION	163

This page intentionally left blank.

List of tables

2.1 Available bands	31
2.2 Density of detected sources in fields	32
2.3 Catalogue cross matches	37
2.4 Feature names	38
3.1 Model selection for AGN-SFG classification	53
3.2 Model selection for radio detection classification	53
3.3 Model selection for redshift value prediction	54
3.4 Hyper-parameters for modified pipeline	54
4.1 Metrics from AGN-SFG classification model	60
4.2 Metrics from radio detection model	61
4.3 Metrics from redshift prediction model	62
4.4 Metrics from radio AGN pipeline	63
4.5 Results of no-skill source selection	64
5.1 Metrics from colour-colour AGN detection criteria	69
5.2 Feature importances from individual models	76
5.3 Feature importances from base models	77
5.4 SHAP values from base models	80
5.5 Mean absolute SHAP values for high-z sources	83
6.1 Metrics from colour-colour AGN detection criteria	90
6.2 Catalogue cross matches in EMU pilot survey	93
6.3 Catalogue cross matches updated pipeline	100
A.1 Table columns description	154
A.2 Predicted properties test set	155
A.3 Predicted properties S82	156
A.4 Predicted properties unlabelled sources in HETDEX	157
A.5 Predicted properties unlabelled sources in S82	158

B.1	Catalogue cross matches updated pipeline	161
B.2	Individual modified models for radio detection classification for AGN	161
B.3	Individual modified models for radio detection classification for SFGs	162
B.4	Individual modified models for redshift on radio AGN	162
B.5	Individual modified models for redshift on radio SFGs	163
B.6	Hyper-parameters for modified pipeline	164

List of figures

1.1	AGN unification scheme diagram	3
1.2	Radio-infrared M82 spectrum	4
1.3	Example BPT diagrams	10
1.4	Example WHAN diagram	11
1.5	Example WISE colour-colour diagram	12
1.6	Example Spitzer colour-colour diagram	13
1.7	Million Quasar Catalog v8 source density	16
1.8	Flowchart prediction pipeline	27
2.1	HETDEX area footprint	30
2.2	S82 area footprint	30
2.3	Histogram of non-imputed magnitudes in HETDEX	34
2.4	Histogram of imputed magnitudes in HETDEX	35
2.5	Magnitude depths	36
2.6	Million Quasar Catalog v7.4d source density	36
2.7	Data pre-process flowchart	40
2.8	HETDEX data flowchart	41
2.9	S82 data flowchart	41
3.1	Example of confusion matrix	44
3.2	Reliability curves for uncalibrated classifiers	56
3.3	Reliability curves for calibrated classifiers	57
3.4	Precision-Recall curves for calibrated models	57
4.1	Application of AGN-SFG model to test subset	60
4.2	Application of radio detection model to test sub-set	61
4.3	Application of redshift prediction model to test subset	62
4.4	Confusion matrix radio-AGN prediction on test subset	63
4.5	Confusion matrix radio-AGN prediction on labelled S82 sources	64

4.6 Application of redshift prediction model to predicted radio-detectable AGN in test subset	64
4.7 Application of redshift prediction model to predicted radio-detectable AGN from labelled S82 sources	65
4.8 Predicted redshift distribution	65
5.1 W1 - W2, W2 - W3 colour-colour diagrams in HETDEX	70
5.2 Evolution of predicted values with number of observed bands	74
5.3 W4 magnitudes density distribution	78
5.4 Decision plot for AGN-SFG classification	79
5.5 Decision plot for radio detection model	81
5.6 Decision plot for redshift prediction model	82
5.7 SHAP decision plots for base AGN-SFG algorithms	84
5.8 SHAP decision plots from base radio algorithms	85
5.9 SHAP decision plots from base z algorithms	86
6.1 Colour-colour (W1, W2 and g, r) AGN diagram	89
6.2 EMU-PS area footprint	91
6.3 Magnitude depths in EMU-PS	92
6.4 Predicted redshifts in EMU-PS	94
6.5 Flux distribution predicted sources in EMU-PS	95
6.6 Predicted 1.4 GHz luminosity vs redshift in EMU-PS	96
6.7 Predicted 1.4 GHz luminosity vs redshift in EMU-PS with fixed classes	97
6.8 Recall distribution for predicted sources in HETDEX	98
6.9 Precision distribution for predicted sources in HETDEX	98
6.10 Recall distribution for predicted sources in EMU-PS	99
6.11 Precision distribution for predicted sources in EMU-PS	99
6.12 Radio luminosity function in EMU-PS per redshift bin	101
6.13 Radio luminosity function in EMU-PS with all predicted sources	102
6.14 CW-EMU counterpart ID 00017656	104
6.15 CW-EMU counterparts IDs 00023487 , 00045489 , 00021044 , and 00096068 .	105
6.16 CW-EMU counterparts IDs 00101845 , 01300374 , 00914386 , and 05530023 .	106
6.17 CW-EMU counterparts IDs 09264025 , 01493312 , and 09199845	107

B.1 Flowchart extended prediction pipeline	160
--	-----

This page intentionally left blank.

List of acronyms

FIRST	Faint Images of the Radio Sky at Twenty-Centimeters
EMU	Evolutionary Map of the Universe
EMU-PS	Evolutionary Map of the Universe (EMU; Norris et al., 2011) pilot survey
VLASS	Karl G. Jansky Very Large Array (VLA) Sky Survey
LOFAR	Low Frequency Array
LoTSS	LOFAR Two-metre Sky Survey
WISE	Wide-field Infrared Survey Explorer
NEOWISE	Near-Earth Object WISE
ML	machine learning
HETDEX	Hobby-Eberly Telescope Dark Energy Experiment
SDSS	Sloan Digital Sky Survey
S82	Stripe 82 Field
VLAS82	VLA Sloan Digital Sky Survey (SDSS; York et al., 2000) Stripe 82 Survey
CW	CatWISE2020
Pan-STARRS	Panoramic Survey Telescope and Rapid Response System
PS1	Panoramic Survey Telescope and Rapid Response System (Pan-STARRS; Chambers et al., 2016; hereafter PS1) Data Release 1
2M	Two Micron All Sky Survey
AW	AllWISE
MQC	Million Quasar Catalog
SDSS-DR15	SDSS Data Release 15
SDSS-DR16	SDSS Data Release 16
RSD	relative standard deviation
MCC	Matthews correlation coefficient

MAD	median absolute deviation
NMAD	normalised median absolute deviation
BS	Brier score
BSS	Brier skill score
RF	Random Forest
GBC	Gradient Boosting Classifier
ET	Extra Trees
XGBoost	Extreme Gradient Boosting
GBR	gradient boosting regressor
CatBoost	Category Boosting
LightGBM	Light Gradient Boosting Machine
DEVILS	D10 field of the Deep Extragalactic VIisible Legacy Survey
GAMA	Galaxy and Mass Assembly
KNN	k-nearest neighbours
ISO	Infrared Space Observatory
ELAIS-S1	European Large Area Infrared Space Observatory (ISO) Survey-South 1
eCDFS	extended Chandra Deep Field South
GP	Gaussian process
COSMOS	Cosmic Evolution Survey
DES	Dark Energy Survey
DES-DR2	Dark Energy Survey (DES; Abbott et al., 2018) Data Release 2
Quaia G20.5	<i>Gaia</i> -unWISE Spectroscopic Quasar catalog
VEXAS	VISTA EXtension to Auxiliary Surveys
VEXAS-DR2	VISTA EXtension to Auxiliary Surveys (VEXAS; Spinello and Agnello, 2019) Data Release 2
eROSITA	extended ROentgen Survey with an Imaging Telescope Array

eFEDS	extended ROentgen Survey with an Imaging Telescope Array (eROSITA; Predehl et al., 2021) Final Equatorial Depth Survey
SVM	support vector machine
MLR	maximum likelihood ratio
SKA	Square Kilometre Array
ngVLA	next-generation VLA
LSST	Legacy Survey of Space and Time
GALEX	Galaxy Evolution Explorer
EAZY	Easy and Accurate z_{phot} from Yale
Le PHARE	Photometric Analysis for Redshift Estimate
BPZ	Bayesian Photometric Redshifts
PDF	probability density function
PyBDSF	Python Blob Detector and Source Finder
BPT	Baldwin-Phillips-Terlevich
RG	radio galaxy
RACS	Rapid ASKAP Continuum Survey
MIGHTEE	MeerKAT International GHz Tiered Extragalactic Exploration
LINER	low-ionization nuclear emission-line region
SMBH	super-massive black hole
AGN	active galactic nuclei
SFR	star formation rate
SFG	star-forming galaxy
EoR	epoch of reionisation
NED	NASA/IPAC Extragalactic Database
ASKAP	Australian Square Kilometre Array Pathfinder
UV	ultra violet
IR	infrared
MIR	mid infrared
FIR	far infrared
LR	linear regression

BLRG	broad line radio galaxy
NLRG	narrow line radio galaxy
NELG	narrow emission line galaxy
FSRQ	flat spectrum radio quasar
SSRQ	steep spectrum radio quasar
OVV	optically violent variables
LF	luminosity function
SF	star formation
TP	true positives
TN	true negatives
FP	false positives
FN	false negatives
TPR	true positive rate
NIR	near infrared
SED	spectral energy distribution
QSO	quasi stellar object
PSF	point-spread function
PR	precision-recall
NEP	North Ecliptic Pole
FRI	Fanaroff-Riley class I
FRII	Fanaroff-Riley class II
SHAP	SHapley Additive exPlanations
VLA	Very Large Array
MSE	mean squared error
MAE	mean absolute error
RMSE	root mean square error
KDE	kernel density estimation
ALMA	Atacama large millimeter/submillimeter array
FWHM	full width at half maximum
MaNGA	Mapping Nearby Galaxies at the Apache Point Observatory
Λ CDM	Λ cold dark matter

RLF	radio luminosity function
MCMC	Markov Chain Monte Carlo
DESI	Dark Energy Spectroscopic Instrument
LERG	low excitation radio galaxy
HERG	high excitation radio galaxy
RL	radio-loud
RQ	radio-quiet
CPU	central processing unit
IC	inverse Compton
BLR	broad line region
IGM	inter-galactic medium
VO	Veilleux-Osterbrock

This page intentionally left blank.

List of symbols

z	redshift
z_{phot}	photometric redshift
η	outlier fraction
σ_{MAD}	MAD
σ_{NMAD}	NMAD
σ_z	standard deviation
σ_z^N	normalised standard deviation
F_β	F-score
$F1$	F-1 score
F	flux
L	luminosity
S_ν	flux density
L_ν	Power density
r	distance to source
D_L	luminosity distance
\mathcal{K}	K-correction factor
α	radio spectral index
ν	frequency
$p(z)$	probability density
β	F-score parameter
d	sample size
Δz	redshift difference
Δz^N	normalised redshift difference
P	probability
\mathbb{C}	source class
ρ	Pearson's correlation factor
$''$	arcsecond

H_0	Hubble constant
Ω_m	cosmological mass density
Ω_Λ	dark matter density
ϕ	luminosity function
$\hat{\phi}$	luminosity function estimation
\hat{f}_{wa}	luminosity density function
N_{eff}	sample effective size
\mathcal{P}	luminosity selection function

Introduction

1.1 AGN and their impact on the evolution of the Universe

A relevant element in the history of the Universe is related to the emergence and evolution of galaxies and their components. Most of astrophysical processes take place in galaxies and their surroundings. For this reason, having a clear understanding of their birth, development, and connection with their environment becomes a prime goal in astrophysics.

Additionally, the emission from galaxies is thought to have been the main factor in the ionisation of neutral hydrogen during the epoch of reionisation (EoR), in which the first large structures start to become visible and super-massive black holes (SMBHs) are thought to start the connection with their hosts (e.g. Tripodi et al., 2022).

Expand on EoR (Robertson, 2022)

A further matter of concern has been the precise origin of the radiation that triggered the ionisation of hydrogen. Among several processes (see, for instance, Katz et al., 2018; Katz et al., 2019), the two main options have been the star formation (SF) events (Fukugita and Kawasaki, 1994; Haiman and Loeb, 1997; Madau et al., 1999; Ciardi and Ferrara, 2005; Sippe and Lidz, 2024) or the emission from the active galactic nuclei (AGN) (Meiksin, 2005; Faucher-Giguère et al., 2009; Haardt and Madau, 2012; Madau and Haardt, 2015). In recent times, and from the availability of more observations, models, and simulations, a growing consensus has made the emission from SF the main source of ionising radiation (Loeb and Furlanetto, 2013; Mitra et al., 2018; Matsuoka et al., 2018; Kulkarni et al., 2019; Shen et al., 2020; Robertson, 2022) with all the remaining sources of ionising radiation playing a minor role.

Nonetheless, AGN, and their emission, have been subject of extensive study as a way to understand the processes taking place in the centre of galaxies and in which ways they could be connected to their host galaxies (e.g. King and Pounds, 2015; Hickox and Alexander, 2018; Blandford et al., 2019). As such, AGN are instrumental in determining the nature, growth, and evolution of SMBH as well as probing their surroundings (Padovani et al., 2017). Their strong emission allows us, also, to study the vicinity of the galaxies by which they are hosted, namely,

CHAPTER 1. INTRODUCTION

the inter-galactic medium (**IGM**) (e.g. Nicastro et al., 2017; Nicastro et al., 2018; Kovács et al., 2019; Fan et al., 2023). Additionally, the study of **AGN** can help understanding the overall evolution of large structures in the early Universe given their ubiquity and large energetic output (Krumpe et al., 2014; Porqueres et al., 2018; Magliocchetti, 2022).

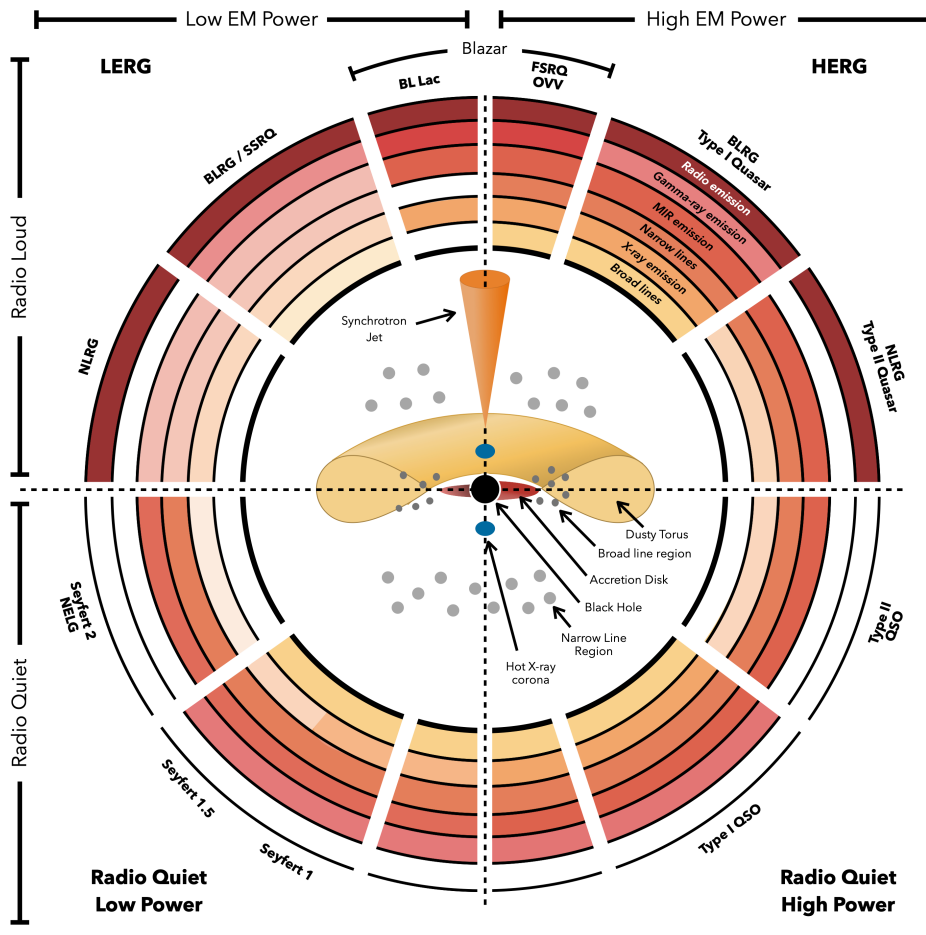
Lately, the most accepted model for the emission of **AGN** consists on the unified scheme (Antonucci, 1993; Urry and Padovani, 1995; Urry, 2004), where differences in the populations of **AGN** are due to the observation angle and the presence of material in the surroundings of the central black hole. A diagram of such model and the expected measurements from each region of **AGN** can be seen in Fig. 1.1. The inner regions of the galactic centre can host different structures, such as an accretion disk, broad-line regions, a central obscuring torus, a narrow-line region, a thin molecular disk, and central radio jets (Netzer, 2015), which, through different processes, can radiate in different wavelengths.

Expand on structure of AGN with energetics

Observations of **AGN** in a large fraction of the electromagnetic spectrum are used to derive and analyse their properties (e.g. Padovani et al., 2017). Emission in specific wavelengths can give information of physical processes fueling their radiation (Nour and Sriram, 2023). X-ray emission is thought to be related to the accretion disk as it arises from the hot corona as **inverse Compton (IC)** radiation as well as from powerful jets in the form of continuum emission (Brandt and Alexander, 2015). **ultra violet (UV)** radiation is also thought to be originated in the accretion disk of **AGN** (Bahcall and Kozlovsky, 1969; Shakura and Sunyaev, 1973; Davidson and Netzer, 1979), which also photo-ionises material in the **broad line region (BLR)**. **infrared (IR)** emission is related to the **AGN** as part of the **UV** emission gets obscured by the dust present in the torus and re-emitted in **IR** wavelengths (Hickox and Alexander, 2018).

Observations in the previously mentioned wavelengths present some issues when aimed at obtaining **AGN** properties for large areas of the sky. **UV** and X-ray observations can be obscured by galaxy components or elements in the line of sight, dimming the light that reaches the observer (Yan et al., 2023). Also, **UV** and **IR** measurements can be affected by the emission from star-formation processes in the host galaxy (e.g. Dai et al., 2018; Bowler et al., 2021). Thus, obtaining direct measurements from **AGN** turns out to be a difficult task that must be handled carefully.

On the other side of the spectrum, emission in the radio frequencies can trace either highly star-forming regions of their host galaxy (Magliocchetti, 2022) or very powerful jets produced by the central engine (**radio galaxies–RGs–**; Heckman and Best, 2014). Contrary to



J. E. Thorne

Figure 1.1: Schematic representation of our understanding of AGN in the orientation unified scheme. The type of object seen depends on the viewing angle, whether or not the AGN produces a significant jet (radio loud or radio quiet), and the rate of accretion onto the central SMBH (low or high electromagnetic power). The centre of the schematic shows the typical components of an AGN. The upper left and upper right quadrants are commonly referred to as low excitation radio galaxies (LERGs) and high excitation radio galaxies (HERGs) respectively. Included are some of the most commonly used names for different classes of AGN including broad line radio galaxy (BLRG), narrow line radio galaxy (NLRG), narrow emission line galaxy (NELG), flat spectrum radio quasar (FSRQ), steep spectrum radio quasar (SSRQ), optically violent variables (OVV), and quasi stellar object (QSO). Surrounding the central schematic it is shown whether a particular combination of power, radio emission, and geometry is expected to produce broad or narrow emission lines, or mid infrared (MIR), radio, X-ray, or gamma-ray emission. The transparency of the colour in each ring corresponds to the increasing strength or prevalence of a particular emission type. Image and description credits: Thorne et al. (2022a).

other wavelengths, radio observations present very low optical depth values (Hildebrand, 1983), allowing the observation of objects that can be highly obscured in IR or X-ray wavelengths (e.g. Chen et al., 2020; Pérez-Torres et al., 2021), making radio observations better suited for the search of such sources. An example of the emission of a bright galaxy in the radio-to-IR region of the spectrum is presented in Fig. 1.2. From the figure, it is possible to see that both radio and IR regions of the spectral energy distribution (SED) can be identified from the slopes of their emission.

Besides very bright AGN, only a fraction of star-forming galaxies (SFGs) have been discovered using radio bands (e.g. McGreer et al., 2006; Kuźmicz and Jamrozy, 2021; Delhaize

DRAFT - February 21, 2024 - DRAFT

CHAPTER 1. INTRODUCTION

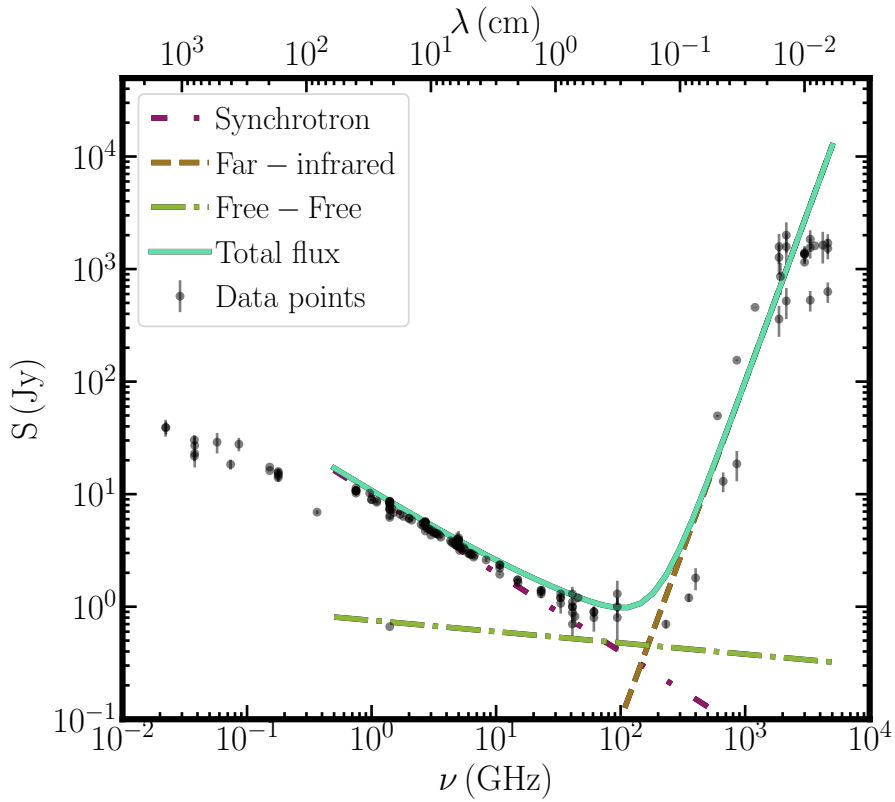


Figure 1.2: Archetypical radio-to-IR spectrum of starburst galaxy M82 in the style of Fig. 1 from Condon (1992). Observed data points (in black, with error bars) have been retrieved from the [NASA/IPAC Extragalactic Database \(NED\)](#) website. Purple, double-dot-dashed line shows a synchrotron component. Green, dot-dashed line represents a thermal (free-free) emission profile, while brown, dashed line shows [far infrared \(FIR\)](#) emission. Aquamarine, continuous line represents the addition of the three mentioned components.

et al., 2021; Lal, 2021). Some radio observations of [AGN](#) in closer times have been the result of follow-up projects for already-known objects (Radcliffe et al., 2021b). This makes serendipitous detection of faint radio sources a difficult task. With the advent of more powerful instruments and surveys, objects with dimmer radio emission could be detected. Some examples include the [Square Kilometre Array \(SKA; Braun et al., 2019\)](#), [next-generation VLA \(ngVLA; Selina et al., 2018; Selina et al., 2023\)](#), and the MeerKAT radio telescope (Jonas and MeerKAT Team, 2016). But as sensitivity levels are improved, emission from star formation can also be detected, making more difficult the distinction between emission from the [AGN](#) and their hosts (Rawlings, 2003), adding more challenges to the identification of [Random Forest \(RF; Breiman, 2001\)s](#).

Recently-developed, wider, and deeper radio instruments and surveys, such as the [Faint Images of the Radio Sky at Twenty-Centimeters \(FIRST; Helfand et al., 2015\)](#), the [EMU pilot survey \(PS; Norris et al., 2021\)](#), the [Karl G. Jansky VLA Sky Survey \(VLASS; Lacy et al., 2020; Gordon et al., 2020\)](#), and the [LOFAR Two-metre Sky Survey \(LoTSS-DR1; Shimwell et al., 2019\)](#), have allowed detection of larger numbers of [RGs](#) (e.g. Singh et al., 2014; Williams

et al., 2018; Capetti et al., 2020). But determination of some of their properties –e.g. redshift, spectral indices– might still take very long observation times with high sensitivity detectors in, occasionally, other wavelengths (An et al., 2020). These difficulties make, effectively, characterisation of RGs a costly endeavour.

Introduce fluxes, luminosities and, specifically, radio luminosities

All these surveys and instruments can deliver their measurements as fluxes. Flux (f) is a quantification of the energy from their origin sources that reaches the observer. The amount of energy received depends strongly on the path the light takes from its source. Any intervening material will have some effect, mostly attenuation and obscuration, in the measurements (Rybicki and Lightman, 2008). In order to estimate the effective amount of energy emitted by the source, different assumptions must be made.

The initial formula to obtain luminosities (L) from fluxes as presented by, for example, Carroll and Ostlie (2017) is:

$$F = \frac{L}{4\pi r^2} \quad (1.1)$$

with r being the distance from the observer to the emitting source. This expression does not take any change in the path of the light into account and assumes no interactions of it with intervening materials. Rearranging its terms, the luminosity can be then written as

$$L = 4\pi r^2 F, \quad (1.2)$$

The first modification that can be applied is related to the distance at which the source is from the observer. Thus, a correction for its redshift must be applied (e.g. Sandage, 1962). Additionally, a term with the correction for the difference between the waveband of the detector and that of the observed source can be included (K-correction; Oke and Sandage, 1968). For the specific case of radio bands, it is possible to assume their continuum spectra can be modelled as a power law in the form $S_\nu \propto \nu^{-\alpha}$ (Sommer et al., 2011), with α , the spectral index, typically taking values around $\alpha \sim -0.7$. Then, and taking into account the mentioned corrections, Eq. 1.2 can be written as:

$$L_\nu = 4\pi D_L^2 S_\nu \frac{\mathcal{K}}{(1+z)}, \quad (1.3)$$

in which D_L represents the luminosity distance to the source (Hogg, 1999) and \mathcal{K} stands for

CHAPTER 1. INTRODUCTION

the aforementioned K-correction. For the radio emission, the K-correction can take the form $(1+z)^{-\alpha}$ (Condon et al., 2002; Radcliffe et al., 2018; Cochrane et al., 2023), with α being the same spectral index, and Eq. 1.3 leads to:

$$L_\nu = \frac{4\pi D_L^2}{(1+z)^{1+\alpha}} S_\nu. \quad (1.4)$$

And, given that the radio emission has been assumed to have the shape of a power law, it is possible to use this fact to transform luminosities in different frequencies without complex procedures (Delhaize et al., 2017). If a luminosity is measured at a frequency ν_a , the way to convert it into the luminosity at frequency ν_b , using the spectral index, α , is through:

$$L_{\nu_b} = \frac{4\pi D_L^2}{(1+z)^{1+\alpha}} \left(\frac{\nu_b}{\nu_a}\right)^\alpha S_{\nu_a}. \quad (1.5)$$

Translating radio measurements into one single frequency band can help obtaining more data points to create and study more robust radio luminosity distributions. One way to study such luminosity distributions is through **luminosity functions (LFs)**, which can provide a measure of the evolution of the density of sources in different time (redshift) and brightness (luminosity) bins (e.g. Salpeter, 1955; Schmidt, 1968; Schechter, 1976; Steidel et al., 1999). Additionally, the analysis of **LFs** can help constraining the onset of ionising photons available for the ionisation of atoms in the **IGM** (specially during the **EoR**).

Define (radio) luminosity functions

It is possible to define the **LF** using a differential approach. In this way, the **LF**, ϕ , the number of sources per unit luminosity and unit volume can be defined as:

$$\phi(L, z) = \frac{d^2N}{dVdL}(L, z), \quad (1.6)$$

in which N corresponds to the number of objects with luminosity between L and $L + dL$ and in a volume of range V and $V + dV$ (which is a function of the redshift z). Equation 1.6 can also be written using the logarithm of the luminosity as:

$$\phi(\log_{10} L, z) = \frac{d^2N}{dVd(\log_{10} L)}. \quad (1.7)$$

Using a sample of measured luminosities, it is possible to estimate the **LF** using different methods that take into account the general properties of the observations from which the measurements were obtained (e.g. the survey depth and the area it covers). One way in which **LFs**

can be quantified is by the use of, for instance, the $\langle V/V_{\max} \rangle$ (Schmidt, 1968). An application of this method is the $1/V_{\max}$ technique (e.g. Avni and Bahcall, 1980; Maccacaro et al., 1991; Ellis et al., 1996).

The $1/V_{\max}$ technique has been devised to measure the space number density (dN/dV) via the small interval approximation:

$$\frac{dN}{dV} \approx \sum_{i=1}^N \frac{1}{V_a(i)}, \quad (1.8)$$

where $V_a(i)$ corresponds to the volume in which the object i , with luminosity $L(i)$ might have been still detected in the redshift bin Δz (Page and Carrera, 2000). With this approximation, the luminosity function can be estimated as:

$$\phi_{1/V_a}(L, z) = \frac{1}{\Delta L} \sum_{i=1}^N \frac{1}{V_a(i)}, \quad (1.9)$$

Another technique for the estimation of the **LF** values is called binned approximation. First described by Page and Carrera (2000), it refines the region in which each step of the **LF** is calculated as assuming a dependence on the redshift of the sources (as originally presented in the definition of **LF**, Eq. 1.6), concept which the $1/V_{\max}$ technique omits.

For the binned **LF**, it is assumed that the plane $L - z$ is divided into bins limited by fixed redshift values and luminosity values that depend on the conditions of the studied survey (i.e. the minimum luminosity at which a source can be detected). Therefore, the **LF** can be approximated as:

$$\phi \approx \phi_{\text{binned}} = \frac{N}{\int_{z_{\min}}^{z_{\max}} \int_{L_{\min}(z)}^{L_{\max}} \frac{dV}{dz} dz dL}, \quad (1.10)$$

where N corresponds to the number of sources in each bin. In this case, Eq. 1.10 needs to be calculated for the central point of each relevant bin of the plane $L - z$.

Finally, further methods to estimate the values of the **LF** can consider more complex mathematical expressions. That is the case of its calculation using a **kernel density estimation (KDE)** approach (Abramson, 1982; Davies et al., 2018b). As presented by Yuan et al. (2020) and Yuan et al. (2022), its implementation incorporates the addition of several kernels (one per source in the sample). Then, its complexity arises at the determination of the bandwidths (and additional parameters) of the kernels. The final expression of the **KDE-based LF** is then:

CHAPTER 1. INTRODUCTION

$$\phi \approx \phi_{\text{KDE}} = \frac{N(z_2 - z_1) \hat{f}(x, y | h_1, h_2)}{(z - z_1)(z_2 - z) \Omega \frac{dV}{dz}}, \quad (1.11)$$

where z_1 and z_2 are the redshift limits of the studied sample, $\hat{f}(x, y | h_1, h_2)$ corresponds to the density function of the pair (x, y) which is the equivalent of (z, L) in the [KDE](#) space, and N is the size of such sample.

Finish description of KDE LF

All the previous methods are non-parametric, meaning that they do not assume any analytic form or shape of the studied [LF](#). Contrary to that, several parametric models have been developed to determine an expression for the [LF](#).

As a way to test the number of sources we observe in different wavelengths, redshifts, and luminosities, simulations have been used to obtain an estimate of the number of [AGN](#) available to be observed with specific instruments and sensitivities (Habouzit et al., 2022). Some of these simulations (e.g. Amarantidis et al., 2019; Thomas et al., 2021; Bonaldi et al., 2019) have shown that the distribution of [AGN](#) and [RG](#) along redshift will lead to the detection of a few hundreds of objects per square degree closer to the end of the [EoR](#) with deep radio observations –e.g. [SKA](#), which is projected to have μ Jy point-source sensitivity levels (Prandoni and Seymour, 2015)–.

These expectations of an statistically significant number of [AGN](#) and [RG](#) in the high-redshift Universe do not match completely with the most recent compilations (e.g. Inayoshi et al., 2020; Ross and Cross, 2020; Fan et al., 2023), which show that close to 300 have been confirmed to exist at redshifts higher than 6 in the whole sky. This mismatch emphasises the need to detect and confirm the presence of more [AGN](#) than can match models and simulations.

1.1.1 AGN detection methods

The presence of an [AGN](#) can be confirmed (or hinted) in several ways depending on the observed, and desired, wavelengths. Historically, one of the first wavelengths used to confirm the nature of [AGN](#), and the dust enshrouding them, was [IR](#) (for a historical review, see Sajina et al., 2022). Assuming that the activity in [SMBHs](#) and some components of their host galaxies are correlated (see, for instance, Magorrian et al., 1998; Ferrarese and Merritt, 2000; Gebhardt et al., 2000; Häring and Rix, 2004; Gültekin et al., 2009; Beifiori et al., 2012; McConnell and Ma, 2013; Kormendy and Ho, 2013; Heckman and Best, 2014; and references therein), and the current unified model for [AGN](#) (Urry and Padovani, 1995; Urry, 2004; Netzer, 2015), most

of the activity from the accretion in **AGN** will be obscured by a dusty torus surrounding the **SMBH** (e.g. Lacy and Sajina, 2020). The peak of this activity will be correlated with that of the SF in the host galaxy, thus, increasing the fraction of obscured light observed in such systems (Madau and Dickinson, 2014). In this way, the highest probability of detecting an **AGN** will be by observing in **IR** wavelengths. **Expand on IR observations of AGN.**

As mentioned previously, X-ray is considered as an efficient way to confirm the presence of an **AGN** (e.g. Donley et al., 2005; Radcliffe et al., 2021a; Andonie et al., 2022). Based upon either their physical extension or the intensity of their emission, sources can be identified as **AGN** without large uncertainties (LSST Science Collaboration et al., 2009; Padovani et al., 2017; Maitra et al., 2019; Osorio-Clavijo et al., 2023). If an X-ray point source has a luminosity higher than $\sim 10^{42}$ erg s $^{-1}$, it is highly likely to be an **AGN** (Stern, 2015; Auge et al., 2023). Thus several sources have been detected in this way (e.g. Chen et al., 2017; Martocchia et al., 2017; Ricci et al., 2017; Goulding et al., 2018; Maitra et al., 2019; Lansbury et al., 2020; Coleman et al., 2022; Wasleske and Baldassare, 2023).

Many traditional **AGN** detection methods make use of spectral or photometric observations of objects which, based upon several criteria, determine their nature or class (Padovani et al., 2017; Hickox and Alexander, 2018; Pouliasis, 2020; Chaves-Montero et al., 2017). In the case of spectroscopy, Optical and **IR** observations have been used to look for the presence of emission lines that might indicate activity from **AGN** in their spectra (Magliocchetti, 2022). This method provides the best way to determine the presence of an **AGN**. One method derived from spectroscopic observations is the use of the **Baldwin-Phillips-Terlevich** (BPT; Baldwin, Phillips, and Terlevich, 1981) diagram, which, with the modifications made by Veilleux and Osterbrock (1987: also called VO diagrams), has been used extensively to detect and diagnose **AGN** and the **SMBH** they host based on detected emission lines (e.g. Toba et al., 2014; Sartori et al., 2015; Latimer et al., 2021; Birchall et al., 2020; Ceccarelli et al., 2022). The **BPT-Veilleux-Osterbrock (VO)** diagram uses ratios of the intensity of optical emission lines [O III] $\lambda 5007/\text{H}\beta$, [N II] $\lambda 6584/\text{H}\alpha$, [S II] $\lambda\lambda 6717, 6731/\text{H}\alpha$, and [O I] $\lambda 6300/\text{H}\alpha$ to determine the source of ionisation of the studied sources and separate them between **SFGs** and **AGN**. Further studies have used the **BPT-VO** diagrams but different thresholds to separate **SFGs** and **AGN** (e.g. Kewley et al., 2001; Kauffmann et al., 2003; Kewley et al., 2006; Schawinski et al., 2007). Figure 1.3 shows an example of the application of the **BPT-VO** diagrams, with different boundaries, to separate between **SFGs**, **AGN**, low-ionization nuclear emission-line region (**LINER**; Heckman, 1980)s, and composite galaxies (an intermediate state between the previous stages).

CHAPTER 1. INTRODUCTION

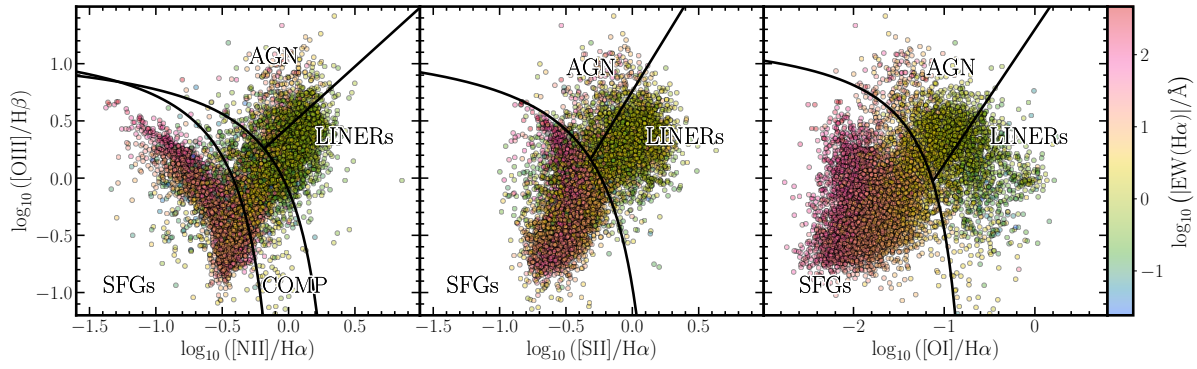


Figure 1.3: Example BPT-VO diagrams using data from sources in the [Mapping Nearby Galaxies at the Apache Point Observatory \(MaNGA\)](#) Pipe3D value added catalog data release 17 (Sánchez et al., 2018; Lacerda et al., 2022). Classification boundaries (as thick, black lines) from Kewley et al. (2001), Kauffmann et al. (2003), Kewley et al. (2006), and Schawinski et al. (2007). Points are coloured by the logarithm of the absolute value of the equivalent width of the H α following the coding of the colorbar and error bars have been omitted for clarity. The plot in the leftmost panel depicts the [O III] $\lambda 5007/\text{H}\beta$, and [N II] $\lambda 6584/\text{H}\alpha$ line ratios, which can help separating [SFGs](#) and composite galaxies from [AGN/LINERs](#). The middle panel, with the [O III] $\lambda 5007/\text{H}\beta$ and [S II] $\lambda\lambda 6717, 6731/\text{H}\alpha$ line ratios, helps classifying [SFGs](#), [AGN](#), and [LINERs](#). Finally, the rightmost panel presents the sources in the [O III] $\lambda 5007/\text{H}\beta$ and [O I] $\lambda 6300/\text{H}\alpha$ line ratios, which can also help separating [SFGs](#), [AGN](#), and [LINERs](#).

Additional diagrams have also been developed with the aim of using different combinations of emission lines. One remarkable example is the WHAN diagram (Cid Fernandes et al., 2010; Cid Fernandes et al., 2011), which uses the information of only two emission lines, the equivalent width of H α and the [N II] $\lambda 6584/\text{H}\alpha$ line ratio for [AGN](#) selection. An example of its application to a sample of sources is shown in Fig. 1.4, where a classification between [SFGs](#), [LINERs](#), and Seyfert galaxies (Osterbrock, 1981) is possible.

In the case of photometry measurements, some of these methods involve the classification of sources using colours (i.e. differences in magnitudes) in different wavebands as a starting point. Usually, one method used to confirm the presence of [AGN](#) in a sample is using [IR](#) or [near infrared \(NIR\)](#) colours. The most highly used data comes from photometric observations carried out with the [Wide-field Infrared Survey Explorer \(WISE\)](#) (Wright et al., 2010) or [Spitzer](#) (Werner et al., 2004). Several works have used combinations of [WISE](#) colours to derive main properties of [AGN](#) and their host galaxies (e.g. Stern et al., 2012; M12; Assef et al., 2013; Toba et al., 2014; Menzel et al., 2016; J17; Assef et al., 2018; Barrows et al., 2021). An example of its application is presented in Fig. 1.5, where sources can be separated between [AGN](#), star-forming disks, intermediate disks and spheroidal galaxies.

With observations from [Spitzer](#), similar schemes have been devised (e.g. Lacy et al., 2004; Donley et al., 2012). Based on the combination of measurements, different scales have been developed (e.g. Stern et al., 2005; Donley et al., 2012), which have been extensively used (e.g. Lacy et al., 2013; İkiz et al., 2020; Bonato et al., 2021; Lacy et al., 2021). Additional colour

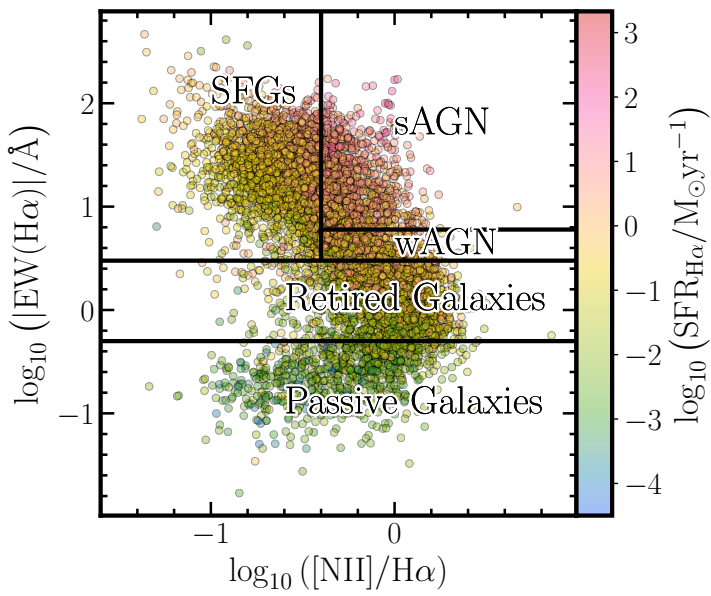


Figure 1.4: Example WHAN diagram using data from sources in the [MaNGA](#) Pipe3D value added catalog data release 17 (Sánchez et al., 2018; Lacerda et al., 2022). Classification boundaries in the $\text{H}\alpha$ equivalent width ($\text{EW}(\text{H}\alpha)$) – $[\text{N II}] \lambda 6584/\text{H}\alpha$ space (in thick, black lines) obtained from Cid Fernandes et al. (2010) and Cid Fernandes et al. (2011) following Kauffmann et al. (2003) and Kewley et al. (2006) which allow the classification of sources between **SFGs** in the upper-left region of the plot, Seyfert galaxies (called strong **AGN**, **sAGN**) in the upper-right corner, and **LINERs** in the bottom-right corner, which have been sub-divided between weak **AGN** (**wAGN**) and retired galaxies. Passive galaxies have been placed in the bottom side of the plot. Points are coloured by the logarithm of the integrated **star formation rate (SFR)** derived from the $\text{H}\alpha$ line following the coding of the colorbar and error bars have been omitted for clarity.

criteria have been developed for the latest and future facilities and observations (e.g. Messias et al., 2012; Kirkpatrick et al., 2017; Langeroodi and Hjorth, 2023; for JWST). An example of the application of such criteria is depicted in Fig. 1.6, in which sources can be selected as **AGN**.

Other techniques to determine the presence of **AGN** are related to the use of **SED** fitting, proper motion measurements, variability, and morphology. In the case of **SED** fitting, it implies comparing the available photometric measurements of an object to a series of model templates (Pacifici et al., 2023). The models have been constructed using different combinations of properties –e.g. age, metallicity, contribution from different constituents, etc.–. Thus, the examined source will be assumed to have the properties from the model which fits the best. If one of the properties included in the selected template is an **AGN**, then the studied source will be assumed to be an **AGN** as well.

High quality astrometric measurements (e.g. the *Gaia* mission; Gaia Collaboration et al., 2016) have allowed using proper motions for the detection of **AGN**. In particular, the use of the extragalactic content (Gaia Collaboration et al., 2023a) of its data release 3 (DR3; Gaia Collaboration et al., 2023b) has allowed to determine which sources have very small proper motions, which are indicative of large distances to a source and compatible with the presence of **AGN** or extragalactic sources in general (e.g. Storey-Fisher et al., 2023).

CHAPTER 1. INTRODUCTION

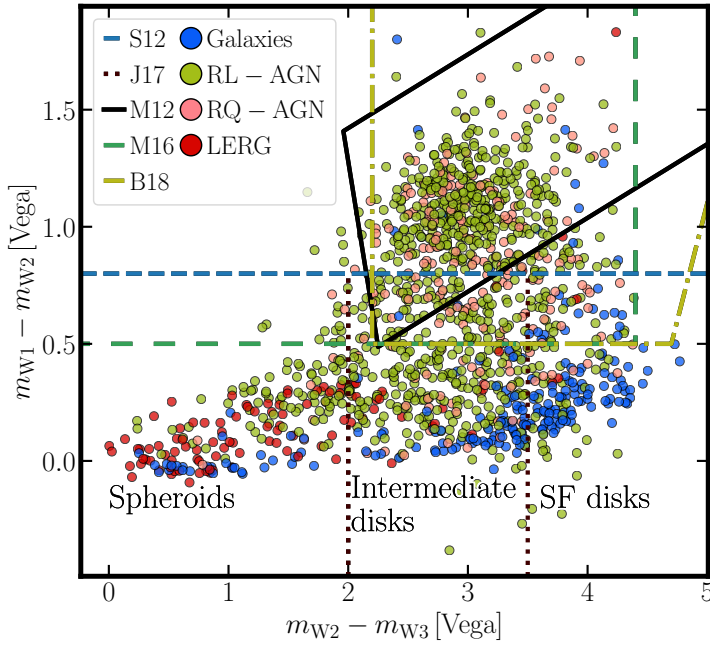


Figure 1.5: Example *WISE* colour-colour diagram for the selection of **AGN** from a set of sources obtained from the MIXR sample of **AGN** and **SFGs** M16. Points show the classification according to Mingo et al. (M16), as galaxies (i.e. **SFGs**), radio-loud (RL) AGN, radio-quiet (RQ) AGN, and LERGs. On top of the points, the lines of several classifications from Stern et al., 2012, M12, M16, J17, and B18 are presented as well as the labelling of the galactic regions of the plot as made by Jarrett et al. (J17). Error bars have been omitted for clarity.

Another way of assessing **AGN** is through the use of photometric measurements in different epochs that allow one to also determine the variability scales of a source. **AGN** present continuum aperiodic variability in all their observed wavelengths in timescales from hours to years (Giveon et al., 1999). There is, for instance, evidence of correlation between the **AGN** variability of fluxes in X-ray, **UV**, optical, and **NIR** bands (Uttley et al., 2003; Arévalo et al., 2008; Arévalo et al., 2009; Breedt et al., 2009; Breedt et al., 2010; McHardy et al., 2016; Troyer et al., 2016; Buisson et al., 2017; Suganuma et al., 2006; Koshida et al., 2009; Koshida et al., 2014; Lira et al., 2011; Lira et al., 2015). This variability also depends on luminosity, wavelength, redshift, presence of radio or X-ray emission, and existence of broad-line systems (Vanden Berk et al., 2004). For these reasons, if particular variability patterns are found in multi-wavelength observations of a source, it can be classified as an **AGN** candidate.

When high spatial resolution observations are used, morphology can be a suitable tool to determine the presence of either an **AGN** or a **SFG**. It has been found that the presence of an **AGN**, even when not observed directly, can affect the morphological parameters of its host galaxy (Getachew-Woreta et al., 2022) regardless of their morphological classification. This effect is due to the flux from the **AGN** that impact some areas of the host galaxy and their properties.

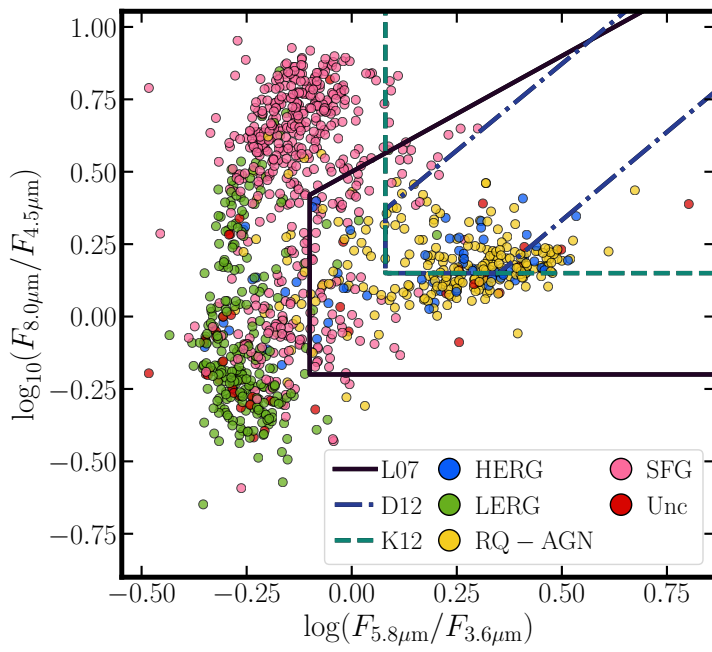


Figure 1.6: Example *Spitzer* colour-colour diagram for the selection of **AGN** from a sample of radio-detected sources obtained by Duncan et al. (2021) and Morabito et al. (2022). Point colours are related to the classification of the sources as given by Best et al. (2023), which can be **HERGs**, **LERGs**, **RQ AGN**, **SFGs**, or uncertain. On top of the points the **AGN** classification criteria from Lacy et al. (2007: L07), Donley et al. (2012: D12), and Kirkpatrick et al. (2012: K12) are plotted. Error bars have been omitted for clarity.

In the case of radio emission from **AGN**, its detection can be triggered by studies in different wavelengths which anticipate such measurement, which might then be confirmed by direct observations (e.g. Glikman et al., 2023). Nevertheless, the most used method for the discovery of sources in radio bands is using, directly, observations from radio surveys (Padovani, 2016; Padovani, 2017). As with measurements in other wavelengths, it is possible to obtain radio colours (called and defined accordingly, in this context, spectral indices, α , Lisenfeld and Völk, 2000), which might help determining whether the emission from a detected source is produced by an **AGN** or not. In the context of radio measurements, spectral indices, between two frequencies (ν_a and ν_b), are defined as the value of the slope a power law fitted to the radio flux would have (e.g. Zajaček et al., 2019),

$$\alpha_{\nu_a, \nu_b} = \frac{\log(F_{\nu_a}/F_{\nu_b})}{\log(\nu_a/\nu_b)}. \quad (1.12)$$

Bright **AGN**, for which most of their radio emission is understood to come from synchrotron processes, show spectral indices that are similar between them. In this way, it is possible to correlate the measured radio emission with the presence of an **AGN** (Condon, 1992). This might be coupled with studies that show a slight correlation between radio spectral index and radio luminosity for **AGN** (e.g. Sabater et al., 2019). Besides their spectral indices, special

CHAPTER 1. INTRODUCTION

care must be taken with sources that show low levels of radio emission. As explored by, for instance, Magliocchetti (2022), radio sources with low luminosities can have, as the source of their emission, both the **AGN** they host or star formation events. At low luminosity ranges, such as those reached by the latest radio observatories and surveys, it becomes difficult to differentiate between radio emission from **AGN** and that from **SF**. One simple approach to separate both populations, and to classify sources with faint radio luminosities, is using a single value for which all sources brighter than that might be labelled as **AGN**. Above a threshold in luminosity, it might be said that the radio emission detected in a source has been originated from the **AGN**. Several thresholds have been proposed using different approaches. Most of them have been devised for low-redshift regimes using the distributions of both **AGN** and **SFGs** (via **LFs**). For instance, one value used is $10^{25} \text{ W Hz}^{-1}$, above which sources can be considered, without large uncertainties, as radio-loud **AGN** (e.g. Williams and Röttgering, 2015; Mo et al., 2020). Conversely, when the derived luminosities are close or below the threshold, the fraction of the emission budget that comes from star-formation events increases.

Expanding on the idea of setting a threshold, it is possible to obtain a function for this limit that might depend on, for instance, redshift values. Given that the distributions of **AGN** and **SFGs** luminosities (i.e. **LFs**) have different behaviours, it is expected that the curves of both values will cross at some point (Magliocchetti, 2022). Following the results from Magliocchetti et al. (2014), which have been based upon the work of Magliocchetti et al. (2002), Mauch and Sadler (2007), and McAlpine et al. (2013), a threshold can be defined as a function of the redshift values of the sources. The expression can be written as follows:

$$\log_{10}(L_{\text{cross}}) = \log_{10}(L_{0,\text{cross}}) + z, \quad (1.13)$$

in which $L_{0,\text{cross}} = 5.01 \times 10^{21} \text{ W Hz}^{-1} \text{ sr}^{-1}$ for $z \leq 1.8$, and $L_{0,\text{cross}} = 3.16 \times 10^{23} \text{ W Hz}^{-1} \text{ sr}^{-1}$ for $z > 1.8$. After the addition of the angular factor 4π , these values can be expressed as $L_{0,\text{cross}} = 6.3 \times 10^{22} \text{ W Hz}^{-1}$ for $z \leq 1.8$ and $L_{0,\text{cross}} = 3.97 \times 10^{24} \text{ W Hz}^{-1}$ for $z > 1.8$.

The detection, selection, and analysis methods presented in the previous paragraphs can also be applied in the opposite direction for the detection of radio emission in **AGN**. This process implies searching for radio detections and, afterwards, classifying them as **AGN** (or any other kind of source). This procedure is based upon analysing the structure of the studied images and looking for features that might indicate the presence of an **AGN** (for instance, from their radio jets). Several tools have been developed to attain this goal. For instance, Python Blob Detector

and Source Finder (PyBDSF; Mohan and Rafferty, 2015), Blobcat (Hales et al., 2012b; Hales et al., 2012a), and Aegean (Hancock et al., 2012; Hancock et al., 2018). In general, these tools look for islands of emission in images and, depending on the selected detection level, they can merge these structures and create larger objects that can be linked to astrophysical sources (not only AGN). Once these radio detections have been determined, they need to be cross-matched with counterparts in different wavelengths in order to apply further methods to classify their nature and estimate further properties. When the characteristics of the detected radio emission are clearly those of AGN (for instance, from their morphology), multi-wavelength associations are not needed for their confirmation (as done, for instance, with the human-associated tasks of radio galaxy zoo projects; Bowles et al., 2023; Hardcastle et al., 2023)).

As already exposed, several techniques exist for the identification and classification of AGN. Given the focus of each of them on different properties of the observed source candidates, several works and techniques might identify the same source, independently, more than once. Thus, additional efforts are needed for the compilation of catalogues of confirmed AGN and the cleaning of duplicate sources across different techniques. Early efforts include the catalogues from de Veny et al. (1971) and Véron-Cetty and Véron (2010: in its last version), with more than 150 000 sources listed in their latest revisions.

In view of the large number of sources and the later focus on the study of high-redshift AGN, newer compilations included, mostly, sources at very far distances. That is the case, for example, of the catalogue by Perger et al. (2017), with sources at $z \geq 4.0$. Similarly, Ross and Cross (2020) compiled almost 500 QSOs at $z \geq 5.0$, Bosman (2022), created a list of $z \geq 5.7$ QSOs, while Inayoshi et al. (2020) and Fan et al. (2023) created lists of more than 200 $z \geq 6.0$ and more than 500 $z \geq 5.3$ AGN, respectively.

With the emphasis on very high-redshift sources, compilations of local-to-moderate redshift AGN have been updated very sparsely, making more difficult the study of large number of diversely confirmed AGN. One of the few catalogues which keeps including local sources is the Million Quasar Catalog (MQC; Flesch, 2015; Flesch, 2019), which attempts to list all confirmed AGN and QSOs. In its last edition (v8; Flesch, 2023), it includes more than 900 000 sources up to redshifts higher than 7.0. A depiction of the spatial distribution of the sources in the version 8 of the MQC is presented in Fig. 1.7. It can be seen that, from its sparse spatial distribution, a large number of individual catalogues and listings have been assembled, highlighting the breathtaking effort needed for creating such compilation.

CHAPTER 1. INTRODUCTION

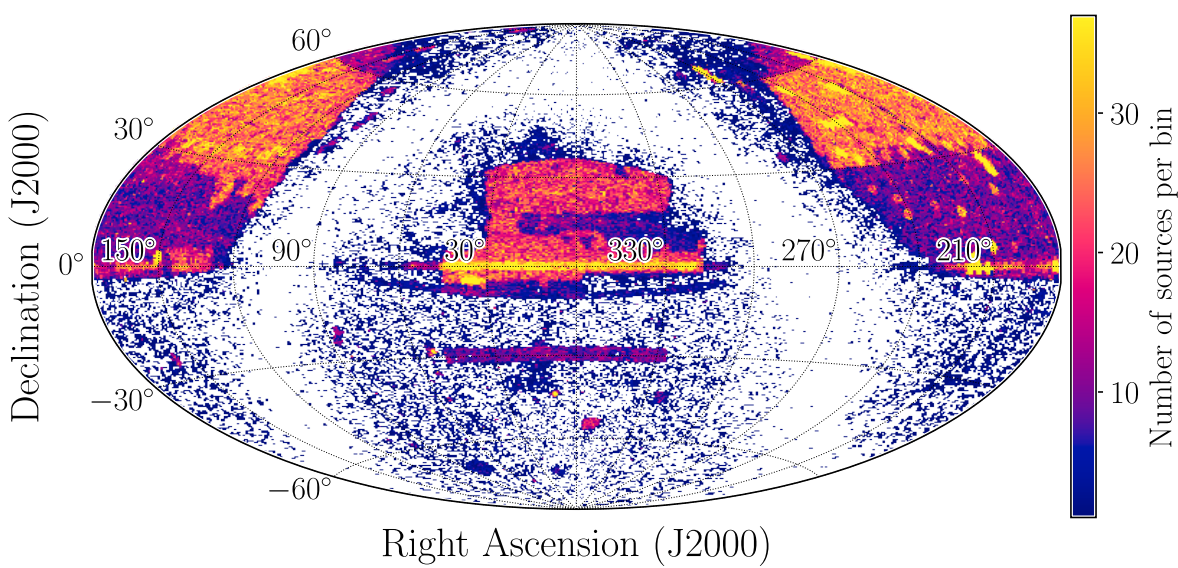


Figure 1.7: Million Quasar Catalog v8 source density in a Hammer-Aitoff projection (Snyder, 1987; Snyder, 1997) of the sky. Each coloured rectangle shows the number of [AGN](#) in that particular region of the sky as catalogued by the [MQC](#) following the code in the colorbar. Each overdensity, with respect to its surroundings, represents a different source catalogue or listing from which [AGN](#) have been drawn. More noticeable are, for instance, the areas covered by the [SDSS](#) observations.

1.1.2 Redshift determination

In order to determine a precise distribution of [AGN](#) across cosmic time, unambiguous redshift measurements are needed (e.g. Huterer et al., 2006; Tanaka et al., 2018; van den Busch et al., 2020; Naidoo et al., 2023). Spectroscopic redshifts, being the most precise measurements, can be determined for a large range of objects, from supernovae (e.g. Frederiksen et al., 2014; Baltay et al., 2021), to galaxies (e.g. Le Fèvre et al., 2015; Galametz et al., 2013), and [AGN](#) (e.g. Rajagopal et al., 2021). Spectroscopic redshifts can be obtained by cross-correlation or fitting of the observed data and set of templates (Tonry and Davis, 1979; Schuecker, 1993; Glazebrook et al., 1998; Aihara et al., 2011; Machado et al., 2013) or by the direct detection and matching of powerful spectral features (Kurtz and Mink, 1998; Stoughton et al., 2002; Garilli et al., 2010). However, their determination can take long and high-quality observations, which are not always available for all sources, rendering them not suited for large-sky catalogues (see, for instance, Silva et al., 2011; Pacifici et al., 2023).

Photometric redshifts are an option which comes from the use of photometry measurements and not explicit spectral features of an object (Salvato et al., 2019; Brescia et al., 2021; Newman and Gruen, 2022). In general, they use observations that take less integration time than a comparable spectroscopic measurement and, thus, are used for large surveys that need measurements for large numbers of objects (e.g. Hoyle et al., 2018; Tanaka et al., 2018). They are also an option for faint sources.

Photometric redshift methods can deliver a probability for their redshift estimations in the form of a [probability density function \(PDF or \$p\(z\)\$ \)](#). These functions can deliver a measure of the uncertainties that photometric redshifts might have. In general terms, photometric redshifts can be obtained using two different methods: template-based techniques and empirical relations.

Template-based methods come from the fitting of multi-wavelength photometry of a source to a model template (Baum, 1957; Baum, 1962; Loh and Spillar, 1986; Newman and Gruen, 2022; Pacifici et al., 2023). The models have been constructed using different combinations of properties –e.g. age, metallicity, contribution from different constituents, etc.–. Thus, the examined source will be assumed to have the properties from the model which fits the best. However, and depending upon the number and quality of the photometry measurements (e.g. low spectral resolution), these properties can have, sometimes, large uncertainties. Even though this method can use less precise values to determine a redshift, it can take a significative amount of time since it needs to contrast the measured [SED](#) to the full set of model templates and, when the number of available measurements is low, the quality of the estimation is largely degraded (e.g. Norris et al., 2019).

Using this method, redshift estimations can be obtained from, for instance, galaxies (e.g. Hernán-Caballero et al., 2021), and [AGN](#) (e.g. Ananna et al., 2017; Brescia et al., 2019). As expected, the quality of photometric redshift estimates is highly correlated with the quality of the photometry data used for their determination (Newman et al., 2015; Newman and Gruen, 2022).

Some example tools that use template-based methods to retrieve photometric redshifts are [Easy and Accurate \$z_{\text{phot}}\$ from Yale \(EAZY; Brammer et al., 2008\)](#), [Bayesian Photometric Redshifts \(BPZ; Benítez, 2000\)](#), and [Photometric Analysis for Redshift Estimate \(Le PHARE; Arnouts et al., 1999; Ilbert et al., 2006\)](#).

Examples of SED fitting tools and how they work

For the case of empirical relations, the retrieval of photometric redshifts relies on the use of statistics and large sets of observables (e.g. fluxes and their uncertainties) to determine redshifts and correlations between them which can be used with future observations. Most of these empirical redshift determination methods are related to the use of [machine learning \(ML; Samuel, 1959\)](#). These techniques will be further described in this work.

Finally, redshift values can also be determined approximately. Using differences among magnitudes –i.e. colours– it is possible to establish the redshift range in which a source is located. This technique –called drop-out (Steidel et al., 1996a; Steidel et al., 1996b)– is, by no means,

CHAPTER 1. INTRODUCTION

precise, but can lead to further investigation of sources that are at relevant redshifts ranges for the researcher (with, for instance, the previously described photometric redshift methods). In this way, drop-outs are employed as a mean to generate candidates for pertinent redshift values. Given that it requires no more calculations than the comparison of some series of colours, it is highly efficient at generating rough redshifts of large samples. It has been, mainly, used to generate and study high-redshift sources or candidates that, otherwise, would not have enough information to produce a precise redshift value (e.g. Bouwens et al., 2020; Carvajal et al., 2020; Merlin et al., 2021; Uzgil et al., 2021; Champagne et al., 2023; Atek et al., 2023).

Since its first uses, this technique has allowed the detection of high-redshift galaxies (Steidel and Hamilton, 1992; Steidel et al., 1996a) through the detection of sharp break in flux between broadband filters that sample the vicinities of the Lyman Break (at a rest-frame wavelength of 912 Å). The location of such break is a function of redshift allowing, thus, to obtain a crude estimate of the redshift for the studied objects.

1.2 Challenges in the analysis of astronomical data

The progress of technology and methods used in astrophysics has been one of the main drivers for the advancement in our knowledge and understanding of the processes taking place in the Universe. But this undeniable improvement has brought some drawbacks that pose serious challenges that might hinder our ability of retrieving useful results from astronomical data. Most of these problems are rooted in the very large number of new and different observational efforts carried out throughout the years. This abundance of measurements can impact the processes that lead to new calculations and results since more resources and steps are needed to treat a large number of measurements consistently.

As more sources are needed to better constrain the properties of astronomical sources, new data sets have been compiled and published. Nowadays, multi-wavelength data are available for large fractions of the sky (e.g Gaia Collaboration et al., 2016; Chambers et al., 2016; Lacy et al., 2020; Kollmeier et al., 2017; Wright et al., 2010; Skrutskie et al., 2006; Abbott et al., 2018). But this profusion of observations has come with new challenges with the most relevant being the volume of data. Lately, analysing all observations, one by one with traditional methods, has become unfeasible in terms of the time needed to fulfil the task (see, for instance, Brescia et al., 2021). This issue will become greater as future surveys and telescopes are put into service, with relevant examples being the SKA and the Legacy Survey of Space and Time (LSST; LSST

Science Collaboration et al., 2009; Ivezić et al., 2019).

Furthermore, over the last couple of decades, the observational capabilities of single instruments have been improved largely. It has become possible to retrieve measurements of very large areas of the sky without important variations in the observational properties (noise, calibration, etc.). The improvement in the overall properties of observations has made possible the production of surveys than can cover relevant fractions of the sky. Some examples include the [FIRST](#), the [Two Micron All Sky Survey \(2MASS\)](#); Cutri et al., 2003a; Cutri et al., 2003b; Skrutskie et al., 2006; Wright et al., 2010; hereafter [2M](#)), the [VLASS](#), the [Pan-STARRS](#), the [Galaxy Evolution Explorer \(GALEX\)](#); Morrissey et al., 2007), and the [AllWISE \(AW\)](#); Cutri et al., 2013; hereafter [AW](#)). In the near future, they will be complemented by the [LSST](#) in the Vera C. Rubin Observatory, the [SKA](#), the [ngVLA](#), and *Euclid* (e.g. Euclid Collaboration et al., 2022), among others.

While being able to obtain information from more sources and regions of the sky is, by itself, a very relevant improvement, such number of new measurements to analyse have brought some issues related to the treatment of very large datasets (for a review focused on the challenges of future radio surveys, see Norris, 2017). Some of these obstacles are described in the following sub-sections.

1.2.1 Computational costs

Using very large surveys and catalogues for any sort of calculation involves, accordingly, very high computational costs. Recent observational catalogues might have up to billions of entries with several attributes each and large-area images can cover thousands of square degrees with very high angular resolution, reaching total sizes of tens of TB of data and tens of PB for future surveys (Mickaelian, 2020). Additionally, survey instruments will have data transfer rates well above the normal capabilities of a medium-sized server, reaching up to several TB/day rates (Enke et al., 2012). Dealing with such large datasets requires large amount of resources that are not completely available to everyone (Garofalo et al., 2017).

Additionally, most of the methods traditionally used for the detection, classification, and extraction of properties for astrophysical sources have not been developed, or updated, to be used with very large catalogues. For this reason, using them in the most recent catalogues and surveys can take restrictive running times that not even the most powerful computing facilities can deal with given their memory or [central processing unit \(CPU\)](#) usage. Even if current

CHAPTER 1. INTRODUCTION

methods are optimised for their use in large computational facilities, running times would still be prohibitively long.

A further factor to consider is that of the energy expense of running such methods for long times in powerful machines. Excessive power consumption can impact negatively, first, in the economical costs of running calculations and, second, in the emission of greenhouse effect gases derived from the energy needed for computation. Reduction of CO₂ emissions from energy consumption can help alleviating the impact from the climate change (IPCC, 2022). While complete net-zero systems are expected to solve this issue, short-term reduction in the use energy spending are needed to help limiting global warming.

With a focus on ease of use and code readability, Python has become a standard language in most of recent astrophysical packages (Astropy Collaboration et al., 2022). Conversely, code written in Python tends to be one of the least efficient in its ecological impact (Portegies Zwart, 2020). Thus, and taking into account that the popularity of Python should not decrease in the short-term, it is needed to use techniques and code that can obtain results in shorter times than those available to date.

If needed, use big data citations (Zhang and Zhao, 2015)

1.2.2 Missing measurements

As with any sort of physical measurement, a fraction of observations might have issues that can render them unusable for any meaningful calculation (Rubin, 1976; Josse and Reiter, 2018). These problems include malfunction of detectors or incorrect cleaning of the data, among others. If different measurements (i.e. in different points in time) are to be combined, some sources might have been observed in one instance but not in the remaining ones. This might affect the study of time series or multi-wavelength, multi-instrument observations.

Furthermore, some analysis methods require that all measurements need to be available and the lack of one of them can render the full set of quantities from a source useless (Little and Rubin, 2014).

1.2.3 Multi-wavelength counterpart identification

In the case of observations with different filters or different instruments, a new problem might arise. It involves the correct identification of the sources observed in each of the filters. Given that the emission in different wavelengths and different moments in time might come from

separate components and processes in the studied objects, each observed instance can present a structure that does not match the others. For this reason, finding and matching counterparts for detected sources can be difficult. This problem is enhanced when observations in several bands and different instruments need to be combined.

Several approaches have been used to mitigate this problem. The simplest of them involves taking the closest source (within a defined search radius) as the counterpart without analysing any physical correlation between the underlying processes that might give rise to the observed emission. If not performed carefully, this technique might introduce identification errors where overlapping sources can be identified as a single object.

More complex procedures attempt to flag as counterpart the sources with the highest likelihood of being produced in the same position in the space (three dimensional space). One such example corresponds to **NWAY** (Salvato et al., 2018), which can match several catalogues using not only sky coordinates but also additional information such as magnitudes or colours.

1.3 Machine-assisted pattern detection

Taking into account all the issues that the analysis of large datasets might pose, new tools have been developed as a way to tackle them. For astrophysics, in particular, the existence of these major **AGN** detection, radio measurement, and redshift determination methods raises the need of new techniques which might be able to obtain these properties for large amounts of astrophysical sources with enough precision within a shorter amount of time.

Given that this is a problem suffered by several scientific and, even, non-scientific disciplines (e.g. business-related applications; Costa-Climent et al., 2023), large efforts have been put in order to solve it and many techniques have been developed to deal with the ever-increasing data volumes. New statistical and computer methods can analyse thousands or millions of elements and find relevant trends among their properties (Garofalo et al., 2017) within reasonable time frames. One branch of these techniques is able to, using previously-fed data, predict, with relevant confidence, the behaviour new data will have –i.e. the values of their properties–. This is what has been called **ML**.

In Astronomy, **ML** has been used in a wide range of subjects, such as redshift determination (e.g. Nakoneczny et al., 2021; Wenzl et al., 2021), morphological classification (e.g. Ma et al., 2019; Lukic et al., 2019; Mostert et al., 2021; Vardoulaki et al., 2021; Burhanudin et al., 2021), emission prediction (e.g. Dobbels and Baes, 2021), anomaly detection (e.g. Baron and

CHAPTER 1. INTRODUCTION

Poznanski, 2017; Giles and Walkowicz, 2019; Lochner and Bassett, 2021; Storey-Fisher et al., 2021; Wagstaff et al., 2022), image reconstruction (e.g. Guglielmetti et al., 2022; Adam et al., 2023; Wilber et al., 2023), observations planning (e.g. Garcia-Piquer et al., 2017; Jia et al., 2023; Sravan et al., 2023), and more (Ball and Brunner, 2010; Baron, 2019; Sen et al., 2022; Huertas-Company and Lanusse, 2023). With **ML**, it is possible to use previously available measurements and extract useful trends and correlations that can suggest the behaviour of properties from future observations or simulations. **ML** models are, in general, only fed with measurements and not with physical assumptions (Desai and Strachan, 2021) and they do not need to check the consistency of the predictions or results they provide. This can bring, as a consequence, that running times for this kind of algorithms might be less than typical physically-based codes (e.g. Buchner, 2019).

1.3.1 Types of machine-assisted analyses

Concentrating our review on the application of **ML**, two main branches exist for the application of such techniques. The first of them, called supervised learning, deals with the idea that, for each set of measurements, there is a response value that, via modelling, we can predict with some degree of confidence (James et al., 2023). On the other side, unsupervised learning refers to the analysis of data that does not have an associated quantity. One of the most popular applications of unsupervised learning is clustering of elements. Modelling data would imply separating them by how similar are their properties (or a combination of them). Then, in the case of supervised learning, further divisions are possible. If the predicted variable (target) is a discrete quantity, this prediction is called a classification. Opposite to that, if the predicted target is continuous, the process is called regression.

1.3.2 Ensemble learning

By design, each **ML** algorithm has been developed and tuned to work better with certain data conditions, that is, balance of target categories, ranges of base features, sparsity of values, etc. One technique used to combine the properties of algorithms and improve the results of a prediction is that of ensemble learning. It involves the joint use of individual results from **ML** models, that have been trained to solve the same problem, into one larger model or rule that can deliver a final prediction (Schapire, 1990; Breiman, 1996; Freund and Schapire, 1996). It has been shown that the combination of several models, and their predictions, can improve the

overall prediction results (Opitz and Maclin, 1999).

In order to combine several prediction into a final result, several options are available. The most used, and one of the earliest, ways to merge all individual predictions consists of averaging each predicted value into the final prediction (e.g. Sollich and Krogh, 1995). This option is useful for both regression and classification tasks (using its output scores). For the specific case of classification, a voting system can be implemented, where the majority of decisions of the base individual predictors is taken as the final predicted class. This method has been proven to work efficiently (Schapire et al., 1998).

The predicting power of different algorithms can be combined with the use of meta-learners (Vanschoren, 2019). Meta-learners use the properties or predictions from other algorithms (base learners) as additional information during their training stages. A simple implementation of this procedure (and a third method to combine individual predictions) is called Generalised Stacking (Wolpert, 1992) which can be interpreted as the addition of priors to the model training stage. In this way, two levels of predictors are used. The first level includes all the individual models that are trained on the training set. The second level corresponds to a single model which is trained only on the outputs of the first-level models. Generalised stacking has been applied in several astrophysical problems. That is the case of Zitlau et al. (2016), Carvajal et al. (2021), Cunha and Humphrey (2022), Moya and López-Sastre (2022), Zammit and Adami (2023), Euclid Collaboration et al. (2023a), and Euclid Collaboration et al. (2023b).

1.3.3 Model explainability and feature importance

Despite the large number of applications it might have, **ML** has received important criticism related to the lack of interpretability –or explainability, as it is called in **ML** jargon– of the their derived models, trends, and correlations. Most **ML** models, after taking a series of measurements and properties as input, deliver a prediction of a different property. But they cannot provide coefficients or an analytical expression, that might allow to find an equation for future predictions (Goebel et al., 2018). An important counter-example of this fact is the use of Symbolic Regression (Gerwin, 1974; Langley, 1977; Langley, 1979; Langley et al., 1981; Langley and Zytkow, 1990), which has been developed to extract explicit analytic expressions from the analysed data. Some examples of the use of symbolic regression in astrophysics are Cranmer et al. (2020), Villaescusa-Navarro et al. (2021), and Cranmer (2023). The lack of explainability implies that, for most **ML** models, it is not a simple task to understand which

CHAPTER 1. INTRODUCTION

properties, and to what extent, help predict and interpret another attribute. This fact hinders our capability to understand the results in physical terms and extrapolate **ML** results into further ranges of properties.

Besides the development of symbolic regression, recent work has been done to overcome the low levels of explainability in **ML** models. The most widely used assessment is done with feature importance (Casalicchio et al., 2019; Roscher et al., 2020), both global and local (Saarela and Jauhainen, 2021). Feature importance analysis helps to know the relative weights that the measured properties have in the decision-making process. In this way, physical insight might be gained about the correlations or triggers between different properties (observed or derived) of the objects of study.

Global importances were retrieved using the so-called ‘decrease in impurity’ approach (see, for example, Breiman, 2001). Local importances have been determined via Shapley values. A more detailed description of what these importances are and how they are calculated is given in the following subsections.

Global feature importances

Overall, mean or global feature importances can be retrieved from models that are based on Decision Trees (e.g. Random Forests and Boosting models, Breiman, 2001; Breiman, 2003). For each feature, the decrease in impurity (a term frequently used in the literature related to **ML**) of the dataset is calculated for all the nodes of the tree in which that feature is used. Features with the highest impurity decrease will be more important for the model (Louppe et al., 2013). For some models that are not based on Decision Trees, feature importances can be obtained from the coefficients that the training process delivers for each feature. These coefficients are related to the level to which each quantity is scaled to obtain a final prediction (as in the coefficients from a polynomial regression). Insight into the decision-making of the pipeline can only rely on the specific weights of the original set of features (see Sect. 3.4).

Local feature importances

As opposed to the global (or mean) assessment of feature importances derived from the decrease in impurity, local (i.e. source by source) information on the performance of such features can be obtained from, for instance, Shapley values. This is a method from coalitional game theory that tells us how to fairly distribute the dividends (the prediction in our case) among

the features (Shapley, 1953). The previous statement means that the relative influence of each property from the dataset can be derived for individual predictions in the decision made by the model (which is not the same as obtaining causal correlations between features and the target; Ma and Tourani, 2020). The combination of Shapley values with several other model explanation methods was used by Lundberg and Lee (2017) to create the SHapley Additive exPlanations (**SHAP**) values. In this work, **SHAP** values are calculated using the python package **SHAP**¹ and, in particular, its module for Tree-based predictors (Lundberg et al., 2020). To speed calculations up, the package **FastTreeSHAP**² (v0.1.2; Yang, 2021) is also used, which allows for multi-thread runs.

One graphical way to display these **SHAP** values is through the so-called decision plots. They can show how individual predictions are driven by the inclusion of each feature. Besides determining the most relevant properties that help the model make a decision, it is possible to detect sources that follow different prediction paths which could be, eventually and upon further examination, labelled as outliers.

Game theory based analyses, such as the Shapley analysis (Shapley, 1953), have also been used to understand the importance of features in astrophysics (e.g. Machado Poletti Valle et al., 2021; Carvajal et al., 2021; Dey et al., 2022; Anbagane et al., 2022; Alegre et al., 2022; Carvajal et al., 2023a).

1.4 This thesis

Attending to the difficulties in relating radio emission from **AGN** with measurements of these sources in additional wavelengths, the main goal of this thesis is to explore and understand possible indicators of the radio emission in **AGN** from multi-wavelength, multi-instrument, measurements. Thus, we want to develop a process that, in particular, can take information from **IR**-detected sources (for which there is all-sky coverage with good sensitivity levels) and deliver an indication of whether these sources can correspond to **AGN** and, more specifically, to radio-detectable **AGN**.

Given the importance of the detection of **AGN** in early epochs of the Universe, we also aim to use the aforementioned machinery to derive estimates of photometric redshifts for the sources labelled as prospective radio-detectable **AGN**. In that way, the focus of our search can

¹<https://github.com/slundberg/shap>

²<https://github.com/linkedin/fasttreeshap>

be put in the selection of sources as close as possible to the epoch of reionisation. Or at least, in redshift ranges suitable for specific studies.

Having outlined the major issues that exist with the use of new astronomical datasets and surveys (cf. Chapter 1), the use of machine-assisted techniques (and in particular, **ML**, which aims at the use of available datasets to find relevant trends among their properties to estimate the behaviour of new, unseen data, Samuel, 1959) becomes more relevant than ever before (see Sect. 1.2). The possibility of analysing very large datasets with reduced computational costs (in time and energy consumption) is one of the main drivers behind the development of this work.

Following the production of candidates for radio-detectable **AGN**, together with their redshift values, we aim to understand the predictions and how they relate to physical properties of the analysed sources. For this goal, we want to apply feature importance analyses to the prediction processes. These techniques can help understanding the inner correlations and trends that allow the creation of several selection rules and prediction schemes for the creation of predicted sources and some of their properties.

Once the mechanisms leading to the prediction of radio-detectable **AGN**, and their redshift values, have been understood, we want to apply such indicators and the candidates derived from their use to the analysis and possible solution of different problems related to the observation, classification, and distribution of radio-detected **AGN**. The application of **ML** techniques can help creating large collections of candidate radio-**AGN** that might not have been available previously. The use of such sources might, then, contribute to the improvement of the answers for the questions previously mentioned.

In Fig. 1.8, we present a flowchart of the prediction pipeline we propose for the generation of radio-detectable **AGN** candidates. We aim to start with a set of **IR**-detected sources with ancillary multi-band data that can be fed into the first step that classifies between **AGN** and **SFGs** (i.e. not hosting an **AGN**). Given that we are interested in **AGN**, we use the predicted **AGN** and feed them into the second step, which classifies **AGN** according to their radio detectability. After this step, we select the predicted **AGN** that have a high likelihood of being radio-detectable. A final step uses the predicted radio-detectable **AGN** and estimates a redshift value for them. Consequently, the prediction pipeline delivers a set of candidate radio-detectable **AGN** with an redshift estimate.

Given the structure of the pipeline, the **ML** models in each step will be trained with a different sample of sources. The first step, classification between **AGN** and **SFGs** will be trained with all available sources that have been labelled previously as either **AGN** or **SFGs**. The second

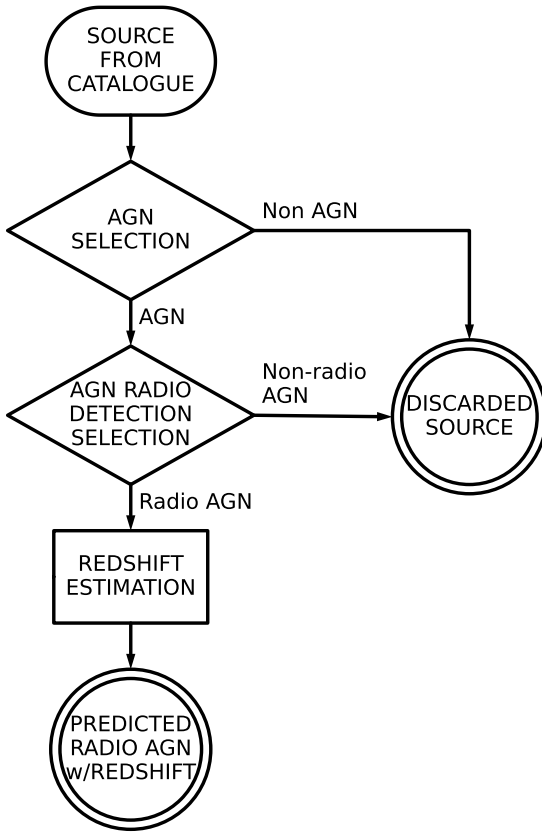


Figure 1.8: Flowchart representing the proposed prediction pipeline used to predict the presence of radio-detected **AGN** and their redshift values from **IR**-detected sources.

step, classification of radio detection in **AGN**, will be modelled only with confirmed **AGN** (with or without radio detections). Finally, the third step of the pipeline, which estimates photometric redshifts, will be trained with radio-detected **AGN**. Our focus on radio-detectable **AGN** is the basis for the omission of the remaining sources in the data sets.

Part of this thesis is based on the work and analyses presented by Carvajal et al. (2021) and Carvajal et al. (2023a). In the following chapters, we present the data sets (as well as the treatment applied to them) used for the generation of the models (Chapter 2), the result of the selection of models and their training (Chapter 3), and the analyses of the use of the prediction pipeline on the selected data sets (Chapter 4). Furthermore, Chapter 5 describes the analysis of the predictions and the models themselves using different approaches. Finally, Chapters 6 and 7 introduce extensions of the use of the results from the prediction pipeline in different contexts as well as future developments to be applied to the prediction pipeline and its individual steps. This thesis concludes with a summary, where final remarks and findings are outlined.

This page intentionally left blank.

Studied datasets

In order to train all models efficiently and test them without fears of obtaining biased metrics, good quality data are needed. This requirement can be translated into selecting a field with coverage in several bands and by diverse instruments. This variety can help the training of the models to cover a broad fraction of the parameter space.

Furthermore, these measurements need to be spread over a sufficiently large area as a way to avoid any bias from using sources that might be connected in some manner. Additionally, in order to validate the predictions from the models, the selected field needs to have a adequate number of sources with certain classifications.

As an extension of the previous requirement, it is desirable that the surveys that cover the selected area also have a much larger footprint. In this way, it will be possible to apply the trained models to different areas of the sky as an further test to our techniques. Thus, all-sky measurements will be prefered over compact (but maybe deeper) surveys.

Finally, and given that one of the goals is predicting radio detectability of sources, the chosen area must have deep and homogeneous radio coverage. If a shallow radio survey is used, the trained model will have access to only a small fraction of possible detections of RGs, which might bias the predictions and their assessment.

2.1 HETDEX Spring field

As training field we selected the area of the Hobby-Eberly Telescope Dark Energy Experiment ([HETDEX](#); Hill et al., 2008) Spring Field covered by the first data release of the [LoTSS](#). The [LoTSS](#) survey covers 424 deg^2 in the [HETDEX](#) Spring field (hereafter, [HETDEX](#) field, see Fig. 2.1) with [Low Frequency Array \(LOFAR\)](#) (van Haarlem et al., 2013) 150 MHz observations that have a median sensitivity of $71 \mu\text{Jy}/\text{beam}$. The deep radio observations in this field can help the training stages to retrieve information from a large fraction of sources in the area. [HETDEX](#) provides, as well, multi-wavelength homogeneous coverage as described in Sect. 2.3.

CHAPTER 2. STUDIED DATASETS

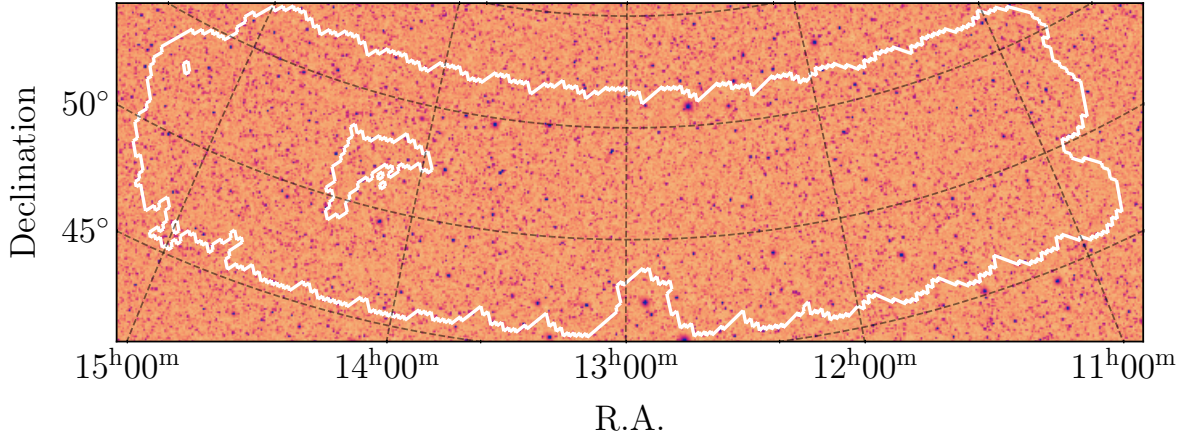


Figure 2.1: Footprint of the area used in the [HETDEX](#) field for this work. In the background, W1 image from the [unWISE](#) coadds (Lang, 2014; Meisner et al., 2022). The white contours limit the area of the [HETDEX](#) field.

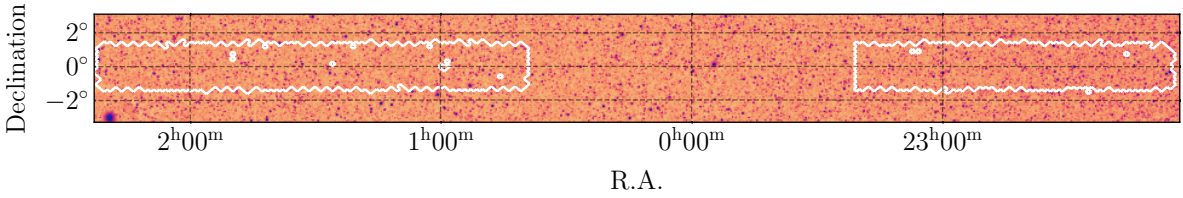


Figure 2.2: Footprint of the area used in the [VLAS82](#) field for this work. In the background, W1 image from the [unWISE](#) coadds (Lang, 2014; Meisner et al., 2022). The white contours limit the area of the [VLAS82](#) field.

2.2 Stripe 82 field

In order to test the performance of the models when applied to different areas of the sky, and with different coverages from radio surveys, we have selected the [SDSS Stripe 82 Field](#) ([S82](#); Annis et al., 2014; Jiang et al., 2014). For [S82](#), we collected data from the same surveys as with the [HETDEX](#) field (see the following section) but with one important caveat: no [LoTSS](#) data is available in the field and, thus, we gathered the radio information from the [VLA SDSS Stripe 82 Survey](#) ([VLAS82](#); Hodge et al., 2011). [VLAS82](#) covers an area of 92 deg^2 with a median rms noise of $52 \mu\text{Jy}/\text{beam}$ at 1.4 GHz. We have selected the [S82](#) field (and, in particular, the area covered by [VLAS82](#), see Fig. 2.2) given that it presents deep radio observations but taken with a different instrument than [LOFAR](#). This difference allows us to test the suitability of our models and procedures in conditions that are not exactly the same as those from the training circumstances.

One expected caveat is that, given the shallower nature of the radio observations in [S82](#), the model might predict the radio detection of a source but it might be fainter than the limit from [S82](#). This will be taken into account when comparing metrics between fields.

Table 2.1: Bands available for model training in our dataset

Survey	Band (Column name)
Pan-STARRS (PS1)	g (<code>gmag</code>), r (<code>rmag</code>), i (<code>imag</code>), z (<code>zmag</code>), y (<code>ymag</code>)
2MASS (2M)	J (<code>Jmag</code>), H (<code>Hmag</code>), Ks (<code>Kmag</code>)
CatWISE2020 (CW)	W1 (<code>W1mproPM</code>), W2 (<code>W2mproPM</code>)
AllWISE (AW)	W3 (<code>W3mag</code>), W4 (<code>W4mag</code>)

^a In parentheses are shown the names of the columns or features in our dataset that represent each band.

2.3 Photometry measurements

The base survey from which all the studied sources have been drawn is the [CatWISE2020](#) ([CW](#); Marocco et al., 2021). It lists [NIR](#)-detected elements selected from [WISE](#) and [Near-Earth Object WISE](#) ([NEOWISE](#); Mainzer et al., 2011; Mainzer et al., 2014) over the entire sky at $3.4\text{ }\mu\text{m}$, $4\text{ }\mu\text{m}$ and $6\text{ }\mu\text{m}$ ([W1](#) and [W2](#) bands, respectively). This catalogue includes sources detected at 5σ in either of the used bands (i.e. $\text{W1} \sim 17.43$ and $\text{W2} \sim 16.47\text{ mag}_{\text{Vega}}$ respectively). The [HETDEX](#) field contains 15 136 878 sources listed in [CW](#). Conversely, in the [S82](#) field, there are 3 590 306 of them.

Multi-wavelength counterparts for [CW](#) sources were found on other catalogues applying a $1''1$ search radius criteria. These catalogues include [Pan-STARRS Data Release 1](#) ([PS1](#); Chambers et al., 2016; Flewelling et al., 2020), [2M](#), and [AW](#)¹. The adopted search radius corresponds to the distance that has been used by Wright et al. (2010) to match radio sources to [PS1](#) and [WISE](#) observations and is the smallest [point-spread function \(PSF\)](#) size of the bands included in [PS1](#) (Chambers et al., 2016). Furthermore, the source density of the radio ([LOFAR](#), [VLA](#)) and [2M](#) catalogues imply a low statistical ($< 1\%$) spurious counterpart association, this is not the case for [PS1](#), where the source density is higher. For these reasons, and to maintain a statistically low spurious association between [CW](#) and [PS1](#), we limited our search radius to $1''1$. A list of used bands and their origin instruments and surveys is shown in Table 2.1.

For the purposes of this work, observations in [LoTSS](#) and [VLAS82](#) are only used to determine whether a source is radio detected, or not. In particular, no check has been performed on whether a selected source is extended or not in any of the radio surveys. A single Boolean feature is created from the radio measurements (see Sect. 2.5) and no further analyses were performed regarding the detection levels that might be found in any of the fields.

¹For the purposes of the analyses, and except when clearly stated otherwise, all photometric measurements were converted to AB magnitudes.

CHAPTER 2. STUDIED DATASETS

Table 2.2: Density of detected sources (in units of sources per square degree) per band and field.

HETDEX Field							
Band	Density (deg ⁻²)	Band	Density (deg ⁻²)	Band	Density (deg ⁻²)	Band	Density (deg ⁻²)
g	6380.66	z	10 331.93	H	1335.55	W2	35 700.18
r	9304.58	y	6735.97	Ks	1335.55	W3	14 045.08
i	11 242.35	J	1335.55	W1	35 700.18	W4	14 044.78

S82 Field							
Band	Density (deg ⁻²)	Band	Density (deg ⁻²)	Band	Density (deg ⁻²)	Band	Density (deg ⁻²)
g	8249.04	z	13 214.70	H	2330.92	W2	39 025.05
r	12 962.35	y	9226.45	Ks	2330.92	W3	15 393.12
i	14 507.01	J	2330.92	W1	39 025.01	W4	15 472.75

Additionally, we have discarded the measurement errors of all bands. Traditionally, ML algorithms cannot incorporate uncertainties in a straightforward way during training (e.g. Jiang et al., 2021; Michelucci and Venturini, 2023) and, thus, we opted to avoid attempting to use them for training. One significant counter-example corresponds to Gaussian process (GP; Rasmussen and Williams, 2005)s, where measurement uncertainties are needed by the algorithm to generate predictions. Additionally, the astronomical community has attempted to modify existing techniques to include uncertainties in their ML studies. Some examples include the works by Ball et al. (2008), Reis et al. (2019), and Shy et al. (2022). Furthermore, Euclid Collaboration et al. (2023b) have shown that, in specific cases, the inclusion of measurement errors does not add new information to the training of the models and can be even detrimental to the prediction metrics. The degradation of the model by including uncertainties can likely be related to the fact that, by virtue of the large number of sources included in the training stages, the uncertainties are already encoded in the dataset in the form of scatter.

The number of valid measurements in Fig. 2.3 for each field and band can be used to determine the relative difference of density of sources between both fields. This density can be obtained by dividing the number of valid measurements over the effective area of each field (Sects. 2.1 and 2.2). Table 2.2 shows these densities.

2.4 Missing data treatment

In general, ML methods (and their underlying statistical methods, as introduced in Sect. 1.2.2) cannot work with catalogues that have empty entries (Allison, 2001; Josse et al.,

2019). Several techniques have been devised to handle datasets that lack some of their entries. The simplest of them is listwise deletion, which drops all observations that miss, at least, one measurement (Pepinsky, 2018). This process is inefficient given that it reduces the size of the parameter space from which the models can obtain information for its training.

A second method is imputation. Imputation is the process of replacing non-available measurements with substitute values. In general, there is enough information in the remaining entries to derive a meaningful substitute value (Kalton and Kasprzyk, 1982). In this way, typical quantities used for replacement are the mean of the remaining entries or a function of the other measurements of the same entry.

Depending on the origin of the substitute value, different categories of imputation exist. Using the definitions from Kalton and Kasprzyk (1982) and Chattopadhyay (2017), it is possible to separate it in multiple and single imputation. In turn, single imputation can be divided into mean, random, regression, hot deck, and cold deck imputation.

Single imputation replaces each missing entry with a single value. Opposite to it, multiple imputation, and as initially proposed by Rubin (1987), creates a set of possible values (usually, based upon statistical arguments) which are included as new instances of the measured object.

Focusing on single imputation, mean imputation replaces all missing measurements with the mean value of the available values. Random imputation uses any value from the existent measurements in the data set to replace the missing entry. Regression imputation uses the full set of available data to derive a possible value for the missing entry. Hot and cold deck imputations replace the missing value with other instances of the data set (or additional data sets in cold deck imputation) that have the same values for the remaining measurements.

Given its simplicity, we have used an ad-hoc variation of single imputation to replace missing values and magnitudes fainter than $5 - \sigma$ limits with meaningful quantities that represent the lack of a measurement. We have opted for the inclusion of the same $5 - \sigma$ limiting magnitudes as the value to impute with. This method of imputation, with some variations, has been successfully applied and tested, recently, by Arsioli and Dedin (2020), Carvajal et al. (2021), Curran (2022), and Curran et al. (2022).

In this way, observations from 12 non-radio bands were gathered (as listed in Table 2.1). The magnitude density distribution for the sample from the **HETDEX** and **S82** fields, without any imputation, is shown in Fig. 2.3. After imputation, the distribution of magnitudes changes, as shown in Fig. 2.4. Each panel of the figure shows the number of sources which have a measurement above its $5 - \sigma$ limit in such band. Additionally, a representation of the

CHAPTER 2. STUDIED DATASETS

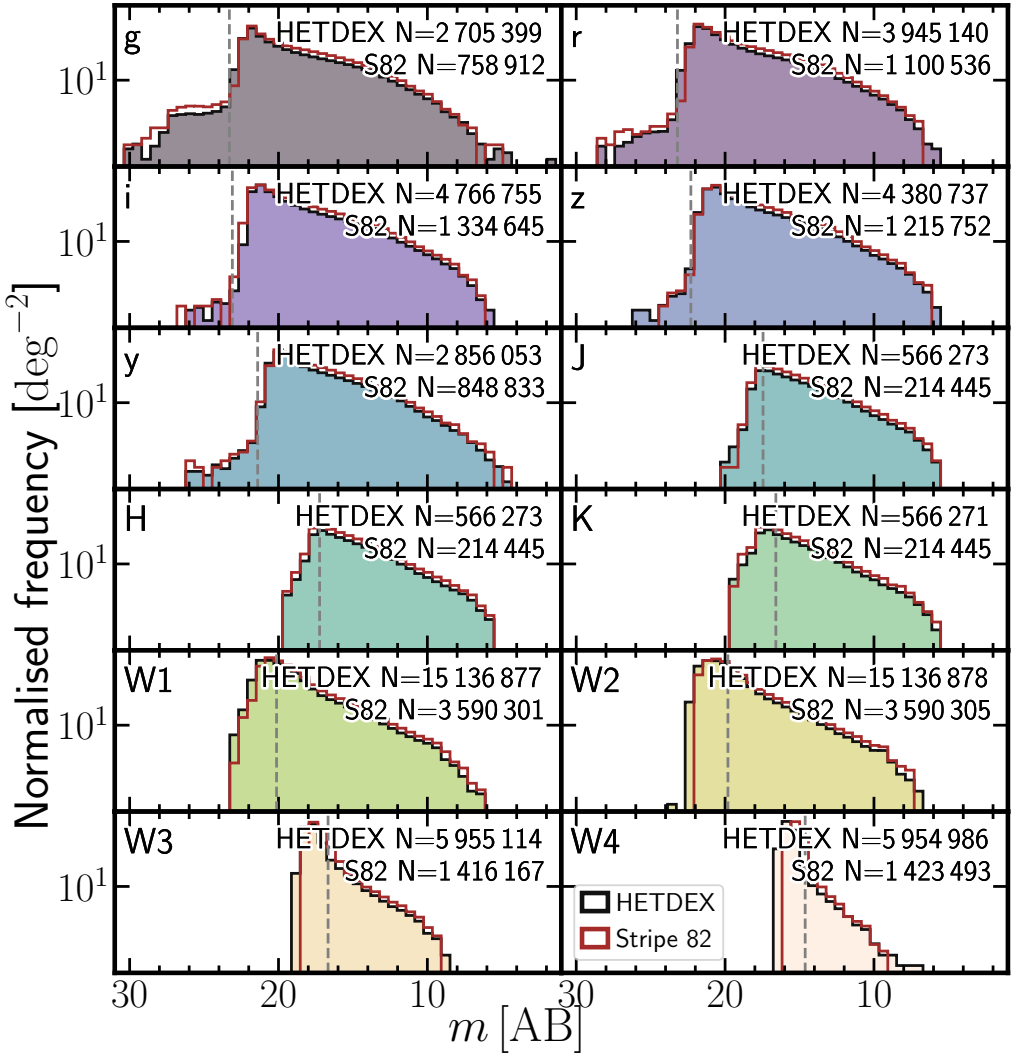


Figure 2.3: Histograms of base collected, non-imputed, non-radio bands for [HETDEX](#) (clean, background histograms) and [S82](#) (empty, brown histograms). Each panel shows the distribution of measured magnitudes of detected sources divided by the total area of the field. Dashed, vertical lines represent the $5 - \sigma$ magnitude limit for each band. The number in the upper right corner of each panel shows the number of measured magnitudes included in their corresponding histogram.

observational $5 - \sigma$ limits of the bands and surveys used in this work is presented in Fig. 2.5. It is worth noting the depth difference between [VLAS82](#) and [LoTSS](#) is ~ 1.5 mag for a typical synchrotron emitting source ($F_\nu \propto \nu^\alpha$ with $\alpha = -0.7$), allowing the latter survey reach fainter sources.

Following the same argument of measurement errors, upper limit values have been removed and a missing value is assumed instead.

2.5 Additional features

As mentioned in the previous sections, each magnitude corresponds to one feature that will be used in the training stages. In order to give the models more information to improve

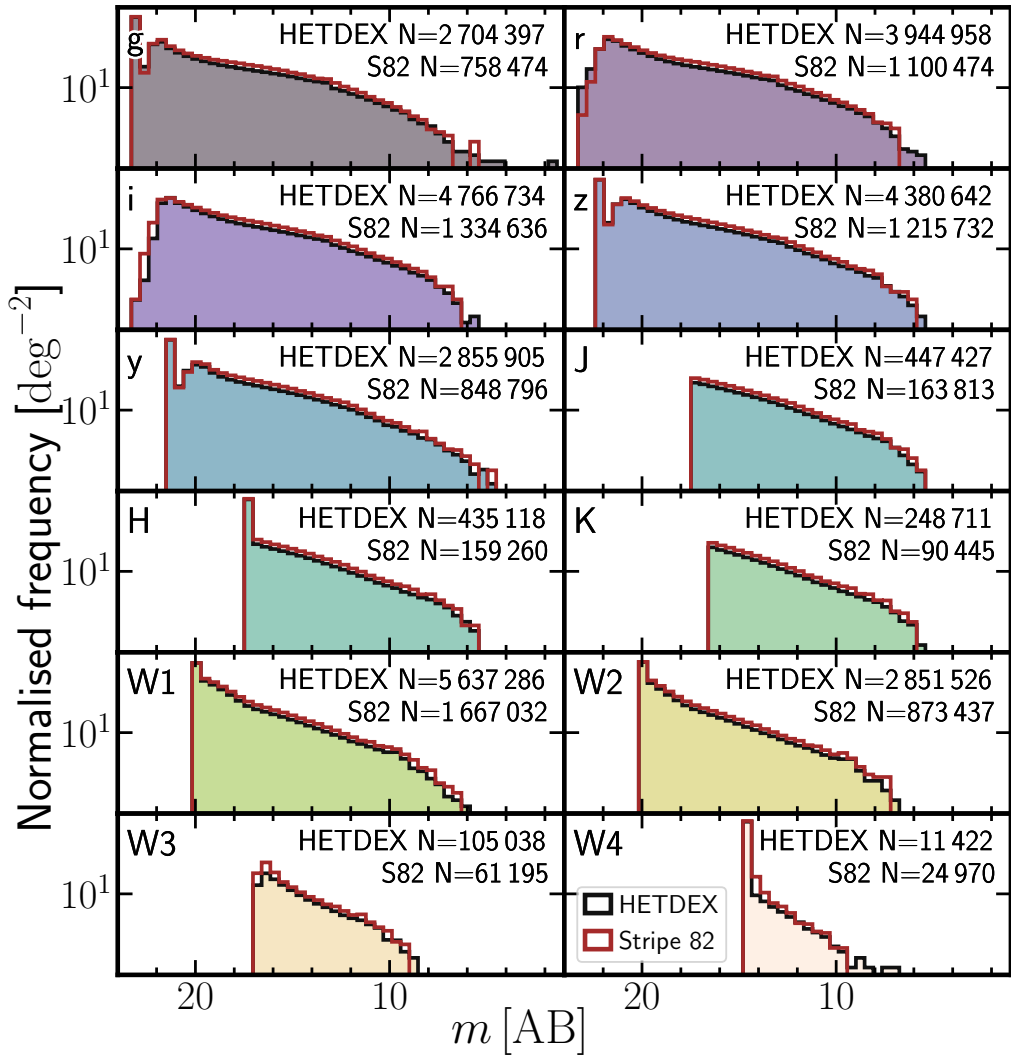


Figure 2.4: Histograms of base collected non-radio bands for **HETDEX** (clean, background histograms) and **S82** (empty, brown histograms) fields. Description as in Fig. 2.3. The number in the upper right corner of each panel shows the number of sources with magnitudes originally measured above the $5 - \sigma$ limit included in their corresponding histogram for each field.

their training, we have generated more quantities as described below.

First, **AGN** labels and redshift information were obtained by cross-matching (with a 1''1 search radius) the catalogue with the version v7.4d of the **MQC** (Flesch, 2021), which lists information from more than 1 500 000 objects that have been classified as optical **QSO**, **AGN**, or Blazars. Sources listed in the **MQC** may have additional counterpart information, including radio or X-ray associations. For the purposes of this work, only sources with secure spectroscopic redshifts were used. The matching yielded 50 538 spectroscopically confirmed **AGN** in **HETDEX** and 17 743 confirmed **AGN** in **S82**. A depiction of the source density in the **MQC** v7.4d is presented in Fig. 2.6.

Similarly, the sources in our parent catalogue were cross-matched with the **SDSS Data Release 16** (SDSS-DR16; Ahumada et al., 2020). This cross-match was done solely to determine

CHAPTER 2. STUDIED DATASETS

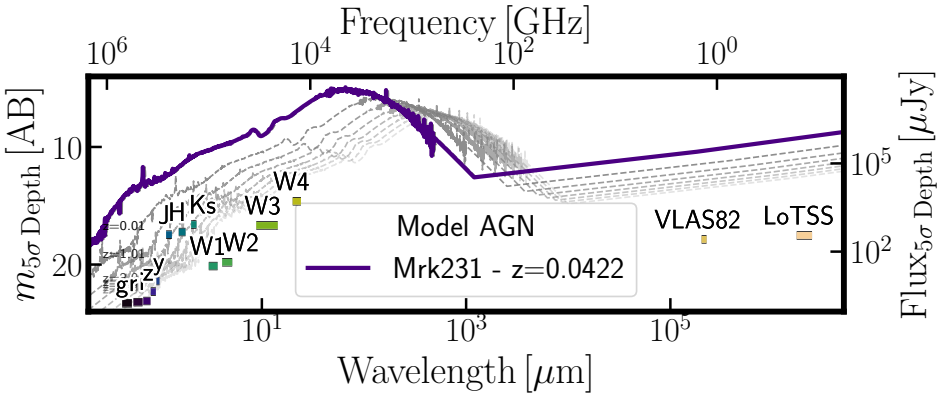


Figure 2.5: Flux and magnitude depths ($5 - \sigma$) from the surveys and bands used in this work. Limiting magnitudes and fluxes were obtained from the description of the surveys, as referenced in Sect. 2.3. In purple, rest-frame SED from Mrk231 ($z = 0.0422$, Brown et al., 2019) is displayed as an example AGN. Redshifted (from $z = 0.001$ to $z = 7$) versions of this SED are shown in dashed grey lines.

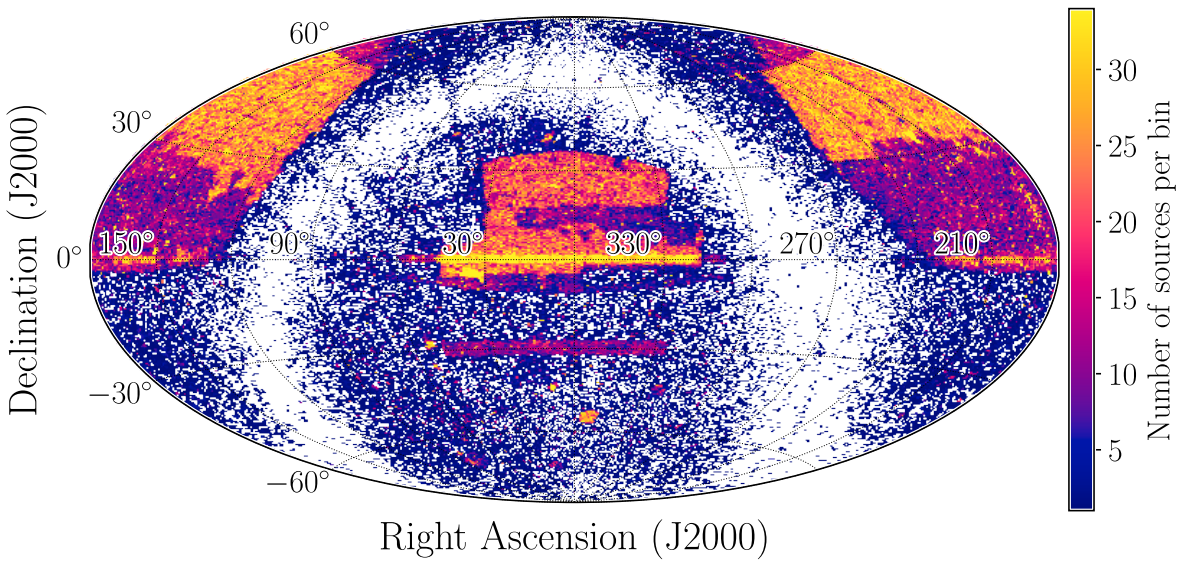


Figure 2.6: Million Quasar Catalog v7.4d source density in a Hammer-Aitoff projection (Snyder, 1987; Snyder, 1997) of the sky. Description as in Fig. 1.7.

which sources have been spectroscopically classified as SFGs (`spClass == GALAXY`) and no magnitude measurements were extracted from it. For most of these SFGs, SDSS-DR16 lists a spectroscopic redshift value, which will be used in some stages of this work. In the HETDEX field, SDSS-DR16 provides 68 196 spectroscopically confirmed galaxies. In the S82, SDSS-DR16 identifies 4085 galaxies spectroscopically. Given that MQC has access to more AGN detection methods than SDSS, when sources were identified as both SFGs (in SDSS-DR16) and AGN (in the MQC), a final label of AGN was given. A description of the number of elements in each field and the multi-wavelength counterparts found for them is presented in Table 2.3.

Then, colours from measured and imputed magnitudes were considered were added as features. We created 66 of them, which correspond to all the available combinations of two

Table 2.3: Composition of initial catalogue and number of cross matches with additional surveys and catalogues.

Survey	HETDEX	Stripe82
CatWISE2020	15 136 878	3 590 306
AllWISE	5 955 123	1 424 576
Pan-STARRS	4 837 580	1 346 915
2MASS	566 273	214 445
LoTSS	187 573	...
VLAS82	...	8747
MQC (AGN)	50 538	17 743
SDSS (Galaxy)	68 196	4085

magnitudes between the 12 selected bands, symbolised by the expression $\binom{12}{2}$. These colours are labelled in the form X_Y where X and Y are the respective magnitudes. Depending on the stage of the training process, the number of used colour might be reduced.

An additional feature shows the number of non-radio bands in which a source has valid (i.e. non imputed) measurements. We have called it `band_num` and it has been produced counting the number of valid values that each source showed before imputation. The values of this feature can range from 2 (source only detected in [CW](#)) up to 12 (source detected in every band of all selected surveys). This feature could be, very loosely, assimilated to the total flux a source can display. A higher `band_num` will imply that such source can be detected in more bands, implying that it has a higher flux (regardless of redshift). The use of features with counting or aggregation of elements in the studied dataset is well established in [ML](#) (see, for example, [Zheng and Casari, 2018](#); [Duboue, 2020](#); [Sánchez-Sáez et al., 2021](#); [Euclid Collaboration et al., 2023b](#)).

In order to test whether or not a source has been detected in any of the radio surveys we have used in Sect. 2.3, we created a feature, called `radio_detect`, which shows a boolean flag. Its value is `True` (1) if we have a valid entry (i.e. a detection) in any of the aforementioned radio catalogues. As such, this flag can only tell if a source can be detected with radio observations similar to the deepest survey from our set and cannot give information of the existence, or not, of radio emission in general.

Lastly, we created an additional boolean feature, called `class`, which shows whether a source has been cross-matched with an element of the [MQC](#) or with a galaxy in [SDSS-DR16](#). A value of zero (0) means that the source has been found in the [SDSS-DR16](#) galaxy sample, a value of one (1) implies that the source has been identified by the [MQC](#). Sources that have not been included neither as [AGN](#) nor as [SFGs](#) (i.e. unknown sources) have not given any value

CHAPTER 2. STUDIED DATASETS

Table 2.4: Names of columns or features used in the code and what they represent.

Photometry measurements (magnitudes and fluxes)								
Code name	Feature	Code name	Feature	Code name	Feature			
gmag	g (PS1)	ymag	y (PS1)	W1mpoPM	W1 (CW)			
rmag	r (PS1)	Jmag	J (2M)	W1mpoPM	W2 (CW)			
imag	i (PS1)	Hmag	H (2M)	W3mag	W3 (AW)			
zmag	z (PS1)	Kmag	Ks (2M)	W4mag	W4 (AW)			
Colours								
66 colours from all combinations of non-radio magnitudes. A sub-sample of them is shown.								
g_r	g - r (PS1)	W2_W3	W2 (CW) - W3 (AW)			
g_i	g - i (PS1)	W2_W4	W2 (CW) - W4 (AW)			
g_z	g - z (PS1)	W3_W4	W3 - W4 (AW)			
Categorical flags								
Code name	Feature							
band_num	Number of bands with measurements							
Boolean flags								
Code name	Feature	Code name	Feature					
class	AGN or SFG	radio_detect	Detection in, at least, one radio band.					
Redshift								
Code name	Feature							
Z	Spectroscopic redshift							
Outputs of base models								
Code name	Feature	Code name	Feature	Code name	Feature			
XGBoost	XGBoost	ET	Extra Trees	GBR	Gradient Boosting			
CatBoost	CatBoost	GBC	Gradient Boosting		Regressor			
RF	Random Forest		Classifier					

for `class`. It is worth mentioning that a value of `0` in this flag does not mean directly that a source is not an [AGN](#). It only implies that the studied source has not been listed in the [MQC](#) as a confirmed [AGN](#).

A list of the features created for this work and their representation in the code and in some of the figures is presented in Table 2.4.

2.6 Data re-scaling and normalisation

Attending to the intrinsic differences between [ML](#) algorithms, not all of them have the same performance when being trained with features that have absolute values spanning a wide range of values (i.e. several orders of magnitude). In particular, linear modelling of data might

overrepresent features with larger absolute values when measuring distances between data point. For this reason, it is customary to re-scale the available values to either be contained within the range [0, 1] or to have similar distributions (e.g. Toth et al., 1993; Sola and Sevilla, 1997). We applied a version of the latter transformation to our features (not the targets) as to have a mean value of $\mu = 0$ and a standard deviation of $\sigma = 1$ for each feature (i.e. standardisation). Additionally, these new values were power-transformed to resemble a Gaussian distribution. This transformation helps the models avoid using the distribution of values as additional information for the training. For this work, a Yeo-Johnson transformation (Yeo and Johnson, 2000) was applied.

A representation of the steps performed for the pre-processing of the data (both in [HETDEX](#) and [S82](#)), and also described in Sects. 2.3, 2.4, and 2.5, is presented in Fig. 2.7.

2.7 Data splitting

Given that we need to be able to compare the results from the training and application of the [ML](#) models with values obtained independently (i.e. ground truth), we divided our dataset into labelled and unlabelled sources. Labelled sources are all elements of our catalogue that have been classified as either [AGN](#) or [SFGs](#). Unlabelled sources are those which lack such classification and that will only be subject to the prediction of our models, not taking part in any training step. Labelled data will be used for training procedures and to, properly, assess the performance of the models.

Before any calculation or transformation is applied to the data from the [HETDEX](#) field, we split the labelled dataset into training, validation, calibration, and testing subsets. The early creation of these subsets helps avoid information leakage from the test subset into the models. Initially, a 20 % of the dataset has been reserved as testing data. Of the remaining elements, an 80 % of them have been used for training, and the rest of the data has been divided equally between calibration and validation subsets (i.e. a 10 % each). In the case of data from [S82](#), the only separation is done between labelled and unlabelled sources. Given that sources from [S82](#) do not take part into the training of the models, they only need to be isolated from the elements in [HETDEX](#). The splitting process and the number of elements for each subset are shown in Figs. 2.8 and 2.9.

Depending on the model, the needed sources are selected from each of the sub-sets that have been already created. The training set will be used to select algorithms for each step and to

CHAPTER 2. STUDIED DATASETS

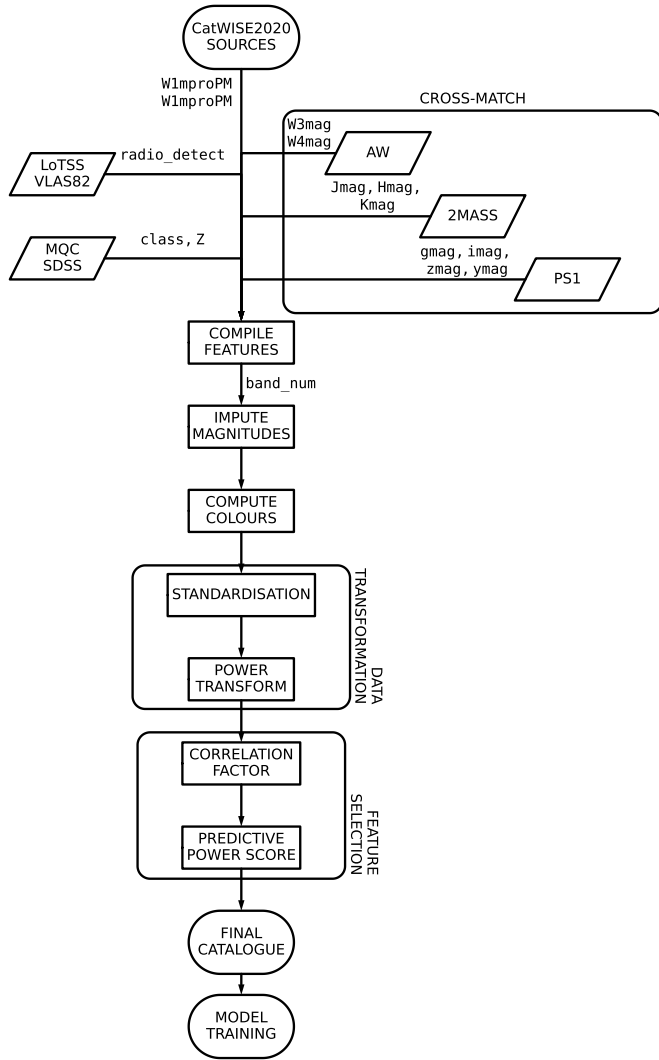


Figure 2.7: Flowchart with steps for data pre-processing. Labels in arrows state the features produced from each step or data catalogue.

optimise their hyper-parameters. The inclusion of the validation sub-set helps in the parameter optimisation of the models. The probability calibration of the trained model is performed over the calibration sub-set and, finally, the completed models are tested on the test sub-set and the labelled sources in S82. The use of these subsets will be expanded further in the text.

It is worth noting that the fraction of labelled sources, both in HETDEX and S82, is very low when compared to the total size of the datasets (0.8 % for HETDEX and 0.6 % for S82). These fractions confirm that the problems exhibited in Chapter 1.2 are ubiquitous and more analysis tools are needed to understand the nature of sources detected in existing catalogues.

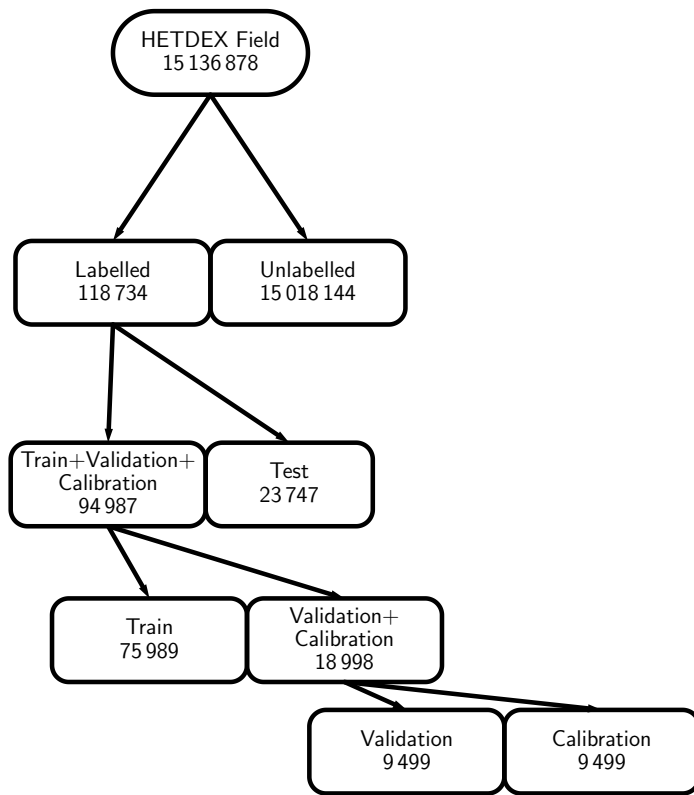


Figure 2.8: Composition of data from [HETDEX](#) used for the different steps of this work.

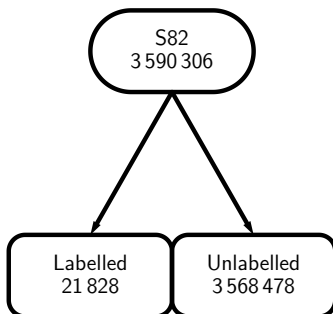


Figure 2.9: Composition of data from [S82](#) used for the different steps of this work.

DRAFT - February 21, 2024 - DRAFT

This page intentionally left blank.

Training of models

In this chapter, we present the results of the creation of the prediction pipeline and the models that make part of it. This procedure includes, for each step, the selection of features, algorithms and hyperparameters.

3.1 Prediction metrics

Several methods exist to assess the results from machine-assisted methods. Most of them, have been designed for supervised tasks. In general, predictions are compared with the original (or true) quantities and a new quantity, a metric, is derived to determine how good the prediction is.

A set of metrics will be used to understand the reliability of the results and put them in context with results in the literature. Since our work includes the use of classification and regression models, we briefly discuss the appropriate metrics in the following sections.

3.1.1 Classification metrics

The main tool to assess the performance of classification methods is the Confusion (or Error) Matrix. It is a two-dimension (predicted vs. true) matrix where the number of true and predicted classes are compared and results stored in cells with the rate of [true positivess \(TPs\)](#), [true negativess \(TNs\)](#), [false positivess \(FPs\)](#), and [false negativess \(FNs\)](#). An example diagram showing the elements of a confusion matrix is shown in Table 3.1. An ideal classifier would be represented by a diagonal matrix with no incorrectly predicted elements. As mentioned earlier in Sect. 1.4, we seek to maximise the number of positive-class sources that are recovered as such. Using the elements of the confusion matrix, this aim can be translated into the maximisation of [TPs](#) and, consequently, the minimisation of [FNs](#).

From the elements of the confusion matrix, we can obtain additional metrics, such as the [F1](#) and [\$F_\beta\$](#) scores (Dice, 1945; Sørenson, 1948; van Rijsbergen, 1979), and the [Matthews](#)

CHAPTER 3. TRAINING OF MODELS

		True Classes	
		SFG	AGN
	SFG	True Negative (TN)	False Positive (FP)
	AGN	False Negative (FN)	True Positive (TP)
Predicted Classes			

Figure 3.1: Diagram of confusion matrix for the classification of sources between AGN and SFGs.

correlation coefficient (MCC; Yule, 1912; Cramér, 1946; Matthews, 1975) which are better suited for unbalanced data (i.e. when the fraction of elements of one class is much higher than that of the other) as they take into account the behaviour and correlations among all elements of the confusion matrix. As such, the F1 coefficient is defined as:

$$F1 = \frac{2TP}{2TP + FN + FP}. \quad (3.1)$$

F1 values can go from 0 (no prediction of positive instances) to 1 (perfect prediction of elements with positive labels). This definition assigns equal weight (importance) to both the number of FNs and FPs. An extension to the F1 score, which adds a non-negative parameter, β , to increase the importance given to each one of them is the F-Score (F_β), defined as:

$$F_\beta = \frac{(1 + \beta^2) \times TP}{(1 + \beta^2) \times TP + \beta^2 \times FN + FP}. \quad (3.2)$$

Using $\beta > 1$, more relevance is given to the optimisation of FNs. When $0 \leq \beta < 1$, the optimisation of FPs is more relevant. If $\beta = 1$, the initial definition of F1 is recovered. As with F1, F_β values can be in the range [0, 1]. Given that we seek to minimise the number of FNs detection, we adopt a conservative value of $\beta = 1.1$, giving more significance to their reduction without removing the aim for FPs. Also, this value is close enough to $\beta = 1$, which will allow

us to compare our scores to those produced in previous works.

MCC is defined as:

$$\text{MCC} = \frac{\text{TP} \times \text{TN} - \text{FP} \times \text{FN}}{\sqrt{(\text{TP} + \text{FP})(\text{TP} + \text{FN})(\text{TN} + \text{FP})(\text{TN} + \text{FN})}}, \quad (3.3)$$

which includes also the information about the **TN** elements. **MCC** can range from -1 (total disagreement between true and predicted values) to $+1$ (perfect prediction) with 0 representing a prediction analogous to a random guess.

The Recall (also called Completeness, Sensitivity, or True Positive Rate –**TPR**–; Yerushalmi, 1947) corresponds to the rate of relevant, or correct, elements that have been recovered by a process. Using the elements from the confusion matrix, it can be defined as:

$$\text{Recall} = \text{TPR} = \frac{\text{TP}}{\text{TP} + \text{FN}}. \quad (3.4)$$

The **true positive rate (TPR)** can go from 0 to 1 , with a value of 1 meaning that the model can recover all the true instances.

The last metric used is Precision (also known as Purity), which can be defined as the ratio between the number of correctly classified elements and the number of sources in the positive class (**AGN** or radio detectable):

$$\text{Precision} = \frac{\text{TP}}{\text{TP} + \text{FP}}. \quad (3.5)$$

Precision can range from 0 to 1 , where higher values show that more real positive instances of the studied set were retrieved as such by the model.

In order to establish a baseline from which the aforementioned metrics can be assessed, it is possible to obtain them in the case of a random, or no-skill prediction. Following, for instance, the derivations and notation from Poisot (2023), no-skill versions of classification metrics (Eqs. 3.2–3.5) are:

$$F_{\beta}^{\text{no-skill}} = p, \quad (3.6)$$

$$\text{MCC}^{\text{no-skill}} = 0, \quad (3.7)$$

$$\text{Recall}^{\text{no-skill}} = p, \quad (3.8)$$

$$\text{Precision}^{\text{no-skill}} = p. \quad (3.9)$$

CHAPTER 3. TRAINING OF MODELS

where p corresponds to the ratio between the elements of the positive class and the total number of elements involved in the prediction.

3.1.2 Regression metrics

Usually, regression tasks are assessed with the use of metrics such as [mean squared error \(MSE\)](#), [root mean square error \(RMSE\)](#), and [mean absolute error \(MAE\)](#). These measure the deviation of the predicted value from the original quantity. If the original value is called y_{True} and its predicted version is $y_{\text{Predicted}}$, these three regression metrics can be defined as follows.

The [MSE](#) is

$$\text{MSE}(y) = \frac{1}{d} \sum_i^d (y_{\text{True}} - y_{\text{Predicted}})^2 , \quad (3.10)$$

with d being the number of elements in the studied sample (i.e. its size). A direct modification of [MSE](#) appears when calculating its square root. Then, the root mean squared error is

$$\text{RMSE}(y) = \sqrt{\frac{1}{d} \sum_i^d (y_{\text{True}} - y_{\text{Predicted}})^2} . \quad (3.11)$$

A third way to quantify the deviation of the predictions from the true values is through the [MAE](#);

$$\text{MAE}(y) = \frac{1}{d} \sum_i^d |y_{\text{True}} - y_{\text{Predicted}}| , \quad (3.12)$$

While [MSE](#) and [RMSE](#) are sensitive to large deviations in the predictions, the [MAE](#) has a linear behaviour with respect to the fluctuations in predicted quantities.

For the case of redshift value determination, the previous metrics are not fully able to assimilate its logarithmic behaviour. Thus, further modifications are needed in order to use suitable metrics. Namely, a factor must be included to take into account the fact that differences between low redshift values should be penalized more strongly than those at higher redshifts.

We can start with the difference between true (z_{True}) and predicted ($z_{\text{Predicted}}$) redshift values,

$$\Delta z = z_{\text{True}} - z_{\text{Predicted}} , \quad (3.13)$$

and its normalised difference,

$$\Delta z^N = \frac{z_{\text{True}} - z_{\text{Predicted}}}{1 + z_{\text{True}}} . \quad (3.14)$$

If the comparison is made over a larger sample of elements, the bias of the redshift is used (Dahlen et al., 2013), with the median of the quantities instead of its mean to avoid the strong influence of extreme values:

$$\Delta z_{\text{Total}} = \text{median}(z_{\text{True}} - z_{\text{Predicted}}) = \text{median}(\Delta z) , \quad (3.15)$$

$$\Delta z_{\text{Total}}^N = \text{median}\left(\frac{z_{\text{True}} - z_{\text{Predicted}}}{1 + z_{\text{True}}}\right) = \text{median}(\Delta z^N) . \quad (3.16)$$

Using the previous definitions, four additional metrics can be calculated. These are the **MAD** and **normalised median absolute deviation (NMAD, σ_{NMAD})** (Hoaglin et al., 1983; Ilbert et al., 2009), which are less sensitive to outliers. Also, the standard deviation of the predictions, σ_z , and its normalised version, σ_z^N are typically used. They are defined as:

$$\sigma_{\text{MAD}} = 1.48 \times \text{median}(|\Delta z|) , \quad (3.17)$$

$$\sigma_{\text{NMAD}} = 1.48 \times \text{median}(|\Delta z^N|) , \quad (3.18)$$

$$\sigma_z = \sqrt{\frac{1}{d} \sum_i^d (\Delta z)^2} , \quad (3.19)$$

$$\sigma_z^N = \sqrt{\frac{1}{d} \sum_i^d (\Delta z^N)^2} , \quad (3.20)$$

Additionally, the outlier fraction (η , as used in Dahlen et al., 2013; Lima et al., 2022) is considered, which is defined as the fraction sources with a predicted redshift difference ($|\Delta z^N|$, Eq. 3.14) larger than a previously set value. Taking the results from Ilbert et al. (2009) and Hildebrandt et al. (2010), we have selected this threshold to be 0.15, leaving the definition of the outlier fraction as:

$$\eta = \frac{\#(|\Delta z^N| > 0.15)}{d} . \quad (3.21)$$

where $\#$ symbolises the number of sources fulfilling the described relation, and d corresponds to the size of the selected sample.

3.2 Classification thresholds

Metrics presented in Sect. 3.1.1 work with a prediction of the status (class) of an element. However, most classifiers deliver a score rather than a definite class prediction. Scores, in the range $[0, 1]$ need to be translated into positive or negative classes. A threshold is defined to separate both states. By default, these models set a threshold at 0.5 in score (which we will call a naive threshold) but, in principle and given the characteristics of the problem, a different optimal threshold might be needed.

In our case, we want to optimise (increase) the number of recovered elements in each model (i.e. AGN or radio-detectable sources). This maximisation corresponds to obtaining thresholds that optimise the recall (Eq. 3.4) given a specific precision limit. By maximising this metric, we improve the number of recovered elements in each classifier. This can be done by decreasing the threshold by which a source is classified as a positive instances. Setting this threshold to its minimum, 0.0, would increase the recall. But every source would be predicted to be an AGN or detected on the radio regardless of their properties. Thus, a different approach must be taken.

That is possible through the use of the statistical tool called **precision-recall (PR)** curve. Thresholds derived from the PR curves will be labelled as PR. PR curves can help to understand the behaviour of a classifier as a function of its threshold. Both quantities, precision (Eq. 3.5) and recall, show an inverse correlation, and both depend on the selected threshold. Thus, they can be used to retrieve the score value for which both quantities are balanced. This optimisation is done by finding the threshold that maximises the F_β score (Eq. 3.2). This operation can be performed over the union of training and validation sets, which have been used to create and train each model.

3.3 Classification calibration

Classifiers deliver scores in the range $[0, 1]$, which could be associated to the probability of a studied source being part of the relevant class (in our work, AGN or radio detectable). The classifier uses a threshold above which, any predicted element would be considered a positive instance.

With the exception of few algorithms (including the family of logistic regressions), scores from classifiers cannot be directly used as probabilities (Caruana and Niculescu-Mizil, 2006).

As a consequence of this inability, such values cannot be compared from one type of model to some other and can not be combined to obtain a joint score. Therefore, in order to retrieve joint scores and treat them as probabilities, scores (and, by extension, the classifiers) need to be calibrated. This calibration means that, when taking all predictions with a probability P of being of a class, a fraction P of them really belong to that class (e.g. Lichtenstein et al., 1982; Silva Filho et al., 2023).

Calibration of these scores can be done by applying a transformation to their values. For our work, we will apply a Beta transformation. Beta transformation functions have the general form

$$\mu_{beta}(S; a, b, c) = \frac{1}{1 + \frac{1}{\left(e^c \frac{S^a}{(1 - S)^b} \right)}}, \quad (3.22)$$

with S being the score from the classifier and a, b, c , free parameters to be optimised. It allows one to re-distribute the scores of a classifier allowing them to get closer to the definition of probability (Kull et al., 2017a; Kull et al., 2017b). Calibration steps in our workflow have been applied using the Python package `betacal`. In the case of the radio detection model, the new scores have a wider range than the original, uncalibrated scores.

Calibration (or reliability) plots (Niculescu-Mizil and Caruana, 2005) show how well calibrated the predicted scores of a classifier are by displaying the fraction of sources that are part of a given class as a function of the predicted probability. A perfectly calibrated classifier would have all its prediction lying in the $x = y$ line. The magnitude of the deviations from that line give information of the miscalibration a model has (see, for instance, Bröcker and Smith, 2007; Van Calster et al., 2019).

3.3.1 Calibration metrics

One of the most used analytical metrics to assess calibration of a model is the **Brier score** (**BS**; Brier, 1950). It measures the mean square difference between the predicted probability of an element and its true class. If the total number of elements in the studied sample is d , the **BS** can be written (for binary classification problems, as the ones studied in this work) as:

$$BS = \frac{1}{d} \sum_i^d (\mathbb{C} - \text{class})^2, \quad (3.23)$$

CHAPTER 3. TRAINING OF MODELS

where \mathbb{C} is the predicted class and class the true class of each of the elements in the sample (0 or 1). The **BS** can range between 0 and 1 with 0 representing a model that is completely reliable in its predictions.

Additionally, the **BS** can be used to compare the reliability (or calibration) between a model and a reference using the [Brier skill score \(BS; Glahn and Jorgensen, 1970\)](#):

$$\text{BSS} = 1 - \frac{\text{BS}}{\text{BS}_{\text{ref}}} . \quad (3.24)$$

In our case, BS_{ref} corresponds to the value calculated from the uncalibrated model. The **BSS** can take values between -1 and 1 . The closer the **BSS** gets to 1 , the more reliable the analysed model is. These values include the case where $\text{BSS} \approx 0$, in which both models perform similarly in terms of calibration.

For our pipeline, after a model has been fully trained, a calibrated version of their scores will be obtained. With both of them, the **BSS** will be calculated and, if it is not considerably lower than 0, that calibrated transformation will be used as the final scores from the prediction.

3.4 Feature selection

[ML](#) algorithms, as most data analysis tools, require execution times which increase with the size of the datasets. In order to reduce training times without losing relevant information for the model, the most important features were selected at each step through a process called feature selection. Feature selection can also help avoiding the inclusion of data that might add noise to the model predictions.

For each model, the process of feature selection begins with 79 base features ([Table 2.4](#)) and three targets (`class`, `LOFAR_detect`, and `Z`). Feature selection is run, independently, for each trained model (i.e. [AGN-SFG](#) classification, radio detection, and redshift predictions), delivering three different sets of features.

To avoid redundancy, the process starts discarding features that have a high correlation with another property of the dataset. For discarding features, we calculated Pearson's correlation matrix for the full train+validation dataset only and selected the pairs of features that showed a correlation factor higher than $\rho = 0.75$, in absolute values. A value of $\rho = 0.75$ is a compromise between very stringent thresholds (e.g. $\rho = 0.5$) and more relaxed values (e.g. $\rho \approx 0.9$). (For an explanation on how to consider different correlation values, see, for instance [Ratner, 2009](#)).

From each pair, we discarded the feature with the lowest relative standard deviation (RSD; Johnson and Leone, 1964). The RSD is defined as the ratio between the standard deviation of a set and its mean value. A feature which covers a small portion of its probable values (i.e. low coverage of parameter space, and lower RSD) will give less information to a model than one with largely spread values. Thus, its elimination might not have a large impact the final model.

Feature selection was applied to the train+validation subset with 85 488 confirmed elements (galaxies from SDSS-DR16 and AGN from MQC, i.e. `class == 0` or `class == 1`). After the selection procedure described in Sect. 3.4, 18 features were selected for training: `band_num`, `W4mag`, `g_r`, `r_i`, `r_J`, `i_z`, `i_y`, `z_y`, `z_W2`, `y_J`, `y_W1`, `y_W2`, `J_H`, `H_K`, `H_W3`, `W1_W2`, `W1_W3`, and `W3_W4`. The target feature is `class`.

Feature selection was applied to the train+validation subset, with 36 387 confirmed AGN. The target feature is `LOFAR_detect` and the base of selected features are: `band_num`, `W4mag`, `g_r`, `g_i`, `r_i`, `r_z`, `i_z`, `z_y`, `z_W1`, `y_J`, `y_W1`, `J_H`, `H_K`, `K_W3`, `K_W4`, `W1_W2`, and `W2_W3`.

Feature selection (cf. Sect. 3.4) was applied to the train+validation subset, with 4612 sources, leading to the selection of 17 features. The target feature is Z and the selected base features are `band_num`, `W4mag`, `g_r`, `g_W3`, `r_i`, `r_z`, `i_z`, `i_y`, `z_y`, `y_J`, `y_W1`, `J_H`, `H_K`, `K_W3`, `K_W4`, `W1_W2`, and `W2_W3`.

3.5 Model stacking

Base and meta learners have been selected based upon the metrics described in Sect. 3.1. We have trained five algorithms with the training subset and calculated the metrics for all of them using a 10-fold cross-validation approach (e.g. Stone, 1974; Allen, 1974) over the same training subset. For each metric, the learners have been given a rank (from 1 to 5) and a mean value has been obtained from them. Out of the analysed algorithms, the one with the best overall performance (i.e. best mean rank) is selected to be the meta learner while the remaining four are used as base learners.

For the AGN-SFG classification and radio detection problems, we tested five classification algorithms: RF, Gradient Boosting Classifier (GBC; Friedman, 2001), Extra Trees (ET; Geurts et al., 2006), Extreme Gradient Boosting (XGBoost, v1.5.1; Chen and Guestrin, 2016), and Category Boosting (CatBoost, v1.0.5; Prokhorenkova et al., 2018; Dorogush et al., 2018). For the redshift prediction problem, we tested five regressors as well: RF, ET, XGBoost, CatBoost, and gradient boosting regressor (GBR; Friedman, 2001). We have used the Python

CHAPTER 3. TRAINING OF MODELS

implementations of these algorithms and, in particular for **RF**, **ET**, **GBC**, and **GBR**, the versions offered by the package `scikit-learn`¹ (v0.23.2; Pedregosa et al., 2011). These algorithms were selected given that they offer tools to interpret the global and local influence of the input features in the training and predictions (cf. Sect. 1.3.3).

All the algorithms selected for this work fall into the broad family of Tree-Based models. Forest models (**RF** and **ET**) rely on a collection of decision trees to, after applying a majority vote, predict either a class or a continuum value. Each of these decision trees uses a different, randomly-selected sub-set of features to make a decision on the training set (Breiman, 2001). Opposite to forests, Gradient Boosting models (**GBC**, **GBR**, **XGBoost**, and **CatBoost**) apply decision trees sequentially to improve the quality of the previous predictions (Friedman, 2001; Friedman, 2002).

3.6 Model training

The procedure described in Sect. 3.5 includes an initial fit of the selected algorithms to the training data (including the selected features) to optimise their parameters. The stacking step includes a new optimisation of the parameters of the meta-learner using 10-fold cross-validation on the training data with the addition of the output from the base learners, which are treated as regular features (see last section of Table 2.4). Then, following Michailidis (2017), the hyper-parameters of the stacked models are optimised over the training sub-set (a brief description of this step is presented in Sect. 3.6.1).

The final step involves a last parameter fitting instance but using, this time, the combined train+validation subset, which includes the output of the base algorithms, to ensure wider coverage of the parameter space and better-performing models. Consequently, only the testing set is available for assessing the quality of the predictions made by the models.

The results of model testing for the **AGN-SFG** classification are reported in Table 3.1. The **CatBoost** algorithm provides the best metric values (highest mean rank) and is therefore selected as the meta-model. **XGBoost**, **RF**, **ET**, and **GBC** were used as base learners.

Training of the radio detection model was applied only to sources confirmed to be **AGN** (`class == 1`). The performance of the tested algorithms is shown in Table 3.2. In this case, **GBC** shows the highest mean rank. For this reason, we used it as the meta-learner and **XGBoost**, **CatBoost**, **RF**, and **ET** were selected as base-learners.

¹<https://scikit-learn.org>

Table 3.1: Best performing models for the AGN-SFG classification

Model	F_β ($\times 100$)	MCC ($\times 100$)	Precision ($\times 100$)	Recall ($\times 100$)	Rank
CatBoost	95.70±0.28	92.46±0.48	95.45±0.32	95.91±0.37	1.00
XGBoost	95.67±0.27	92.40±0.48	95.41±0.39	95.88±0.34	2.00
RF	95.52±0.36	92.14±0.63	95.28±0.46	95.71±0.40	3.00
ET	95.40±0.40	91.94±0.69	95.13±0.43	95.63±0.47	4.00
GBC	95.26±0.31	91.66±0.54	94.82±0.41	95.63±0.35	5.00

^a Metrics obtained using the default probability threshold of 0.5.^b Algorithms are sorted by decreasing recall values.^c For display purposes, all metrics have been multiplied by 100.^d Uncertainties show standard deviation of metrics obtained across all 10 training folds (cf. Sect. 3.5)

Table 3.2: Best performing models the radio detection classification

Model	F_β ($\times 100$)	MCC ($\times 100$)	Precision ($\times 100$)	Recall ($\times 100$)	Rank
XGBoost	29.98±2.29	29.81±2.17	56.74±2.93	21.61±2.00	2.75
CatBoost	29.57±1.62	30.56±1.71	60.10±2.85	20.85±1.36	2.25
GBC	29.60±1.66	31.31±1.93	62.55±3.95	20.66±1.40	1.75
RF	29.16±2.47	30.26±2.65	60.03±3.73	20.48±1.96	3.75
ET	28.40±1.27	29.73±1.47	60.06±2.85	19.80±1.05	4.50

^a Values and uncertainties as in Table 3.1.

The redshift value prediction model was applied to sources confirmed to be radio-detected AGN (i.e. `class == 1` and `radio_detect == 1`). The tested algorithms performed as shown in Table 3.3. Based on their mean rank values, RF, CatBoost, XGBoost, and GBR were selected as base learners and ET (which shows the best σ_{MAD} value of the two models with the best rank) was used as meta-learner.

It is worth noting that, while the use of the mean rank is helpful to select a meta learner, the proper differences in metric values between models are small. These similarities might imply that most algorithms (at least classifiers) can extract the same level of information from the data. For this reason, the use of ensemble learning is justified to help the algorithms extract more information than that they can retrieve on their own.

3.6.1 Hyperparameters optimisation

After the selection of the meta learners of each prediction stage of our pipeline, the predicted values (scores for classifiers and redshift for the regressor) are incorporated to the feature set as new quantities to learn from. Thus, and as shown in Table 2.4, four new feature are added per training instance.

CHAPTER 3. TRAINING OF MODELS

Table 3.3: Results of initial fit for redshift value prediction

Model	σ_{MAD} ($\times 100$)	σ_{NMAD} ($\times 100$)	σ_z ($\times 100$)	σ_z^N ($\times 100$)	η ($\times 100$)	Rank
RF	17.88±1.41	07.95±0.50	42.02±5.28	19.38±2.44	19.51±1.98	2.0
ET	18.53±1.03	08.42±0.43	41.12±4.16	18.65±2.26	19.24±1.16	1.8
CatBoost	21.71±1.38	10.08±0.47	40.35±3.03	18.52±1.39	21.93±1.55	2.2
XGBoost	22.89±1.05	10.84±0.78	43.14±3.99	19.62±1.78	24.15±1.84	4.0
GBR	27.73±1.57	12.72±0.74	44.82±3.80	20.41±1.67	28.67±2.25	5.0

^a Algorithms sorted by increasing σ_{MAD} values.

^b Uncertainties as in Table 3.1.

Table 3.4: Hyper-parameters values for meta-learners in modified pipeline after tuning.

AGN-SFG model (CatBoost)			
Parameter	Value	Parameter	Value
learning_rate	0.0075	random_strength	0.1
depth	6	l2_leaf_reg	10
Radio detection model (GradientBoosting)			
Parameter	Value	Parameter	Value
n_estimators	187	min_samples_leaf	2
learning_rate	0.0560	max_depth	9
subsample	0.3387	max_features	0.5248
min_samples_split	5		
Redshift prediction model (ET)			
Parameter	Value	Parameter	Value
n_estimators	100	criterion	mae
max_depth	None	min_samples_split	2
max_features	auto	min_samples_leaf	1
bootstrap	False		

^a This table shows the parameters which were subject to tuning.

^b Remaining hyper-parameters used their default values as defined by their developers.

In Table 3.4, we present the optimised hyper-parameters from our meta-learners. For all three instances of modelling (AGN-SFG, radio detection, and redshift), hyper-parameters were optimised using the SkoptSearch algorithm embedded in the package tune-sklearn² (v0.4.1; Head et al., 2021), which implements a Bayesian search in the hyper-parameter space.

3.6.2 Calibration of models

In Fig. 3.2, we present the reliability curves for the uncalibrated classifiers. It can be seen that the scores for the AGN-SFG classifier can be found clustered in a small range around 0.5. This behaviour might indicate some issue with the predictions. But, as presented in

²<https://github.com/ray-project/tune-sklearn>

Table 3.1, all models used in the training show very high (i.e. satisfactory) metric values. This apparent contradiction might be explained by two factors. First, the sample used for training is highly unbalanced, with most of the sources being labelled as galaxies. Then, there might be a fraction of elements of both classes that share a significant region of the parameter space. When ML algorithms try to classify elements under these two circumstances, they tend to deliver predictions with very low certainties (see, for instance, Vuttipittayamongkol et al., 2021; Santos et al., 2022). This issue can be solved, among other techniques, with the use of probability calibration, which has been implemented in our pipeline.

The previously presented problem does not seem to be present, in the same fashion, in the classification of radio-detectable AGN. There, the distribution of prediction scores ranges from 0.0 up to ~ 0.8 . In this case, and given the conditions of the problem of finding indicators of the detection of radio sources from optical and infrared measurements, the source of a lack of scores close to 1.0 can be related to the impossibility of the models of finding stronger connections between all measurements.

In Fig. 3.3, we present the reliability curves for the calibrated versions of the classifiers. For the AGN-SFG classifier, the improvement is remarkable. Now, predicted probabilities are distributed in the range [0, 1] and they follow closely the line of perfect calibration. In the case of the radio detectability prediction, the improvement is milder, with the new probabilities getting closer to the line of perfect probability calibration. Nevertheless, the new probabilities maintain the same distribution as the original scores (between 0.0 and ~ 0.8). This result implies that probability calibration cannot be used to solve issues with the extraction of information from the available features.

From a numerical point of view, when obtaining the BSS values for both classification, the AGN-SFG classifier has a score of $BSS = -0.002$, demonstrating that no major changes were applied to the intrinsic distribution of scores. For the radio detection classifier, the score is $BSS = -0.434$. Even though the BSS value is slightly negative for the AGN-SFG classifier, we keep it since its range of values now can be compared and combined with additional probabilities. In the case of the radio detection classifier, the BSS shows a degradation of the calibration, but we will keep the calibrated model given that it provides, overall, better values for the remaining metrics. This effect can be seen, more strongly, with recall.

CHAPTER 3. TRAINING OF MODELS

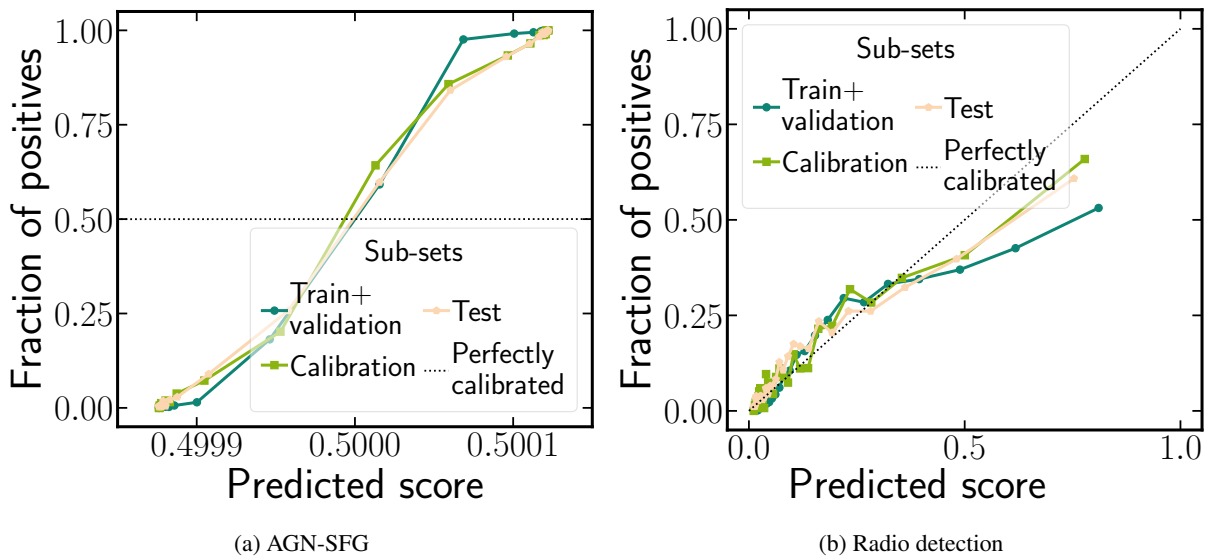


Figure 3.2: Reliability curves for uncalibrated classifiers. Each line represents the calibration curve for each subset in [HETDEX](#) field. Data has been binned and each bin (represented by the points) has the same number of elements per curve. Dashed line represents a perfectly calibrated model. (a) [AGN-SFG](#) classification model. (b) Radio detection model.

3.6.3 Threshold selection

[PR](#) curves for all subsets used in our classification models are shown in Fig. 3.4.

In the case of [AGN-SFG](#) classification, it can be seen that the [PR](#) curve does not present any abnormality. From the optimisation of the F_β score, the optimal threshold for the calibrated meta model is 0.348 95. This value was used for the [AGN-SFG](#) model throughout this work.

The [PR](#) curves for the calibrated radio-detectability meta model present a diffent behaviour, with noticeable variation among subsets. The optimal threshold for this model is found to be 0.204 60.

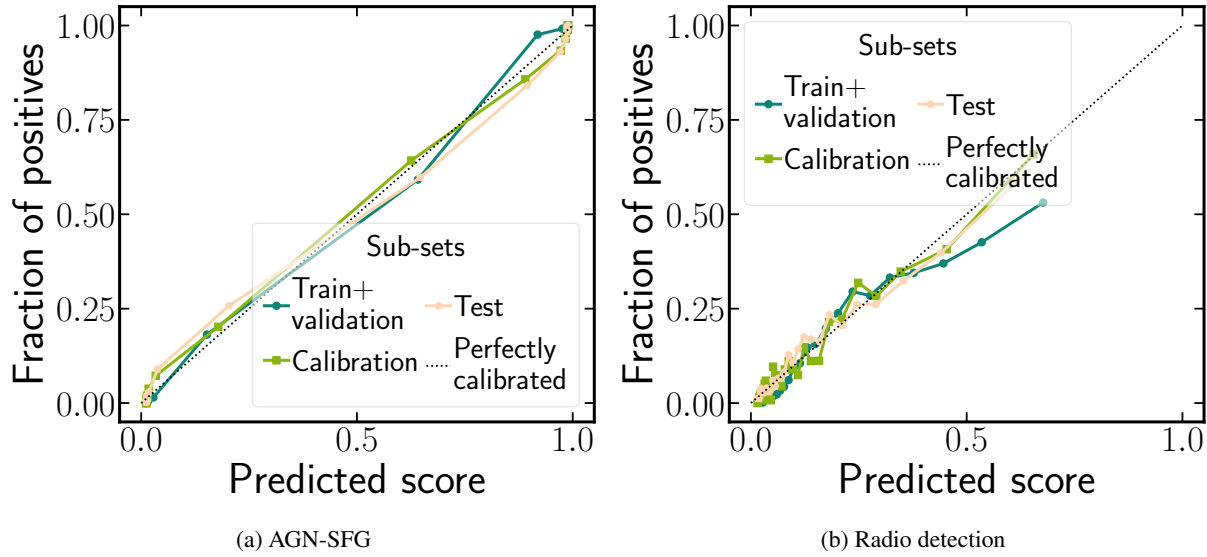


Figure 3.3: Reliability curves for calibrated classifiers. (a) AGN-SFG classification model. (b) Radio detection model. Details as in Fig. 3.2.

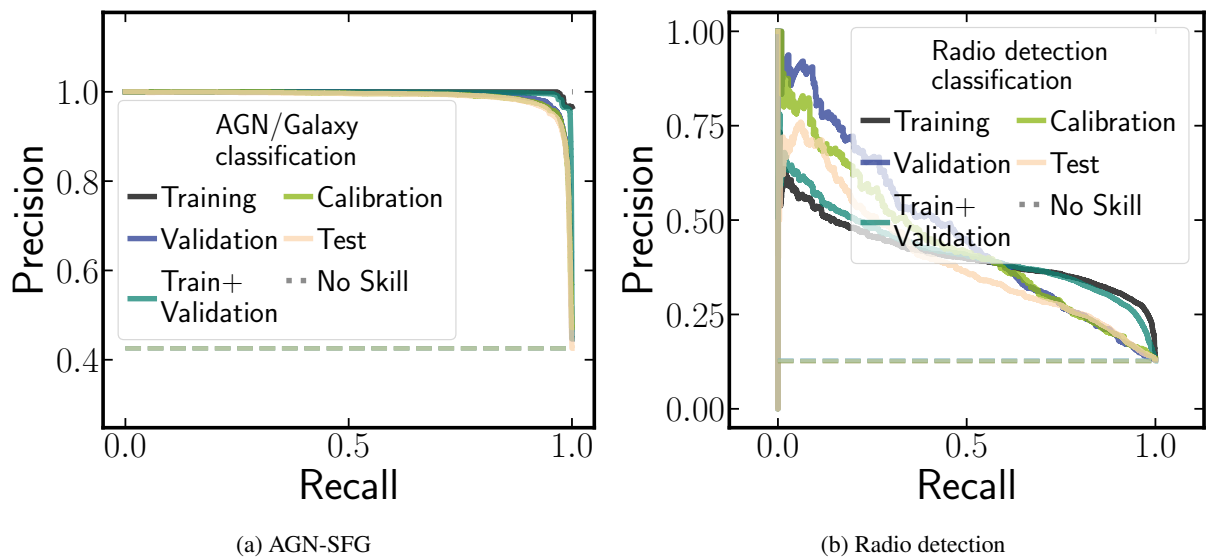


Figure 3.4: Precision-Recall curves for the (a) AGN-SFG and (b) radio detection classification models.

DRAFT - February 21, 2024 - DRAFT

This page intentionally left blank.

Prediction of radio-AGN candidates

After training the models, tuning their hyperparameters, and calibrating their scores, we were able to use them for predicting values in data sets which have not been used in the previous stages. In our case, this is the testing sub-set, which is different for each [ML](#) problem (classification or regression) and the labelled sources from [S82](#).

4.1 AGN-SFG classification

The results of the application of the stacked and calibrated model for the testing subset and the labelled sources in [S82](#) are presented in Table 4.1. The metrics are shown for the use of two different thresholds, the naive value of 0.5 and the [PR](#)-derived value of 0.348 95. The confusion matrix (calculated on the testing dataset) is shown in Fig. 4.1.

Overall, the model is able to separate [AGN](#) from [SFGs](#) with a very high (recall $\gtrsim 94\%$) success rate. It is possible to see that the [MCC](#) scores for the three sub-sets are in similar levels. That might be an indication of a good training process, in which no substantial over-fitting can be detected.

A closer inspection to the confusion matrix in Fig. 4.1 shows that close to a 45 % of the [AGN](#) from the [MQC](#) were discarded by our model. And less than 26 % of the predicted [AGN](#) are not labelled as such by the [MQC](#). An in-depth analysis of these results is presented in the following sections.

4.2 Radio detection classification

The application of the stacked model for the prediction of the radio detection of the training, testing, and validation sub-set is summarised in Table 4.2. Similarly, the confusion matrix derived from the prediction results over the test sample is shown in Fig. 4.2.

CHAPTER 4. PREDICTION OF RADIO-AGN CANDIDATES

Table 4.1: Resulting metrics of [AGN-SFG](#) classification model for the test subset and the labelled sources in [S82](#) using two different threshold values. [HETDEX](#) and [S82](#) pipeline results are described in Sect. 4.4.

Subset	Threshold	F_β ($\times 100$)	MCC ($\times 100$)	Precision ($\times 100$)	Recall ($\times 100$)
HETDEX-test	Naive	95.37 \pm 0.36	91.81 \pm 0.67	97.47 \pm 0.69	95.89 \pm 2.27
	PR	95.42 \pm 0.38	91.85 \pm 0.70	94.49 \pm 0.65	96.21 \pm 0.43
S82-label	Naive	94.15 \pm 0.44	70.54 \pm 2.02	95.16 \pm 0.41	93.33 \pm 0.66
	PR	94.37 \pm 0.36	70.67 \pm 1.72	94.81 \pm 0.40	94.01 \pm 0.59
HETDEX-pipe	Naive	95.37 \pm 0.36	91.81 \pm 0.67	97.47 \pm 0.69	95.89 \pm 2.27
	PR	95.42 \pm 0.38	91.85 \pm 0.70	94.49 \pm 0.65	96.21 \pm 0.43
S82-pipe	Naive	94.15 \pm 0.44	70.54 \pm 2.02	95.16 \pm 0.41	93.33 \pm 0.66
	PR	94.37 \pm 0.36	70.67 \pm 1.72	94.81 \pm 0.40	94.01 \pm 0.59

^a All metrics have been multiplied by 100.

^b Uncertainties show standard deviation of metrics obtained across all 10 training folds (cf. Sect. 3.5)

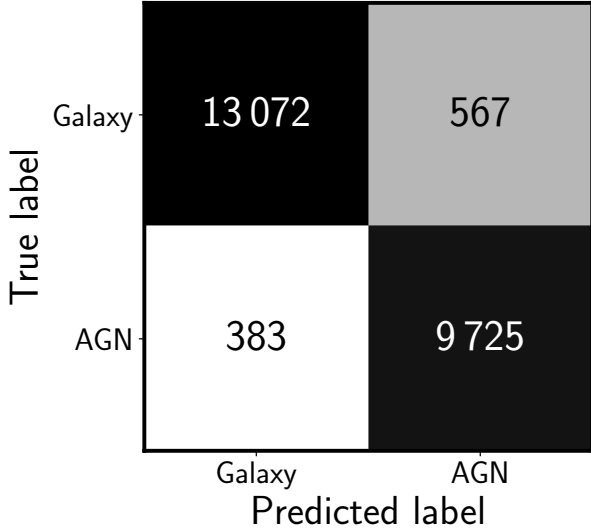


Figure 4.1: Confusion matrix from the results of application of [AGN-SFG](#) classification model to the [HETDEX](#) test subset.

4.3 Redshift prediction

In the case of redshift values prediction, the application of the stacked model over the testing sub-set is summarised in Table 4.3. Likewise, the comparison between the original redshift values and those derived from the prediction results is shown in Fig. 4.3.

The results in Table 4.3 show some degree of over-fitting, since the testing scores are a factor of two worse than those from the training and test sub-sets. This happens for all used metrics.

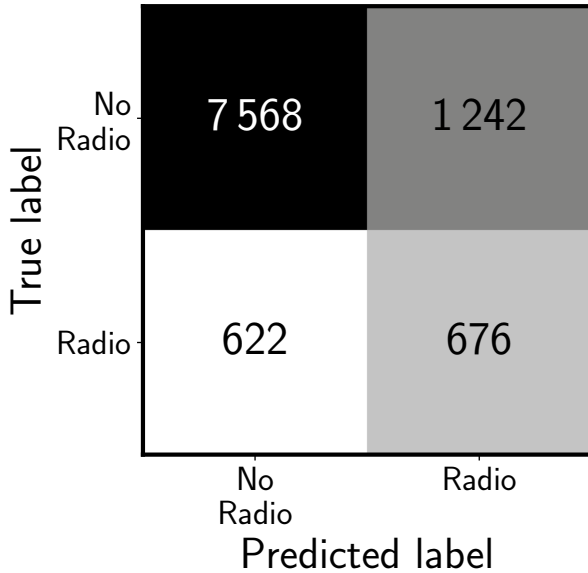


Figure 4.2: Confusion matrix from the results of application of radio-detection classification model for AGN to the HETDEX test subset.

Table 4.2: Resulting metrics of the radio detection model on the test subset and the labelled sources in S82 using two different threshold values. HETDEX and S82 pipeline results shown as part of the discussion in Sect. 4.4

Subset	Threshold	F_β ($\times 100$)	MCC ($\times 100$)	Precision ($\times 100$)	Recall ($\times 100$)
HETDEX-test	Naive	24.87±2.94	27.36±3.46	60.61±8.18	16.72±2.31
	PR	42.88±2.93	32.47±3.49	35.28±2.74	52.16±3.59
S82-label	Naive	27.15±2.28	23.36±2.27	25.72±1.91	28.47±3.24
	PR	21.62±1.20	19.37±1.64	12.29±0.73	58.16±3.06
HETDEX-pipe	Naive	24.37±3.53	26.93±4.18	59.36±7.17	16.38±2.63
	PR	41.57±4.16	31.67±4.81	34.65±3.24	49.80±5.85
S82-pipe	Naive	26.52±5.44	23.29±5.73	25.71±5.89	27.72±5.21
	PR	20.19±2.84	18.40±4.07	11.45±1.58	54.78±8.44

^a Values and uncertainties as in Table 4.1.

4.4 Prediction from pipeline

The sequential combination of the models described in Sect. 3.6 defines the pipeline for the prediction of radio-detectable AGN and their redshift. As separate tasks, the pipeline was applied to the labelled sources in the HETDEX testing subset, to the labelled sources in S82, and to all unlabelled sources across both fields. S82 provides an independent test of the pipeline as no data in this field was used for training the different models. A full candidate catalogue is extracted from this exercise and based on the unlabelled datasets.

As the metrics discussed in the previous sections correspond to each individual model, new –combined– metrics, based on the knowledge for labelled sources, are calculated for HETDEX and S82 and presented in Figs. 4.4, 4.5, 4.6, and 4.7 and Tables 4.3 and 4.4. Overall, we observe

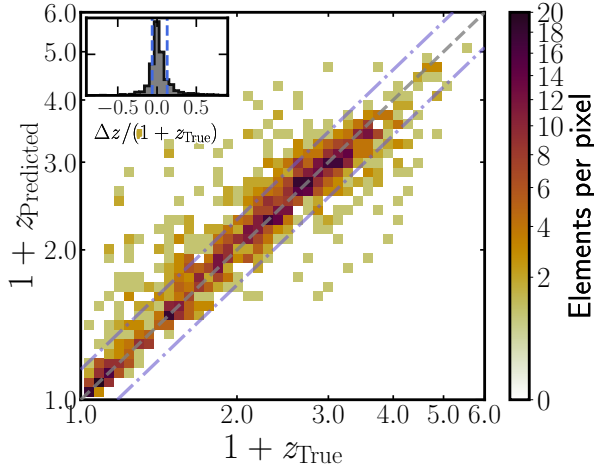


Figure 4.3: Density plot of comparison between original and predicted redshifts from the results of application of redshift prediction model to testing subset. Each point is colour-coded following the colorbar. Grey, dashed line shows $x = y$ relation and purple, dot-dashed lines show the limits where outliers are defined (cf. Eqn. 3.21). Inset shows the distribution of Δz^N values from the points shown in main plot, with a $\langle \Delta z^N \rangle = 0.0442$.

Table 4.3: Redshift prediction metrics for the test subset from [HETDEX](#) and [S82](#) labelled sources as discussed in Sect. 4.4

Subset	σ_{MAD} ($\times 100$)	σ_{NMAD} ($\times 100$)	σ_z ($\times 100$)	σ_z^N ($\times 100$)	η ($\times 100$)
HETDEX-test	16.54 ± 2.55	7.27 ± 0.99	41.14 ± 09.97	20.56 ± 5.98	19.03 ± 3.35
S82-label	18.66 ± 2.26	9.28 ± 1.37	51.08 ± 11.62	24.69 ± 4.36	24.29 ± 4.68
HETDEX-pipe-Naive	08.11 ± 3.95	5.42 ± 2.19	32.00 ± 12.27	20.97 ± 9.69	19.01 ± 8.22
HETDEX-pipe-PR	15.86 ± 1.77	7.17 ± 0.81	37.80 ± 03.06	22.93 ± 2.73	18.91 ± 1.59
S82-pipe-Naive	15.17 ± 2.70	9.14 ± 1.23	43.05 ± 07.20	24.32 ± 5.00	24.09 ± 4.52
S82-pipe-PR	20.71 ± 1.23	9.84 ± 0.56	45.14 ± 04.42	26.14 ± 3.77	25.18 ± 2.26

^a Values and uncertainties as in Table 4.1.

worse combined metrics with respect to the ones calculated for individual models (e.g. recall of 45 % for [HETDEX](#) and 47 % for [S82](#)). This degradation might be understood by the fact that the pipeline is composed of three sequential models. Each additional step is fed with sources classified by the previous algorithm. And some of these sources might not be similar, in terms of features, to those used for training, thus adding noise to the output of such model. A small sample of the output of the pipeline for five high- z labelled radio **AGN** sources in [HETDEX](#) and [S82](#) are shown in Tables A.2 and A.3 respectively.

The application of the prediction pipeline to the unlabelled sources from the [HETDEX](#) field led to 9 974 990 predicted **AGN**, from which 68 252 were predicted to be radio detectable. The pipeline predicts, as well, 2 073 997 **AGN** in the unlabelled data from [S82](#), being 22 445 of them candidates to be detected in the radio (to the detection level of [LoTSS](#)). The distribution of the predicted redshifts for radio-**AGN** in [HETDEX](#) and [S82](#) is presented in Fig. 4.8. The pipeline outputs for a small sample of the predicted radio **AGN** are presented in Tables A.4 and

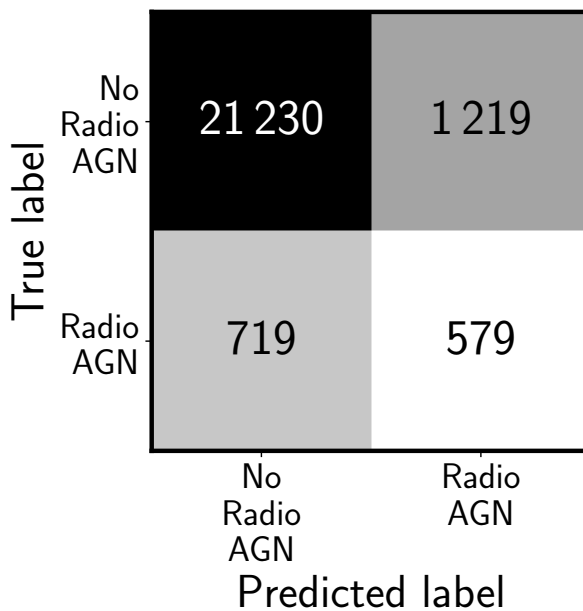


Figure 4.4: Combined confusion matrix from the full radio-AGN detectability prediction computed using the testing subset from [HETDEX](#).

Table 4.4: Results of application of radio AGN prediction pipeline to the labelled sources in the [HETDEX](#) and [S82](#) fields

Subset	Threshold	F_β ($\times 100$)	MCC ($\times 100$)	Precision ($\times 100$)	Recall ($\times 100$)
HETDEX-test	Naive	20.68 \pm 3.17	24.93 \pm 3.72	52.34 \pm 6.56	13.79 \pm 2.27
	PR	37.99 \pm 2.59	33.66 \pm 2.79	32.20 \pm 2.72	44.61 \pm 2.46
S82-label	Naive	24.08 \pm 3.44	21.43 \pm 3.53	25.44 \pm 3.64	23.07 \pm 3.72
	PR	19.42 \pm 2.31	17.23 \pm 3.08	11.33 \pm 1.32	47.36 \pm 6.22

^a Values and uncertainties as in Table 4.1.

A.5 for [HETDEX](#) and [S82](#) respectively.

4.5 No-skill classification

As presented in Sect. 3.1.1, Eqs. 3.6–3.9 show the base results for a classification with no skill. Table 4.5 presents the scores generated by using this technique. These values are the base from which any improvement can be assessed.

Subsets and prediction modes displayed in Table 4.5 coincide with those exhibited in Tables 4.1, 4.2, and 4.4. For instance, in the test [HETDEX](#) sub-sample, $\sim 43\%$ of sources are labelled as [AGN](#). From all [AGN](#), $\sim 13\%$ of them have radio detections. These percentages can be summarised stating that $\sim 6\%$ of all sources in the test sub-sample are radio-detected [AGN](#).

CHAPTER 4. PREDICTION OF RADIO-AGN CANDIDATES

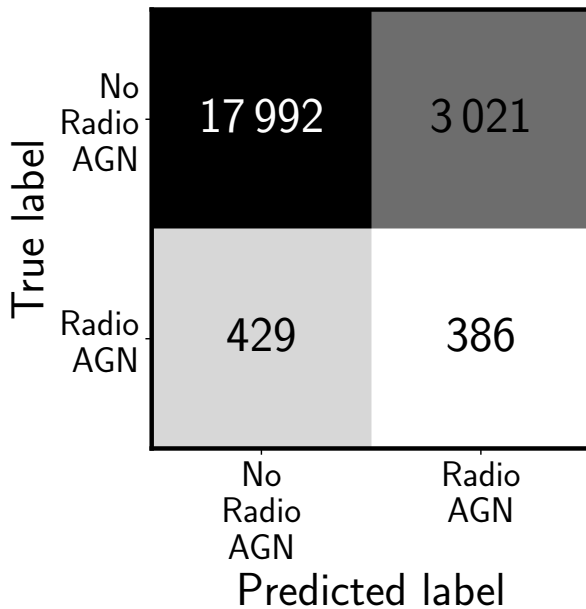


Figure 4.5: Combined confusion matrix from the full radio-AGN detectability prediction computed using the labelled sources from the [S82](#) field.

Table 4.5: Results of no-skill selection of sources in different stages of pipeline to the labelled sources in the [HETDEX](#) test subset and [S82](#) fields

Subset	Prediction	F_β ($\times 100$)	MCC ($\times 100$)	Precision ($\times 100$)	Recall ($\times 100$)
HETDEX	AGN-SFG	42.57	0.00	42.57	42.57
	Radio-detection (label)	12.84	0.00	12.84	12.84
	Radio AGN	5.47	0.00	5.47	5.47
S82	AGN-SFG	81.29	0.00	81.29	81.29
	Radio-detection (label)	4.59	0.00	4.59	4.59
	Radio AGN	3.73	0.00	3.73	3.73

^a All metrics have been multiplied by 100.

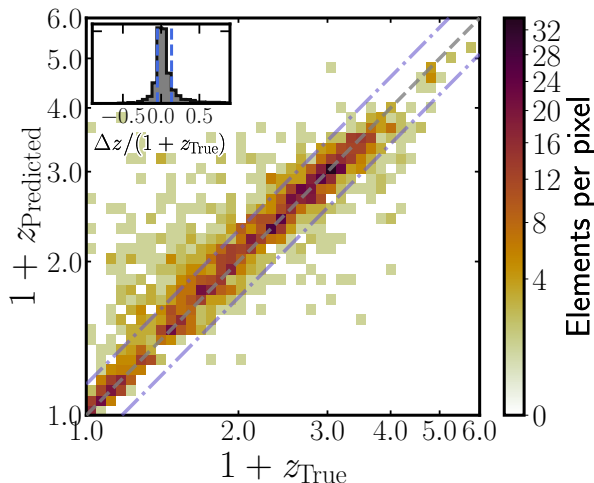


Figure 4.6: Density plot of comparison between original and predicted redshifts from the results of application of redshift prediction model to sources predicted to be radio-detectable AGN in the testing subset. Details as in Fig. 4.3.

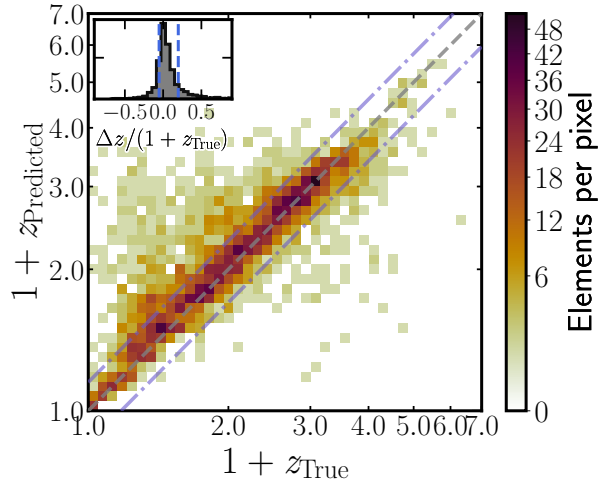


Figure 4.7: Density plot of comparison between original and predicted redshifts from the results of application of redshift prediction model to sources predicted to be radio-detectable AGN among labelled sources in the S82 field. Details as in Fig. 4.3.

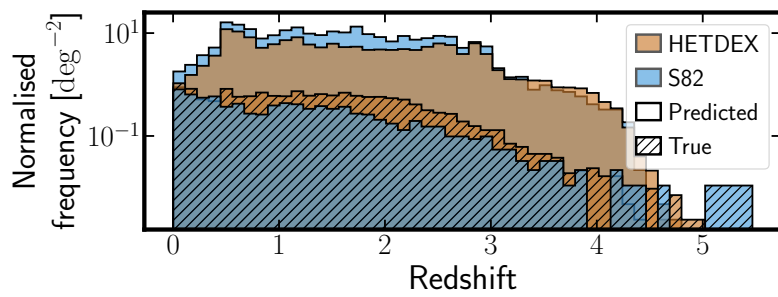


Figure 4.8: Redshift density distribution of the predicted radio-AGN within the unlabelled sources (clean histograms) in HETDEX (ochre histograms) and S82 (blue histograms) and true redshifts from labelled radio-AGN (dashed histograms).

This page intentionally left blank.

Analysis of prediction method and results

5.1 Comparison with previous works

In this section, we provide a few examples of related published works as well as plausible explanations for observed discrepancies when these are present. This comparison attempts to be representative of the literature on the subject but does not intend to be complete in any way.

5.1.1 AGN detection prediction

In order to understand the significance of our results and ways for future improvement, we separate the comparison with previous works in two parts. First, we present previously published results from traditional methodologies. In second place, we offer a comparison with [ML](#) methods.

Traditional [AGN](#) selection methods are based on the comparison of the measured [SED](#) photometry to a template library (Walcher et al., 2011). A recent example of its application is presented by Thorne et al. (2022b) where best fit classifications were calculated for more than 700 000 galaxies in the [D10](#) field of the Deep Extragalactic VIsible Legacy Survey ([DEVILS](#); Davies et al., 2018a) and the [Galaxy and Mass Assembly](#) ([GAMA](#); Driver et al., 2011; Liske et al., 2015). The 91 % recovery rate of [AGN](#), selected through various means (X-ray measurements, narrow and broad emission lines, and [MIR](#) colours), is very much in line with our findings in [S82](#), where our rate (recall) reaches 89 %.

Traditional methods also encompass the colour-based selection of [AGN](#). While less precise, they provide access to a much larger base of candidates with a very low computational cost. We implemented some of the most common colour criteria on the data from [S82](#). Of particular interest is the predicting power of the [MIR](#) colour selection due to its potential to detect hidden or heavily obscured [AGN](#) activity.

Based on [WISE](#) data, Stern et al., 2012 proposed a threshold at $W1 - W2 \geq 0.8$ to separate [AGN](#) from non-[AGN](#) using data from [AGN](#) in the [Cosmic Evolution Survey](#) ([COSMOS](#); Scoville

et al., 2007) field. A more stringent criterion was developed by M12, the AGN wedge, which can be defined by the sources located inside the region defined by the relations $W1 - W2 < 0.315 \times (W2 - W3) + 0.791$, $W1 - W2 > 0.315 \times (W2 - W3) - 0.222$, and $W1 - W2 > -3.172 \times (W2 - W3) + 7.624$. In order to define this wedge, they used data from X-ray selected AGN over an area of 44.43 deg^2 in the northern sky. M16 cross-correlated data from *WISE* observations with X-ray and radio surveys creating a sample of SFGs and AGN in the northern sky. They developed individual relations to separate classes of SFGs and AGN in the $W1 - W2$, $W2 - W3$ space and, for AGN the criterion, the relation is $W1 - W2 \geq 0.5$ and $W2 - W3 < 4.4$. More recently, B18 analysed the quality of MIR colour selection methods for the identification of obscured AGN involved in mergers. Using hydrodynamic simulations for the evolution of AGN in galaxy mergers, they developed a selection criterion from *WISE* colours which is shown to be able to separate, with high reliability, starburst galaxies from AGN. The expressions have the form $W1 - W2 > 0.5$, $W2 - W3 > 2.2$, and $W1 - W2 > 2 \times (W2 - W3) - 8.9$.

The results from the application of these criteria to our samples in the testing subset and in the labelled sources of S82 field are summarised in Table 5.1 and a graphical representation of the boundaries they create in their respective parameter spaces is presented in Fig. 5.1.

Table 5.1 shows that previous colour-colour criteria have been designed and calibrated to have very high precision values. Most of the sources deemed to be AGN by them are, indeed, of such class. Despite being tuned to maximise their recall (and F_β to a lesser extent), our classifier, and the criterion derived from it, still show precision values compatible with those of such criteria. This result underlines the power of ML methods. They can be on a par with traditional colour-colour criteria and excel in additional metrics.

Figure 5.1 is constructed as a confusion matrix, plotting in each quadrant the whole *WISE* population in the background and in colour contours the corresponding fraction of the testing set (TP, TN, FP, and FN, see Fig. 4.1 and Sect. 3.1.1). As expected, our pipeline is able to separate with high confidence sources which are closer to the AGN or the SFG locus (TP and TN) while sources in the FN and FP quadrant show a different situation. AGN predicted to be SFGs (FN, 1.6 % of sources for HETDEX, and 4.9 % for S82) are located in the SFG region of the colour-colour diagram. On the opposite corner of the plot, SFGs predicted to be AGN (FP, 2.4 % of sources for HETDEX, and 4.2 % for S82) cover the areas of AGN and SFGs uniformly. FN sources might be sources that are identified as AGN by means not included in our feature set (e.g. X-ray, radio emission). Sources in FP quadrant, alternatively, might be SFGs with extreme properties, similar to AGN.

Table 5.1: Results of application of several **AGN** detection criteria to our testing subset and the labelled sources from the **S82** field.

HETDEX test set				
Method	F_β (×100)	MCC (×100)	Precision (×100)	Recall (×100)
S12	86.10	78.78	93.98	80.51
M12	51.80	49.71	98.87	37.18
M16	67.21	61.30	97.48	53.48
B18	82.14	75.76	97.54	72.66

S82 (labelled)				
Method	F_β (×100)	MCC (×100)	Precision (×100)	Recall (×100)
S12	83.59	45.47	93.93	76.62
M12	46.80	28.22	99.59	32.54
M16	64.69	37.76	98.80	50.32
B18	79.71	51.07	98.72	68.77

^a Naming codes for the used methods are described in the main text (cf. Sect. 5.1.1)

^b All metrics have been multiplied by 100.

For the case of **ML**-based models for **AGN-SFG** classification, several analyses have been published in recent years. An example of their application is provided in Clarke et al. (2020) where a Random Forest model for the classification of stars, **SFGs** and **AGN** using photometric data was trained from more than 3 000 000 sources in the **SDSS** (DR15; Aguado et al., 2019) and **WISE** with associated spectroscopic observations. Close to 400 000 sources have a quasar spectroscopic label and from the application of their model to a validation subset, they obtain a recall of 0.929 and **F1**-score of 0.943 for the quasar classification. These scores are of the same order as the ones obtained when applying our **AGN-SFG** model to the testing set (see Table 4.1). Thus, and despite using an order of magnitude fewer sources for the full training and validation process, our model can achieve equivalently good scores.

Expanding on the results from Clarke et al. (2020), Cunha and Humphrey (2022) built a **ML** pipeline, **SHEEP**, for the classification of sources into stars, **SFGs** and **QSO**. In contrast to Clarke et al. (2020) or the pipeline described in this thesis, the first step in their analysis is the redshift prediction, which is used as part of the training features by the subsequent classifiers. They extracted **WISE** and **SDSS Data Release 15** (SDSS-DR15; Aguado et al., 2019) photometric data for almost 3 500 000 sources classified as stars, **SFGs** or **QSO**. The application of their pipeline to sources predicted to be **QSO** led to a recall of 0.960 and an **F1** score of 0.967. The improved scores in their pipeline might be a consequence not only of the slightly larger pool of sources,

CHAPTER 5. ANALYSIS OF PREDICTION METHOD AND RESULTS

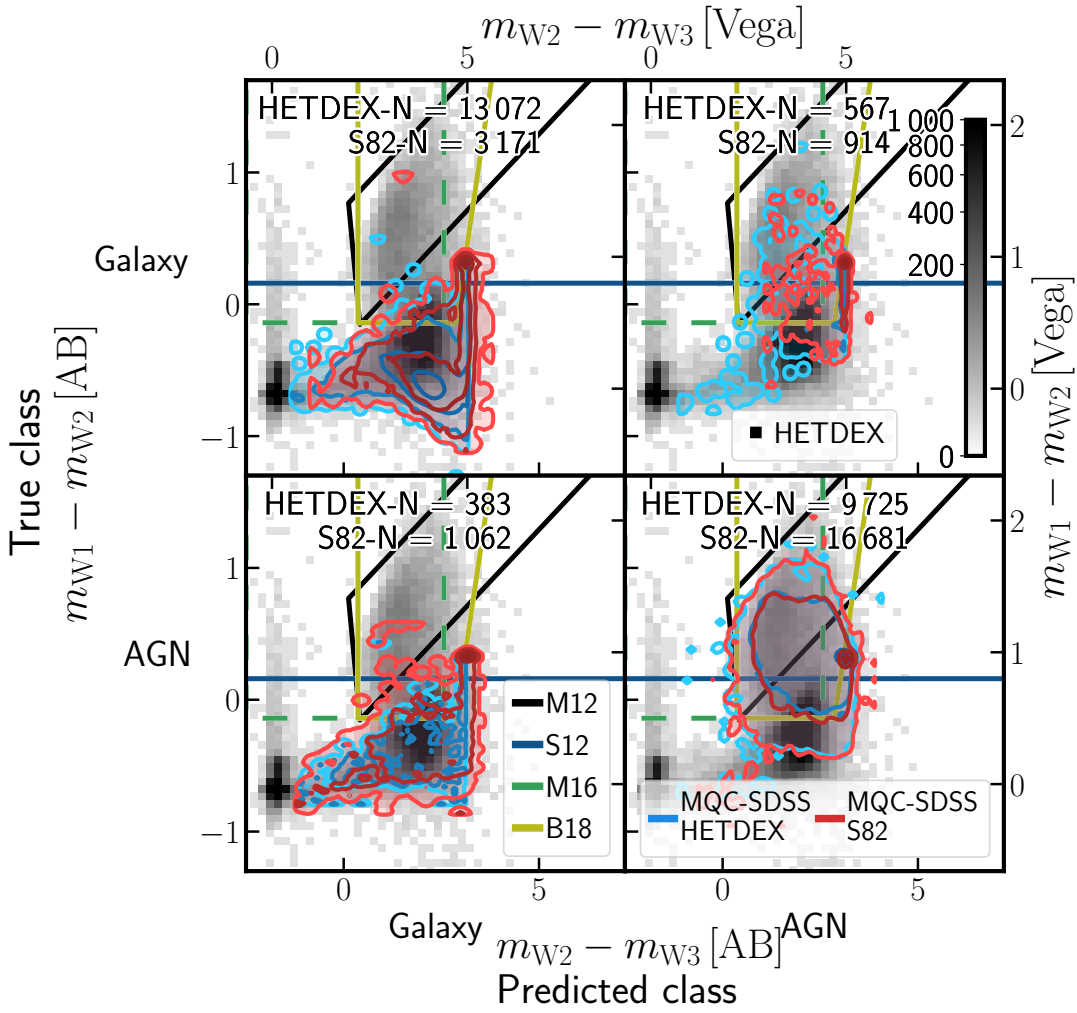


Figure 5.1: $W_1 - W_2$, $W_2 - W_3$ colour-colour diagrams for sources in the testing subset, from [HETDEX](#), and labelled sources from [S82](#) given their position in the [AGN-SFG](#) confusion matrix (see, for [HETDEX](#), Fig. 4.4 and, for [S82](#), Fig. 4.5). In the background, density plot of all [CW](#)-detected sources in the full [HETDEX](#) field sample is displayed. Colour of each square represents the number of sources in that position of parameter space, with darker squares having more sources (as defined in the colorbar of the upper-right panel). Contours represent distribution of sources for each of the aforementioned subsets at 1, 2, 3 and 4 σ levels (shades of blue, for testing set and shades of red for labelled [S82](#) sources). Coloured, solid lines display limits from the criteria for the detection of [AGN](#) described in Sect. 5.1.1.

but also the inclusion of the coordinates of the sources (right ascension, declination) and the predicted redshift values as features in the training.

A test with a larger number of [ML](#) methods was performed by Polisczuk et al. (2021). For training, they used optical and infrared data from close to 1500 sources ([SFGs](#) and [AGN](#)) located at the AKARI [North Ecliptic Pole \(NEP\)](#) Wide-field (Lee et al., 2009; Kim et al., 2012) covering a 5.4 deg^2 area. They tested [linear regression \(LR\)](#), [support vector machine \(SVM\)](#); Vapnik, 1995; Cortes and Vapnik, 1995), [RF](#), [ET](#), and [XGBoost](#) including the possibility of generalised stacking. In general, they obtained results with [F1](#)-scores between 0.60 – 0.70 and recall values in the range of 50 % – 80 %. These values, lower than the works described here, can be fully understood given the small size of the training sample. A larger photometric sample

covers a wider range of the parameter space which significantly helps the metrics of any given model.

5.1.2 Radio detection prediction

We have not found in the literature any work attempting the prediction of **AGN** radio detection at any level and therefore this is the first attempt at doing so. In the literature we do find several correlations between the **AGN** radio emission (flux) and that at other wavelengths (e.g. with **IR** emission, Helou et al., 1985; Condon, 1992) and substantial effort has been done towards classifying radio galaxies based upon their morphology (e.g. Aniyan and Thorat, 2017; Wu et al., 2019; Fanaroff-Riley class I (**FRI**), Fanaroff-Riley class II (**FRII**), bent jets, etc.) and its connection to environment (Miley and De Breuck, 2008; Magliocchetti, 2022). None of these extensive works has directly focused on the a priori presence or absence of radio emission above a certain threshold. Therefore, the results presented here are the first attempt at such an effort.

The $\sim 2x$ success rate of the pipeline to identify radio emission in **AGN** ($\sim 44.61\%$ recall and $\sim 32.20\%$ precision; see Table 4.4) with the respect to a 'no-skill' or random ($\lesssim 30\%$) selection, provides the opportunity to understand what the model has learned from the data and, therefore, gain some insight into the nature or triggering mechanisms of the radio emission. We, therefore, reserve the discussion of the most important features, and the linked physical processes, driving the pipeline improved predictions to Sects. 5.3 and 5.4.

5.1.3 Redshift prediction

We compare our results to that of Ananna et al. (2017: Stripe 82X) where the authors analysed multi-wavelength data from more than 6100 X-ray detected **AGN** from the 31.3 deg^2 of the Stripe 82X survey. They obtained photometric redshifts for almost 6000 of these sources using the template-based fitting code LePhare (Arnouts et al., 1999; Ilbert et al., 2006). Their results present a normalised median absolute deviation of $\sigma_{\text{NMAD}} = 0.062$ and an outlier fraction of $\eta = 13.69\%$, values which are similar to our results in **HETDEX** and **S82** except for a better outlier fraction (as shown in Table 4.3, we obtain $\eta_{\text{S82}} = 25.18\%$, $\sigma_{\text{NMAD}}^{\text{HETDEX}} = 0.071$, and $\eta^{\text{HETDEX}} = 18.9\%$).

On the **ML** side, we compare our results to those produced by Carvajal et al. (2021) in **S82**, with $\sigma_{\text{NMAD}} = 0.1197$ and $\eta = 29.72\%$, and find that our redshift prediction model improves

by at least 25 % for any given metric. The source of improvement is probably many-fold. First, it might be related to the different sets of features used (colours vs ratios) and second, the more specific population of radio-[AGN](#) used to train our models. Carvajal et al. (2021) used a limited set of colours to train their model, while we have allowed the use of all available combinations of magnitudes (Sect. 2.5). Additionally, their redshift model was trained on all available [AGN](#) in [HETDEX](#), while we have trained (and tested) it only with radio-detected [AGN](#). Using a more constrained sample reduces the likelihood of handling sources that are too different in the parameter space.

Another example of the use of [ML](#) for [AGN](#) redshift prediction has been presented by Luken et al. (2019). They studied the use of the [k-nearest neighbours \(KNN; Cover and Hart, 1967\)](#) algorithm, a non-parametric supervised learning approach, to derive redshift values for radio-detectable sources. They combined 1.4 GHz radio measurements, infrared, and optical photometry in the [European Large Area ISO Survey-South 1 \(ELAIS-S1; Oliver et al., 2000\)](#) and [extended Chandra Deep Field South \(eCDFS; Lehmer et al., 2005\)](#) fields, matching their sensitivities and depths to the expected values in the [EMU](#). From the different experiments they run, their resulting [NMAD](#) values are in the range $\sigma_{\text{NMAD}} = 0.05$ to 0.06, and their outlier fraction can be found between $\eta = 7.35\%$ and $\eta = 13.88\%$. As an extension to the previous results, Luken et al. (2022) analysed multi-wavelength data from radio-detected sources the [eCDFS](#) and the [ELAIS-S1](#) fields. Using [KNN](#) and [RF](#) methods to predict the redshifts of more than 1300 [RGs](#), they have developed regression methods that show [NMAD](#) values between $\sigma_{\text{NMAD}} = 0.03$ and $\sigma_{\text{NMAD}} = 0.06$, $\sigma_z = 0.10$ to 0.19, and outlier fractions of $\eta = 6.36\%$ and $\eta = 12.75\%$.

In addition to the previous work, Norris et al. (2019) compared a number of methodologies, mostly related with [ML](#) but also LePhare, for predicting redshift values for radio sources. They have used more than 45 photometric measurements (including 1.4 GHz fluxes) from different surveys in the [COSMOS](#) field. From several settings of features, sensitivities, and parameters, they retrieved redshift predictions with [NMAD](#) values between $\sigma_{\text{NMAD}} = 0.054$ and $\sigma_{\text{NMAD}} = 0.48$ and outlier fractions that range between $\eta = 7\%$ and $\eta = 80\%$. The broad span of obtained values might be due to the combinations of properties for each individual training set (including the use of radio or X-ray measurements, the selection depth, and others) and to the size of these sets, which was small for [ML](#) purposes (less than 400 sources). The slightly better results can be understood given the heavily populated photometric data available in [COSMOS](#).

Specifically related to the [HETDEX](#) field, it is possible to compare our results to those from

Duncan et al. (2019). They use a hybrid photometric redshift approach combining traditional template fitting redshift determination (Brammer et al., 2008; Salvato et al., 2018; Salvato et al., 2011; Brown et al., 2014) and ML-based methods. In particular, they implemented a GP algorithm (GPz; Almosallam et al., 2016b; Almosallam et al., 2016a), which is able to model both the intrinsic noise and the uncertainties of the training features. Their redshift prediction analysis of AGN sources with a spectroscopic redshift detected in the LoTSS DR1 (6.811 sources) found a NMAD value of $\sigma_{\text{NMAD}} = 0.102$ and an outlier fraction of $\eta = 26.6\%$. The differences between these results and those obtained from the application of our models (individually and as part of the prediction pipeline) might be due to the differences in the creation of the training sets. Duncan et al. (2019) use information from all available sources in the HETDEX field for training the redshift GP whilst our redshift model has been only trained on radio-detected AGN, giving it the opportunity to focus its parameter exploration only on these sources.

Finally, Cunha and Humphrey (2022) also produced photometric redshift predictions for almost 3 500 000 sources (stars, SFGs, and QSO) as part of their pipeline (see Sect. 5.1.1). They combined three algorithms for their predictions: XGBoost, CatBoost, and Light Gradient Boosting Machine (LightBGM; Ke et al., 2017). This procedure leads to $\sigma_{\text{NMAD}} = 0.018$ and $\eta = 2\%$. As with previous examples, the differences with our results can be a consequence of the number of training samples. Also, in the case of Cunha and Humphrey (2022), they applied an additional post-processing step to the redshift predictions attempting to predict and understand the appearance of catastrophic outliers.

5.2 Influence of data imputation

One effect which might influence the training of the models and, consequently, the prediction for new sources is related to the imputation of missing values (cf. Sect. 2.4). In Fig. 5.2, we have plotted the distributions of predicted scores (for classification models) and predicted redshift values as a function of the number of measured bands (band_num) for each step of the pipeline as applied to sources predicted to be of each class in the test sub-set.

The top panel of Fig. 5.2 shows the influence of the degree of imputation in the classification between AGN and SFGs. For most of the bins, probabilities for predicted SFGs are distributed close to 0.0, without any noticeable trend. In the case of predicted AGN, the combination of low number of sources and high degree of imputation (band_num < 5) lead to low mean

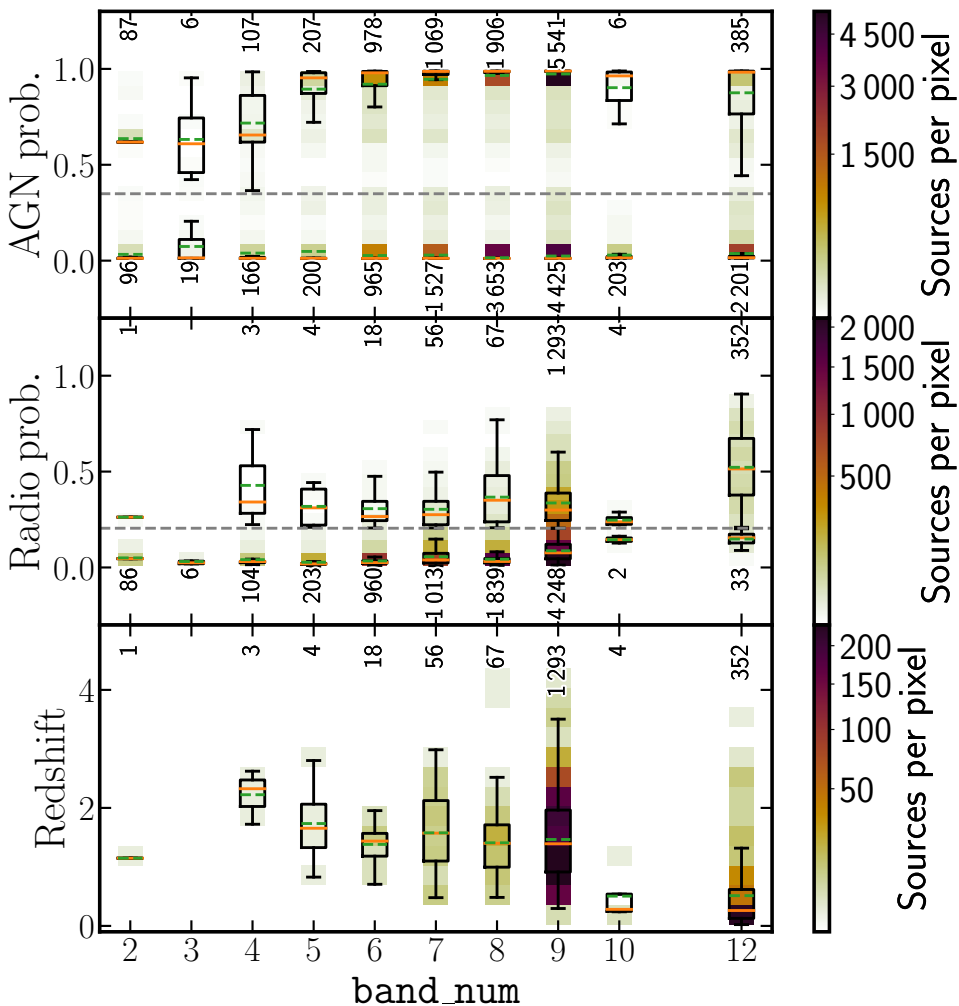


Figure 5.2: Evolution of predicted probabilities (top: probability to be **AGN**, middle: probability of **AGN** to be radio-detected) and redshift values for radio-detectable **AGN** (bottom panel) as function of number of observed bands for sources in test set. In top panel, sources have been divided between those predicted to be **AGN** and **SFGs**. In middle panel, sources are divided between predicted **AGN** that are predicted to be radio-detected and those predicted to not have radio detection. Background density plots (following colour coding in colorbars) show location of predicted values. Overlaid boxplots display main statistics for each number of measured bands. Black rectangles encompass sources in second and third quartiles. Vertical lines show place of sources from first and fourth quartiles. Orange lines represent median value of sample and dashed, green lines indicate their mean values. Dashed, grey lines show PR thresholds for **AGN-SFG** and radio detection classifications. Close to each boxplot, written values correspond to number of sources considered to create each set of statistics.

probabilities.

The case of radio detection classification is somewhat different. Given the number and distribution of sources per bin, it is not possible to extract any strong trend for the probabilities of radio-predicted sources. The absence of evolution with the number of observed bands is stronger for sources predicted to be devoid of radio detection.

Finally, a stronger effect can be seen with the evolution of predicted redshift values for radio-detectable **AGN**. Despite the lower number of available sources, it is possible to recognise that sources with higher number of available measurements are predicted to have lower redshift values. Sources that are closer to us have higher probabilities to be detected in a large number of

bands. Thus, it is expected that our model predicts lower redshift values for the most measured sources in the field.

One interesting feature of all panels in Fig. 5.2 is the lack of sources with `band_num` = 11. This effect can be caused by the inclusion of measurements from **2M**. As seen in Fig. 2.3, all three **2M** bands have the highest (and almost the same) number of missing measurements. Thus, it is possible to infer that the inclusion of a measurement in one of the **2M** bands will imply the addition of the two remaining bands.

In consequence, Fig. 5.2 allows us to understand the influence of imputation over the predictions. The most highly affected quantity is the redshift, where large fractions of measured magnitudes are needed to obtain scores that are in line with previous results (cf. Sect. 5.1.3). The **AGN-SFG** and radio detection classifications show a mild influence of imputation in their results.

5.3 Global feature importances

Overall, mean or global feature importances can be retrieved from models that are based on Decision Trees (e.g. Random Forests and Boosting models, Breiman, 2001; Breiman, 2003). All algorithms selected in this work (**RF**, **CatBoost**, **XGBoost**, **ET**, **GBR**, and **GBC**) belong to these two classes. For each feature, the decrease in impurity (a term frequently used in the literature related to **ML**, for instance, in Breiman, 2001) of the dataset is calculated for all the nodes of the tree in which that feature is used. Features with the highest impurity decrease will be more important for the model (Louppe et al., 2013). For some models that are not based on Decision Trees, feature importances can be obtained from the coefficients that the training process delivers for each feature. These coefficients are related to the level to which each quantity is scaled to obtain a final prediction (as in the coefficients from a polynomial regression).

Insight into the decision-making of the pipeline can only rely on the specific weight of the original set of features (see Sect. 3.4). Table 5.2 presents the ranked combined importances from the observables selected in each of the three sequential models that compose the pipeline. They have been combined using the importances from the meta-learner (as shown in Table 5.3) and that of base-learners. The derived importances will be dependent on the dataset used, including any imputation for the missing data, and the details of the models, that is, algorithms used and stacking procedure. We first notice in Table 5.2 that the order of the features is different for all three models. This difference reinforces the need, as stated in Chapter 4, of developing separate

CHAPTER 5. ANALYSIS OF PREDICTION METHOD AND RESULTS

Table 5.2: Relative importances (rescaled to add to 100) for observed features from the three models combined between meta and base models.

AGN-SFG (meta-model: CatBoost)					
Feature	Importance	Feature	Importance	Feature	Importance
W1_W2	68.945	H_K	1.715	z_W2	1.026
W1_W3	4.753	y_W1	1.659	z_y	0.722
g_r	4.040	y_W2	1.513	W3_W4	0.669
r_J	4.006	i_y	1.441	W4mag	0.558
r_i	3.780	i_z	1.366	H_W3	0.408
band_num	1.842	y_J	1.187	J_H	0.371
Radio detection (meta-model: GBC)					
Feature	Importance	Feature	Importance	Feature	Importance
W2_W3	9.609	y_W1	7.150	W4mag	4.759
y_J	8.102	g_r	7.123	K_W4	2.280
W1_W2	8.010	z_W1	7.076	J_H	1.283
g_i	7.446	r_z	6.981	H_K	1.030
K_W3	7.357	i_z	6.867	band_num	1.018
z_y	7.321	r_i	6.588		
Redshift prediction (meta-model: ET)					
Feature	Importance	Feature	Importance	Feature	Importance
y_W1	35.572	y_J	3.018	i_z	1.215
W1_W2	13.526	r_z	3.000	J_H	1.162
W2_W3	12.608	r_i	2.896	g_W3	1.000
band_number	6.358	z_y	2.827	K_W3	0.925
H_K	4.984	W4mag	2.784	K_W4	0.762
g_r	4.954	i_y	2.408		

^a Relative feature importance values are specific to each model training and cannot be compared, numerically, to the values obtained in a different model. A meaningful comparison can be done by contrasting the order in which features are sorted.

models for each of the prediction stages of this work that would evaluate the best feature weights for the related classification or regression task.

For the AGN-SFG classification model, it is very interesting to note that the most important feature for the predicted probability of a source to be an AGN is the WISE colour W1 - W2 (as well as W1 - W3). This colour is indeed one of the axes of the widely used WISE colour-colour selection, with the second axis being the W2 - W3 colour (cf. Sect 5.1.1). The WISE W3 photometry is though significantly less sensitive than W1, W2 or PS1 (see Fig. 2.5) and a significant number of sources will be represented as upper limits in such plot (see Table 2.3).

One of the main potential uses of the pipeline is its capability to pinpoint radio-detectable AGN. The global features analysis for the radio detection model shows a high dependence on the near- and mid-IR magnitudes and colours, especially those coming from WISE. As a useful

Table 5.3: Relative feature importances (rescaled to add to 100) for base algorithms in each prediction step.

AGN-SFG model (CatBoost)			
Feature	Importance	Feature	Importance
gbc	49.709	xgboost	14.046
et	19.403	rf	8.981
Remaining feature importances:			7.861
Radio detection model (GBC)			
Feature	Importance	Feature	Importance
rf	12.024	catboost	7.137
et	7.154	xgboost	6.604
Remaining importances:			67.081
Redshift prediction model (ET)			
Feature	Importance	Feature	Importance
xgboost	25.138	catboost	21.072
gbr	21.864	rf	13.709
Remaining importances:			18.217

^a Relative feature importance values are specific to each model training and cannot be compared, numerically, to the values obtained in a different model. A meaningful comparison can be done by contrasting the order in which features are sorted.

outcome similar to the AGN-SFG classification, we can use the most relevant features to build useful plots for the pre-selection of these sources and get insight into the origin of the radio emission. This is the case for the W4 histogram, shown in Fig. 5.3, where sources predicted to be radio-emitting AGN extend to brighter measured W4 magnitudes. This added MIR flux might be simply due to an increased SFRs in these sources. In fact the 24 μm flux is often used, together with that of H α as a proxy for SFR (Kennicutt et al., 2009). The radio detection for these sources might have a strong component linked to the ongoing SF, especially for the sources with real or predicted redshift below $z \sim 1.5$.

Finally, the redshift prediction model shows again that the final estimate is mostly driven by the results of the base learners, accounting for $\sim 82\%$ of the predicting power. The overall combined importance of features shows also in this case a strong dependence on several NIR colours of which y - W1 and W1 - W2 are the most relevant ones. The model still relies, to a lesser extent, on a broad range of optical features needed to trace the broad range of redshift possibilities ($z \in [0, 6]$).

CHAPTER 5. ANALYSIS OF PREDICTION METHOD AND RESULTS

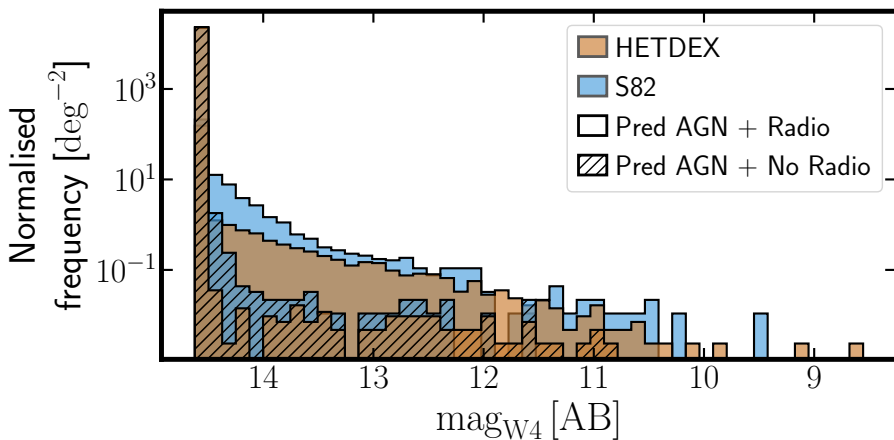


Figure 5.3: W4 magnitudes density distribution of the newly predicted radio-AGN (clean histograms) in [HETDEX](#) (ochre histograms) and [S82](#) (blue histograms) and W4 magnitudes from predicted AGN that are predicted to not have radio detection (dashed histograms).

5.4 Local feature importances

As opposed to the global (mean) assessment of feature importances derived from the decrease in impurity, local (i.e. source by source) information on the performance of such features can be obtained from Shapley values. This is a method from coalitional game theory that tells us how to fairly distribute the dividends (the prediction in our case) among the features (Shapley, 1953). The previous statement means that the relative influence of each property from the dataset can be derived for individual predictions in the decision made by the model (which is not the same as obtaining causal correlations between features and the target; Ma and Tourani, 2020). The combination of Shapley values with several other model explanation methods was used by Lundberg and Lee (2017) to create the [SHAP](#) values. In this work, SHAP values were calculated using the python package [SHAP](#)¹ and, in particular, its module for Tree-based predictors (Lundberg et al., 2020). To speed calculations up, the package [FastTreeSHAP](#)² ([v0.1.2](#); Yang, 2021) was also used, which allows the user to run multi-thread computations.

One way to display these [SHAP](#) values is through the so-called decision plots. They can show how individual predictions are driven by the inclusion of each feature. Besides determining the most relevant properties that help the model make a decision, it is possible to detect sources that follow different prediction paths which could be, eventually and upon further examination, labelled as outliers. An example of this decision plot, linked to the [AGN-SFG](#) classification, is shown in Fig. 5.4 for a subsample of the high-redshift ($z \geq 4.0$) spectroscopically classified AGN in the [HETDEX](#) field (121 sources, regardless of them being part of any sub-set involved

¹<https://github.com/slundberg/shap>

²<https://github.com/linkedin/fasttreeshap>

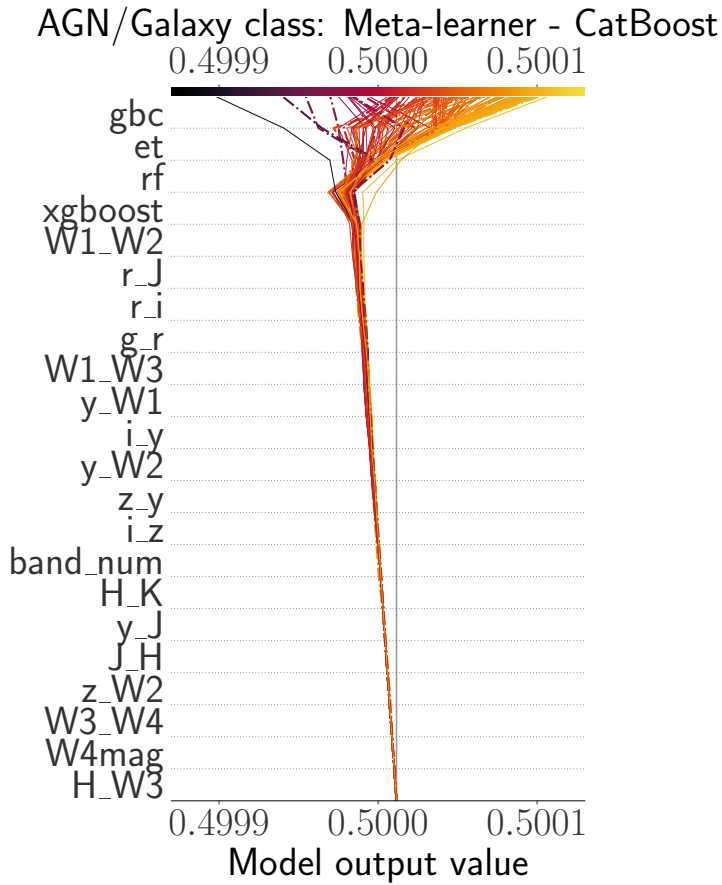


Figure 5.4: Decision plot from **SHAP** values for **AGN-SFG** classification from the 121 high redshift ($z \geq 4$) spectroscopically confirmed **AGN** in **HETDEX**. Horizontal axis represents the model’s output with a starting value for each source centred on the selected naive threshold for classification. Vertical axis shows features used in the model sorted, from top to bottom, by decreasing mean absolute **SHAP** value. Each prediction is represented by a coloured line corresponding to its final predicted value as shown by the colorbar at the top. Moving from the bottom of the plot to the top, **SHAP** values for each feature are added to the previous value in order to highlight how each feature contributes to the overall prediction. Predictions for sources detected by **LOFAR** are highlighted with a dotted, dashed line.

in the training or validation of the models). The different features used by the meta-learner are stacked on the vertical axis with increasing weight and these final weight are summarised in Table 5.4. Similarly, **SHAP** decision plots for the radio-detection and redshift prediction are presented in Figs. 5.5 and 5.6, respectively.

As it can be seen, for the three models, base learners are amongst the features with the highest influence. This result raises the question of what drives these individual base predictions. Figs. 5.7, 5.8, and 5.9 show **SHAP** decision plots for all base learners used in this work. Additionally, and to be able to compare these results with the features importances from Sect. 5.3, we constructed Table 5.5, which displays the combined **SHAP** values of base and meta learners but, in this case, for the same 121 high-redshift confirmed **AGN** (with 29 of them detected by **LoTSS**). Table 5.5 shows, as Table 5.2, that the colour W1 - W2 is the most important discriminator between **AGN** and **SFGs** for this specific set of sources. The importance of the

CHAPTER 5. ANALYSIS OF PREDICTION METHOD AND RESULTS

Table 5.4: SHAP values (rescaled to add to 100) for base algorithms in each prediction step for observed features using 121 spectroscopically confirmed AGN at high redshift values ($z > 4$).

AGN-SFG model (CatBoost)			
Feature	SHAP value	Feature	SHAP value
gbc	36.250	rf	21.835
et	30.034	xgboost	7.198
Remaining SHAP values:			4.683
Radio detection model (GBC)			
Feature	SHAP value	Feature	SHAP value
rf	11.423	catboost	5.696
xgboost	7.741	et	5.115
Remaining SHAP values:			70.025
Redshift prediction model (ET)			
Feature	SHAP value	Feature	SHAP value
xgboost	41.191	gbr	13.106
catboost	20.297	rf	11.648
Remaining SHAP values:			13.758

^a SHAP values are specific to each model training and cannot be compared, numerically, to the values obtained in a different model and with different data. A meaningful comparison can be done by contrasting the order in which features are sorted.

rest of the features is mixed: similar colours are located on the top spots (e.g. g - r, W1 - W3 or r - i).

For the radio classification step of the pipeline, we find that features linked to those 121 high- z AGN perform at the same level as for the overall population. As introduced in Sect. 4.2, radio-detection model shows difficulties when producing a classification based on the provided dataset. This issue is reflected in the narrow decision margin for the non-calibrated stacked model (see model output values –x-axis– close to ~ 0.5 in Fig. 5.5). The improved metrics with respect to those obtained from the no-skill selection do indicate that the model has learned some connections between the data and the radio emission. Feature importance has changed when compared to the overall population. If the radio emission observed from these sources were exclusively due to SF, this connection would imply SFR of several hundred $M_{\odot} \text{ yr}^{-1}$. This explanation can not be completely ruled out from the model side but some contribution of radio emission from the AGN is expected.

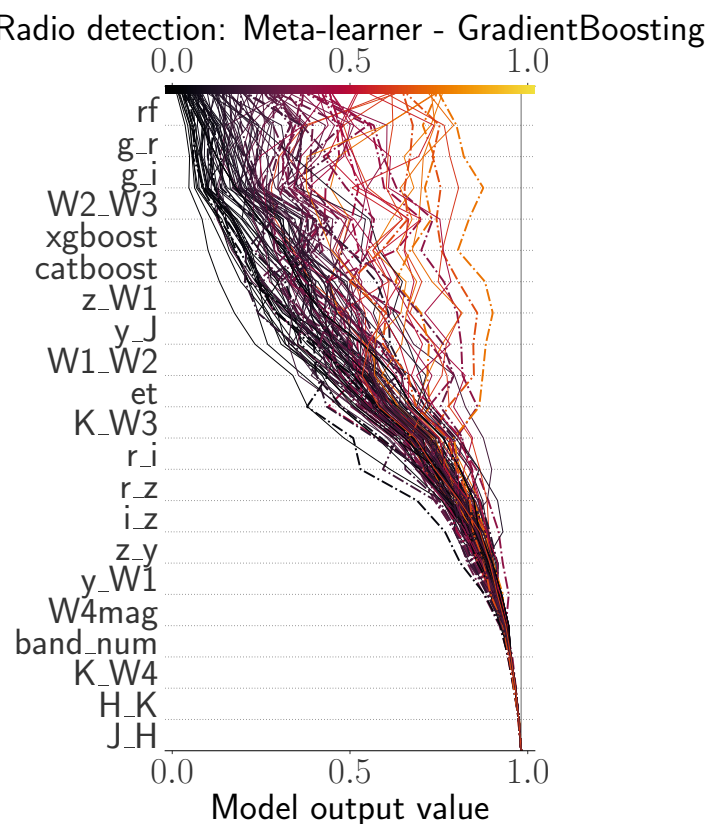


Figure 5.5: Decision plot from the [SHAP](#) values for all features from the radio detection model in the 121 high redshift ($z \geq 4$) spectroscopically confirmed AGN from [HETDEX](#). Description as in Fig. 5.4.

DRAFT - February 21, 2024 - DRAFT

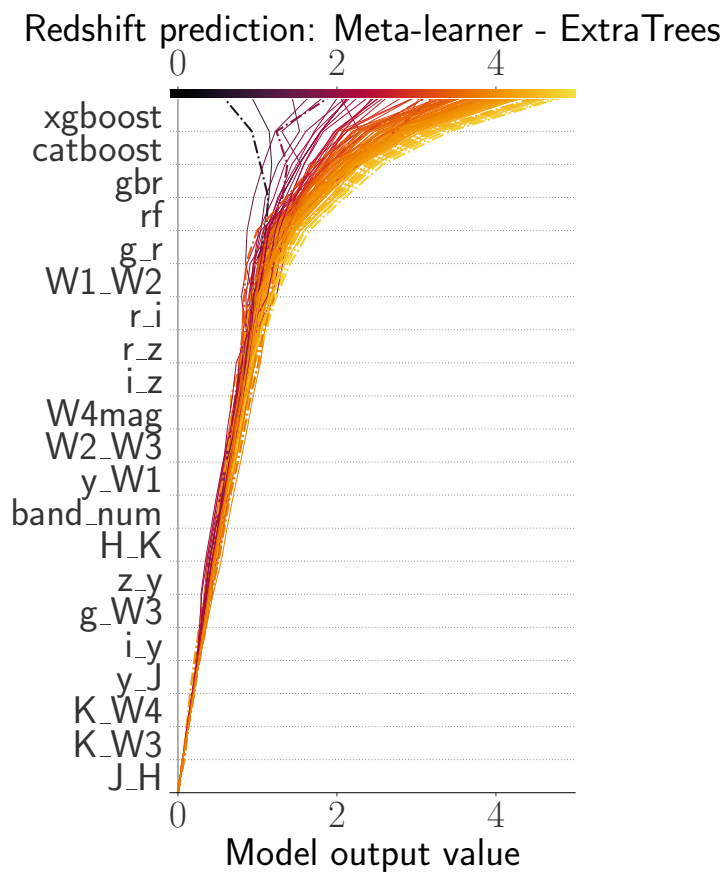


Figure 5.6: Decision plot from the SHAP values for all features from the redshift prediction model in the 121 high redshift ($z \geq 4$) spectroscopically confirmed AGN from HETDEX. Description as in Fig. 5.4.

Table 5.5: Combined and normalised (rescaled to add to 100) mean absolute SHAP values for observed features from the three models using 121 spectroscopically confirmed AGN at high redshift values ($z \geq 4$).

AGN-SFG model					
Feature	SHAP value	Feature	SHAP value	Feature	SHAP value
W1_W2	32.458	i_y	5.086	z_y	1.591
g_r	11.583	y_W1	4.639	H_W3	1.048
W1_W3	8.816	band_num	4.050	W4mag	0.514
r_i	7.457	y_W2	3.228	H_K	0.466
i_z	6.741	z_W2	2.348	W3_W4	0.466
r_J	6.613	y_J	1.718	J_H	0.178
Radio detection model					
Feature	SHAP value	Feature	SHAP value	Feature	SHAP value
g_i	14.120	z_W1	6.751	W4mag	2.691
W2_W3	13.201	r_i	5.577	band_num	2.661
g_r	12.955	r_z	5.161	K_W4	0.939
y_J	8.224	i_z	4.512	H_K	0.719
K_W3	7.441	z_y	4.121	J_H	0.190
W1_W2	6.874	y_W1	3.864		
Redshift prediction model					
Feature	SHAP value	Feature	SHAP value	Feature	SHAP value
g_r	32.594	z_y	3.557	W4mag	1.639
y_W1	20.770	y_J	3.010	g_W3	1.479
W2_W3	12.462	band_num	2.595	K_W3	0.853
W1_W2	5.692	i_y	2.381	K_W4	0.451
r_i	4.381	H_K	2.230	J_H	0.146
r_z	3.755	i_z	2.005		

CHAPTER 5. ANALYSIS OF PREDICTION METHOD AND RESULTS

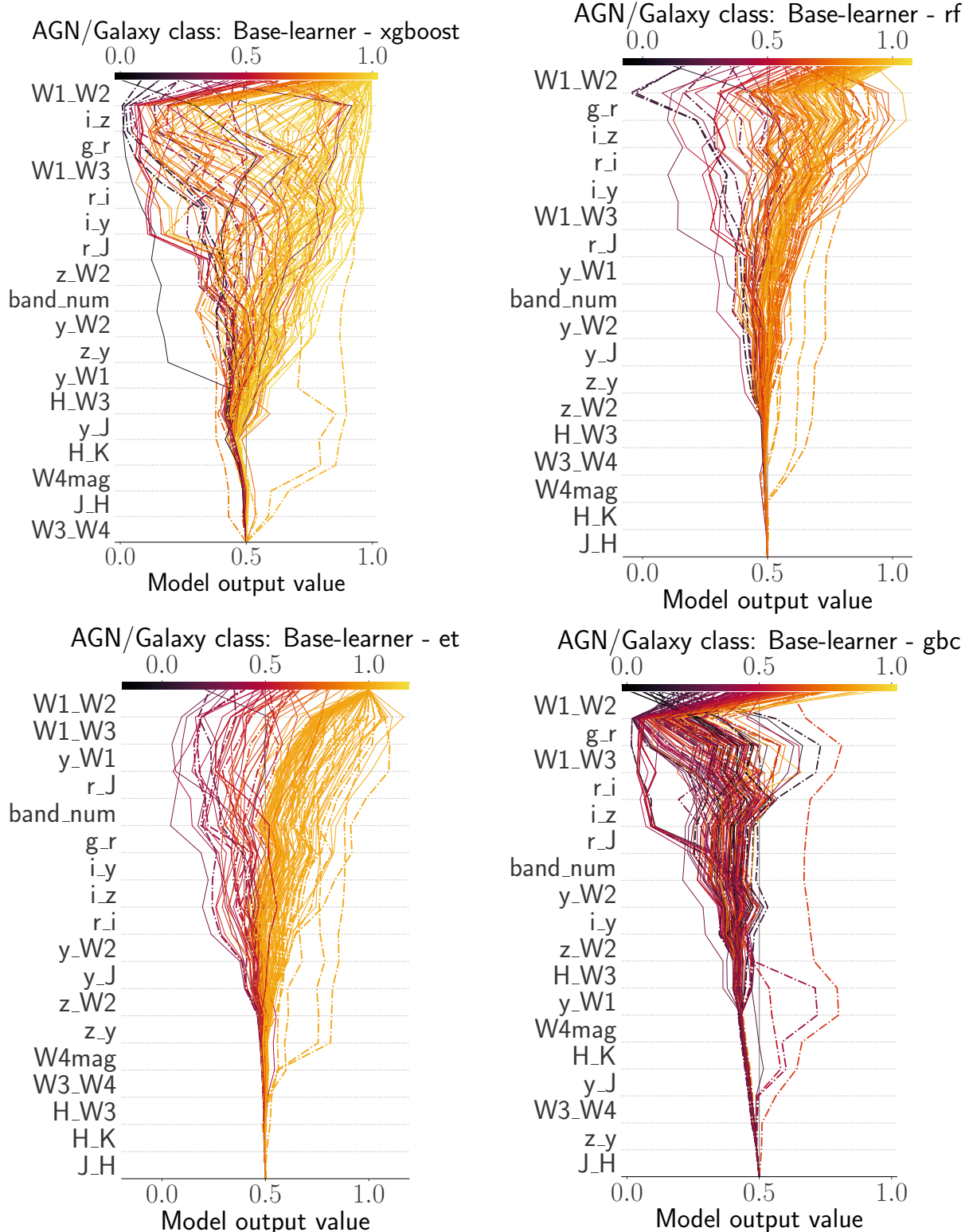


Figure 5.7: SHAP decision plots for base AGN-SFG algorithms. Details as described in Figs. 5.4. Starting point of predictions is the naive classification threshold. From left to right and from top to bottom, each panel shows the results from XGBoost, RF, ET, and GBC.

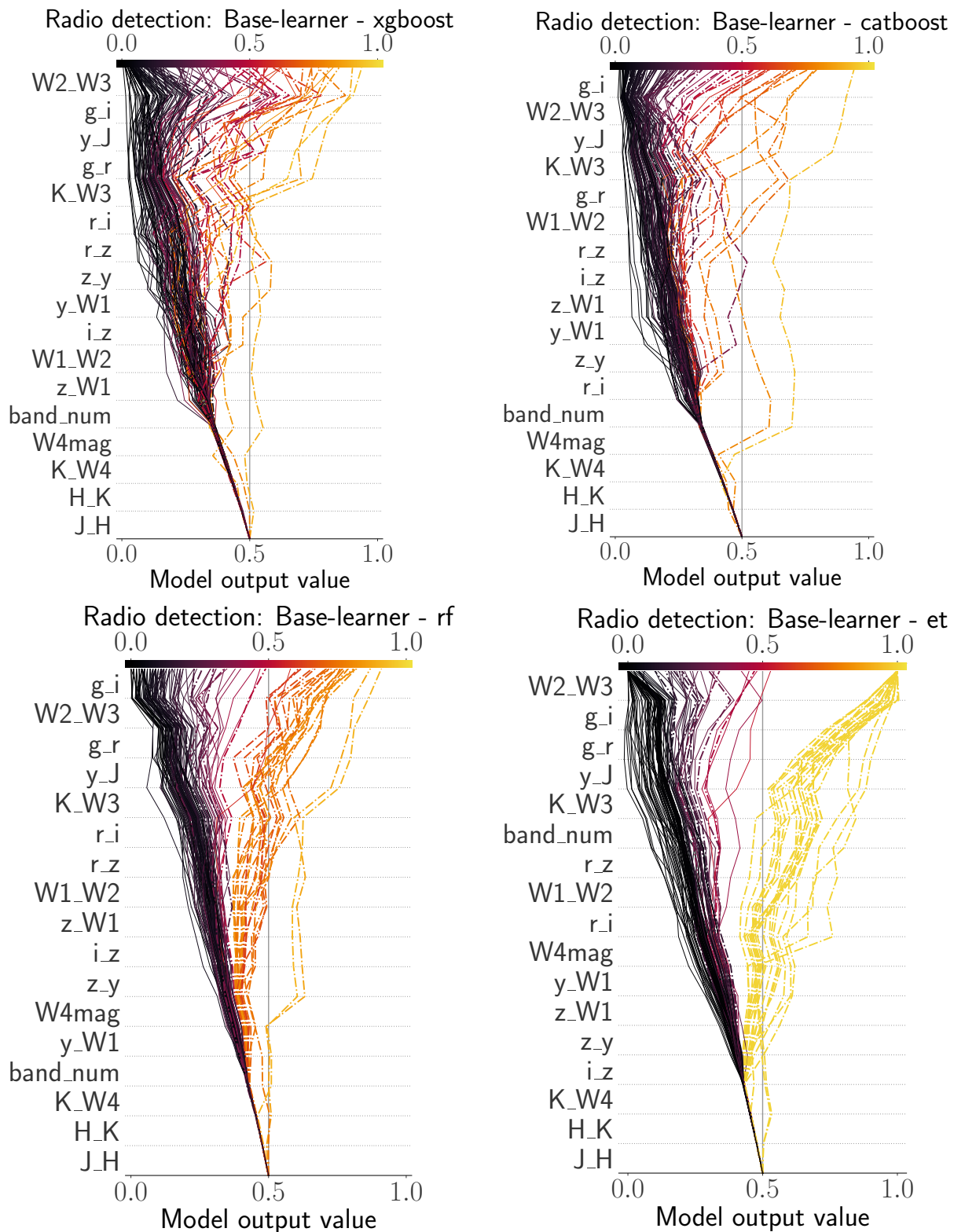


Figure 5.8: SHAP decision plots from base radio algorithms. Details as Figs. 5.4 and 5.7. Each panel with results for [XGBoost](#), [CatBoost](#), [RF](#), and [ET](#).

DRAFT - February 21, 2024 - DRAFT

CHAPTER 5. ANALYSIS OF PREDICTION METHOD AND RESULTS

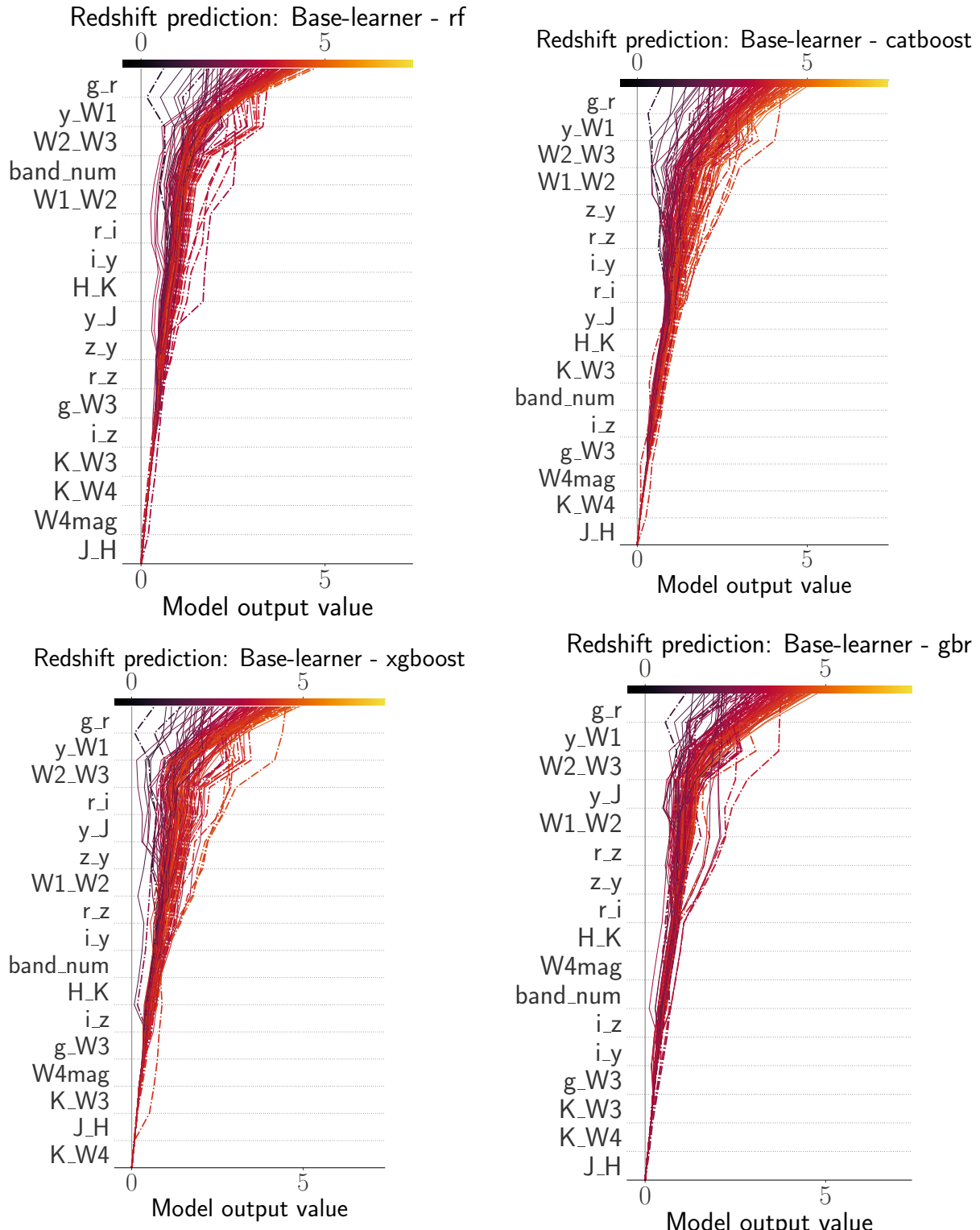


Figure 5.9: [SHAP](#) decision plots from base redshift algorithms. Details as in Fig 5.4. Each panel shows results for [ET](#), [CatBoost](#), [XGBoost](#), and [GBR](#).

Machine-assisted learning from models

The use of ML methods can be extended beyond the predictions specific models were trained to perform. Given that ML models need to extract correlations and connections between the features they have had access to, they can deliver additional information about the behaviour of the properties of the studied sources (not only those used for training, but also the test or prediction sets). Thanks to its sequential, and fairly independent stages, the prediction pipeline presented in this thesis can be used to extract information for a number of different aspects of the analysis of radio-detectable AGN (together with their redshift values).

In this chapter, we present three instances in which the prediction pipeline can be used to extend the knowledge about our object of study, radio-detectable AGN. In first instance, an example of the extraction of information from the learning process the models use to derive a new, and simple, AGN selection criterion. Then, an example of the use of how the outputs from the prediction pipeline can be directly applied to extract further knowledge from the distribution of radio-detectable AGN in different epochs. And finally, we present the concept of the use of the results of the prediction pipeline for a different goal from its initial purpose, that is, the assessment of multi-wavelength counterparts of radio detections.

6.1 Colour-colour AGN selection criterion

In the introduction of AGN selection methods in Sect. 1.1.1, it was shown that a combination of photometric colours can be used to determine selection criteria for different sub-sets of AGN. Each one of these criteria is able to retrieve information on specific properties (e.g. redshift) or processes from AGN and their hosts. Additionally, it is possible to extract details from the evolutionary state of some sources by observing the position of them in the colour-colour, or colour-magnitude diagrams.

From the feature importances in Table 5.5 and the values presented in Fig. 2.3 we infer that using optical colours could in principle create novel selection criteria with metrics equivalent to

those shown in Table 5.1 but for a much larger number of sources (100 000 sources for colour plots using W3 vs 4 700 000 sources for colours based in r, i or z magnitudes, cf. Fig. 2.3 and Table 2.2). We tested this hypothesis and derived a selection criterion in the $g - r$ vs $W1 - W2$ colour-colour parameter space as shown in Fig. 6.1 using the labelled sources in the test sub-set of the HETDEX field. The results of the application of this criterion to the testing data and to the labelled sources in S82 is presented in the last row of Table 5.1. Their limits are defined by the following expressions:

$$g - r > -0.76, \quad (6.1)$$

$$g - r < 1.8, \quad (6.2)$$

$$W1 - W2 > 0.227 \times (g - r) + 0.43, \quad (6.3)$$

where $W1$, $W2$, g , and r are Vega magnitudes. Our colour criteria provides better and more homogeneous scores across the different metrics with purity (precision) and completeness (recall) above 87 %. Avoiding the use of the longer *WISE* wavelength (W3 and W4), the criteria can be applied to a much larger dataset. These boundaries were drawn to contain, at least, 86 % and, and most 99 % of the AGN (as presented by their distribution contours).

Table 6.1 displays metrics for our new criterion in comparison with previous $W1 - W2$ vs $W2 - W3$ AGN colour-colour selection criteria (as presented in Sect. 5.1.1 and Table 5.1). Our classification method can recover, in the HETDEX field, 15 % and 59 % more AGN than said formulae. In the S82 field, these differences range between 17 % and 61 %. Such differences highlight the fact that most of the information that separates AGN from SFGs is traced by the selected features (mostly colours). Also, the increase in the recovery rate underlines the importance of using photometric information from several bands for such task, as opposed to traditional colour-colour criteria.

Depending on the degree of available information, the step of the pipeline and the research goals, other combination of colours and features could be used to create more selection criteria for AGN, radio-detected sources, and sources at specific redshift ranges. The use of such methods can be seen as an alternative to the recurrent use of the full set of ML models in our pipeline. Additionally, the creation of these colour-based criteria can be thought as a direct application of the knowledge gathered by the models, rather than a blind application of the latter.

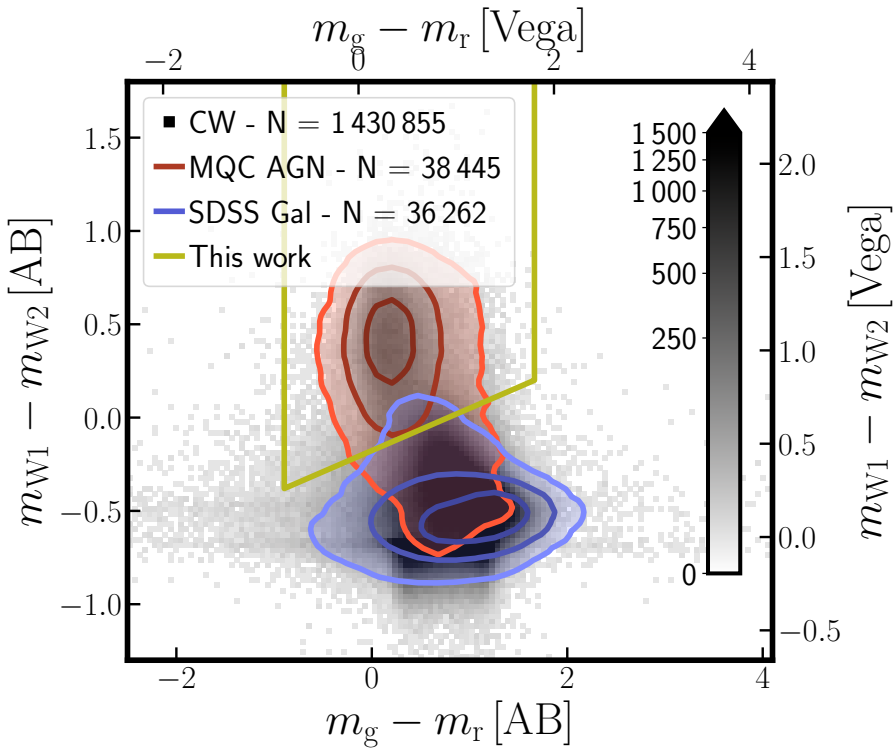


Figure 6.1: AGN classification colour-colour plot in the HETDEX field using CW (W1, W2) and PS1 (g, r) passbands. Grey-scale density plot include all CW detected and non-imputed sources. Red contours highlight the density distribution of the AGN in the MQC and blue contours show the density distribution for the SFGs from SDSS-DR16. Contours are located at 1, 2 and 3σ levels.

6.2 Radio luminosity function

A full study of the evolution of the distribution of sources in a region of the sky can be done with the use of LFs, which, using the definition from Salpeter (1955), correspond to the density of sources of a defined class in a range of luminosities (or, equivalently, magnitudes).

Add more context here!

As the performance and inner works of our prediction pipeline have already been assessed (cf. Chapters 3, 4, and 5), we can apply small variations to it as a way to emphasise the goals of this section. For this reason, we decided to run the full training sequence one more time. This time, two changes has been introduced. The first change relates to the cross-match of the radio information for the training set. Instead of using a $1''1$ search radius to find radio detections around the CW-selected sources, we adopted a $6''$ circle. With this change, we ensure the selection of radio detections for a larger fraction of sources. This modification is done at the expense of possible miss-identifications of radio counterparts. The second change is the inclusion of a complete new branch of predictions. Taking the description of the pipeline of Fig. 1.8, new models have been added to analyse the sources that have been predicted as SFGs (i.e.

CHAPTER 6. MACHINE-ASSISTED LEARNING

Table 6.1: Results of application of several **AGN** detection criteria to our testing subset and the labelled sources from the **S82** field. Same as Table 5.1 but including colour-colour criteria from this work.

Method	HETDEX test set			
	F_β ($\times 100$)	MCC ($\times 100$)	Precision ($\times 100$)	Recall ($\times 100$)
S12	86.10	78.78	93.98	80.51
M12	51.80	49.71	98.87	37.18
M16	67.21	61.30	97.48	53.48
B18	82.14	75.76	97.54	72.66
This work	92.71	87.64	94.00	91.67

Method	S82 (labelled)			
	F_β ($\times 100$)	MCC ($\times 100$)	Precision ($\times 100$)	Recall ($\times 100$)
S12	83.59	45.47	93.93	76.62
M12	46.80	28.22	99.59	32.54
M16	64.69	37.76	98.80	50.32
B18	79.71	51.07	98.72	68.77
This work	90.63	58.53	94.15	87.91

^a Naming codes for the used methods are described in the main text (cf. Sect. 5.1.1)

^b Last row of each sub-table corresponds to the criterion derived in this work.

^c All metrics have been multiplied by 100.

not as **AGN**) by the first model. Thus, these sources will be subject to a prediction of their radio detectability and, those predicted as being radio detectable, will have their photometric redshift values predicted. The inclusion of a new branch is related to the need to compare the radio luminosity distributions between **AGN** and regular **SFGs** across time. A detailed description of the modified datasets and the models produced with them can be found in Appendix B.

As a way to study the distribution of luminosities of **AGN** as derived from our prediction pipeline, and as part of the efforts to study the behaviour in areas that will be subject to future radio surveys, we have selected, as test field, the area of the **EMU-PS**. The **EMU-PS** catalogue¹ has radio information, at 944 MHz from 178 921 compact sources in an area of 270 deg² in the southern sky with a depth of 25 μ Jy/beam to 30 μ Jy/beam rms and a spatial resolution of 18'' (see Fig. 6.2 for a footprint of the area of **EMU-PS**). If we assume a synchrotron radio slope of $\alpha = -0.7$ (e.g. Sabater et al., 2019) and detection limits of $5 - \sigma$, the detection limit of **LoTSS** (355 μ Jy/beam) at the frequency of **EMU-PS** would be ≈ 95 μ Jy/beam, which is below the $5 - \sigma$ detection limit of **EMU-PS**, 125 μ Jy/beam. Thus, and assuming ideal conditions, if **LoTSS** had observed the **EMU-PS** area, some of its fainter detections might have not been caught by the

¹EMU-PS data can be obtained from <https://doi.org/10.25919/exq5-t894>

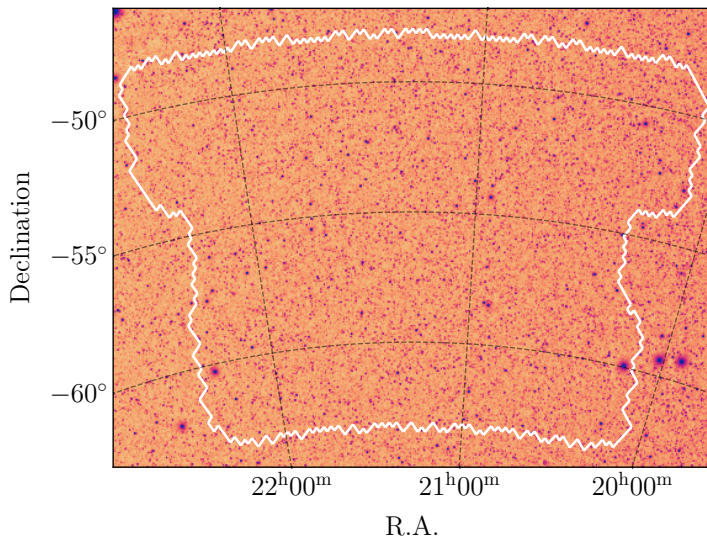


Figure 6.2: Footprint of the area of the [EMU-PS](#) field. In the background, W1 image from the [unWISE](#) coadds (Lang, 2014; Meisner et al., 2022). The white countours limit the area of the [EMU-PS](#) field.

[EMU-PS](#) catalogue.

For the purposes of this exercise, and as presented in Sect. 2.3, we have collected measurements in the [EMU-PS](#) area to apply the prediction pipeline. Thus, we have started with the selection of [CW](#)-detected sources in the area, finding 10 355 457 detections and successive cross-matches were performed using a search radius of 1'1. One exception to this distance was used for the cross-match with the [EMU-PS](#) catalogue itself, where a 10'' radius was used instead, which is the maximum search radius used by Norris et al. (2021) to find [CW](#) counterparts for their radio detections. The reason for this change is twofold: a larger distance is similar to the size of the restoring beam (18'') and the need for testing the effectiveness of the use of our models for the assessment of radio counterparts. As aforementioned, and additional branch of two models has been included in the prediction pipeline. One that can predict the radio detectability of [SFGs](#) (i.e. not [AGN](#)) and a second model that can predict photometric redshift values for radio-detected [SFGs](#).

Given that [PS1](#) does not cover the [EMU-PS](#) area, a different survey was selected to obtain optical measurements of the studied sources. Thus, we have obtained them from the [DES Data Release 2 \(DES-DR2\)](#); Abbott et al., 2021). We have used the same search radius to obtain the counterparts for the [CW](#)-detected sources.

In contrast to the identification of sources in [HETDEX](#) and [S82](#) fields and due to their different positions in the sky, the [EMU-PS](#) catalogue was cross-matched with alternative catalogues for the association of known [AGN](#) and [SFGs](#). In the case of [AGN](#), a more recent version

CHAPTER 6. MACHINE-ASSISTED LEARNING

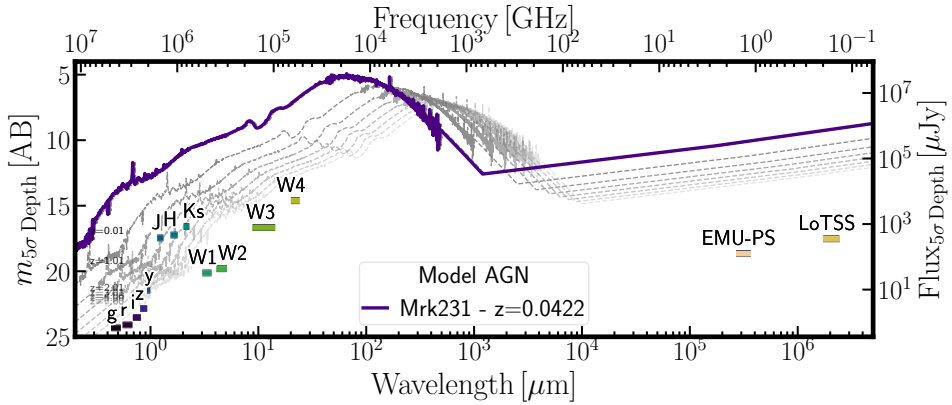


Figure 6.3: Flux and magnitude depths ($5 - \sigma$) from the surveys and bands covering the [EMU-PS](#) area. Limiting magnitudes and fluxes were obtained from the description of the surveys, as referenced in the main text. In purple, rest-frame [SED](#) from Mrk231 ($z = 0.0422$, Brown et al., 2019) is displayed as an example [AGN](#). Redshifted (from $z = 0.001$ to $z = 7$) versions of this [SED](#) are shown in dashed grey lines.

of [MQC](#) (v8; Flesch, 2023) was used² as well as [QSO](#) identifications from the spectroscopic sample of [DES-DR2](#) (Yang and Shen, 2023) and the [Gaia-unWISE Spectroscopic Quasar catalog](#) (Quaia G20.5; Storey-Fisher et al., 2023) based upon observations from [Gaia](#) data release 3 (DR3) extragalactic content (Gaia Collaboration et al., 2023a) and the *unWISE* reprocessing (Lang, 2014; Meisner et al., 2019) of the [WISE](#) data. For the [SFGs](#) present in the [EMU-PS](#) field, and from the lack of [SDSS](#) measurements, we have included the identifications from the spectroscopic catalogue in the final [VEXAS Data Release 2](#) (VEXAS-DR2; Kramtsov et al., 2021). In this way, the [EMU-PS](#) area harbours 12 692 known [AGN](#) and 1806 known [SFGs](#), from which 2375 and 870, respectively, have a counterpart in the [EMU-PS](#) catalogue.

In order to retrieve a large sample of redshift measurements, we included those provided by [MQC](#) v8, [Quaia G20.5](#), and spectroscopic redshifts from the [Dark Energy Spectroscopic Instrument \(DESI\)](#) imaging surveys (Dey et al., 2019; Zou et al., 2019), which are contained in the full [EMU-PS](#) catalogue. A summary of the number of sources and counterparts found in all different catalogues and surveys can be seen in Table 6.2.

The application of the modified prediction pipeline to the data from the [EMU-PS](#) area creates 89 040 candidates to be radio-detectable [AGN](#) and 116 400 to be radio-detectable [SFGs](#). Out of them, 36 466 have a radio counterpart in the [EMU-PS](#) catalogue (15 123 [AGN](#) and 21 343 [SFGs](#)), that is, a measured radio flux. To have a sense of the number of predicted sources, the area of the [EMU-PS](#) catalogue has 1509 radio-detected [AGN](#) and 544 radio-detected [SFGs](#) with confirmed identification. These numbers imply a 1000 % and 3900 % increment of sources

²For this exercise, all sources identified as [AGN](#) by [MQC](#) were selected, not only those with a redshift measurement, as done in the main model training.

Table 6.2: Composition of initial catalogue and number of cross matches with additional surveys and catalogues in the area of the [EMU-PS](#)

Survey	EMU-PS area
CatWISE2020	10 355 457
DES-DR2	7 091 485
AllWISE	4 066 594
2MASS	932 926
EMU-PS (10 '')	170 702
MQC v8 (AGN)	614
Quaia G20.5 (AGN)	12 491
DES-DR2 (AGN)	46
Total AGN	12 692
VEXAS Spec V2 (SFG)	1806

for radio-detected [AGN](#) and radio-detected [SFGs](#) respectively. The distribution of predicted photometric redshifts of both samples is depicted in Fig 6.4.

It can be seen in Fig 6.4 that the distribution of radio-detectable [SFGs](#) is concentrated between redshift 0 to 1.2. This behaviour corresponds to the original distribution of [SFGs](#) used for training in the [HETDEX](#) field and thus, to the parameter space coverage of such sources. As expected the model trained with them can only associate new sources to the values in that region of the space of parameters. For the same reason, the distribution of predicted redshifts for radio-detectable AGN spans a larger range, similar to the values of the training in the [HETDEX](#) field.

Radio luminosities can be obtained from the use of radio fluxes and redshift values of the sources. Fluxes are obtained from the [EMU-PS](#) catalogue, which lists them in its column `flux_int`. A distribution of these values is presented in Fig 6.5. Using Eq. 1.4, they can be transformed into luminosities, at 944 MHz, with the predicted photometric redshift and, either assuming a radio spectral index of $\alpha = -0.7$ (see, for instance, Simpson et al., 2012; Magliocchetti et al., 2014; Šlaus et al., 2020; Mandal et al., 2021; van der Vlugt et al., 2022; Lyu et al., 2022) or using, in the case of [EMU-PS](#), the α values provided by the catalogue. These spectral indices have been calculated from the use of the Taylor terms at the peak pixel of each fitted component (Norris et al., 2021). In order to obtain the luminosity distances for the sources, we have adopted a flat Λ cold dark matter (Λ CDM) cosmology, with $\Omega_m = 0.31$, $\Omega_\Lambda = 0.69$, and $H_0 = 67.7 \text{ km s}^{-1} \text{Mpc}^{-1}$, as presented by the Planck Collaboration et al. (2020).

Most of works on [radio luminosity functions \(RLFs\)](#) have used luminosity values at 1.4 GHz (e.g. Mauch and Sadler, 2007; Simpson et al., 2012; McAlpine et al., 2013; Šlaus et al.,

CHAPTER 6. MACHINE-ASSISTED LEARNING

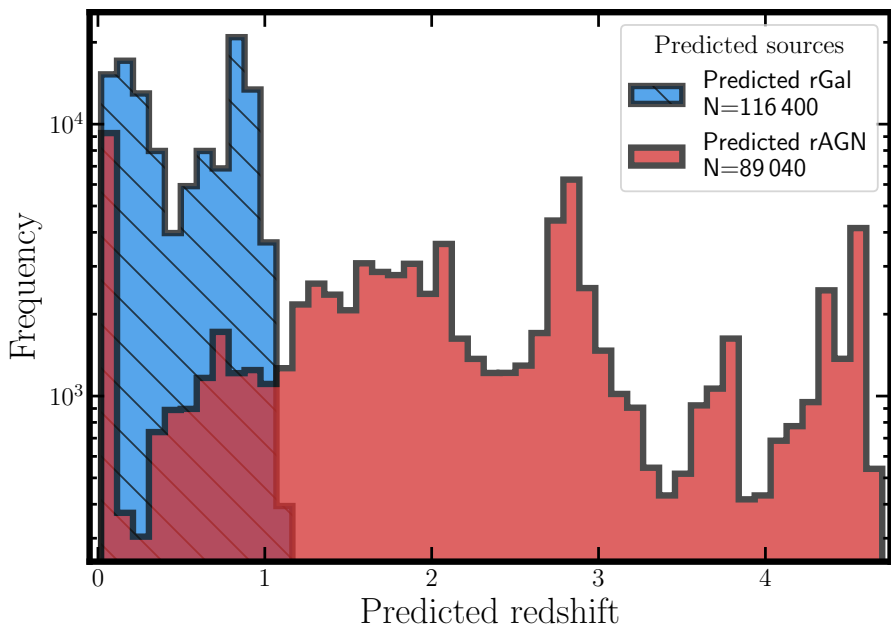


Figure 6.4: Distribution of predicted photometric redshift values for, in hatched blue, predicted radio-detectable SFGs and, in red, predicted radio-detectable AGN in the area of the EMU-PS catalogue.

2020). In order to have the opportunity to compare our results with previous literature, we will convert our EMU luminosities to be at that frequency. Using Eq. 1.5, we can obtain luminosities at 1.4 GHz from our values at 944 MHz. The distribution of such luminosities, as a function of predicted photometric redshift, is presented for both samples, in Fig. 6.6.

Attending to the intrinsic uncertainties of the original pipeline and the changes introduced to the models in the extended prediction pipeline, the luminosity distributions of Fig. 6.6 appear to be relatively clean. Two potential issues can be, nevertheless, identified. First, a fraction of luminosities are located below the $5 - \sigma$ detection limit of EMU-PS. The presence of these populations (both SFGs and AGN) can be explained by two interrelated factors. One of them is that the detection limit presented in Fig. 6.6 has been calculated with the mean detection depth of the survey ($25 \mu\text{Jy}/\text{beam}$) and the other issue is that the detection limit used the fixed spectral index $\alpha = -0.7$, while the detected sources have been analysed with their own spectral indices.

Recalling the overview given in Sect. 1.1.1, an additional issue is related to sources with radio luminosities that are low enough to have a high probability of being originated, mostly, from star formation episodes but are labelled as AGN. As a way to reduce this potential problem, we decided to use the thresholds of Eq. 1.1.1 and its description in our EMU-PS sample to alleviate the existence of too-bright radio SFGs. Thus, all predicted radio SFGs that presented a 1.4 GHz luminosity above the mentioned limit were re-labelled as predicted AGN and the corresponding branch of the prediction pipeline is applied to them. That is, a new photometric

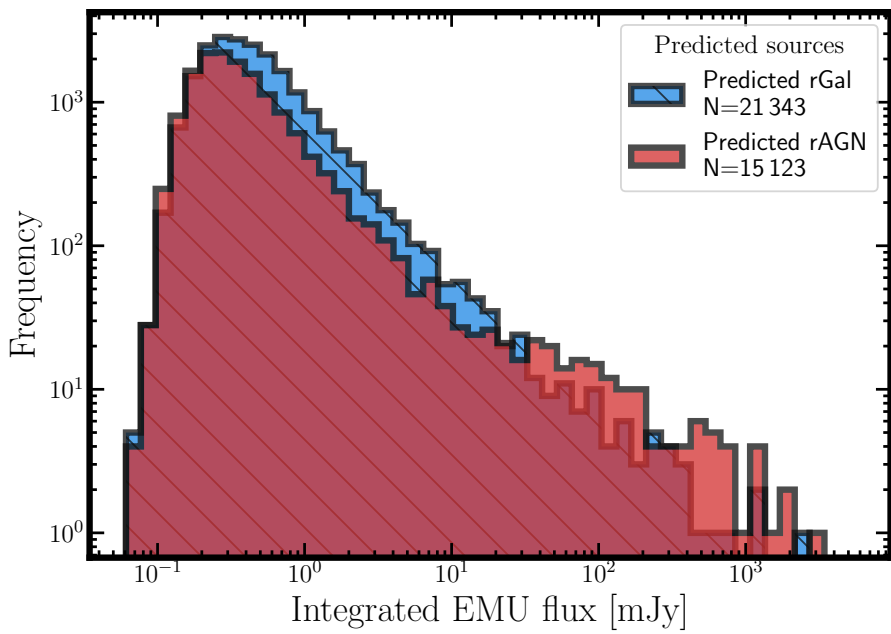


Figure 6.5: Distribution of EMU integrated fluxes (at 944 MHz) for, in hatched blue, predicted radio-detectable SFGs and, in red, predicted radio-detectable AGN in the area of the EMU-PS catalogue.

redshift value is predicted for all of them. The modified distributions of luminosities and redshifts of the re-labelled AGN and SFGs sets are presented in Fig. 6.7.

It is possible to see, in Fig. 6.7, that the locus, in the (z, L) plane, of predicted radio-detectable SFGs is much smaller than previously (see Fig. 6.6). The new distribution is consistent with the expectation that, in general, radio emission from AGN is stronger than that of SF episodes. After the re-labelling, 12 561 sources are classified as predicted radio SFGs, and 23 712, as predicted AGN.

In order to obtain RLFs for our predicted radio-detected AGN, and from the description in Sect. 1.1.1, we implemented a version of the determination method presented by Page and Carrera (2000), which is called a binned estimator. This method **complete text here**.

The selection function, $\mathcal{P}(z, L)$, summarises the corrections that the distribution of sources must suffer in order to be as close as possible to our best guess of their real distribution in the space of redshifts and luminosities. Taking advantage of the use of ML predictions, it is possible to obtain a correction for both completeness (recall) and purity (precision) of the radio-AGN and radio-SFGs in our selected sample that can be added to the selection function. In order to obtain these values, we took all known radio-detected sources (i.e. AGN and SFGs) in the HETDEX field as well as their predicted class, redshift values, and estimated 1.4 GHz luminosities (assuming a spectral index $\alpha = -0.7$; Sabater et al., 2019). For each element in the $(z_{\text{pred}}, \log_{10}(L_{1.4 \text{GHz}}))$ plane, all the sources located within a dimensionless distance of 1

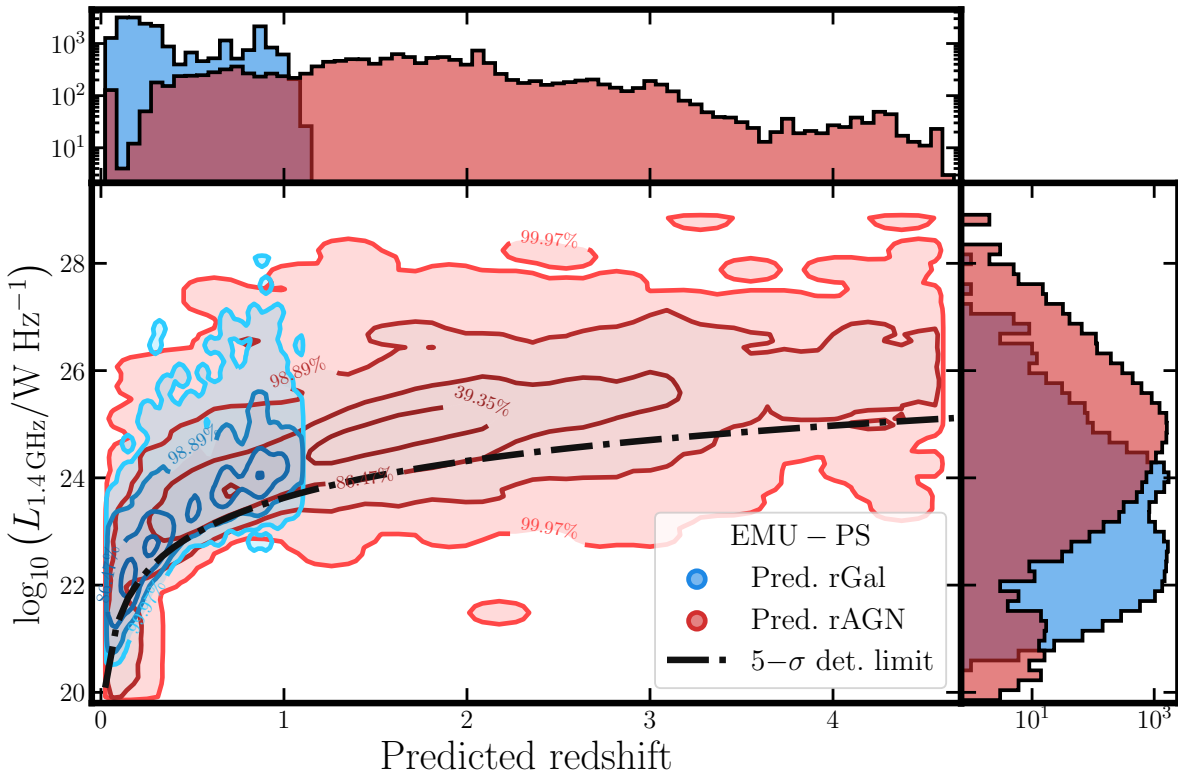


Figure 6.6: Distribution of predicted 1.4 GHz luminosities vs predicted photometric redshifts for radio-detectable AGN (in red) and radio-detectable SFGs (blue) in the area of the EMU-PS catalogue. In the top panel, the histograms of the predicted redshifts for both populations are presented. In the right-hand side of the figure, the distributions of predicted 1.4 GHz luminosities are displayed following the color code of the legend. In the central panel, two contour plots represent the joint distribution of 1.4 GHz luminosities and predicted photometric redshifts of both predicted radio-detectable AGN and radio-detectable SFGs. Contours represent the 1, 2, 3 and 4 – σ two-dimensional levels of the distribution (39.35 %, 86.47 %, 98.89 % and 99.97 %, respectively, of the corresponding sample). Black, dashed line represents the luminosity of a source at five times the noise level of the EMU-PS survey (25 mJy). That is to say, it represents the detection limit of the EMU-PS catalogue.

are selected (i.e. their nearest neighbours). For these subsets of known radio sources, the class recall (cf. Eq. 3.4) and precision (cf. Eq. 3.5) are calculated independently. Their distribution of values is presented in Figs. 6.8 and 6.9.

Then, each of the predicted sources from the EMU-PS catalogue is placed in the same plane of their corresponding class among the HETDEX sources. The ten closest HETDEX sources, with a Euclidean distance, are selected and their recall, or precision, values are averaged with the inverse of their distance to the EMU-PS source as weights. This averaged value is assigned to the predicted source as their estimated recall or precision. The distributions of such values are presented in Figs. 6.10 and 6.11.

Having obtained the completeness and purity values for the predicted sources among the EMU-PS sources, it is possible to generate an initial definition for the selection function. In first place, and from the definitions in Sect. 3.1.1, the recall indicates the fraction of sources that a prediction is missing given that they are present. Conversely, the purity is related to, given the

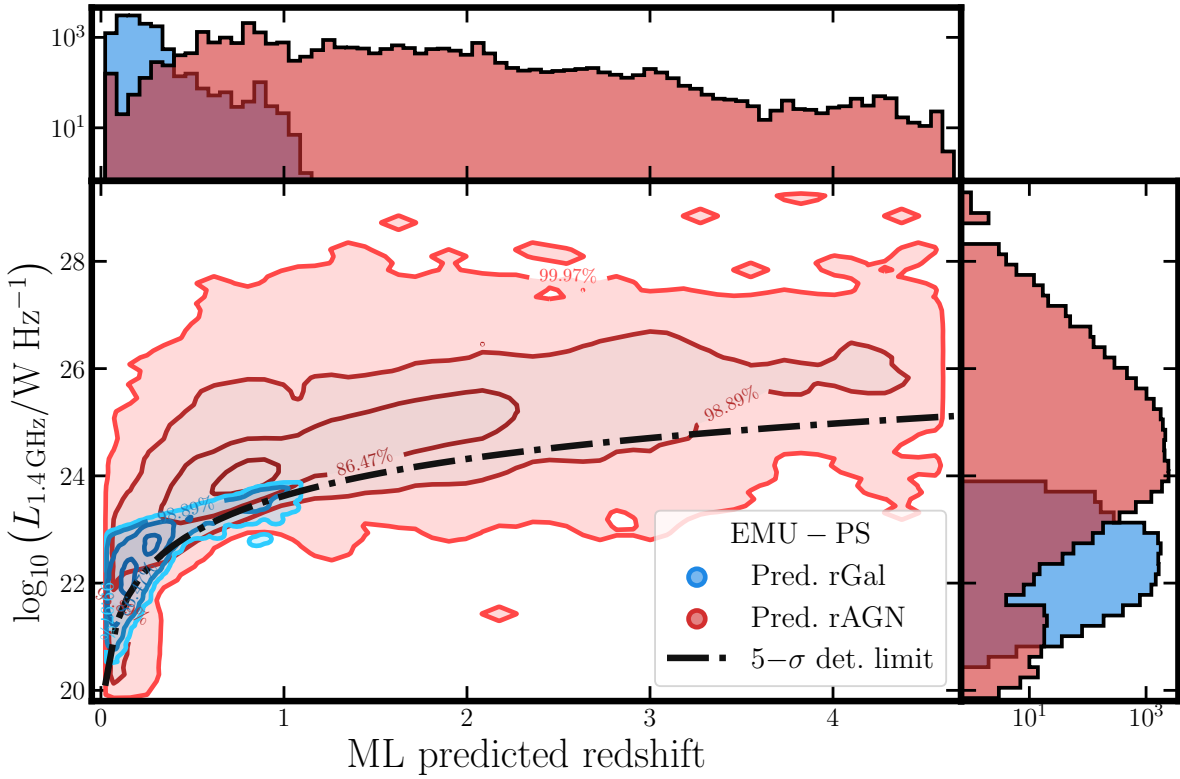


Figure 6.7: Distribution of predicted 1.4 GHz luminosities vs predicted photometric redshifts for radio-detectable AGN (in red) and radio-detectable SFGs (blue) in the area of the EMU-PS catalogue. SFGs with high 1.4 GHz luminosities have been re-labelled as AGN, following the prescriptions by Magliocchetti et al. (2014) and Magliocchetti (2022). Description as in Fig. 6.6.

predicted elements, how many of them are not part of the desired class. Any correction based on those quantities will use the completeness as a reducing factor and the purity as an increasing quantity. In this way, the selection function, $\mathcal{P}(z_i, L_i)$, can be written as:

$$\mathcal{P}(z_i, L_i) = \frac{\text{Recall}_{\text{ML}}(z_i, L_i)}{\text{Precision}_{\text{ML}}(z_i, L_i)}, \quad (6.4)$$

with the ML-based recall and precision ranging between 0 and 1. Then, the selection function values can be any non-negative real quantity. It can be seen, then, as the recall decreases, the selection function follows the same behaviour, while an decrease of the precision will imply an increment of the selection function values. Additional factors might be included in the definition of the selection function. Some of them involve a correction for the resolution bias (e.g. Prandoni et al., 2001; Prandoni et al., 2018; Mandal et al., 2021) and a correction for the Eddington bias (Eddington, 1913; Eddington, 1940). For our project, and since it is more a proof of concept rather than a full analysis, only a ML-based correction (i.e. precision and recall) will be applied to the studied sources.

Taking into account the distribution of predicted redshifts from our set of predicted radio-

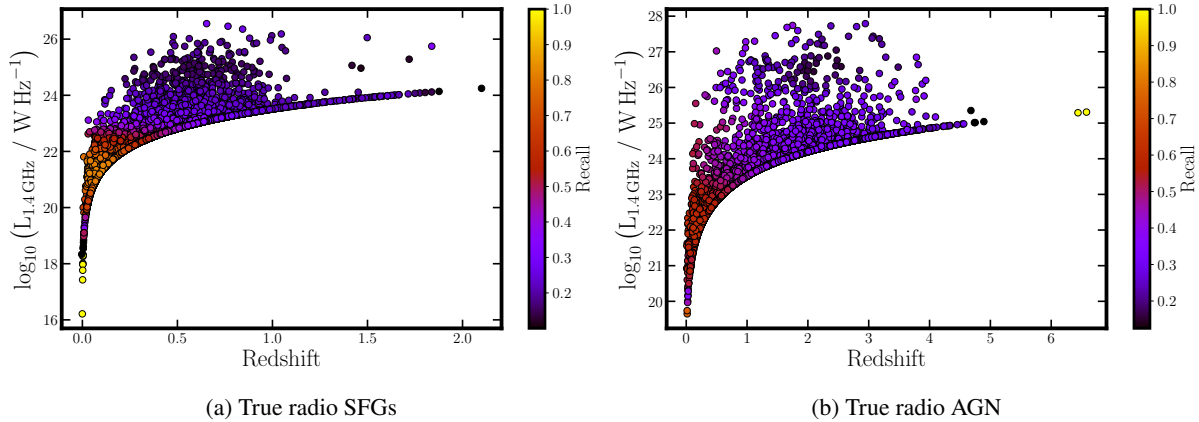


Figure 6.8: True 1.4 GHz luminosity vs redshift for (a) radio SFGs and (b) radio AGN in the HETDEX catalogue. Sources are coloured according to their estimated recall values and following each individual colourbar.

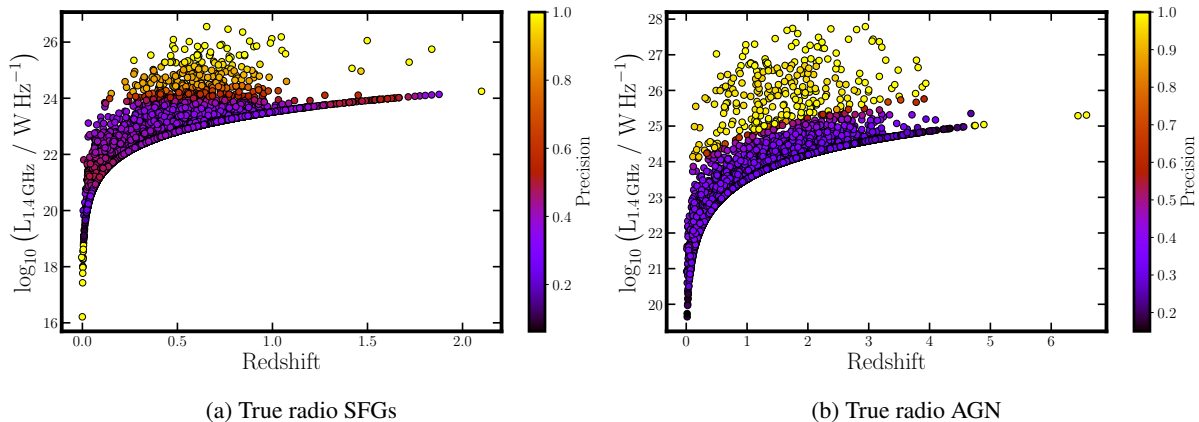


Figure 6.9: True 1.4 GHz luminosity vs redshift for (a) radio SFGs and (b) radio AGN in the HETDEX catalogue. Colour coding as in Fig. 6.8.

detected AGN and the search for a distribution of sources that has a smooth number evolution across redshifts and radio luminosities (as done, for example, with radio-detected SFGs by van der Vlugt et al., 2022), eleven redshift bins were created: (0.01, 0.2], (0.2, 0.3], (0.3, 0.5], (0.5, 0.7], (0.7, 1.0], (1.0, 1.3], (1.3, 1.6], (1.6, 2.0], (2.0, 2.5], (2.5, 3.2], and (3.2, 4.8]. In the case of radio-detected SFGs, the first six redshift bins contain sources of this type (i.e. up to $z = 1.30$). The number of sources in each redshift bin is shown in Table 6.3.

We will obtain LF values from the use of binned estimations in each predicted redshift bin with a chosen bin of size $\Delta \log_{10} L = 0.3$ following, for instance, Ross et al. (2013), Kondapally et al. (2022), Yuan et al. (2022), and Alqasim and Page (2023). Binned LFs, for each redshift bin, are displayed in Fig. 6.12.

Before establishing any comparison with previously derived RLFs, it is important to note that the values derived by us should be considered as an upper limit for a full RLF. The sources considered for this work are selected, as described earlier in the text, by their detection in the

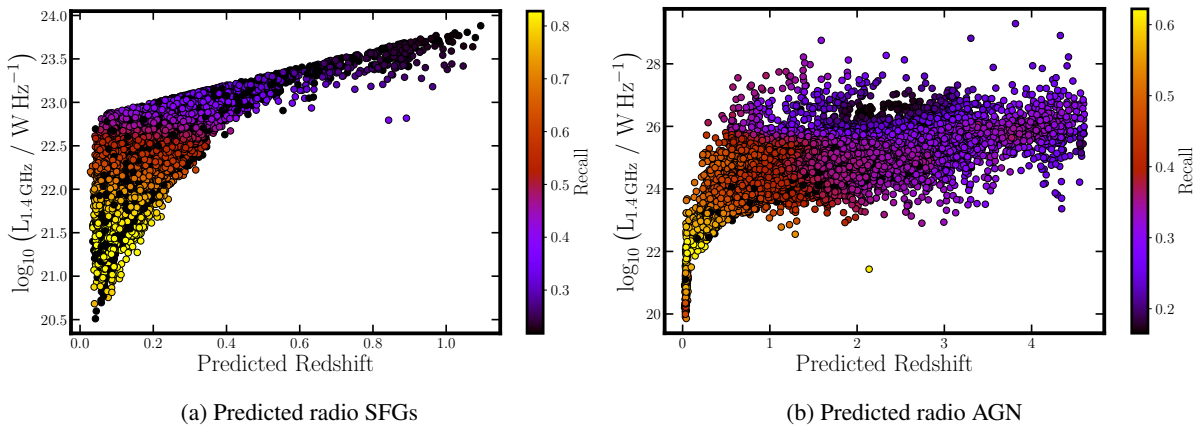


Figure 6.10: Predicted 1.4 GHz luminosity vs predicted redshift for predicted (a) radio SFGs and (b) radio AGN in the EMU-PS catalogue. Sources are coloured according to their estimated recall values and following each individual colourbar.

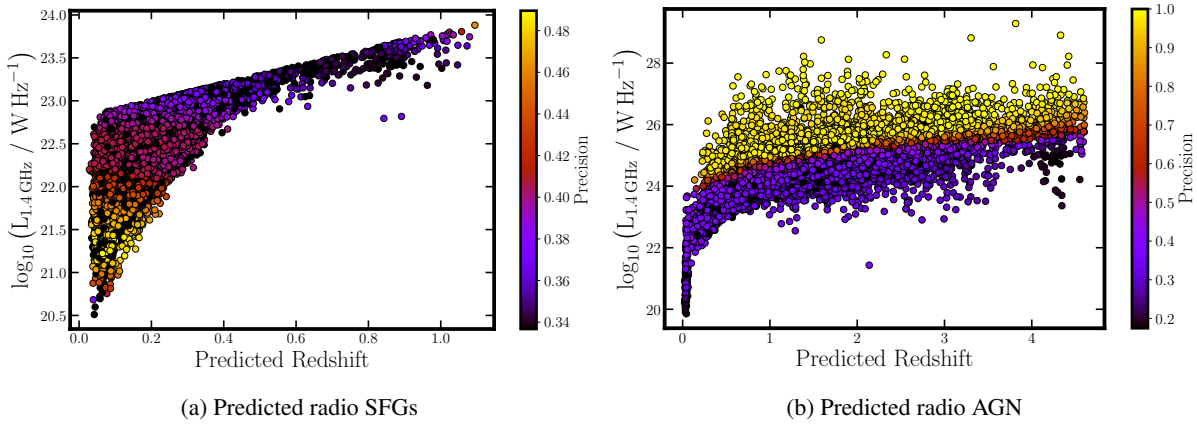


Figure 6.11: Predicted 1.4 GHz luminosity vs predicted redshift for predicted (a) radio SFGs and (b) radio AGN in the EMU-PS catalogue. Sources are coloured according to their estimated precision values and following each individual colourbar.

CW catalogue. That means, all our predicted sources need to be IR-detected. This construction does not include sources (either AGN or SFGs) that can be detected in radio bands (in particular, in EMU-PS) but lack of IR detections. **Quantify this difference?** For this reason, our RLFs should be called, more precisely, IR-detected RLF. Nevertheless, we will keep the usual RLF nomenclature for the sake of simplicity and easiness of comparison with previous works.

In the case of the binned LF, it can be seen that, for higher luminosities, it presents a noticeable raise. This effect has been discussed in previous works. For instance, Miyaji et al. (2001), Croom et al. (2009), and Palanque-Delabrouille et al. (2016) have noted that the method by Page and Carrera (2000: binned LF), might cause pronounced biases. The choice of the specific point in the $\log(L)$ bin can seriously impact in the final estimated value. Additionally, by assuming a uniform distribution in every luminosity bin, this method is unable to correct for the incompleteness in each individual sub-range. This last issue can be of the utmost relevance in the brightest end of the LF, where the number of sources decreases significantly.

CHAPTER 6. MACHINE-ASSISTED LEARNING

Table 6.3: Number of predicted radio-detectable sources ([AGN](#) and [SFGs](#)) in the [EMU-PS](#) area by predicted redshift bin.

z bin	Radio AGN	Radio SFGs
$0.01 < z \leq 0.2$	210	7063
$0.2 < z \leq 0.3$	271	3143
$0.3 < z \leq 0.5$	1090	1701
$0.5 < z \leq 0.7$	3082	228
$0.7 < z \leq 1.0$	5599	222
$1.0 < z \leq 1.3$	2477	17
$1.3 < z \leq 1.6$	2633	...
$1.6 < z \leq 2.0$	3432	...
$2.0 < z \leq 2.5$	2515	...
$2.5 < z \leq 3.2$	1828	...
$3.2 < z \leq 4.8$	749	...

A modification can be implemented in the previous calculations. If all the sources that are predicted to be radio detectable but do not have a counterpart in the [EMU-PS](#) catalogue are assumed to have a low flux (below the detection limit of [EMU-PS](#)), then the number of available sources for the determination of the [RLF](#) can clearly increase. It is important to notice that such change cannot be treated **Complete description of imputed fluxes for calculations.**

6.3 Radio counterpart assessment

One of the main issues of multi-wavelength studies of astrophysical sources is the identification of counterparts in observations from different instruments and bands (cf. Sect. 1.2.3). Accurate positioning of sources is crucial to allow further studies (e.g. spectroscopic targeting). While optical and [IR](#) observations have reached sub-arcsecond positional accuracy (e.g. [WISE](#), Wright et al., 2010; [PS1](#), Chambers et al., 2016), deep radio surveys have only recently obtained such resolutions (e.g. Sweijen et al., 2022; Ye et al., 2023; for the [LOFAR](#) radio telescope). Thus, most of radio identifications lack accurate positional measurements needed for precise counterpart identification and to reduce uncertainties in the use of [SED](#) modelling.

There are a few approaches to find and link multi-wavelength, multi-instrument counterparts of sources. One of the simplest way to find such sources is through direct cross match between catalogues. A search radius is defined and centred in the position of the source for which counterparts are needed. Then, all sources in the target catalogue located inside the circle of the previously defined radius are considered candidate counterparts. Depending on the conditions of the problem and the used catalogues, one of these candidates can be selected as

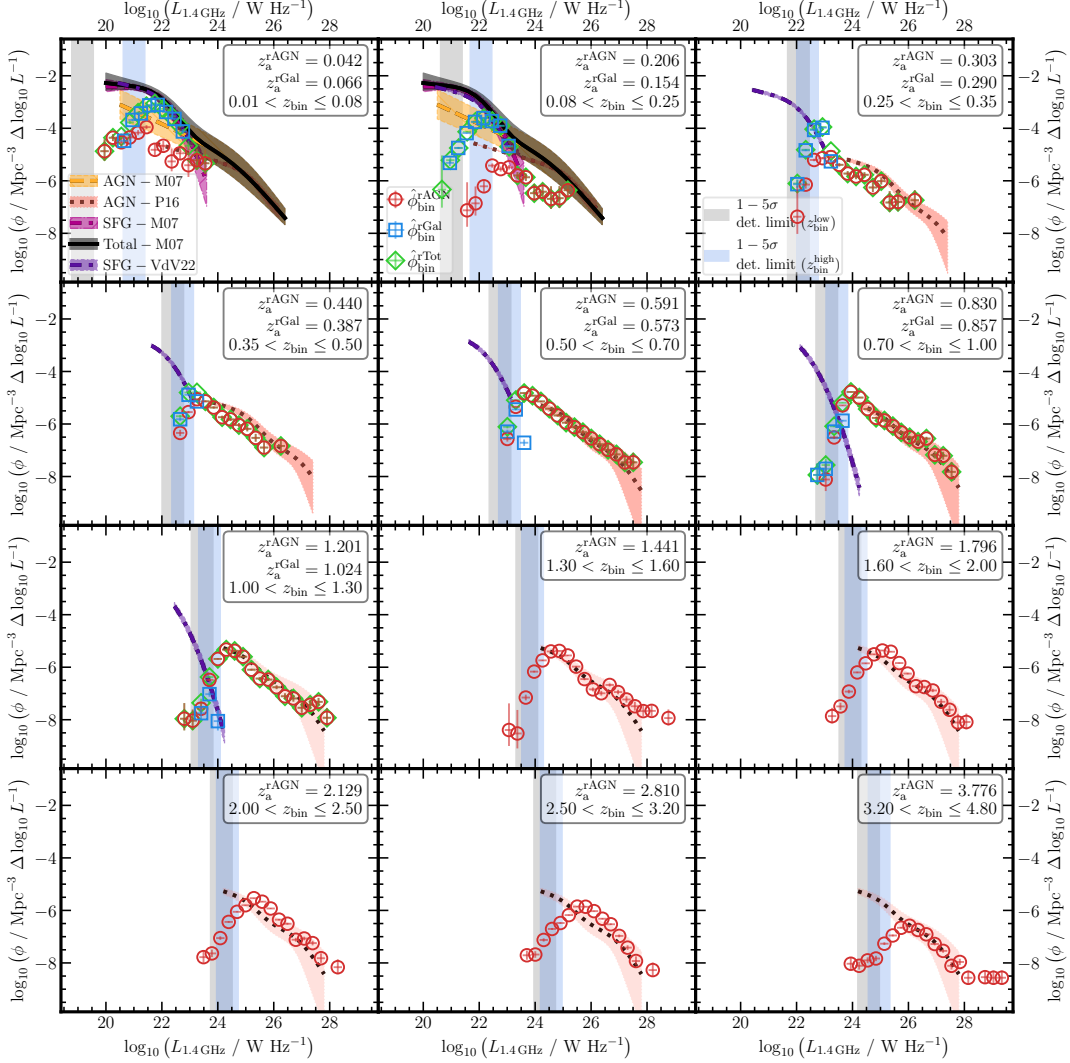


Figure 6.12: RLF (1.4 GHz) in EMU-PS binned by predicted z values. In red circles, values for predicted radio AGN and, in blue squares, for predicted radio SFGs. $1 - \sigma$ uncertainty error bars are included. Horizontal uncertainties correspond to a bin of $\Delta \log L = 0.3$, and vertical uncertainties have been obtained following Clopper and Pearson (1934) and Gehrels (1986). Solid lines and shadowed regions show previous RLF determinations with $1 - \sigma$ uncertainties (AGN, SFGs, and total values; Mauch and Sadler, 2007; M07; AGN; Pracy et al., 2016; P16; SFGs; van der Vlugt et al., 2022; VdV22). Grey regions show 1 to $5 - \sigma$ detection levels from EMU-PS measurements. Upper-right corner of each panel shows median z of radio-AGN and radio-SFG, and z bin.

the proper counterpart (e.g. the closest source either in angular or geometrical distance). This thesis is an example of the use of this technique (cf. Sect. 2.3). Other instances of the use of direct cross match of catalogues are Barbieri and Bertola (1972), Agüeros et al. (2005), Bianchi et al. (2007), Drake et al. (2014), Norris et al. (2021), and Storey-Fisher et al. (2023).

When postional errors are large or PSF or synthesised beams are large enough to have several sources from the other catalogue inside it, direct cross matching cannot be used. A more advanced approach is that of maximum likelihood ratio (MLR; Richter, 1975; de Ruiter et al., 1977; Prestage and Peacock, 1983; Wolstencroft et al., 1986; Sutherland and Saunders, 1992). As defined by Sutherland and Saunders (1992), it looks for the sources that optimise the ratio of

CHAPTER 6. MACHINE-ASSISTED LEARNING

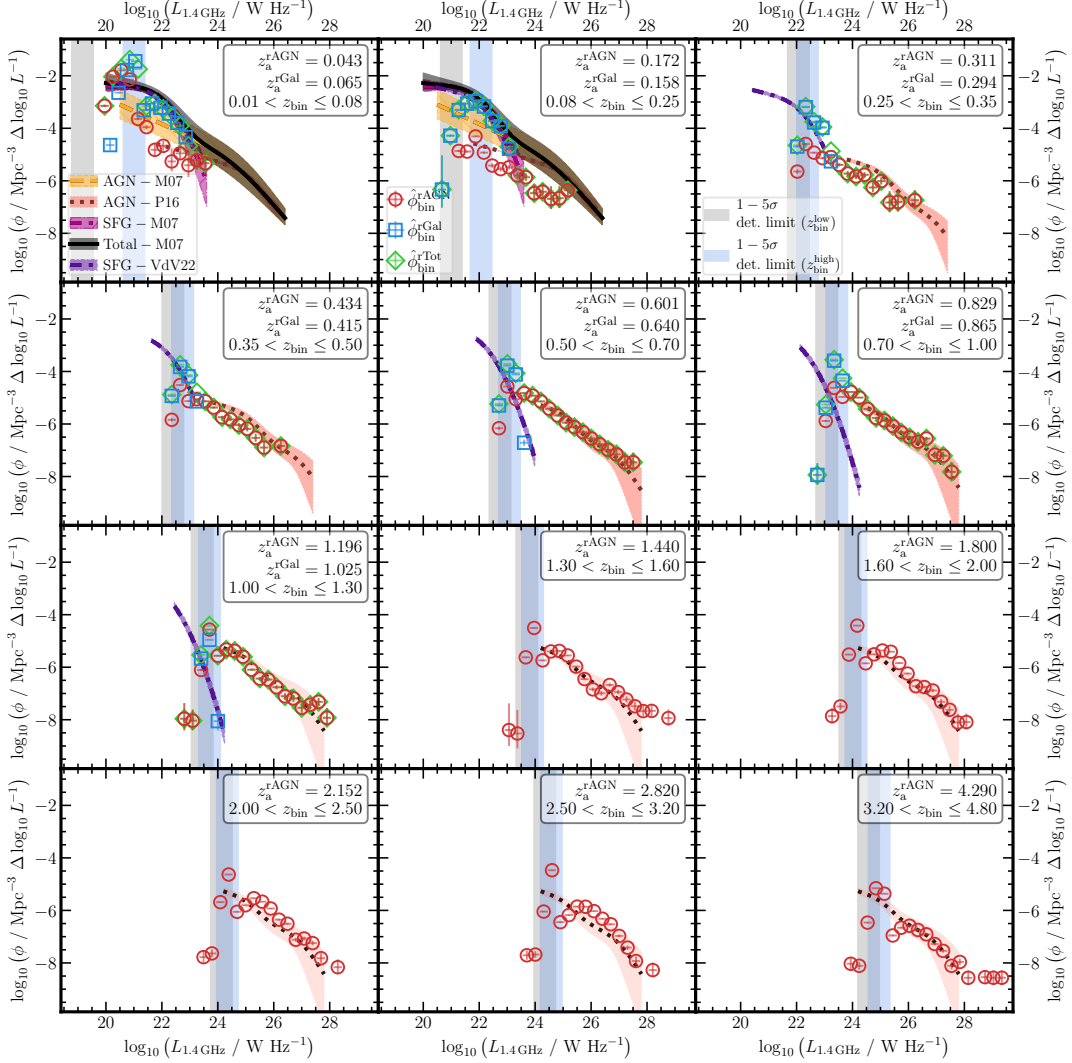


Figure 6.13: RLF (1.4 GHz) in EMU-PS binned by predicted z values using all sources predicted to be radio-AGN and radio-SFGs with assumed fluxes when missing. Figure description as in Fig. 6.12.

the likelihoods of being a genuine counterpart over that of being a background candidate. These likelihoods depend on the density of sources in both catalogues, their magnitude distributions, and their positional errors (Brusa et al., 2007). One advantage of this technique is that it can output the degree of reliability of each counterpart allowing the researcher to select, if needed, the most secure sources. Some examples of the application of the MLR method include Brusa et al. (XMM-COSMOS; 2007), Abdo et al. (Fermi; 2010), Xue et al. (Chandra Deep Field-South; 2011), LaMassa et al. (Stripe 82X; 2016), Marchesi et al. (Chandra COSMOS; 2016), Ananna et al. (Stripe 82X; 2017), Auge et al. (2023), Hardcastle et al. (LoTSS; 2023), and Whittam et al. (MIGHTEE-COSMOS; 2024).

A third method is the Bayesian approach. Contrary to the previous techniques, it does not rely on the specific distribution of sources in the studied catalogues, using Bayesian priors

to derive the most likely counterparts of the base catalogue. In this way, it does not suffer from being applied to small areas (Salvato et al., 2018). This method was first introduced by Budavári and Szalay (2008) and it can be applied to the search for counterparts in simultaneous catalogues.

Additionally, **ML** can be used to derive the most likely counterpart of sources in catalogues. By using photometric information (or other properties) from sources detected in other wavelengths, it is possible to train a model and extract the probability of that source to have a counterpart in a new catalogue. One early example of such technique is the work by Rohde et al. (2005) and Rohde et al. (2006) where the authors used **SVMs**, together with model calibration (see Sect. 3.3) in order to obtain a counterpart probability. More recently, Liu et al. (2019) used **GP** modelling to quantify the confidence of associations of **Atacama large millimeter/submillimeter array (ALMA)** detections in the **COSMOS** fields. Furthermore, Schneider et al. (2022) used **SVMs** to extract stellar counterparts of sources in the **eROSITA Final Equatorial Depth Survey (eFEDS; Brunner et al., 2022)**.

In particular, the radio astronomical community has forecast that the use of **ML** will be instrumental to find radio counterparts of large catalogues (Lazio et al., 2014). Nevertheless, and as stated in Sect. 5.1.2, the number of works using **ML** for predicting the radio detectability of sources (problem comparable to finding radio counterparts) is, to date, very low.

The lack of such studies prompts us to investigate the potential use of **ML** techniques to quantify the probability of a detection to have a counterpart in a different photometric catalogue. In order to assess the idea, we will utilise the radio-detection classification model described in Sect. 6.2 and Appendix B (which is a modification of the model presented in Chapters 4 and 6). Following the discussion of Rohde et al. (2006), we can make directly use of the output probabilities given by the models since they have been calibrated and their distribution is well behaved.

The pipeline described in Sect. 6.2 and Appendix B was applied to the IR-detected sources in the **EMU-PS** area. In order to test the radio counterparts, we selected the sources, regardless of their initial classification, that were predicted to be radio-detectable **AGN**. In particular, we focused on the sources that presented high probabilities to be of such class (i.e. probability of being **AGN** higher than $P(\mathbb{C}) = 0.7$ and probability to have radio detection higher than $P(\mathbb{C}) = 0.8$). Then, we plotted these predicted radio-detectable sources on top of the map of **EMU-PS** together with all other **IR**-detections in the surrounding region. Some sources from this selection are shown in Figs. 6.14 to 6.17a.

CHAPTER 6. MACHINE-ASSISTED LEARNING

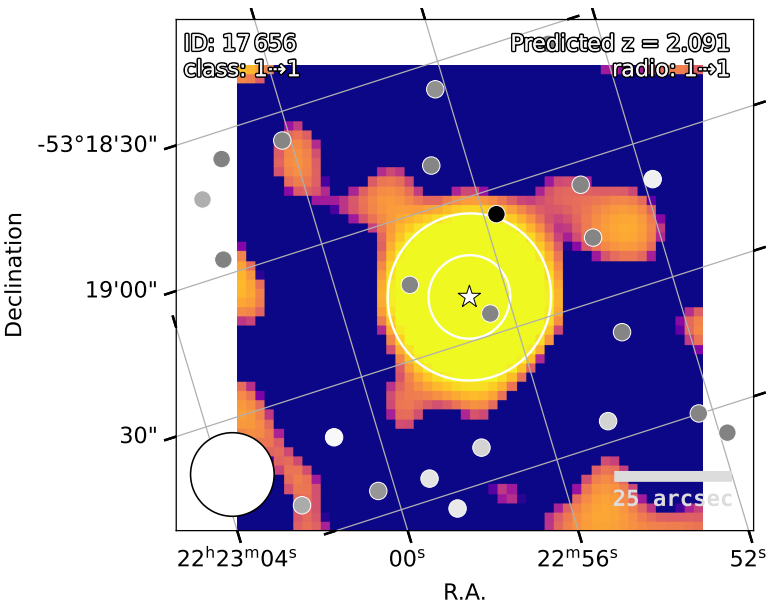


Figure 6.14: Postage stamp of **CW**-detected source ID **00017656** in the **EMU-PS** area (located in the centre of the image). All small circles show the position of a **CW** detection in the displayed region without a radio counterpart, while all stars are **CW** detections with a confirmed radio detection. Face colours of stars and small circles correlate with the predicted probability of such **CW** detections to have a radio detection associated to them, where a brighter hue represents a higher probability. For displaying purposes, all emission below a $1 - \sigma$ detection limit has been set to zero (0). Concentric white circles in the centre of the image limit two regions with a radius of 1 and 2 **full width at half maximum (FWHM)** centred in the selected source. White circle in bottom right corner represents the **EMU-PS** synthesised beam size and gray horizontal lines in the bottom right corner denote a $25''$ scale. In the top left corner of figure, the identification number of source is written, as well as its confirmed and predicted **AGN** (i.e. **class**) states, where 0 represents a **SFGs**, 1 represents an **AGN**, and -1, a source without prior identification. In the top right corner of the figure, the predicted redshift of the source is included, as well as its confirmed and predicted radio detection (i.e. **radio_detect**) status, with 0 representing a source without radio detection (confirmed or predicted) and 1 stands for radio detection.

It is worth noting that in each image, all **IR**-detected sources have been plotted, regardless of their initial or predicted class. The inclusion of the full sample implies that the radio prediction model was applied to all candidates and thus, more uncertainties have been included in the results from its application. This uncertainties do not hinder the analysis regarding counterparts.

A first example is shown in Fig. 6.14. It presents a radio-detected **AGN** (ID **00017656**) that has been predicted to have be in the same category (i.e. radio-detectable **AGN**, an accurate prediction). The star in the middle of the field shows that the source has been detected in the **EMU-PS** data, as shown by the bright region in the background image. There are two additional **CW**-detected sources within one synthesised beam of distance from the selected target. They present a darker face colour, indicating that their probability of having a radio counterpart is lower than that of **00017656**. Thus, the use of the pipeline with the selected source shows that it can be inferred that the large radio source in the background (and only associated by means of distance) can be the counterpart of **00017656** with a high likelihood. What Fig. 6.14 presents, then, is the expected output of our prediction pipeline.

The same behaviour can be seen in Figs. 6.15a, 6.15b, 6.15c, 6.15d, and 6.16a. In

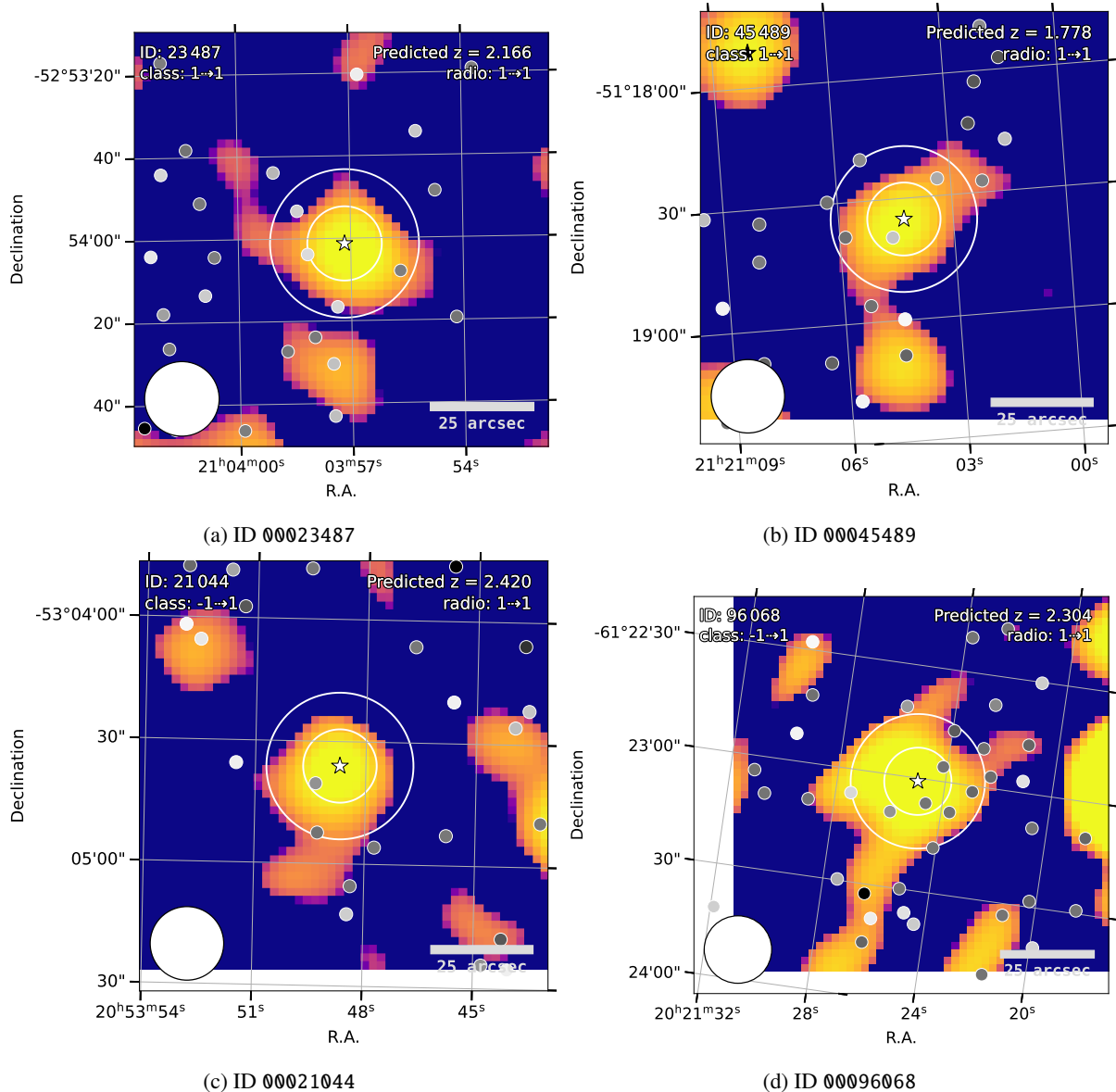


Figure 6.15: Postage stamp of [CW](#)-detected sources IDs 00023487, 00045489, 00021044, and 00096068 in the [EMU-PS](#) area. Description and details as in Fig. 6.14.

particular, Figs. 6.15a and 6.15b show two confirmed radio-detected [AGN](#) that have been correctly predicted surrounded by several [CW](#) sources with lower probability of having radio counterparts. Interestingly, the radio source in Fig. 6.15b resembles the emission of a central source with two lobular arms, as radio [AGN](#) with a bent jet. Then, Figs. 6.15c, 6.15d, and 6.16a depict [EMU-PS](#) confirmed detections that do not have an associated [AGN](#) or [SFGs](#) confirmation. Nevertheless, they have been predicted as [AGN](#) with high confidence. As previously, these predictions have the highest likelihood of being detected in the radio in their surroundings (within two [FWHM](#) from their position). It is important to note that the emission depicted in Fig. 6.15d might not remind the reader of an [AGN](#) or a similar source. Even though the radio prediction and the cross-match are in agreement, further studies are needed to confirm the nature

CHAPTER 6. MACHINE-ASSISTED LEARNING

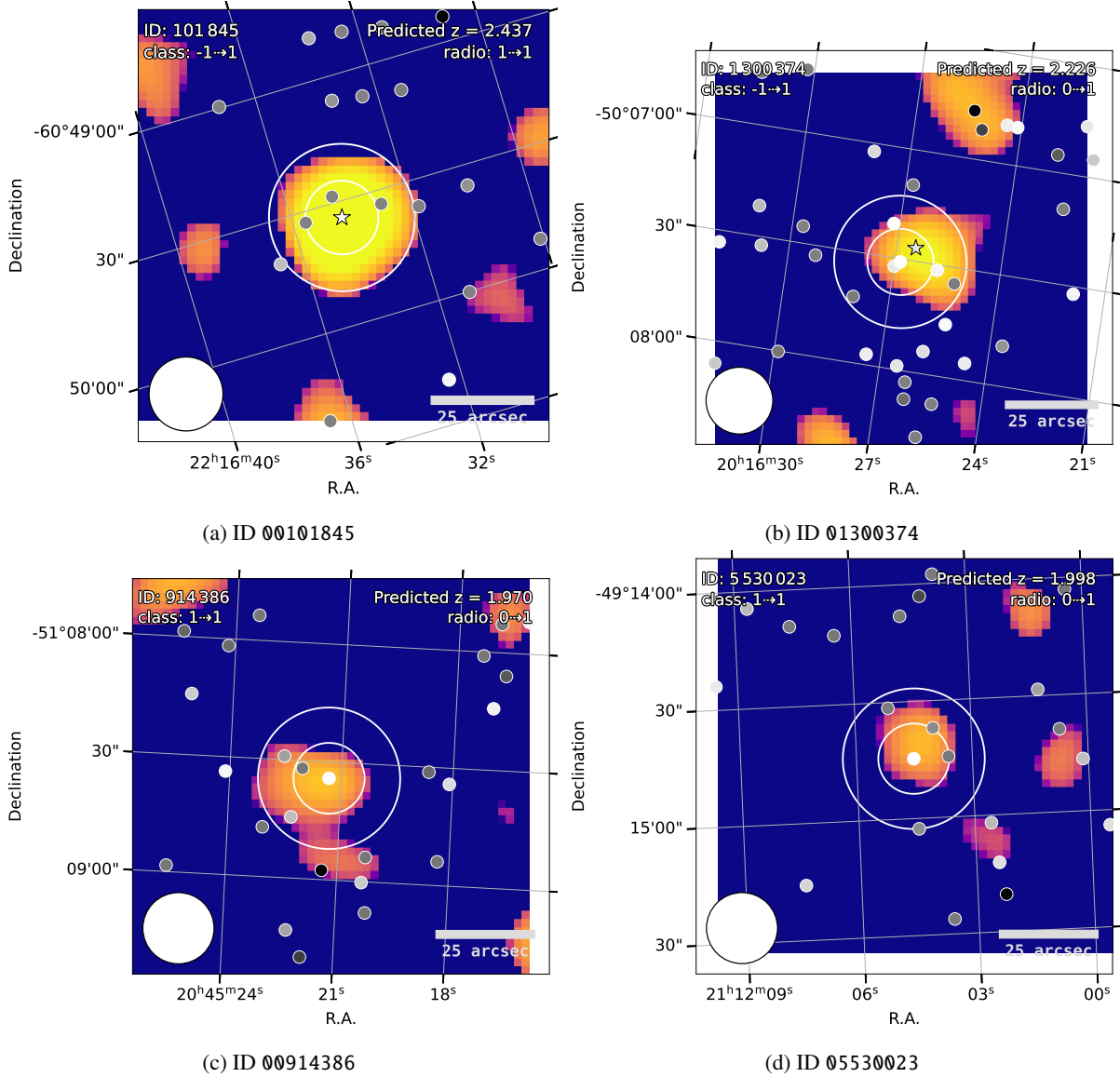


Figure 6.16: Postage stamp of [CW](#)-detected sources IDs 00101845, 01300374, 00914386, and 05530023 in the [EMU-PS](#) area. Description and details as in Fig. 6.14.

of such source.

A different scenario is shown in Figs. 6.16b, 6.16c, 6.16d, 6.17a, 6.17b, and 6.17c, where all [CW](#)-detected sources could not be associated (with a direct cross-match) to a source in [EMU-PS](#). It is important to note that all emission shown in the postage stamps is above a $1 - \sigma$ limit, while the detections listed in the [EMU-PS](#) catalogue are above the $5 - \sigma$ limit (Norris et al., 2021). Thus, it is possible that the catalogue misses faint sources that are picked and predicted by our pipeline.

Figure 6.16b presents an example worth noting. Source ID 01300374, which does not present any prior classification, shows the highest probability of radio detection in its surroundings, but there is an additional source that has been labelled as the counterpart to the

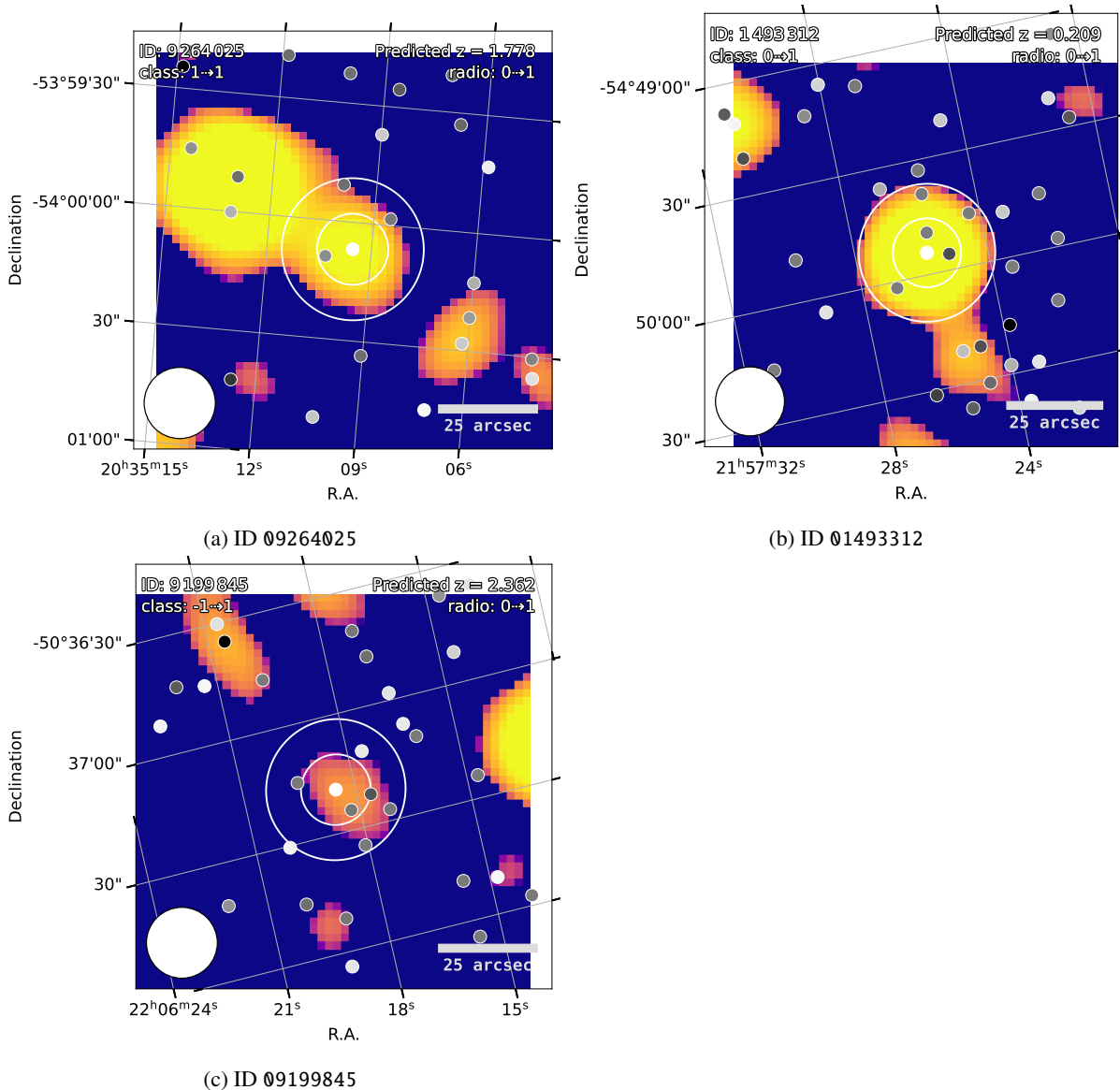


Figure 6.17: Postage stamp of CW-detected sources IDs 09264025, 01493312, and 09199845 in the EMU-PS area. Description and details as in Fig. 6.14.

background radio source. This source, shown as a star with a darker face colour, has obtained a lower probability to be detected in the radio bands. Therefore, our detection pipeline has contested the radio counterpart assignation by distance. Additional measurements are needed to determine the most likely counterpart.

Sources ID 00914386 and ID 05530023, depicted in Figs. 6.16c and 6.16d, have been originally labelled as an AGN without any radio detection. Our pipeline has assigned to them a high probability to have a radio counterpart over their neighbouring sources. At the same time, their background images show a bright source in the same position. Thus, we have predicted that these source can have a radio counterpart (which might have been previously catalogued should EMU-PS have used a lower detection threshold). A similar situation can be seen in

CHAPTER 6. MACHINE-ASSISTED LEARNING

Fig. 6.17a with source ID 09264025. Its main difference is that it is located in what might be a more radio-populated region that could present some overlapping sources.

Finally, two sources without an **AGN** label are presented. Source ID 01493312 (Fig. 6.17b), without a prior label as **SFG**, is located in a very **IR**-crowded region and it has been given, by our prediction pipeline, the highest radio-detection likelihood over their neighbours. In the background **EMU-PS** image, it is possible to see bright radio emission from a point-like source that has a bright appendix. Thus, we have been able to predict the existence of radio emission that was missed by the **EMU-PS** catalogue. Our last example source is ID 09199845 in Fig. 6.17c. Without any prior label (`class` or `radio_detect`), it has been predicted to be a radio-detectable **AGN** among all its neighbouring detections. The **EMU-PS** image shows a relatively bright source that might be associated to our prediction.

All these examples show that our prediction pipeline can be used, without any further modification, to understand the location and distribution of radio counterparts of **IR**-detected sources. By virtue of its training with very deep radio observations (i.e. **LoTSS**), our pipeline can also help finding sources that might have been overlooked or discarded by other radio surveys and catalogues, as was the case with the **EMU-PS** catalogue.

Future developments

The results presented here allow us to look for further developments. We list here some steps that can be taken in order to expand our knowledge on either the prediction pipeline or the results obtained from its use.

7.1 Extensive feature importance analysis

Expanding on the analysis of Chapter 5, the behaviour of the model, when applied to different data sets, can be studied extensively.

7.2 Evolutionary Map of the Universe

Starting with Sects. 6.2 and 6.3, which show possible applications of the prediction pipeline on data from the EMU-PS, more studies can be performed on the areas covered by EMU. The full products from the EMU survey can be subject to our prediction pipeline and as a way to obtain a large number of radio-AGN candidates. The main barrier to achieve such goal is related to the existence of coverage from deep and homogeneous optical surveys. Our training data incorporates measurements from PS1, which is not fully available in the southern hemisphere. For the EMU-PS data, measurements from the

7.3 Square Kilometre Array

Ultimately, our prediction pipeline can be applied to the full area covered by the future SKA in order to accelerate the detection of AGN.

This page intentionally left blank.

Summary

This is the summary of the text we have produced.

With the ultimate intention of better understanding the triggering of radio emission in **AGN**, in this paper, we have shown that it is possible to build a pipeline to detect **AGN**, determine their detectability in radio, within a given flux limit, and predict their redshift value.

Most importantly, we have described a series of methodologies to understand the driving properties of the different decisions, in particular for the radio detection which is, to our best knowledge, the first attempt at doing so.

We have trained the models using multi-wavelength photometry from almost 120 000 spectroscopically identified infrared-detected sources in the **HETDEX** field and created stacked models with them.

These models were applied, sequentially, to 15 018 144 infrared detections in the **HETDEX** Spring field, arriving to the creation of 68 252 radio **AGN** candidates with their corresponding predicted redshift values. Additionally, we applied the models to 3 568 478 infrared detections in the **S82** field, obtaining 22 445 new radio **AGN** candidates with their predicted redshift values.

We have, then, applied a number of analyses on the models to understand the influence of the observed properties over the predictions and their confidence levels. In particular, the use of **SHAP** values gives the opportunity to extract the influence that the feature set has for each individual prediction.

From the application of the prediction pipeline on labelled and unlabelled sources and the analysis of the predictions and the models themselves, the following conclusions can be drawn.

- Generalised stacking is a useful procedure which collects results from individual **ML** algorithms into a single model that can outperform each of the individual models, while preventing the inclusion of biases from individual algorithms. Proper selection of models and input features, together with detailed probability and threshold calibration maximises the metrics of the final model.
- Classification between **AGN** and **SFGs** derived from our model is in line with previous works. Our pipeline is able to retrieve a high fraction of previously-classified **AGN** from

CHAPTER 7. FUTURE DEVELOPMENTS

[HETDEX](#) (recall = 0.9621, precision = 0.9449) and from the [S82](#) field (recall = 0.9401, precision = 0.9481).

- Radio detection classification for predicted [AGN](#) has proven to be highly demanding in terms of data needed for creating the models. Thanks to the use of the techniques shown in this article (i.e. feature creation and selection, generalised stacking, probability calibration, and threshold optimisation), we are able to retrieve previously-known radio-detectable [AGN](#) in the [HETDEX](#) field (recall = 0.5216, precision = 0.3528) and in the [S82](#) field (recall = 0.5816, precision = 0.1229). These rates improve significantly upon a purely random selection(4 times better for the [HETDEX](#) field and 13 times better for [S82](#)), showing the power of [ML](#) methods for obtaining new [RG](#) candidates.
- The prediction of redshift values for sources classified to be radio-detectable [AGN](#) can deliver results that are in line with works that use either traditional or [ML](#) methods.
- Our models (classification and regression) can be applied to areas of the sky which have different radio coverage from that used for training without a strong degradation of the prediction results. This feature can lead to the use of our pipeline over very distinct datasets (in radio and multi-wavelength coverage) expecting to recover the sources predicted to be radio-detectable [AGN](#) with a high probability.
- [ML](#) models cannot be only used for a direct prediction of a value (or a set of values). They can also be subject to analyses that allow to extract additional results. We took advantage of this fact by using global and local feature importances to derive novel colour-colour [AGN](#) selection methods.

With the next generation of observatories already producing source catalogues with an order of magnitude better sensitivity over large areas of the sky than previously (e.g. the Rapid ASKAP Continuum Survey -RACS-, [EMU](#), and the MeerKAT International GHz Tiered Extragalactic Exploration -MIGHTEE-; McConnell et al., 2020; Norris et al., 2011; Jarvis et al., 2016; respectively), the need to understand the fraction of those radio detections related to [AGN](#) and determine counterparts across wavelengths is more necessary than ever.

Although we developed the pipeline as a tool to better understand the aforementioned issues, we foresee additional possibilities in which the pipeline can be of great use. The first of this possibilities involves the use of the pipeline to assist with the selection of radio-detectable

AGN within any set of observations. This application might turn particularly valuable in recent surveys carried out with MeerKAT (Jonas and MeerKAT Team, 2016) or the future **SKA** where the population at the faintest sources will be dominated by **SFGs**. This change needs to use the corresponding data in the training set.

Future developments of the pipeline will concentrate on minimising the existent biases in the training sample as well as in increasing the coverage of the parameter space. We also plan to generalise the pipeline to make it useful for non-radio or galaxy-related research communities. These developments include, for instance, the capability to carry the full analysis for the galactic and stellar populations (i.e. models to determine if a **SFG** can be detected in the radio and to predict redshift values for **SFGs** and non-radio **AGN**).

In order to increase the parameter space of our training sets, we plan to include information from radio surveys with different characteristics. Namely, shallower, but with larger area, and less extended but with deeper multi-wavelength data. Similarly, the inclusion of **FIR**, X-ray, and multi-survey radio measurements makes part of our efforts to improve detections, not only in radio, but in additional wavelengths.

This page intentionally left blank.

Data and software acknowledgements

This publication makes use of data products from the Wide-field Infrared Survey Explorer, which is a joint project of the University of California, Los Angeles, and the Jet Propulsion Laboratory/California Institute of Technology, funded by the National Aeronautics and Space Administration.

LOFAR data products were provided by the LOFAR Surveys Key Science project (LSKSP¹) and were derived from observations with the International LOFAR Telescope (ILT). LOFAR (van Haarlem et al., 2013) is the Low Frequency Array designed and constructed by ASTRON. It has observing, data processing, and data storage facilities in several countries, which are owned by various parties (each with their own funding sources), and which are collectively operated by the ILT foundation under a joint scientific policy. The efforts of the LSKSP have benefited from funding from the European Research Council, NOVA, NWO, CNRS-INSU, the SURF Co-operative, the UK Science and Technology Funding Council and the Jülich Supercomputing Centre.

The Pan-STARRS1 Surveys (PS1) and the PS1 public science archive have been made possible through contributions by the Institute for Astronomy, the University of Hawaii, the Pan-STARRS Project Office, the Max-Planck Society and its participating institutes, the Max Planck Institute for Astronomy, Heidelberg and the Max Planck Institute for Extraterrestrial Physics, Garching, The Johns Hopkins University, Durham University, the University of Edinburgh, the Queen’s University Belfast, the Harvard-Smithsonian Center for Astrophysics, the Las Cumbres Observatory Global Telescope Network Incorporated, the National Central University of Taiwan, the Space Telescope Science Institute, the National Aeronautics and Space Administration under Grant No. NNX08AR22G issued through the Planetary Science Division of the NASA Science Mission Directorate, the National Science Foundation Grant No. AST-1238877, the University of Maryland, Eötvös Loránd University (ELTE), the Los Alamos National Laboratory, and the Gordon and Betty Moore Foundation.

This publication makes use of data products from the Two Micron All Sky Survey, which is a joint project of the University of Massachusetts and the Infrared Processing and Ana-

¹<https://lofar-surveys.org/>

lysis Center/California Institute of Technology, funded by the National Aeronautics and Space Administration and the National Science Foundation.

This work made use of public data from the Sloan Digital Sky Survey, Data Release 16. Funding for the Sloan Digital Sky Survey IV has been provided by the Alfred P. Sloan Foundation, the U.S. Department of Energy Office of Science, and the Participating Institutions.

SDSS-IV acknowledges support and resources from the Center for High Performance Computing at the University of Utah. The SDSS website is www.sdss.org. SDSS-IV is managed by the Astrophysical Research Consortium for the Participating Institutions of the SDSS Collaboration including the Brazilian Participation Group, the Carnegie Institution for Science, Carnegie Mellon University, Center for Astrophysics | Harvard & Smithsonian, the Chilean Participation Group, the French Participation Group, Instituto de Astrofísica de Canarias, The Johns Hopkins University, Kavli Institute for the Physics and Mathematics of the Universe (IPMU) / University of Tokyo, the Korean Participation Group, Lawrence Berkeley National Laboratory, Leibniz Institut für Astrophysik Potsdam (AIP), Max-Planck-Institut für Astronomie (MPIA Heidelberg), Max-Planck-Institut für Astrophysik (MPA Garching), Max-Planck-Institut für Extraterrestrische Physik (MPE), National Astronomical Observatories of China, New Mexico State University, New York University, University of Notre Dame, Observatório Nacional / MCTI, The Ohio State University, Pennsylvania State University, Shanghai Astronomical Observatory, United Kingdom Participation Group, Universidad Nacional Autónoma de México, University of Arizona, University of Colorado Boulder, University of Oxford, University of Portsmouth, University of Utah, University of Virginia, University of Washington, University of Wisconsin, Vanderbilt University, and Yale University.

This scientific work uses data obtained from Inyarrimanha Ilgari Bundara / the Murchison Radio-astronomy Observatory. We acknowledge the Wajarri Yamaji People as the Traditional Owners and native title holders of the Observatory site. CSIRO's ASKAP radio telescope is part of the Australia Telescope National Facility (<https://ror.org/05qajvd42>). Operation of ASKAP is funded by the Australian Government with support from the National Collaborative Research Infrastructure Strategy. ASKAP uses the resources of the Pawsey Supercomputing Research Centre. Establishment of ASKAP, Inyarrimanha Ilgari Bundara, the CSIRO Murchison Radio-astronomy Observatory and the Pawsey Supercomputing Research Centre are initiatives of the Australian Government, with support from the Government of Western Australia and the Science and Industry Endowment Fund.

Part of this work is based on data obtained from the ESO Science Archive Facility with

DOI(s): <https://doi.org/10.18727/archive/56>.

This project used public archival data from the Dark Energy Survey (DES). Funding for the DES Projects has been provided by the U.S. Department of Energy, the U.S. National Science Foundation, the Ministry of Science and Education of Spain, the Science and Technology Facilities Council of the United Kingdom, the Higher Education Funding Council for England, the National Center for Supercomputing Applications at the University of Illinois at Urbana-Champaign, the Kavli Institute of Cosmological Physics at the University of Chicago, the Center for Cosmology and Astro-Particle Physics at the Ohio State University, the Mitchell Institute for Fundamental Physics and Astronomy at Texas A&M University, Financiadora de Estudos e Projetos, Fundação Carlos Chagas Filho de Amparo à Pesquisa do Estado do Rio de Janeiro, Conselho Nacional de Desenvolvimento Científico e Tecnológico and the Ministério da Ciência, Tecnologia e Inovação, the Deutsche Forschungsgemeinschaft, and the Collaborating Institutions in the Dark Energy Survey. The Collaborating Institutions are Argonne National Laboratory, the University of California at Santa Cruz, the University of Cambridge, Centro de Investigaciones Energéticas, Medioambientales y Tecnológicas-Madrid, the University of Chicago, University College London, the DES-Brazil Consortium, the University of Edinburgh, the Eidgenössische Technische Hochschule (ETH) Zürich, Fermi National Accelerator Laboratory, the University of Illinois at Urbana-Champaign, the Institut de Ciències de l'Espai (IEEC/CSIC), the Institut de Física d'Altes Energies, Lawrence Berkeley National Laboratory, the Ludwig-Maximilians Universität München and the associated Excellence Cluster Universe, the University of Michigan, the National Optical Astronomy Observatory, the University of Nottingham, The Ohio State University, the OzDES Membership Consortium, the University of Pennsylvania, the University of Portsmouth, SLAC National Accelerator Laboratory, Stanford University, the University of Sussex, and Texas A&M University. Based in part on observations at Cerro Tololo Inter-American Observatory, National Optical Astronomy Observatory, which is operated by the Association of Universities for Research in Astronomy (AURA) under a cooperative agreement with the National Science Foundation.

This work has made use of data from the European Space Agency (ESA) mission *Gaia* (<https://www.cosmos.esa.int/gaia>), processed by the *Gaia* Data Processing and Analysis Consortium (DPAC, <https://www.cosmos.esa.int/web/gaia/dpac/consortium>). Funding for the DPAC has been provided by national institutions, in particular the institutions participating in the *Gaia* Multilateral Agreement.

The Legacy Surveys imaging of the DESI footprint is supported by the Director, Office

of Science, Office of High Energy Physics of the U.S. Department of Energy under Contract No. DE-AC02-05CH1123, by the National Energy Research Scientific Computing Center, a DOE Office of Science User Facility under the same contract; and by the U.S. National Science Foundation, Division of Astronomical Sciences under Contract No. AST-0950945 to NOAO.

This project makes use of the MaNGA-Pipe3D dataproducts. We thank the IA-UNAM MaNGA team for creating this catalogue, and the Conacyt Project CB-285080 for supporting them.

This research has made use of NASA’s Astrophysics Data System, TOPCAT² (Taylor, 2005), JupyterLab³ (Kluyver et al., 2016), ‘Aladin sky atlas’ (v11.0.24; Bonnarel et al., 2000) developed at CDS, Strasbourg Observatory, France, and the VizieR catalogue access tool, CDS, Strasbourg, France (DOI : 10.26093/cds/vizier). The original description of the VizieR service was published in Ochsenbein et al. (2000). This research has also made use of hips2fits,⁴ a service provided by CDS.

This research has made use of the Spanish Virtual Observatory (<https://svo.ca.b.inta-csic.es>; Rodrigo and Solano, 2020; Rodrigo et al., 2012) project funded by MCIN/AEI/10.13039/501100011033/ through grant PID2020-112949GB-I00

This work made extensive use of the Python packages PyCaret⁵ (v2.3.10; Ali, 2020), scikit-learn (v0.23.2; Pedregosa et al., 2011), pandas⁶ (v1.4.2; McKinney, 2010), Astropy⁷, a community-developed core Python package for Astronomy (v5.0; Astropy Collaboration et al., 2013; Astropy Collaboration et al., 2018; Astropy Collaboration et al., 2022), Matplotlib (v3.5.1; Hunter, 2007), betacal⁸ (v1.1.0), CMasher⁹ (v1.6.3; van der Velden, 2020), faiss¹⁰ (v1.7.2; Johnson et al., 2019), skyproj¹¹ (v1.1.0), and mocpy¹² (v0.13.1; Baumann et al., 2023).

²<http://www.star.bris.ac.uk/~mbt/topcat/>

³<https://jupyter.org>

⁴<https://alasky.cds.unistra.fr/hips-image-services/hips2fits>

⁵<https://pycaret.org>

⁶<https://pandas.pydata.org>

⁷<https://www.astropy.org>

⁸<https://betacal.github.io>

⁹<https://github.com/1313e/CMasher>

¹⁰<https://faiss.ai>

¹¹<https://github.com/LSSTDESC/skyproj>

¹²<https://github.com/cds-astro/mocpy/>

References

- Abbott, T. M. C., Abdalla, F. B., et al. (Dec. 2018). ‘The Dark Energy Survey: Data Release 1’. In: ApJS 239.2, 18, p. 18. doi: [10.3847/1538-4365/aae9f0](https://doi.org/10.3847/1538-4365/aae9f0).
- Abbott, T. M. C., Adamów, M., et al. (Aug. 2021). ‘The Dark Energy Survey Data Release 2’. In: ApJS 255.2, 20, p. 20. doi: [10.3847/1538-4365/ac00b3](https://doi.org/10.3847/1538-4365/ac00b3).
- Abdo, A. A., Ackermann, M., et al. (May 2010). ‘The First Catalog of Active Galactic Nuclei Detected by the Fermi Large Area Telescope’. In: ApJ 715.1, pp. 429–457. doi: [10.1088/0004-637X/715/1/429](https://doi.org/10.1088/0004-637X/715/1/429).
- Abramson, I. S. (1982). ‘On Bandwidth Variation in Kernel Estimates-A Square Root Law’. In: *The Annals of Statistics* 10.4, pp. 1217–1223. ISSN: 00905364. URL: <http://www.jstor.org/stable/2240724> (visited on 20/01/2024).
- Adam, A., Perreault-Levasseur, L., et al. (July 2023). ‘Pixelated Reconstruction of Foreground Density and Background Surface Brightness in Gravitational Lensing Systems Using Recurrent Inference Machines’. In: ApJ 951.1, 6, p. 6. doi: [10.3847/1538-4357/accf84](https://doi.org/10.3847/1538-4357/accf84).
- Aguado, D. S., Ahumada, R., et al. (Feb. 2019). ‘The Fifteenth Data Release of the Sloan Digital Sky Surveys: First Release of MaNGA-derived Quantities, Data Visualization Tools, and Stellar Library’. In: ApJS 240.2, 23, p. 23. doi: [10.3847/1538-4365/aaf651](https://doi.org/10.3847/1538-4365/aaf651).
- Agüeros, M. A., Ivezić, Ž., et al. (Sept. 2005). ‘The Ultraviolet, Optical, and Infrared Properties of Sloan Digital Sky Survey Sources Detected by GALEX’. In: AJ 130.3, pp. 1022–1036. doi: [10.1086/432160](https://doi.org/10.1086/432160).
- Ahumada, R., Prieto, C. A., et al. (July 2020). ‘The 16th Data Release of the Sloan Digital Sky Surveys: First Release from the APOGEE-2 Southern Survey and Full Release of eBOSS Spectra’. In: ApJS 249.1, 3, p. 3. doi: [10.3847/1538-4365/ab929e](https://doi.org/10.3847/1538-4365/ab929e).
- Aihara, H., Allende Prieto, C., et al. (Apr. 2011). ‘The Eighth Data Release of the Sloan Digital Sky Survey: First Data from SDSS-III’. In: ApJS 193.2, 29, p. 29. doi: [10.1088/0067-0049/193/2/29](https://doi.org/10.1088/0067-0049/193/2/29).
- Alegre, L., Sabater, J., et al. (Nov. 2022). ‘A machine-learning classifier for LOFAR radio galaxy cross-matching techniques’. In: MNRAS 516.4, pp. 4716–4738. doi: [10.1093/mnras/stac1888](https://doi.org/10.1093/mnras/stac1888).
- Ali, M. (Apr. 2020). *PyCaret: An open source, low-code machine learning library in Python*. PyCaret version 2.3. URL: <https://www.pycaret.org>.
- Allen, D. M. (1974). ‘The Relationship Between Variable Selection and Data Agumentation and a Method for Prediction’. In: *Technometrics* 16.1, pp. 125–127. doi: [10.1080/00401706.1974.10489157](https://doi.org/10.1080/00401706.1974.10489157).
- Allison, P. (2001). *Missing Data*. Quantitative Applications in the Social Sciences. SAGE Publications. ISBN: 9781452207902. URL: <https://books.google.pt/books?id=LJB2AwAAQBAJ>.
- Almosallam, I. A., Jarvis, M. J., and Roberts, S. J. (Oct. 2016a). ‘GPZ: non-stationary sparse Gaussian processes for heteroscedastic uncertainty estimation in photometric redshifts’. In: MNRAS 462.1, pp. 726–739. doi: [10.1093/mnras/stw1618](https://doi.org/10.1093/mnras/stw1618).

REFERENCES

- Almosallam, I. A., Lindsay, S. N., et al. (Jan. 2016b). ‘A sparse Gaussian process framework for photometric redshift estimation’. In: MNRAS 455.3, pp. 2387–2401. doi: [10.1093/mnras/stv2425](https://doi.org/10.1093/mnras/stv2425).
- Alqasim, A. and Page, M. J. (Apr. 2023). ‘A new method to determine X-ray luminosity functions of AGN and their evolution with redshift’. In: MNRAS 520.3, pp. 3827–3846. doi: [10.1093/mnras/stad007](https://doi.org/10.1093/mnras/stad007).
- Amarantidis, S., Afonso, J., et al. (May 2019). ‘The first supermassive black holes: indications from models for future observations’. In: MNRAS 485.2, pp. 2694–2709. doi: [10.1093/mnras/stz551](https://doi.org/10.1093/mnras/stz551).
- An, T., Zhang, Y., and Frey, S. (Sept. 2020). ‘A method for checking high-redshift identification of radio AGNs’. In: MNRAS 497.2, pp. 2260–2264. doi: [10.1093/mnras/staa2132](https://doi.org/10.1093/mnras/staa2132).
- Ananna, T. T., Salvato, M., et al. (Nov. 2017). ‘AGN Populations in Large-volume X-Ray Surveys: Photometric Redshifts and Population Types Found in the Stripe 82X Survey’. In: ApJ 850.1, 66, p. 66. doi: [10.3847/1538-4357/aa937d](https://doi.org/10.3847/1538-4357/aa937d).
- Anbajagane, D., Evrard, A. E., and Farahi, A. (Jan. 2022). ‘Baryonic imprints on DM haloes: population statistics from dwarf galaxies to galaxy clusters’. In: MNRAS 509.3, pp. 3441–3461. doi: [10.1093/mnras/stab3177](https://doi.org/10.1093/mnras/stab3177).
- Andonie, C., Alexander, D. M., et al. (Dec. 2022). ‘A panchromatic view of infrared quasars: excess star formation and radio emission in the most heavily obscured systems’. In: MNRAS 517.2, pp. 2577–2598. doi: [10.1093/mnras/stac2800](https://doi.org/10.1093/mnras/stac2800).
- Aniyan, A. K. and Thorat, K. (June 2017). ‘Classifying Radio Galaxies with the Convolutional Neural Network’. In: ApJS 230.2, 20, p. 20. doi: [10.3847/1538-4365/aa7333](https://doi.org/10.3847/1538-4365/aa7333).
- Annis, J., Soares-Santos, M., et al. (Oct. 2014). ‘The Sloan Digital Sky Survey Coadd: 275 deg² of Deep Sloan Digital Sky Survey Imaging on Stripe 82’. In: ApJ 794.2, 120, p. 120. doi: [10.1088/0004-637X/794/2/120](https://doi.org/10.1088/0004-637X/794/2/120).
- Antonucci, R. (Jan. 1993). ‘Unified models for active galactic nuclei and quasars.’ In: ARA&A 31, pp. 473–521. doi: [10.1146/annurev.aa.31.090193.002353](https://doi.org/10.1146/annurev.aa.31.090193.002353).
- Arévalo, P., Uttley, P., et al. (Sept. 2008). ‘Correlated X-ray/optical variability in the quasar MR2251-178’. In: MNRAS 389.3, pp. 1479–1488. doi: [10.1111/j.1365-2966.2008.13719.x](https://doi.org/10.1111/j.1365-2966.2008.13719.x).
- Arévalo, P., Uttley, P., et al. (Aug. 2009). ‘Correlation and time delays of the X-ray and optical emission of the Seyfert Galaxy NGC 3783’. In: MNRAS 397.4, pp. 2004–2014. doi: [10.1111/j.1365-2966.2009.15110.x](https://doi.org/10.1111/j.1365-2966.2009.15110.x).
- Arnouts, S., Cristiani, S., et al. (Dec. 1999). ‘Measuring and modelling the redshift evolution of clustering: the Hubble Deep Field North’. In: MNRAS 310.2, pp. 540–556. doi: [10.1046/j.1365-8711.1999.02978.x](https://doi.org/10.1046/j.1365-8711.1999.02978.x).
- Arsioli, B. and Dediu, P. (Oct. 2020). ‘Machine learning applied to multifrequency data in astrophysics: blazar classification’. In: MNRAS 498.2, pp. 1750–1764. doi: [10.1093/mnras/staa2449](https://doi.org/10.1093/mnras/staa2449).
- Assef, R. J., Stern, D., et al. (July 2013). ‘Mid-infrared Selection of Active Galactic Nuclei with the Wide-field Infrared Survey Explorer. II. Properties of WISE-selected Active Galactic Nuclei in the NDWFS Boötes Field’. In: ApJ 772.1, 26, p. 26. doi: [10.1088/0004-637X/772/1/26](https://doi.org/10.1088/0004-637X/772/1/26).
- Assef, R. J., Stern, D., et al. (Feb. 2018). ‘The WISE AGN Catalog’. In: ApJS 234.2, 23, p. 23. doi: [10.3847/1538-4365/aaa00a](https://doi.org/10.3847/1538-4365/aaa00a).
- Astropy Collaboration, Price-Whelan, A. M., et al. (Sept. 2018). ‘The Astropy Project: Building an Open-science Project and Status of the v2.0 Core Package’. In: AJ 156.3, 123, p. 123. doi: [10.3847/1538-3881/aabc4f](https://doi.org/10.3847/1538-3881/aabc4f).

- Astropy Collaboration, Price-Whelan, A. M., et al. (Aug. 2022). ‘The Astropy Project: Sustaining and Growing a Community-oriented Open-source Project and the Latest Major Release (v5.0) of the Core Package’. In: ApJ 935.2, 167, p. 167. doi: [10.3847/1538-4357/ac7c74](https://doi.org/10.3847/1538-4357/ac7c74).
- Astropy Collaboration, Robitaille, T. P., et al. (Oct. 2013). ‘Astropy: A community Python package for astronomy’. In: A&A 558, A33, A33. doi: [10.1051/0004-6361/201322068](https://doi.org/10.1051/0004-6361/201322068).
- Atek, H., Chemerynska, I., et al. (Oct. 2023). ‘JWST UNCOVER: discovery of $z > 9$ galaxy candidates behind the lensing cluster Abell 2744’. In: MNRAS 524.4, pp. 5486–5496. doi: [10.1093/mnras/stad1998](https://doi.org/10.1093/mnras/stad1998).
- Auge, C., Sanders, D., et al. (Nov. 2023). ‘The Accretion History of AGN: The Spectral Energy Distributions of X-Ray-luminous Active Galactic Nuclei’. In: ApJ 957.1, 19, p. 19. doi: [10.3847/1538-4357/acf21a](https://doi.org/10.3847/1538-4357/acf21a).
- Avni, Y. and Bahcall, J. N. (Feb. 1980). ‘On the simultaneous analysis of several complete samples. The V/Vmax and Ve/Va variables, with applications to quasars.’ In: ApJ 235, pp. 694–716. doi: [10.1086/157673](https://doi.org/10.1086/157673).
- Bahcall, J. N. and Kozlovsky, B.-Z. (Mar. 1969). ‘Some Models of the Emission-Line Region of 3c 273’. In: ApJ 155, p. 1077. doi: [10.1086/149935](https://doi.org/10.1086/149935).
- Baldwin, J. A., Phillips, M. M., and Terlevich, R. (Feb. 1981). ‘Classification parameters for the emission-line spectra of extragalactic objects.’ In: PASP 93, pp. 5–19. doi: [10.1086/130766](https://doi.org/10.1086/130766).
- Ball, N. M. and Brunner, R. J. (Jan. 2010). ‘Data Mining and Machine Learning in Astronomy’. In: *International Journal of Modern Physics D* 19.7, pp. 1049–1106. doi: [10.1142/S0218271810017160](https://doi.org/10.1142/S0218271810017160).
- Ball, N. M., Brunner, R. J., et al. (Aug. 2008). ‘Robust Machine Learning Applied to Astronomical Data Sets. III. Probabilistic Photometric Redshifts for Galaxies and Quasars in the SDSS and GALEX’. In: ApJ 683.1, pp. 12–21. doi: [10.1086/589646](https://doi.org/10.1086/589646).
- Baltay, C., Grossman, L., et al. (Apr. 2021). ‘Low-redshift Type Ia Supernova from the LSQ/LCO Collaboration’. In: PASP 133.1022, 044002, p. 044002. doi: [10.1088/1538-3873/abd417](https://doi.org/10.1088/1538-3873/abd417).
- Barbieri, C. and Bertola, F. (Jan. 1972). ‘Identification of 5C4 radio sources.’ In: MNRAS 156, pp. 399–409. doi: [10.1093/mnras/156.4.399](https://doi.org/10.1093/mnras/156.4.399).
- Baron, D. (Apr. 2019). ‘Machine Learning in Astronomy: a practical overview’. In: *arXiv e-prints*, arXiv:1904.07248, arXiv:1904.07248.
- Baron, D. and Poznanski, D. (Mar. 2017). ‘The weirdest SDSS galaxies: results from an outlier detection algorithm’. In: MNRAS 465.4, pp. 4530–4555. doi: [10.1093/mnras/stw3021](https://doi.org/10.1093/mnras/stw3021).
- Barrows, R. S., Comerford, J. M., et al. (Dec. 2021). ‘A Catalog of Host Galaxies for WISE-selected AGN: Connecting Host Properties with Nuclear Activity and Identifying Contaminants’. In: ApJ 922.2, 179, p. 179. doi: [10.3847/1538-4357/ac1352](https://doi.org/10.3847/1538-4357/ac1352).
- Baum, W. A. (Feb. 1957). ‘Photoelectric determinations of redshifts beyond 0.2 c.’ In: AJ 62, pp. 6–7. doi: [10.1086/107433](https://doi.org/10.1086/107433).
- (Jan. 1962). ‘Photoelectric Magnitudes and Red-Shifts’. In: *Problems of Extra-Galactic Research*. Ed. by G. C. McVittie. Vol. 15, p. 390.
- Baumann, M., Marchand, M., et al. (Dec. 2023). *cds-astro/mocpy: Release v0.13.1*. Version v0.13.1. doi: [10.5281/zenodo.10257390](https://doi.org/10.5281/zenodo.10257390).
- Beifiori, A., Courteau, S., et al. (Jan. 2012). ‘On the correlations between galaxy properties and supermassive black hole mass’. In: MNRAS 419.3, pp. 2497–2528. doi: [10.1111/j.1365-2966.2011.19903.x](https://doi.org/10.1111/j.1365-2966.2011.19903.x).

REFERENCES

- Benítez, N. (June 2000). ‘Bayesian Photometric Redshift Estimation’. In: ApJ 536.2, pp. 571–583. doi: [10.1086/308947](https://doi.org/10.1086/308947).
- Best, P. N., Kondapally, R., et al. (Aug. 2023). ‘The LOFAR Two-metre Sky Survey: Deep Fields data release 1. V. Survey description, source classifications, and host galaxy properties’. In: MNRAS 523.2, pp. 1729–1755. doi: [10.1093/mnras/stad1308](https://doi.org/10.1093/mnras/stad1308).
- Bianchi, L., Rodriguez-Merino, L., et al. (Dec. 2007). ‘Statistical Properties of the GALEX-SDSS Matched Source Catalogs, and Classification of the UV Sources’. In: ApJS 173.2, pp. 659–672. doi: [10.1086/516648](https://doi.org/10.1086/516648).
- Birchall, K. L., Watson, M. G., and Aird, J. (Feb. 2020). ‘X-ray detected AGN in SDSS dwarf galaxies’. In: MNRAS 492.2, pp. 2268–2284. doi: [10.1093/mnras/staa040](https://doi.org/10.1093/mnras/staa040).
- Blandford, R., Meier, D., and Readhead, A. (Aug. 2019). ‘Relativistic Jets from Active Galactic Nuclei’. In: ARA&A 57, pp. 467–509. doi: [10.1146/annurev-astro-081817-051948](https://doi.org/10.1146/annurev-astro-081817-051948).
- Blecha, L., Snyder, G. F., et al. (Aug. 2018). ‘The power of infrared AGN selection in mergers: a theoretical study’. In: MNRAS 478.3, pp. 3056–3071. doi: [10.1093/mnras/sty1274](https://doi.org/10.1093/mnras/sty1274).
- Bonaldi, A., Bonato, M., et al. (Jan. 2019). ‘The Tiered Radio Extragalactic Continuum Simulation (T-RECS)’. In: MNRAS 482.1, pp. 2–19. doi: [10.1093/mnras/sty2603](https://doi.org/10.1093/mnras/sty2603).
- Bonato, M., Prandoni, I., et al. (Jan. 2021). ‘New constraints on the 1.4 GHz source number counts and luminosity functions in the Lockman Hole field’. In: MNRAS 500.1, pp. 22–33. doi: [10.1093/mnras/staa3218](https://doi.org/10.1093/mnras/staa3218).
- Bonnarel, F., Fernique, P., et al. (Apr. 2000). ‘The ALADIN interactive sky atlas. A reference tool for identification of astronomical sources’. In: A&AS 143, pp. 33–40. doi: [10.1051/aas:2000331](https://doi.org/10.1051/aas:2000331).
- Bosman, S. E. I. (Feb. 2022). *All z>5.7 quasars currently known*. Version 1.15. Zenodo. doi: [10.5281/zenodo.6039724](https://doi.org/10.5281/zenodo.6039724).
- Bouwens, R., González-López, J., et al. (Oct. 2020). ‘The ALMA Spectroscopic Survey Large Program: The Infrared Excess of $z = 1.5\text{--}10$ UV-selected Galaxies and the Implied High-redshift Star Formation History’. In: ApJ 902.2, 112, p. 112. doi: [10.3847/1538-4357/abb830](https://doi.org/10.3847/1538-4357/abb830).
- Bowler, R. A. A., Adams, N. J., et al. (Mar. 2021). ‘The rapid transition from star formation to AGN-dominated rest-frame ultraviolet light at $z \simeq 4'$ '. In: MNRAS 502.1, pp. 662–677. doi: [10.1093/mnras/stab038](https://doi.org/10.1093/mnras/stab038).
- Bowles, M., Tang, H., et al. (June 2023). ‘Radio galaxy zoo EMU: towards a semantic radio galaxy morphology taxonomy’. In: MNRAS 522.2, pp. 2584–2600. doi: [10.1093/mnras/stad1021](https://doi.org/10.1093/mnras/stad1021).
- Brammer, G. B., van Dokkum, P. G., and Coppi, P. (Oct. 2008). ‘EAZY: A Fast, Public Photometric Redshift Code’. In: ApJ 686.2, pp. 1503–1513. doi: [10.1086/591786](https://doi.org/10.1086/591786).
- Brandt, W. N. and Alexander, D. M. (Jan. 2015). ‘Cosmic X-ray surveys of distant active galaxies. The demographics, physics, and ecology of growing supermassive black holes’. In: A&A Rev. 23, 1, p. 1. doi: [10.1007/s00159-014-0081-z](https://doi.org/10.1007/s00159-014-0081-z).
- Braun, R., Bonaldi, A., et al. (Dec. 2019). ‘Anticipated Performance of the Square Kilometre Array – Phase 1 (SKA1)’. In: *arXiv e-prints*, arXiv:1912.12699, arXiv:1912.12699. doi: [10.48550/arXiv.1912.12699](https://doi.org/10.48550/arXiv.1912.12699).
- Breedt, E., Arévalo, P., et al. (Mar. 2009). ‘Long-term optical and X-ray variability of the Seyfert galaxy Markarian 79’. In: MNRAS 394.1, pp. 427–437. doi: [10.1111/j.1365-2966.2008.14302.x](https://doi.org/10.1111/j.1365-2966.2008.14302.x).
- Breedt, E., McHardy, I. M., et al. (Apr. 2010). ‘Twelve years of X-ray and optical variability in the Seyfert galaxy NGC 4051’. In: MNRAS 403.2, pp. 605–619. doi: [10.1111/j.1365-2966.2009.16146.x](https://doi.org/10.1111/j.1365-2966.2009.16146.x).

- Breiman, L. (Aug. 1996). ‘Bagging predictors’. In: *Machine Learning* 24.2, pp. 123–140. issn: 1573-0565. doi: [10.1007/BF00058655](https://doi.org/10.1007/BF00058655).
- (Oct. 2001). ‘Random Forests’. In: *Machine Learning* 45.1, pp. 5–32. issn: 1573-0565. doi: [10.1023/A:1010933404324](https://doi.org/10.1023/A:1010933404324).
- (2003). ‘Manual on setting up, using, and understanding random forests v4. 0’. In: *Statistics Department University of California Berkeley, CA, USA*.
- Brescia, M., Cavuoti, S., et al. (2021). ‘Photometric Redshifts With Machine Learning, Lights and Shadows on a Complex Data Science Use Case’. In: *Frontiers in Astronomy and Space Sciences* 8, p. 70. issn: 2296-987X. doi: [10.3389/fspas.2021.658229](https://doi.org/10.3389/fspas.2021.658229).
- Brescia, M., Salvato, M., et al. (Oct. 2019). ‘Photometric redshifts for X-ray-selected active galactic nuclei in the eROSITA era’. In: *MNRAS* 489.1, pp. 663–680. doi: [10.1093/mnras/stz2159](https://doi.org/10.1093/mnras/stz2159).
- Brier, G. W. (1950). ‘Verification of Forecasts Expressed in Terms of Probability’. In: *Monthly Weather Review* 78.1, pp. 1–3. doi: [10.1175/1520-0493\(1950\)078<0001:VOFEIT>2.0.CO;2](https://doi.org/10.1175/1520-0493(1950)078<0001:VOFEIT>2.0.CO;2).
- Bröcker, J. and Smith, L. A. (2007). ‘Increasing the Reliability of Reliability Diagrams’. In: *Weather and Forecasting* 22.3, pp. 651–661. doi: [10.1175/WAF993.1](https://doi.org/10.1175/WAF993.1).
- Brown, M. J. I., Duncan, K. J., et al. (Nov. 2019). ‘The spectral energy distributions of active galactic nuclei’. In: *MNRAS* 489.3, pp. 3351–3367. doi: [10.1093/mnras/stz2324](https://doi.org/10.1093/mnras/stz2324).
- Brown, M. J. I., Moustakas, J., et al. (June 2014). ‘An Atlas of Galaxy Spectral Energy Distributions from the Ultraviolet to the Mid-infrared’. In: *ApJS* 212.2, 18, p. 18. doi: [10.1088/0067-0049/212/2/18](https://doi.org/10.1088/0067-0049/212/2/18).
- Brunner, H., Liu, T., et al. (May 2022). ‘The eROSITA Final Equatorial Depth Survey (eFEDS). X-ray catalogue’. In: *A&A* 661, A1, A1. doi: [10.1051/0004-6361/202141266](https://doi.org/10.1051/0004-6361/202141266).
- Brusa, M., Zamorani, G., et al. (Sept. 2007). ‘The XMM-Newton Wide-Field Survey in the COSMOS Field. III. Optical Identification and Multiwavelength Properties of a Large Sample of X-Ray-Selected Sources’. In: *ApJS* 172.1, pp. 353–367. doi: [10.1086/516575](https://doi.org/10.1086/516575).
- Buchner, J. (Oct. 2019). ‘Collaborative Nested Sampling: Big Data versus Complex Physical Models’. In: *PASP* 131.1004, p. 108005. doi: [10.1088/1538-3873/aae7fc](https://doi.org/10.1088/1538-3873/aae7fc).
- Budavári, T. and Szalay, A. S. (May 2008). ‘Probabilistic Cross-Identification of Astronomical Sources’. In: *ApJ* 679.1, pp. 301–309. doi: [10.1086/587156](https://doi.org/10.1086/587156).
- Buisson, D. J. K., Lohfink, A. M., et al. (Jan. 2017). ‘Ultraviolet and X-ray variability of active galactic nuclei with Swift’. In: *MNRAS* 464.3, pp. 3194–3218. doi: [10.1093/mnras/stw2486](https://doi.org/10.1093/mnras/stw2486).
- Burhanudin, U. F., Maund, J. R., et al. (Aug. 2021). ‘Light-curve classification with recurrent neural networks for GOTO: dealing with imbalanced data’. In: *MNRAS* 505.3, pp. 4345–4361. doi: [10.1093/mnras/stab1545](https://doi.org/10.1093/mnras/stab1545).
- Capetti, A., Brienza, M., et al. (Oct. 2020). ‘The LOFAR view of FR 0 radio galaxies’. In: *A&A* 642, A107, A107. doi: [10.1051/0004-6361/202038671](https://doi.org/10.1051/0004-6361/202038671).
- Carroll, B. W. and Ostlie, D. A. (2017). *An Introduction to Modern Astrophysics*. 2nd ed. Cambridge University Press. doi: [10.1017/9781108380980](https://doi.org/10.1017/9781108380980).
- Caruana, R. and Niculescu-Mizil, A. (2006). ‘An Empirical Comparison of Supervised Learning Algorithms’. In: *Proceedings of the 23rd International Conference on Machine Learning*. ICML ’06. Pittsburgh,

REFERENCES

- Pennsylvania, USA: Association for Computing Machinery, pp. 161–168. ISBN: 1595933832. doi: [10.1145/1143844.1143865](https://doi.org/10.1145/1143844.1143865).
- Carvajal, R., Bauer, F. E., et al. (Jan. 2020). ‘The ALMA Frontier Fields Survey. V. ALMA Stacking of Lyman-Break Galaxies in Abell 2744, Abell 370, Abell S1063, MACSJ0416.1-2403 and MACSJ1149.5+2223’. In: A&A 633, A160, A160. doi: [10.1051/0004-6361/201936260](https://doi.org/10.1051/0004-6361/201936260).
- Carvajal, R., Matute, I., et al. (Nov. 2023a). ‘Selection of powerful radio galaxies with machine learning’. In: A&A 679, A101, A101. doi: [10.1051/0004-6361/202245770](https://doi.org/10.1051/0004-6361/202245770).
- Carvajal, R., Matute, I., et al. (Oct. 2021). ‘Exploring New Redshift Indicators for Radio-Powerful AGN’. In: Galaxies 9.4, p. 86. doi: [10.3390/galaxies9040086](https://doi.org/10.3390/galaxies9040086).
- Carvajal, R., Matute, I., et al. (Dec. 2023b). *Selection of powerful radio galaxies with machine learning*. doi: [10.5281/zenodo.10220009](https://doi.org/10.5281/zenodo.10220009).
- Casalicchio, G., Molnar, C., and Bischl, B. (2019). ‘Visualizing the Feature Importance for Black Box Models’. In: *Machine Learning and Knowledge Discovery in Databases*. Ed. by M. Berlingero, F. Bonchi, et al. Cham: Springer International Publishing, pp. 655–670. ISBN: 978-3-030-10925-7.
- Ceccarelli, L., Duplancic, F., and Garcia Lambas, D. (Jan. 2022). ‘The impact of void environment on AGN’. In: MNRAS 509.2, pp. 1805–1819. doi: [10.1093/mnras/stab2902](https://doi.org/10.1093/mnras/stab2902).
- Chambers, K. C., Magnier, E. A., et al. (Dec. 2016). ‘The Pan-STARRS1 Surveys’. In: *arXiv e-prints*, arXiv:1612.05560.
- Champagne, J. B., Casey, C. M., et al. (Aug. 2023). ‘A Mixture of LBG Overdensities in the Fields of Three 6 < z < 7 Quasars: Implications for the Robustness of Photometric Selection’. In: ApJ 952.2, 99, p. 99. doi: [10.3847/1538-4357/acda8d](https://doi.org/10.3847/1538-4357/acda8d).
- Chattopadhyay, A. K. (2017). ‘Incomplete Data in Astrostatistics’. In: *Wiley StatsRef: Statistics Reference Online*. American Cancer Society, pp. 1–12. ISBN: 9781118445112. doi: <https://doi.org/10.1002/9781118445112.stat07942>.
- Chaves-Montero, J., Bonoli, S., et al. (Dec. 2017). ‘ELDAR, a new method to identify AGN in multi-filter surveys: the ALHAMBRA test case’. In: MNRAS 472.2, pp. 2085–2106. doi: [10.1093/mnras/stx2054](https://doi.org/10.1093/mnras/stx2054).
- Chen, C. . J., Brandt, W. N., et al. (Mar. 2017). ‘Hard X-Ray-selected AGNs in Low-mass Galaxies from the NuSTAR Serendipitous Survey’. In: ApJ 837.1, 48, p. 48. doi: [10.3847/1538-4357/aa5d5b](https://doi.org/10.3847/1538-4357/aa5d5b).
- Chen, H., Garrett, M. A., et al. (June 2020). ‘Searching for obscured AGN in z ~ 2 submillimetre galaxies’. In: A&A 638, A113, A113. doi: [10.1051/0004-6361/201937162](https://doi.org/10.1051/0004-6361/201937162).
- Chen, T. and Guestrin, C. (2016). ‘XGBoost: A Scalable Tree Boosting System’. In: *Proceedings of the 22nd ACM SIGKDD International Conference on Knowledge Discovery and Data Mining*. KDD ’16. San Francisco, California, USA: ACM, pp. 785–794. ISBN: 978-1-4503-4232-2. doi: [10.1145/2939672.2939785](https://doi.org/10.1145/2939672.2939785).
- Ciardi, B. and Ferrara, A. (Feb. 2005). ‘The First Cosmic Structures and Their Effects’. In: Space Sci. Rev. 116.3-4, pp. 625–705. doi: [10.1007/s11214-005-3592-0](https://doi.org/10.1007/s11214-005-3592-0).
- Cid Fernandes, R., Stasińska, G., et al. (Apr. 2010). ‘Alternative diagnostic diagrams and the ‘forgotten’ population of weak line galaxies in the SDSS’. In: MNRAS 403.2, pp. 1036–1053. doi: [10.1111/j.1365-2966.2009.16185.x](https://doi.org/10.1111/j.1365-2966.2009.16185.x).

- Cid Fernandes, R., Stasińska, G., et al. (May 2011). ‘A comprehensive classification of galaxies in the Sloan Digital Sky Survey: how to tell true from fake AGN?’ In: MNRAS 413.3, pp. 1687–1699. doi: [10.1111/j.1365-2966.2011.18244.x](https://doi.org/10.1111/j.1365-2966.2011.18244.x).
- Clarke, A. O., Scaife, A. M. M., et al. (July 2020). ‘Identifying galaxies, quasars, and stars with machine learning: A new catalogue of classifications for 111 million SDSS sources without spectra’. In: A&A 639, A84, A84. doi: [10.1051/0004-6361/201936770](https://doi.org/10.1051/0004-6361/201936770).
- Clopper, C. J. and Pearson, E. S. (Dec. 1934). ‘The Use of Confidence or Fiducial Limits Illustrated in the Case of the Binomial’. In: *Biometrika* 26.4, pp. 404–413. ISSN: 0006-3444. doi: [10.1093/biomet/26.4.404](https://doi.org/10.1093/biomet/26.4.404).
- Cochrane, R. K., Kondapally, R., et al. (Aug. 2023). ‘The LOFAR Two-metre Sky Survey: the radio view of the cosmic star formation history’. In: MNRAS 523.4, pp. 6082–6102. doi: [10.1093/mnras/stad1602](https://doi.org/10.1093/mnras/stad1602).
- Coleman, B., Kirkpatrick, A., et al. (Sept. 2022). ‘Accretion history of AGN: Estimating the host galaxy properties in X-ray luminous AGN from $z = 0\text{--}3$ ’. In: MNRAS 515.1, pp. 82–98. doi: [10.1093/mnras/stac1679](https://doi.org/10.1093/mnras/stac1679).
- Condon, J. J. (Jan. 1992). ‘Radio emission from normal galaxies.’ In: ARA&A 30, pp. 575–611. doi: [10.1146/annurev.aa.30.090192.003043](https://doi.org/10.1146/annurev.aa.30.090192.003043).
- Condon, J. J., Cotton, W. D., and Broderick, J. J. (Aug. 2002). ‘Radio Sources and Star Formation in the Local Universe’. In: AJ 124.2, pp. 675–689. doi: [10.1086/341650](https://doi.org/10.1086/341650).
- Cortes, C. and Vapnik, V. (Sept. 1995). ‘Support-vector networks’. In: *Machine Learning* 20.3, pp. 273–297. ISSN: 1573-0565. doi: [10.1007/BF00994018](https://doi.org/10.1007/BF00994018).
- Costa-Climent, R., Haftor, D. M., and Staniewski, M. W. (2023). ‘Using machine learning to create and capture value in the business models of small and medium-sized enterprises’. In: *International Journal of Information Management* 73, p. 102637. ISSN: 0268-4012. doi: <https://doi.org/10.1016/j.ijinfomgt.2023.102637>.
- Cover, T. and Hart, P. (1967). ‘Nearest neighbor pattern classification’. In: *IEEE Transactions on Information Theory* 13.1, pp. 21–27. doi: [10.1109/TIT.1967.1053964](https://doi.org/10.1109/TIT.1967.1053964).
- Cramér, H. (1946). *Mathematical methods of statistics*. English. Princeton University Press Princeton, xvi, 575 p.
- Cranmer, M. (May 2023). ‘Interpretable Machine Learning for Science with PySR and SymbolicRegression.jl’. In: *arXiv e-prints*, arXiv:2305.01582, arXiv:2305.01582. doi: [10.48550/arXiv.2305.01582](https://doi.org/10.48550/arXiv.2305.01582).
- Cranmer, M., Sanchez-Gonzalez, A., et al. (June 2020). ‘Discovering Symbolic Models from Deep Learning with Inductive Biases’. In: *arXiv e-prints*, arXiv:2006.11287.
- Croom, S. M., Richards, G. T., et al. (Nov. 2009). ‘The 2dF-SDSS LRG and QSO survey: the QSO luminosity function at $0.4 < z < 2.6$ ’. In: MNRAS 399.4, pp. 1755–1772. doi: [10.1111/j.1365-2966.2009.15398.x](https://doi.org/10.1111/j.1365-2966.2009.15398.x).
- Cunha, P. A. C. and Humphrey, A. (Oct. 2022). ‘Photometric redshift-aided classification using ensemble learning’. In: A&A 666, A87, A87. doi: [10.1051/0004-6361/202243135](https://doi.org/10.1051/0004-6361/202243135).
- Curran, S. J. (May 2022). ‘Quasar photometric redshifts from incomplete data using deep learning’. In: MNRAS 512.2, pp. 2099–2109. doi: [10.1093/mnras/stac660](https://doi.org/10.1093/mnras/stac660).
- Curran, S. J., Moss, J. P., and Perrott, Y. C. (July 2022). ‘Redshifts of radio sources in the Million Quasars Catalogue from machine learning’. In: MNRAS 514.1, pp. 1–19. doi: [10.1093/mnras/stac1333](https://doi.org/10.1093/mnras/stac1333).
- Cutri, R. M., Skrutskie, M. F., et al. (2003a). *2MASS All Sky Catalog of point sources*.

REFERENCES

- Cutri, R. M., Skrutskie, M. F., et al. (June 2003b). ‘VizieR Online Data Catalog: 2MASS All-Sky Catalog of Point Sources (Cutri+ 2003)’. In: *VizieR Online Data Catalog*, II/246, pp. II/246.
- Cutri, R. M., Wright, E. L., et al. (Nov. 2013). *Explanatory Supplement to the AllWISE Data Release Products*.
- Dahlen, T., Mobasher, B., et al. (Oct. 2013). ‘A Critical Assessment of Photometric Redshift Methods: A CANDELS Investigation’. In: *ApJ* 775.2, 93, p. 93. doi: [10.1088/0004-637X/775/2/93](https://doi.org/10.1088/0004-637X/775/2/93).
- Dai, Y. S., Wilkes, B. J., et al. (Aug. 2018). ‘Is there a relationship between AGN and star formationin IR-bright AGNs?’ In: *MNRAS* 478.3, pp. 4238–4254. doi: [10.1093/mnras/sty1341](https://doi.org/10.1093/mnras/sty1341).
- Davidson, K. and Netzer, H. (Oct. 1979). ‘The emission lines of quasars and similar objects’. In: *Reviews of Modern Physics* 51.4, pp. 715–766. doi: [10.1103/RevModPhys.51.715](https://doi.org/10.1103/RevModPhys.51.715).
- Davies, L. J. M., Robotham, A. S. G., et al. (Oct. 2018a). ‘Deep Extragalactic VIable Legacy Survey (DEVILS): motivation,design, and target catalogue’. In: *MNRAS* 480.1, pp. 768–799. doi: [10.1093/mnras/sty1553](https://doi.org/10.1093/mnras/sty1553).
- Davies, T. M., Marshall, J. C., and Hazelton, M. L. (2018b). ‘Tutorial on kernel estimation of continuous spatial and spatiotemporal relative risk’. In: *Statistics in Medicine* 37.7, pp. 1191–1221. doi: <https://doi.org/10.1002/sim.7577>.
- de Ruiter, H. R., Willis, A. G., and Arp, H. C. (May 1977). ‘A Westerbork 1415 MHz survey of background radio sources. II. Optical identifications with deep IIIa-J plates.’ In: *A&AS* 28, pp. 211–293.
- de Veny, J. B., Osborn, W. H., and Janes, K. (Oct. 1971). ‘A Catalogue of Quasars’. In: *PASP* 83.495, p. 611. doi: [10.1086/129187](https://doi.org/10.1086/129187).
- Delhaize, J., Heywood, I., et al. (Mar. 2021). ‘MIGHTEE: are giant radio galaxies more common than we thought?’ In: *MNRAS* 501.3, pp. 3833–3845. doi: [10.1093/mnras/staa3837](https://doi.org/10.1093/mnras/staa3837).
- Delhaize, J., Smolčić, V., et al. (June 2017). ‘The VLA-COSMOS 3 GHz Large Project: The infrared-radio correlation of star-forming galaxies and AGN to $z \lesssim 6$ ’. In: *A&A* 602, A4, A4. doi: [10.1051/0004-6361/201629430](https://doi.org/10.1051/0004-6361/201629430).
- Desai, S. and Strachan, A. (June 2021). ‘Parsimonious neural networks learn interpretable physical laws’. In: *Scientific Reports* 11.1, p. 12761. ISSN: 2045-2322. doi: [10.1038/s41598-021-92278-w](https://doi.org/10.1038/s41598-021-92278-w).
- Dey, A., Schlegel, D. J., et al. (May 2019). ‘Overview of the DESI Legacy Imaging Surveys’. In: *AJ* 157.5, 168, p. 168. doi: [10.3847/1538-3881/ab089d](https://doi.org/10.3847/1538-3881/ab089d).
- Dey, B., Andrews, B. H., et al. (Oct. 2022). ‘Photometric redshifts from SDSS images with an interpretable deep capsule network’. In: *MNRAS* 515.4, pp. 5285–5305. doi: [10.1093/mnras/stac2105](https://doi.org/10.1093/mnras/stac2105).
- Dice, L. R. (1945). ‘Measures of the Amount of Ecologic Association Between Species’. In: *Ecology* 26.3, pp. 297–302. ISSN: 00129658, 19399170. URL: <http://www.jstor.org/stable/1932409> (visited on 04/10/2022).
- Dobbels, W. and Baes, M. (Nov. 2021). ‘Predicting far-infrared maps of galaxies via machine learning techniques’. In: *A&A* 655, A34, A34. doi: [10.1051/0004-6361/202142084](https://doi.org/10.1051/0004-6361/202142084).
- Donley, J. L., Koekemoer, A. M., et al. (Apr. 2012). ‘Identifying Luminous Active Galactic Nuclei in Deep Surveys: Revised IRAC Selection Criteria’. In: *ApJ* 748.2, 142, p. 142. doi: [10.1088/0004-637X/748/2/142](https://doi.org/10.1088/0004-637X/748/2/142).
- Donley, J. L., Rieke, G. H., et al. (Nov. 2005). ‘Unveiling a Population of AGNs Not Detected in X-Rays’. In: *ApJ* 634.1, pp. 169–182. doi: [10.1086/491668](https://doi.org/10.1086/491668).

DRAFT - February 21, 2024 - DRAFT

- Dorogush, A. V., Ershov, V., and Gulin, A. (2018). ‘CatBoost: gradient boosting with categorical features support’. In: *CoRR* abs/1810.11363. URL: <http://arxiv.org/abs/1810.11363>.
- Drake, A. J., Graham, M. J., et al. (July 2014). ‘The Catalina Surveys Periodic Variable Star Catalog’. In: *ApJS* 213.1, 9, p. 9. doi: [10.1088/0067-0049/213/1/9](https://doi.org/10.1088/0067-0049/213/1/9).
- Driver, S. P., Hill, D. T., et al. (May 2011). ‘Galaxy and Mass Assembly (GAMA): survey diagnostics and core data release’. In: *MNRAS* 413.2, pp. 971–995. doi: [10.1111/j.1365-2966.2010.18188.x](https://doi.org/10.1111/j.1365-2966.2010.18188.x).
- Duboue, P. (2020). *The Art of Feature Engineering: Essentials for Machine Learning*. Cambridge University Press. ISBN: 9781108709385. URL: https://books.google.pt/books?id=%5C_BzhDwAAQBAJ.
- Duncan, K. J., Kondapally, R., et al. (Apr. 2021). ‘The LOFAR Two-meter Sky Survey: Deep Fields Data Release 1. IV. Photometric redshifts and stellar masses’. In: *A&A* 648, A4, A4. doi: [10.1051/0004-6361/202038809](https://doi.org/10.1051/0004-6361/202038809).
- Duncan, K. J., Sabater, J., et al. (Feb. 2019). ‘The LOFAR Two-metre Sky Survey. IV. First Data Release: Photometric redshifts and rest-frame magnitudes’. In: *A&A* 622, A3, A3. doi: [10.1051/0004-6361/201833562](https://doi.org/10.1051/0004-6361/201833562).
- Eddington, A. S. (Mar. 1913). ‘On a formula for correcting statistics for the effects of a known error of observation’. In: *MNRAS* 73, pp. 359–360. doi: [10.1093/mnras/73.5.359](https://doi.org/10.1093/mnras/73.5.359).
- Eddington A. S., S. (Mar. 1940). ‘The correction of statistics for accidental error’. In: *MNRAS* 100, p. 354. doi: [10.1093/mnras/100.5.354](https://doi.org/10.1093/mnras/100.5.354).
- Ellis, R. S., Colless, M., et al. (May 1996). ‘Autofib Redshift Survey - I. Evolution of the galaxy luminosity function’. In: *MNRAS* 280.1, pp. 235–251. doi: [10.1093/mnras/280.1.235](https://doi.org/10.1093/mnras/280.1.235).
- Enke, H., Partl, A., et al. (Nov. 2012). ‘Handling Big Data in Astronomy and Astrophysics: Rich Structured Queries on Replicated Cloud Data with XtreemFS’. In: *Datenbank-Spektrum* 12.3, pp. 173–181. ISSN: 1610-1995. doi: [10.1007/s13222-012-0099-1](https://doi.org/10.1007/s13222-012-0099-1).
- Euclid Collaboration, Bisigello, L., et al. (Apr. 2023a). ‘Euclid preparation - XXIII. Derivation of galaxy physical properties with deep machine learning using mock fluxes and H-band images’. In: *MNRAS* 520.3, pp. 3529–3548. doi: [10.1093/mnras/stac3810](https://doi.org/10.1093/mnras/stac3810).
- Euclid Collaboration, Humphrey, A., et al. (Mar. 2023b). ‘Euclid preparation. XXII. Selection of quiescent galaxies from mock photometry using machine learning’. In: *A&A* 671, A99, A99. doi: [10.1051/0004-6361/202244307](https://doi.org/10.1051/0004-6361/202244307).
- Euclid Collaboration, Scaramella, R., et al. (June 2022). ‘Euclid preparation. I. The Euclid Wide Survey’. In: *A&A* 662, A112, A112. doi: [10.1051/0004-6361/202141938](https://doi.org/10.1051/0004-6361/202141938).
- Fan, X., Banados, E., and Simcoe, R. A. (2023). ‘Quasars and the Intergalactic Medium at Cosmic Dawn’. In: *ARA&A* 61. doi: [10.1146/annurev-astro-052920-102455](https://doi.org/10.1146/annurev-astro-052920-102455).
- Faucher-Giguère, C.-A., Lidz, A., et al. (Oct. 2009). ‘A New Calculation of the Ionizing Background Spectrum and the Effects of He II Reionization’. In: *ApJ* 703.2, pp. 1416–1443. doi: [10.1088/0004-637X/703/2/1416](https://doi.org/10.1088/0004-637X/703/2/1416).
- Ferrarese, L. and Merritt, D. (Aug. 2000). ‘A Fundamental Relation between Supermassive Black Holes and Their Host Galaxies’. In: *ApJ* 539.1, pp. L9–L12. doi: [10.1086/312838](https://doi.org/10.1086/312838).
- Flesch, E. W. (Mar. 2015). ‘The Half Million Quasars (HMQ) Catalogue’. In: *PASA* 32, e010, e010. doi: [10.1017/pasa.2015.10](https://doi.org/10.1017/pasa.2015.10).

REFERENCES

- Flesch, E. W. (Dec. 2019). ‘The Million Quasars (Milliquas) Catalogue, v6.4’. In: *arXiv e-prints*, arXiv:1912.05614, arXiv:1912.05614. doi: [10.48550/arXiv.1912.05614](https://doi.org/10.48550/arXiv.1912.05614).
- Flesch, E. W. (May 2021). ‘The Million Quasars (Milliquas) v7.2 Catalogue, now with VLASS associations. The inclusion of SDSS-DR16Q quasars is detailed’. In: *arXiv e-prints*, arXiv:2105.12985, arXiv:2105.12985.
- (Dec. 2023). ‘The Million Quasars (Milliquas) Catalogue, v8’. In: *The Open Journal of Astrophysics* 6, 49, p. 49. doi: [10.21105/astro.2308.01505](https://doi.org/10.21105/astro.2308.01505).
- Flewelling, H. A., Magnier, E. A., et al. (Nov. 2020). ‘The Pan-STARRS1 Database and Data Products’. In: *ApJS* 251.1, 7, p. 7. doi: [10.3847/1538-4365/abb82d](https://doi.org/10.3847/1538-4365/abb82d).
- Frederiksen, T. F., Graur, O., et al. (Mar. 2014). ‘Spectroscopic identification of a redshift 1.55 supernova host galaxy from the Subaru Deep Field Supernova Survey’. In: *A&A* 563, A140, A140. doi: [10.1051/0004-6361/201321795](https://doi.org/10.1051/0004-6361/201321795).
- Freund, Y. and Schapire, R. E. (1996). ‘Experiments with a New Boosting Algorithm’. In: *Proceedings of the Thirteenth International Conference on International Conference on Machine Learning*. ICML’96. Bari, Italy: Morgan Kaufmann Publishers Inc., pp. 148–156. ISBN: 1558604197.
- Friedman, J. H. (2001). ‘Greedy function approximation: A gradient boosting machine.’ In: *The Annals of Statistics* 29.5, pp. 1189–1232. doi: [10.1214/aos/1013203451](https://doi.org/10.1214/aos/1013203451).
- (2002). ‘Stochastic gradient boosting’. In: *Computational Statistics & Data Analysis* 38.4. Nonlinear Methods and Data Mining, pp. 367–378. ISSN: 0167-9473. doi: [https://doi.org/10.1016/S0167-9473\(01\)00065-2](https://doi.org/10.1016/S0167-9473(01)00065-2).
- Fukugita, M. and Kawasaki, M. (Aug. 1994). ‘Reionization during Hierarchical Clustering in a Universe Dominated by Cold Dark Matter’. In: *MNRAS* 269, p. 563. doi: [10.1093/mnras/269.3.563](https://doi.org/10.1093/mnras/269.3.563).
- Gaia Collaboration, Bailer-Jones, C. A. L., et al. (June 2023a). ‘Gaia Data Release 3. The extragalactic content’. In: *A&A* 674, A41, A41. doi: [10.1051/0004-6361/202243232](https://doi.org/10.1051/0004-6361/202243232).
- Gaia Collaboration, Prusti, T., et al. (Nov. 2016). ‘The Gaia mission’. In: *A&A* 595, A1, A1. doi: [10.1051/0004-6361/201629272](https://doi.org/10.1051/0004-6361/201629272).
- Gaia Collaboration, Vallenari, A., et al. (June 2023b). ‘Gaia Data Release 3. Summary of the content and survey properties’. In: *A&A* 674, A1, A1. doi: [10.1051/0004-6361/202243940](https://doi.org/10.1051/0004-6361/202243940).
- Galametz, A., Grazian, A., et al. (June 2013). ‘CANDELS Multiwavelength Catalogs: Source Identification and Photometry in the CANDELS UKIDSS Ultra-deep Survey Field’. In: *ApJS* 206.2, 10, p. 10. doi: [10.1088/0067-0049/206/2/10](https://doi.org/10.1088/0067-0049/206/2/10).
- Garcia-Piquer, A., Morales, J. C., et al. (Aug. 2017). ‘Efficient scheduling of astronomical observations. Application to the CARMENES radial-velocity survey’. In: *A&A* 604, A87, A87. doi: [10.1051/0004-6361/201628577](https://doi.org/10.1051/0004-6361/201628577).
- Garilli, B., Fumana, M., et al. (July 2010). ‘EZ: A Tool For Automatic Redshift Measurement’. In: *PASP* 122.893, p. 827. doi: [10.1086/654903](https://doi.org/10.1086/654903).
- Garofalo, M., Botta, A., and Ventre, G. (June 2017). ‘Astrophysics and Big Data: Challenges, Methods, and Tools’. In: *Astroinformatics*. Ed. by M. Brescia, S. G. Djorgovski, et al. Vol. 325, pp. 345–348. doi: [10.1017/S1743921316012813](https://doi.org/10.1017/S1743921316012813).

- Gebhardt, K., Bender, R., et al. (Aug. 2000). ‘A Relationship between Nuclear Black Hole Mass and Galaxy Velocity Dispersion’. In: *ApJ* 539.1, pp. L13–L16. doi: [10.1086/312840](https://doi.org/10.1086/312840).
- Gehrels, N. (Apr. 1986). ‘Confidence Limits for Small Numbers of Events in Astrophysical Data’. In: *ApJ* 303, p. 336. doi: [10.1086/164079](https://doi.org/10.1086/164079).
- Gerwin, D. (1974). ‘Information processing, data inferences, and scientific generalization’. In: *Behavioral Science* 19.5, pp. 314–325. doi: <https://doi.org/10.1002/bs.3830190504>.
- Getachew-Woreta, T., Pović, M., et al. (July 2022). ‘Effect of AGN on the morphological properties of their host galaxies in the local Universe’. In: *MNRAS* 514.1, pp. 607–620. doi: [10.1093/mnras/stac851](https://doi.org/10.1093/mnras/stac851).
- Geurts, P., Ernst, D., and Wehenkel, L. (Apr. 2006). ‘Extremely randomized trees’. In: *Machine Learning* 63.1, pp. 3–42. issn: 1573-0565. doi: [10.1007/s10994-006-6226-1](https://doi.org/10.1007/s10994-006-6226-1).
- Giles, D. and Walkowicz, L. (Mar. 2019). ‘Systematic serendipity: a test of unsupervised machine learning as a method for anomaly detection’. In: *MNRAS* 484.1, pp. 834–849. doi: [10.1093/mnras/sty3461](https://doi.org/10.1093/mnras/sty3461).
- Giveon, U., Maoz, D., et al. (July 1999). ‘Long-term optical variability properties of the Palomar-Green quasars’. In: *MNRAS* 306.3, pp. 637–654. doi: [10.1046/j.1365-8711.1999.02556.x](https://doi.org/10.1046/j.1365-8711.1999.02556.x).
- Glahn, H. R. and Jorgensen, D. L. (1970). ‘Climatological Aspects of the Brier p-score’. In: *Monthly Weather Review* 98.2, pp. 136–141. doi: [10.1175/1520-0493\(1970\)098<0136:CAOTBP>2.3.CO;2](https://doi.org/10.1175/1520-0493(1970)098<0136:CAOTBP>2.3.CO;2).
- Glazebrook, K., Offer, A. R., and Deeley, K. (Jan. 1998). ‘Automatic Redshift Determination by Use of Principal Component Analysis. I. Fundamentals’. In: *ApJ* 492.1, pp. 98–109. doi: [10.1086/305039](https://doi.org/10.1086/305039).
- Glikman, E., Langgin, R., et al. (July 2023). ‘A Candidate Dual QSO at Cosmic Noon’. In: *ApJ* 951.1, L18, p. L18. doi: [10.3847/2041-8213/acda2f](https://doi.org/10.3847/2041-8213/acda2f).
- Goebel, R., Chander, A., et al. (2018). ‘Explainable ai: the new 42?’ In: *International cross-domain conference for machine learning and knowledge extraction*. Springer. Springer International Publishing, pp. 295–303. ISBN: 978-3-319-99740-7.
- Gordon, Y. A., Boyce, M. M., et al. (Oct. 2020). ‘A Catalog of Very Large Array Sky Survey Epoch 1 Quick Look Components, Sources, and Host Identifications’. In: *Research Notes of the American Astronomical Society* 4.10, 175, p. 175. doi: [10.3847/2515-5172/abbe23](https://doi.org/10.3847/2515-5172/abbe23).
- Goulding, A. D., Zakamska, N. L., et al. (Mar. 2018). ‘High-redshift Extremely Red Quasars in X-Rays’. In: *ApJ* 856.1, 4, p. 4. doi: [10.3847/1538-4357/aab040](https://doi.org/10.3847/1538-4357/aab040).
- Guglielmetti, F., Arras, P., et al. (Dec. 2022). ‘Bayesian and Machine Learning Methods in the Big Data Era for Astronomical Imaging’. In: *Physical Sciences Forum*. Vol. 5. Physical Sciences Forum, 50, p. 50. doi: [10.3390/psf2022005050](https://doi.org/10.3390/psf2022005050).
- Gültekin, K., Richstone, D. O., et al. (June 2009). ‘The M- σ and M-L Relations in Galactic Bulges, and Determinations of Their Intrinsic Scatter’. In: *ApJ* 698.1, pp. 198–221. doi: [10.1088/0004-637X/698/1/198](https://doi.org/10.1088/0004-637X/698/1/198).
- Haardt, F. and Madau, P. (Feb. 2012). ‘Radiative Transfer in a Clumpy Universe. IV. New Synthesis Models of the Cosmic UV/X-Ray Background’. In: *ApJ* 746.2, 125, p. 125. doi: [10.1088/0004-637X/746/2/125](https://doi.org/10.1088/0004-637X/746/2/125).
- Habouzit, M., Onoue, M., et al. (Apr. 2022). ‘Co-evolution of massive black holes and their host galaxies at high redshift: discrepancies from six cosmological simulations and the key role of JWST’. In: *MNRAS* 511.3, pp. 3751–3767. doi: [10.1093/mnras/stac225](https://doi.org/10.1093/mnras/stac225).

REFERENCES

- Haiman, Z. and Loeb, A. (July 1997). ‘Signatures of Stellar Reionization of the Universe’. In: ApJ 483.1, pp. 21–37. doi: [10.1086/304238](https://doi.org/10.1086/304238).
- Hales, C. A., Murphy, T., et al. (Aug. 2012a). *BLOBCAT: Software to Catalog Blobs*. Astrophysics Source Code Library, record ascl:1208.009.
- (Sept. 2012b). ‘BLOBCAT: software to catalogue flood-filled blobs in radio images of total intensity and linear polarization’. In: MNRAS 425.2, pp. 979–996. doi: [10.1111/j.1365-2966.2012.21373.x](https://doi.org/10.1111/j.1365-2966.2012.21373.x).
- Hancock, P. J., Murphy, T., et al. (May 2012). ‘Compact continuum source finding for next generation radio surveys’. In: MNRAS 422.2, pp. 1812–1824. doi: [10.1111/j.1365-2966.2012.20768.x](https://doi.org/10.1111/j.1365-2966.2012.20768.x).
- Hancock, P. J., Trott, C. M., and Hurley-Walker, N. (Mar. 2018). ‘Source Finding in the Era of the SKA (Precursors): Aegean 2.0’. In: PASA 35, e011, e011. doi: [10.1017/pasa.2018.3](https://doi.org/10.1017/pasa.2018.3).
- Hardcastle, M. J., Horton, M. A., et al. (Oct. 2023). ‘The LOFAR Two-Metre Sky Survey. VI. Optical identifications for the second data release’. In: A&A 678, A151, A151. doi: [10.1051/0004-6361/202347333](https://doi.org/10.1051/0004-6361/202347333).
- Häring, N. and Rix, H.-W. (Apr. 2004). ‘On the Black Hole Mass-Bulge Mass Relation’. In: ApJ 604.2, pp. L89–L92. doi: [10.1086/383567](https://doi.org/10.1086/383567).
- Head, T., Kumar, M., et al. (Oct. 2021). *scikit-optimize/scikit-optimize*. Version v0.9.0. doi: [10.5281/zenodo.5565057](https://doi.org/10.5281/zenodo.5565057).
- Heckman, T. M. (July 1980). ‘An Optical and Radio Survey of the Nuclei of Bright Galaxies - Activity in the Normal Galactic Nuclei’. In: A&A 87, p. 152.
- Heckman, T. M. and Best, P. N. (Aug. 2014). ‘The Coevolution of Galaxies and Supermassive Black Holes: Insights from Surveys of the Contemporary Universe’. In: ARA&A 52, pp. 589–660. doi: [10.1146/annurev-astro-081913-035722](https://doi.org/10.1146/annurev-astro-081913-035722).
- Helfand, D. J., White, R. L., and Becker, R. H. (Mar. 2015). ‘The Last of FIRST: The Final Catalog and Source Identifications’. In: ApJ 801.1, 26, p. 26. doi: [10.1088/0004-637X/801/1/26](https://doi.org/10.1088/0004-637X/801/1/26).
- Helou, G., Soifer, B. T., and Rowan-Robinson, M. (Nov. 1985). ‘Thermal infrared and nonthermal radio : remarkable correlation in disks of galaxies.’ In: ApJ 298, pp. L7–L11. doi: [10.1086/184556](https://doi.org/10.1086/184556).
- Hernán-Caballero, A., Varela, J., et al. (Oct. 2021). ‘The miniJPAS survey: Photometric redshift catalogue’. In: A&A 654, A101, A101. doi: [10.1051/0004-6361/202141236](https://doi.org/10.1051/0004-6361/202141236).
- Hickox, R. C. and Alexander, D. M. (Sept. 2018). ‘Obscured Active Galactic Nuclei’. In: ARA&A 56, pp. 625–671. doi: [10.1146/annurev-astro-081817-051803](https://doi.org/10.1146/annurev-astro-081817-051803).
- Hildebrand, R. H. (Sept. 1983). ‘The determination of cloud masses and dust characteristics from submillimetre thermal emission.’ In: QJRAS 24, pp. 267–282.
- Hildebrandt, H., Arnouts, S., et al. (Nov. 2010). ‘PHAT: PHoto-z Accuracy Testing’. In: A&A 523, A31, A31. doi: [10.1051/0004-6361/201014885](https://doi.org/10.1051/0004-6361/201014885).
- Hill, G. J., Gebhardt, K., et al. (Oct. 2008). ‘The Hobby-Eberly Telescope Dark Energy Experiment (HETDEX): Description and Early Pilot Survey Results’. In: *Panoramic Views of Galaxy Formation and Evolution*. Ed. by T. Kodama, T. Yamada, and K. Aoki. Vol. 399. Astronomical Society of the Pacific Conference Series, p. 115.

- Hoaglin, D., Mosteller, F., et al. (1983). *Understanding Robust and Exploratory Data Analysis*. Wiley Series in Probability and Statistics: Probability and Statistics Section Series. John Wiley & Sons. ISBN: 9780471097778. URL: <https://books.google.pt/books?id=FRnvAAAAQBAJ>.
- Hodge, J. A., Becker, R. H., et al. (July 2011). ‘High-resolution Very Large Array Imaging of Sloan Digital Sky Survey Stripe 82 at 1.4 GHz’. In: AJ 142.1, 3, p. 3. doi: [10.1088/0004-6256/142/1/3](https://doi.org/10.1088/0004-6256/142/1/3).
- Hogg, D. W. (May 1999). ‘Distance measures in cosmology’. In: *arXiv e-prints*, astro-ph/9905116, astro-ph/9905116. doi: [10.48550/arXiv.astro-ph/9905116](https://doi.org/10.48550/arXiv.astro-ph/9905116).
- Hoyle, B., Gruen, D., et al. (July 2018). ‘Dark Energy Survey Year 1 Results: redshift distributions of the weak-lensing source galaxies’. In: MNRAS 478.1, pp. 592–610. doi: [10.1093/mnras/sty957](https://doi.org/10.1093/mnras/sty957).
- Huertas-Company, M. and Lanusse, F. (Jan. 2023). ‘The Dawes Review 10: The impact of deep learning for the analysis of galaxy surveys’. In: PASA 40, e001, e001. doi: [10.1017/pasa.2022.55](https://doi.org/10.1017/pasa.2022.55).
- Hunter, J. D. (2007). ‘Matplotlib: A 2D graphics environment’. In: *Computing in Science & Engineering* 9.3, pp. 90–95. doi: [10.1109/MCSE.2007.55](https://doi.org/10.1109/MCSE.2007.55).
- Huterer, D., Takada, M., et al. (Feb. 2006). ‘Systematic errors in future weak-lensing surveys: requirements and prospects for self-calibration’. In: MNRAS 366.1, pp. 101–114. doi: [10.1111/j.1365-2966.2005.09782.x](https://doi.org/10.1111/j.1365-2966.2005.09782.x).
- İkiz, T., Peletier, R. F., et al. (Aug. 2020). ‘Infrared-detected AGNs in the local Universe’. In: A&A 640, A68, A68. doi: [10.1051/0004-6361/201935971](https://doi.org/10.1051/0004-6361/201935971).
- Ilbert, O., Arnouts, S., et al. (Oct. 2006). ‘Accurate photometric redshifts for the CFHT legacy survey calibrated using the VIMOS VLT deep survey’. In: A&A 457.3, pp. 841–856. doi: [10.1051/0004-6361:20065138](https://doi.org/10.1051/0004-6361:20065138).
- Ilbert, O., Capak, P., et al. (Jan. 2009). ‘Cosmos Photometric Redshifts with 30-Bands for 2-deg²’. In: ApJ 690.2, pp. 1236–1249. doi: [10.1088/0004-637X/690/2/1236](https://doi.org/10.1088/0004-637X/690/2/1236).
- Inayoshi, K., Visbal, E., and Haiman, Z. (Aug. 2020). ‘The Assembly of the First Massive Black Holes’. In: ARA&A 58, pp. 27–97. doi: [10.1146/annurev-astro-120419-014455](https://doi.org/10.1146/annurev-astro-120419-014455).
- IPCC (2022). *Climate Change 2022: Mitigation of Climate Change. Contribution of Working Group III to the Sixth Assessment Report of the Intergovernmental Panel on Climate Change*. Ed. by P. Shukla, J. Skea, et al. Cambridge, UK and New York, NY, USA: Cambridge University Press. doi: [10.1017/9781009157926](https://doi.org/10.1017/9781009157926).
- Ivezic, Ž., Kahn, S. M., et al. (Mar. 2019). ‘LSST: From Science Drivers to Reference Design and Anticipated Data Products’. In: ApJ 873.2, 111, p. 111. doi: [10.3847/1538-4357/ab042c](https://doi.org/10.3847/1538-4357/ab042c).
- James, G., Witten, D., et al. (2023). *An Introduction to Statistical Learning: with Applications in Python*. Springer Texts in Statistics. Springer International Publishing. ISBN: 9783031387470. URL: <https://books.google.com/books?id=ygzJEAAQBAJ>.
- Jarrett, T. H., Cluver, M. E., et al. (Feb. 2017). ‘Galaxy and Mass Assembly (GAMA): Exploring the WISE Web in G12’. In: ApJ 836.2, 182, p. 182. doi: [10.3847/1538-4357/836/2/182](https://doi.org/10.3847/1538-4357/836/2/182).
- Jarvis, M., Taylor, R., et al. (Jan. 2016). ‘The MeerKAT International GHz Tiered Extragalactic Exploration (MIGHTEE) Survey’. In: *MeerKAT Science: On the Pathway to the SKA*, 6, p. 6. doi: [10.22323/1.277.0006](https://doi.org/10.22323/1.277.0006).
- Jia, P., Jia, Q., et al. (June 2023). ‘Observation Strategy Optimization for Distributed Telescope Arrays with Deep Reinforcement Learning’. In: AJ 165.6, 233, p. 233. doi: [10.3847/1538-3881/accceb](https://doi.org/10.3847/1538-3881/accceb).

REFERENCES

- Jiang, L., Fan, X., et al. (July 2014). ‘The Sloan Digital Sky Survey Stripe 82 Imaging Data: Depth-optimized Co-adds over 300 deg² in Five Filters’. In: *ApJS* 213.1, 12, p. 12. doi: [10.1088/0067-0049/213/1/12](https://doi.org/10.1088/0067-0049/213/1/12).
- Jiang, T., Gradus, J. L., et al. (Feb. 2021). ‘Addressing Measurement Error in Random Forests Using Quantitative Bias Analysis’. In: *American Journal of Epidemiology* 190.9, pp. 1830–1840. issn: 0002-9262. doi: [10.1093/aje/kwab010](https://doi.org/10.1093/aje/kwab010).
- Johnson, J., Douze, M., and Jégou, H. (2019). ‘Billion-scale similarity search with GPUs’. In: *IEEE Transactions on Big Data* 7.3, pp. 535–547.
- Johnson, N. and Leone, F. (1964). *Statistics and Experimental Design in Engineering and the Physical Sciences*. Vol. 2. Wiley, p. 125. isbn: 9780471444893. url: <https://books.google.pt/books?id=IBjvAAAAMAAJ>.
- Jonas, J. and MeerKAT Team (Jan. 2016). ‘The MeerKAT Radio Telescope’. In: *MeerKAT Science: On the Pathway to the SKA*, 1, p. 1. doi: [10.22323/1.277.0001](https://doi.org/10.22323/1.277.0001).
- Josse, J., Prost, N., et al. (Feb. 2019). ‘On the consistency of supervised learning with missing values’. In: *arXiv e-prints*, arXiv:1902.06931, arXiv:1902.06931. doi: [10.48550/arXiv.1902.06931](https://doi.org/10.48550/arXiv.1902.06931).
- Josse, J. and Reiter, J. P. (2018). ‘Introduction to the Special Section on Missing Data’. In: *Statistical Science* 33.2, pp. 139–141. doi: [10.1214/18-STS332IN](https://doi.org/10.1214/18-STS332IN).
- Kalton, G. and Kasprzyk, D. (1982). ‘Imputing for missing survey responses’. In: *Proceedings of the section on survey research methods, American Statistical Association*. Vol. 22. American Statistical Association Cincinnati, p. 31.
- Katz, H., Kimm, T., et al. (Aug. 2018). ‘A Census of the LyC photons that form the UV background during reionization’. In: *MNRAS* 478.4, pp. 4986–5005. doi: [10.1093/mnras/sty1225](https://doi.org/10.1093/mnras/sty1225).
- Katz, H., Kimm, T., et al. (Feb. 2019). ‘Tracing the sources of reionization in cosmological radiation hydrodynamics simulations’. In: *MNRAS* 483.1, pp. 1029–1041. doi: [10.1093/mnras/sty3154](https://doi.org/10.1093/mnras/sty3154).
- Kauffmann, G., Heckman, T. M., et al. (Dec. 2003). ‘The host galaxies of active galactic nuclei’. In: *MNRAS* 346.4, pp. 1055–1077. doi: [10.1111/j.1365-2966.2003.07154.x](https://doi.org/10.1111/j.1365-2966.2003.07154.x).
- Ke, G., Meng, Q., et al. (2017). ‘LightGBM: A Highly Efficient Gradient Boosting Decision Tree’. In: *Advances in Neural Information Processing Systems*. Ed. by I. Guyon, U. V. Luxburg, et al. Vol. 30. Curran Associates, Inc. url: <https://proceedings.neurips.cc/paper/2017/file/6449f44a102fde848669bdd9eb6b76fa-Paper.pdf>.
- Kennicutt Robert C., J., Hao, C.-N., et al. (Oct. 2009). ‘Dust-corrected Star Formation Rates of Galaxies. I. Combinations of H α and Infrared Tracers’. In: *ApJ* 703.2, pp. 1672–1695. doi: [10.1088/0004-637X/703/2/1672](https://doi.org/10.1088/0004-637X/703/2/1672).
- Kewley, L. J., Dopita, M. A., et al. (July 2001). ‘Theoretical Modeling of Starburst Galaxies’. In: *ApJ* 556.1, pp. 121–140. doi: [10.1086/321545](https://doi.org/10.1086/321545).
- Kewley, L. J., Groves, B., et al. (Nov. 2006). ‘The host galaxies and classification of active galactic nuclei’. In: *MNRAS* 372.3, pp. 961–976. doi: [10.1111/j.1365-2966.2006.10859.x](https://doi.org/10.1111/j.1365-2966.2006.10859.x).
- Khrantsov, V., Spinelli, C., et al. (July 2021). ‘VEXAS: VISTA EXtension to Auxiliary Surveys. Data Release 2: Machine-learning based classification of sources in the Southern Hemisphere’. In: *A&A* 651, A69, A69. doi: [10.1051/0004-6361/202040131](https://doi.org/10.1051/0004-6361/202040131).

- Kim, S. J., Lee, H. M., et al. (Dec. 2012). ‘The North Ecliptic Pole Wide survey of AKARI: a near- and mid-infrared source catalog’. In: A&A 548, A29, A29. doi: [10.1051/0004-6361/201219105](https://doi.org/10.1051/0004-6361/201219105).
- King, A. and Pounds, K. (Aug. 2015). ‘Powerful Outflows and Feedback from Active Galactic Nuclei’. In: ARA&A 53, pp. 115–154. doi: [10.1146/annurev-astro-082214-122316](https://doi.org/10.1146/annurev-astro-082214-122316).
- Kirkpatrick, A., Alberts, S., et al. (Nov. 2017). ‘The AGN-Star Formation Connection: Future Prospects with JWST’. In: ApJ 849.2, 111, p. 111. doi: [10.3847/1538-4357/aa911d](https://doi.org/10.3847/1538-4357/aa911d).
- Kirkpatrick, A., Pope, A., et al. (Nov. 2012). ‘GOODS-Herschel: Impact of Active Galactic Nuclei and Star Formation Activity on Infrared Spectral Energy Distributions at High Redshift’. In: ApJ 759.2, 139, p. 139. doi: [10.1088/0004-637X/759/2/139](https://doi.org/10.1088/0004-637X/759/2/139).
- Kluyver, T., Ragan-Kelley, B., et al. (2016). ‘Jupyter Notebooks – a publishing format for reproducible computational workflows’. In: *Positioning and Power in Academic Publishing: Players, Agents and Agendas*. Ed. by F. Loizides and B. Schmidt. IOS Press, pp. 87–90.
- Kollmeier, J. A., Zasowski, G., et al. (Nov. 2017). ‘SDSS-V: Pioneering Panoptic Spectroscopy’. In: arXiv e-prints, arXiv:1711.03234, arXiv:1711.03234. doi: [10.48550/arXiv.1711.03234](https://doi.org/10.48550/arXiv.1711.03234).
- Kondapally, R., Best, P. N., et al. (July 2022). ‘Cosmic evolution of low-excitation radio galaxies in the LOFAR two-metre sky survey deep fields’. In: MNRAS 513.3, pp. 3742–3767. doi: [10.1093/mnras/stac1128](https://doi.org/10.1093/mnras/stac1128).
- Kormendy, J. and Ho, L. C. (Aug. 2013). ‘Coevolution (Or Not) of Supermassive Black Holes and Host Galaxies’. In: ARA&A 51.1, pp. 511–653. doi: [10.1146/annurev-astro-082708-101811](https://doi.org/10.1146/annurev-astro-082708-101811).
- Koshida, S., Minezaki, T., et al. (June 2014). ‘Reverberation Measurements of the Inner Radius of the Dust Torus in 17 Seyfert Galaxies’. In: ApJ 788.2, 159, p. 159. doi: [10.1088/0004-637X/788/2/159](https://doi.org/10.1088/0004-637X/788/2/159).
- Koshida, S., Yoshii, Y., et al. (Aug. 2009). ‘Variation of Inner Radius of Dust Torus in NGC4151’. In: ApJ 700.2, pp. L109–L113. doi: [10.1088/0004-637X/700/2/L109](https://doi.org/10.1088/0004-637X/700/2/L109).
- Kovács, O. E., Bogdán, Á., et al. (Feb. 2019). ‘Detection of the Missing Baryons toward the Sightline of H1821+643’. In: ApJ 872.1, 83, p. 83. doi: [10.3847/1538-4357/aaef78](https://doi.org/10.3847/1538-4357/aaef78).
- Krumpe, M., Miyaji, T., and Coil, A. L. (Nov. 2014). ‘Clustering Measurements of broad-line AGNs: Review and Future’. In: *Multifrequency Behaviour of High Energy Cosmic Sources*, pp. 71–78. doi: [10.14311/APP.2014.01.0071](https://doi.org/10.14311/APP.2014.01.0071).
- Kulkarni, G., Worseck, G., and Hennawi, J. F. (Sept. 2019). ‘Evolution of the AGN UV luminosity function from redshift 7.5’. In: MNRAS 488.1, pp. 1035–1065. doi: [10.1093/mnras/stz1493](https://doi.org/10.1093/mnras/stz1493).
- Kull, M., Filho, T. M. S., and Flach, P. (2017a). ‘Beyond sigmoids: How to obtain well-calibrated probabilities from binary classifiers with beta calibration’. In: *Electronic Journal of Statistics* 11.2, pp. 5052–5080. doi: [10.1214/17-EJS1338SI](https://doi.org/10.1214/17-EJS1338SI).
- Kull, M., Filho, T. S., and Flach, P. (Apr. 2017b). ‘Beta calibration: a well-founded and easily implemented improvement on logistic calibration for binary classifiers’. In: *Proceedings of the 20th International Conference on Artificial Intelligence and Statistics*. Ed. by A. Singh and J. Zhu. Vol. 54. Proceedings of Machine Learning Research. PMLR, pp. 623–631. URL: <https://proceedings.mlr.press/v54/kull17a.html>.
- Kurtz, M. J. and Mink, D. J. (Aug. 1998). ‘RVSAO 2.0: Digital Redshifts and Radial Velocities’. In: PASP 110.750, pp. 934–977. doi: [10.1086/316207](https://doi.org/10.1086/316207).

REFERENCES

- Kuźmicz, A. and Jamrozy, M. (Mar. 2021). ‘Giant Radio Quasars: Sample and Basic Properties’. In: ApJS 253.1, 25, p. 25. doi: [10.3847/1538-4365/abd483](https://doi.org/10.3847/1538-4365/abd483).
- Lacerda, E. A. D., Sánchez, S. F., et al. (Nov. 2022). ‘pyFIT3D and pyPipe3D - The new version of the integral field spectroscopy data analysis pipeline’. In: New A 97, 101895, p. 101895. doi: [10.1016/j.newast.2022.101895](https://doi.org/10.1016/j.newast.2022.101895).
- Lacy, M., Baum, S. A., et al. (Mar. 2020). ‘The Karl G. Jansky Very Large Array Sky Survey (VLASS). Science Case and Survey Design’. In: PASP 132.1009, 035001, p. 035001. doi: [10.1088/1538-3873/ab63eb](https://doi.org/10.1088/1538-3873/ab63eb).
- Lacy, M., Petric, A. O., et al. (Jan. 2007). ‘Optical Spectroscopy and X-Ray Detections of a Sample of Quasars and Active Galactic Nuclei Selected in the Mid-Infrared from Two Spitzer Space Telescope Wide-Area Surveys’. In: AJ 133.1, pp. 186–205. doi: [10.1086/509617](https://doi.org/10.1086/509617).
- Lacy, M., Ridgway, S. E., et al. (Oct. 2013). ‘The Spitzer Mid-infrared Active Galactic Nucleus Survey. I. Optical and Near-infrared Spectroscopy of Obscured Candidates and Normal Active Galactic Nuclei Selected in the Mid-infrared’. In: ApJS 208.2, 24, p. 24. doi: [10.1088/0067-0049/208/2/24](https://doi.org/10.1088/0067-0049/208/2/24).
- Lacy, M., Storrie-Lombardi, L. J., et al. (Sept. 2004). ‘Obscured and Unobscured Active Galactic Nuclei in the Spitzer Space Telescope First Look Survey’. In: ApJS 154.1, pp. 166–169. doi: [10.1086/422816](https://doi.org/10.1086/422816).
- Lacy, M., Surace, J. A., et al. (Feb. 2021). ‘A Spitzer survey of Deep Drilling Fields to be targeted by the Vera C. Rubin Observatory Legacy Survey of Space and Time’. In: MNRAS 501.1, pp. 892–910. doi: [10.1093/mnras/staa3714](https://doi.org/10.1093/mnras/staa3714).
- Lacy, M. and Sajina, A. (Apr. 2020). ‘Active galactic nuclei as seen by the Spitzer Space Telescope’. In: *Nature Astronomy* 4, pp. 352–363. doi: [10.1038/s41550-020-1071-x](https://doi.org/10.1038/s41550-020-1071-x).
- Lal, D. V. (July 2021). ‘The Discovery of a Remnant Radio Galaxy in A2065 Using GMRT’. In: ApJ 915.2, 126, p. 126. doi: [10.3847/1538-4357/ac042d](https://doi.org/10.3847/1538-4357/ac042d).
- LaMassa, S. M., Urry, C. M., et al. (Feb. 2016). ‘The 31 Deg² Release of the Stripe 82 X-Ray Survey: The Point Source Catalog’. In: ApJ 817.2, 172, p. 172. doi: [10.3847/0004-637X/817/2/172](https://doi.org/10.3847/0004-637X/817/2/172).
- Lang, D. (May 2014). ‘unWISE: Unblurred Coadds of the WISE Imaging’. In: AJ 147.5, 108, p. 108. doi: [10.1088/0004-6256/147/5/108](https://doi.org/10.1088/0004-6256/147/5/108).
- Langeroodi, D. and Hjorth, J. (Apr. 2023). ‘PAH Emission from Star-forming Galaxies in JWST Mid-infrared Imaging of the Lensing Cluster SMACS J0723.3-7327’. In: ApJ 946.2, L40, p. L40. doi: [10.3847/2041-8213/acc1e0](https://doi.org/10.3847/2041-8213/acc1e0).
- Langley, P. (1977). ‘BACON: A Production System That Discovers Empirical Laws’. In: *International Joint Conference on Artificial Intelligence*. URL: <https://api.semanticscholar.org/CorpusID:2320342>.
- (1979). ‘Rediscovering Physics with BACON.3’. In: *Proceedings of the 6th International Joint Conference on Artificial Intelligence - Volume 1*. IJCAI’79. Tokyo, Japan: Morgan Kaufmann Publishers Inc., pp. 505–507. ISBN: 0934613478.
- Langley, P., Bradshaw, G. L., and Simon, H. A. (1981). ‘BACON.5: The Discovery of Conservation Laws’. In: *Proceedings of the 7th International Joint Conference on Artificial Intelligence - Volume 1*. IJCAI’81. Vancouver, BC, Canada: Morgan Kaufmann Publishers Inc., pp. 121–126.
- Langley, P. and Zytkow, J. M. (1990). ‘Data-Driven Approaches to Empirical Discovery’. In: *Machine Learning: Paradigms and Methods*. USA: Elsevier North-Holland, Inc., pp. 283–312. ISBN: 0262530880.

- Lansbury, G. B., Banerji, M., et al. (Jan. 2020). ‘X-ray observations of luminous dusty quasars at $z > 2$ ’. In: MNRAS 495.3, pp. 2652–2663. doi: [10.1093/mnras/staa1220](https://doi.org/10.1093/mnras/staa1220).
- Latimer, C. J., Reines, A. E., et al. (June 2021). ‘A Chandra and HST View of WISE-selected AGN Candidates in Dwarf Galaxies’. In: ApJ 914.2, 133, p. 133. doi: [10.3847/1538-4357/abfe0c](https://doi.org/10.3847/1538-4357/abfe0c).
- Lazio, J. W., Kimball, A., et al. (Feb. 2014). ‘Radio Astronomy in LSST Era’. In: PASP 126.936, p. 196. doi: [10.1086/675262](https://doi.org/10.1086/675262).
- Le Fèvre, O., Tasca, L. A. M., et al. (Apr. 2015). ‘The VIMOS Ultra-Deep Survey: $\sim 10\,000$ galaxies with spectroscopic redshifts to study galaxy assembly at early epochs $2 < z \simeq 6$ ’. In: A&A 576, A79, A79. doi: [10.1051/0004-6361/201423829](https://doi.org/10.1051/0004-6361/201423829).
- Lee, H. M., Kim, S. J., et al. (Feb. 2009). ‘North Ecliptic Pole Wide Field Survey of AKARI: Survey Strategy and Data Characteristics’. In: PASJ 61, p. 375. doi: [10.1093/pasj/61.2.375](https://doi.org/10.1093/pasj/61.2.375).
- Lehmer, B. D., Brandt, W. N., et al. (Nov. 2005). ‘The Extended Chandra Deep Field-South Survey: Chandra Point-Source Catalogs’. In: ApJS 161.1, pp. 21–40. doi: [10.1086/444590](https://doi.org/10.1086/444590).
- Lichtenstein, S., Fischhoff, B., and Phillips, L. D. (1982). ‘Calibration of probabilities: The state of the art to 1980’. In: *Judgment under Uncertainty: Heuristics and Biases*. Ed. by D. Kahneman, P. Slovic, and A. Tversky. Cambridge University Press, pp. 306–334. doi: [10.1017/CBO9780511809477.023](https://doi.org/10.1017/CBO9780511809477.023).
- Lima, E. V. R., Sodré, L., et al. (Jan. 2022). ‘Photometric redshifts for the S-PLUS Survey: Is machine learning up to the task?’ In: *Astronomy and Computing* 38, 100510, p. 100510. doi: [10.1016/j.ascom.2021.100510](https://doi.org/10.1016/j.ascom.2021.100510).
- Lira, P., Arévalo, P., et al. (Aug. 2011). ‘Optical and near-IR long-term monitoring of NGC 3783 and MR 2251-178: evidence for variable near-IR emission from thin accretion discs’. In: MNRAS 415.2, pp. 1290–1303. doi: [10.1111/j.1365-2966.2011.18774.x](https://doi.org/10.1111/j.1365-2966.2011.18774.x).
- Lira, P., Arévalo, P., et al. (Nov. 2015). ‘Long-term monitoring of the archetype Seyfert galaxy MCG-6-30-15: X-ray, optical and near-IR variability of the corona, disc and torus’. In: MNRAS 454.1, pp. 368–379. doi: [10.1093/mnras/stv1945](https://doi.org/10.1093/mnras/stv1945).
- Lisenfeld, U. and Völk, H. J. (Feb. 2000). ‘On the radio spectral index of galaxies’. In: A&A 354, pp. 423–430.
- Liske, J., Baldry, I. K., et al. (Sept. 2015). ‘Galaxy And Mass Assembly (GAMA): end of survey report and data release 2’. In: MNRAS 452.2, pp. 2087–2126. doi: [10.1093/mnras/stv1436](https://doi.org/10.1093/mnras/stv1436).
- Little, R. and Rubin, D. (2014). *Statistical Analysis with Missing Data*. Wiley Series in Probability and Statistics. Wiley. ISBN: 9781118625880. URL: <https://books.google.pt/books?id=AyVeBAAQBAJ>.
- Liu, D., Lang, P., et al. (Oct. 2019). ‘Automated Mining of the ALMA Archive in the COSMOS Field (A^3 COSMOS). I. Robust ALMA Continuum Photometry Catalogs and Stellar Mass and Star Formation Properties for ~ 700 Galaxies at $z = 0.5\text{--}6$ ’. In: ApJS 244.2, 40, p. 40. doi: [10.3847/1538-4365/ab42da](https://doi.org/10.3847/1538-4365/ab42da).
- Lochner, M. and Bassett, B. A. (July 2021). ‘ASTRONOMALY: Personalised active anomaly detection in astronomical data’. In: *Astronomy and Computing* 36, 100481, p. 100481. doi: [10.1016/j.ascom.2021.100481](https://doi.org/10.1016/j.ascom.2021.100481).
- Loeb, A. and Furlanetto, S. R. (2013). *The First Galaxies in the Universe*. Princeton Series in Astrophysics. Princeton University Press. ISBN: 9780691144924. URL: <https://books.google.pt/books?id=hj98RVlnRRgC>.
- Loh, E. D. and Spillar, E. J. (Apr. 1986). ‘Photometric Redshifts of Galaxies’. In: ApJ 303, p. 154. doi: [10.1086/164062](https://doi.org/10.1086/164062).

REFERENCES

- Louppe, G., Wehenkel, L., et al. (2013). ‘Understanding variable importances in forests of randomized trees’. In: *Advances in Neural Information Processing Systems*. Ed. by C. J. C. Burges, L. Bottou, et al. Vol. 26. Curran Associates, Inc. URL: <https://proceedings.neurips.cc/paper/2013/file/e3796ae838835da0b6f6ea37bcf8bcb7-Paper.pdf>.
- LSST Science Collaboration, Abell, P. A., et al. (Dec. 2009). ‘LSST Science Book, Version 2.0’. In: *arXiv e-prints*, arXiv:0912.0201, arXiv:0912.0201. doi: [10.48550/arXiv.0912.0201](https://doi.org/10.48550/arXiv.0912.0201).
- Luken, K., Norris, R., et al. (2022). ‘Estimating galaxy redshift in radio-selected datasets using machine learning’. In: *Astronomy and Computing* 39, p. 100557. issn: 2213-1337. doi: <https://doi.org/10.1016/j.ascom.2022.100557>.
- Luken, K. J., Norris, R. P., and Park, L. A. F. (Oct. 2019). ‘Preliminary Results of Using k-Nearest Neighbors Regression to Estimate the Redshift of Radio-selected Data Sets’. In: PASP 131.1004, p. 108003. doi: [10.1088/1538-3873/aaea17](https://doi.org/10.1088/1538-3873/aaea17).
- Lukic, V., Brüggen, M., et al. (Aug. 2019). ‘Morphological classification of radio galaxies: capsule networks versus convolutional neural networks’. In: MNRAS 487.2, pp. 1729–1744. doi: [10.1093/mnras/stz1289](https://doi.org/10.1093/mnras/stz1289).
- Lundberg, S. M. and Lee, S.-I. (2017). ‘A Unified Approach to Interpreting Model Predictions’. In: *Advances in Neural Information Processing Systems 30*. Ed. by I. Guyon, U. V. Luxburg, et al. Curran Associates, Inc., pp. 4765–4774. URL: <http://papers.nips.cc/paper/7062-a-unified-approach-to-interpreting-model-predictions.pdf>.
- Lundberg, S. M., Erion, G., et al. (2020). ‘From local explanations to global understanding with explainable AI for trees’. In: *Nature Machine Intelligence* 2.1, pp. 2522–5839.
- Lyu, J., Alberts, S., et al. (Dec. 2022). ‘AGN Selection and Demographics in GOODS-S/HUDF from X-Ray to Radio’. In: ApJ 941.2, 191, p. 191. doi: [10.3847/1538-4357/ac9e5d](https://doi.org/10.3847/1538-4357/ac9e5d).
- Ma, S. and Tourani, R. (Aug. 2020). ‘Predictive and Causal Implications of using Shapley Value for Model Interpretation’. In: *Proceedings of the 2020 KDD Workshop on Causal Discovery*. Vol. 127. Proceedings of Machine Learning Research. PMLR, pp. 23–38. URL: <https://proceedings.mlr.press/v127/ma20a.html>.
- Ma, Z., Xu, H., et al. (Feb. 2019). ‘A Machine Learning Based Morphological Classification of 14,245 Radio AGNs Selected from the Best-Heckman Sample’. In: ApJS 240.2, 34, p. 34. doi: [10.3847/1538-4365/aaf9a2](https://doi.org/10.3847/1538-4365/aaf9a2).
- Maccacaro, T., della Ceca, R., et al. (June 1991). ‘The Properties of X-Ray-selected Active Galactic Nuclei. I. Luminosity Function, Cosmological Evolution, and Contribution to the Diffuse X-Ray Background’. In: ApJ 374, p. 117. doi: [10.1086/170102](https://doi.org/10.1086/170102).
- Machado, D. P., Leonard, A., et al. (Dec. 2013). ‘Darth Fader: Using wavelets to obtain accurate redshifts of spectra at very low signal-to-noise’. In: A&A 560, A83, A83. doi: [10.1051/0004-6361/201219857](https://doi.org/10.1051/0004-6361/201219857).
- Machado Poletti Valle, L. F., Avestruz, C., et al. (Oct. 2021). ‘SHAPing the gas: understanding gas shapes in dark matter haloes with interpretable machine learning’. In: MNRAS 507.1, pp. 1468–1484. doi: [10.1093/mnras/stab2252](https://doi.org/10.1093/mnras/stab2252).
- Madau, P. and Dickinson, M. (Aug. 2014). ‘Cosmic Star-Formation History’. In: ARA&A 52, pp. 415–486. doi: [10.1146/annurev-astro-081811-125615](https://doi.org/10.1146/annurev-astro-081811-125615).

- Madau, P. and Haardt, F. (Nov. 2015). ‘Cosmic Reionization after Planck: Could Quasars Do It All?’ In: ApJ 813.1, L8, p. L8. doi: [10.1088/2041-8205/813/1/L8](https://doi.org/10.1088/2041-8205/813/1/L8).
- Madau, P., Haardt, F., and Rees, M. J. (Apr. 1999). ‘Radiative Transfer in a Clumpy Universe. III. The Nature of Cosmological Ionizing Sources’. In: ApJ 514.2, pp. 648–659. doi: [10.1086/306975](https://doi.org/10.1086/306975).
- Magliocchetti, M., Lutz, D., et al. (July 2014). ‘The PEP survey: infrared properties of radio-selected AGN’. In: MNRAS 442.1, pp. 682–693. doi: [10.1093/mnras/stu863](https://doi.org/10.1093/mnras/stu863).
- Magliocchetti, M. (Dec. 2022). ‘Hosts and environments: a (large-scale) radio history of AGN and star-forming galaxies’. In: A&A Rev. 30.1, 6, p. 6. doi: [10.1007/s00159-022-00142-1](https://doi.org/10.1007/s00159-022-00142-1).
- Magliocchetti, M., Maddox, S. J., et al. (June 2002). ‘The 2dF Galaxy Redshift Survey: the population of nearby radio galaxies at the 1-mJy level’. In: MNRAS 333.1, pp. 100–120. doi: [10.1046/j.1365-8711.2002.05386.x](https://doi.org/10.1046/j.1365-8711.2002.05386.x).
- Magorrian, J., Tremaine, S., et al. (June 1998). ‘The Demography of Massive Dark Objects in Galaxy Centers’. In: AJ 115.6, pp. 2285–2305. doi: [10.1086/300353](https://doi.org/10.1086/300353).
- Mainzer, A., Bauer, J., et al. (Apr. 2011). ‘Preliminary Results from NEOWISE: An Enhancement to the Wide-field Infrared Survey Explorer for Solar System Science’. In: ApJ 731.1, 53, p. 53. doi: [10.1088/0004-637X/731/1/53](https://doi.org/10.1088/0004-637X/731/1/53).
- Mainzer, A., Bauer, J., et al. (Sept. 2014). ‘Initial Performance of the NEOWISE Reactivation Mission’. In: ApJ 792.1, 30, p. 30. doi: [10.1088/0004-637X/792/1/30](https://doi.org/10.1088/0004-637X/792/1/30).
- Maitra, C., Haberl, F., et al. (Feb. 2019). ‘Identification of AGN in the XMM-Newton X-ray survey of the SMC’. In: A&A 622, A29, A29. doi: [10.1051/0004-6361/201833663](https://doi.org/10.1051/0004-6361/201833663).
- Mandal, S., Prandoni, I., et al. (Apr. 2021). ‘Extremely deep 150 MHz source counts from the LoTSS Deep Fields’. In: A&A 648, A5, A5. doi: [10.1051/0004-6361/202039998](https://doi.org/10.1051/0004-6361/202039998).
- Marchesi, S., Civano, F., et al. (Jan. 2016). ‘The Chandra COSMOS Legacy survey: optical/IR identifications’. In: ApJ 817.1, 34, p. 34. doi: [10.3847/0004-637X/817/1/34](https://doi.org/10.3847/0004-637X/817/1/34).
- Marocco, F., Eisenhardt, P. R. M., et al. (Mar. 2021). ‘The CatWISE2020 Catalog’. In: ApJS 253.1, 8, p. 8. doi: [10.3847/1538-4365/abd805](https://doi.org/10.3847/1538-4365/abd805).
- Martocchia, S., Piconcelli, E., et al. (Dec. 2017). ‘The WISSH quasars project. III. X-ray properties of hyper-luminous quasars’. In: A&A 608, A51, A51. doi: [10.1051/0004-6361/201731314](https://doi.org/10.1051/0004-6361/201731314).
- Mateos, S., Alonso-Herrero, A., et al. (Nov. 2012). ‘Using the Bright Ultrahard XMM-Newton survey to define an IR selection of luminous AGN based on WISE colours’. In: MNRAS 426.4, pp. 3271–3281. doi: [10.1111/j.1365-2966.2012.21843.x](https://doi.org/10.1111/j.1365-2966.2012.21843.x).
- Matsuoka, Y., Strauss, M. A., et al. (Dec. 2018). ‘Subaru High-z Exploration of Low-luminosity Quasars (SHELLQs). V. Quasar Luminosity Function and Contribution to Cosmic Reionization at $z = 6$ ’. In: ApJ 869.2, 150, p. 150. doi: [10.3847/1538-4357/aaee7a](https://doi.org/10.3847/1538-4357/aaee7a).
- Matthews, B. (1975). ‘Comparison of the predicted and observed secondary structure of T4 phage lysozyme’. In: *Biochimica et Biophysica Acta (BBA) - Protein Structure* 405.2, pp. 442–451. ISSN: 0005-2795. doi: [https://doi.org/10.1016/0005-2795\(75\)90109-9](https://doi.org/10.1016/0005-2795(75)90109-9).

REFERENCES

- Mauch, T. and Sadler, E. M. (Mar. 2007). ‘Radio sources in the 6dFGS: local luminosity functions at 1.4 GHz for star-forming galaxies and radio-loud AGN’. In: MNRAS 375.3, pp. 931–950. doi: [10.1111/j.1365-2966.2006.11353.x](https://doi.org/10.1111/j.1365-2966.2006.11353.x).
- McAlpine, K., Jarvis, M. J., and Bonfield, D. G. (Dec. 2013). ‘Evolution of faint radio sources in the VIDEO-XMM3 field’. In: MNRAS 436.2, pp. 1084–1095. doi: [10.1093/mnras/stt1638](https://doi.org/10.1093/mnras/stt1638).
- McConnell, D., Hale, C. L., et al. (Nov. 2020). ‘The Rapid ASKAP Continuum Survey I: Design and first results’. In: PASA 37, e048, e048. doi: [10.1017/pasa.2020.41](https://doi.org/10.1017/pasa.2020.41).
- McConnell, N. J. and Ma, C.-P. (Feb. 2013). ‘Revisiting the Scaling Relations of Black Hole Masses and Host Galaxy Properties’. In: ApJ 764.2, 184, p. 184. doi: [10.1088/0004-637X/764/2/184](https://doi.org/10.1088/0004-637X/764/2/184).
- McGreer, I. D., Becker, R. H., et al. (Nov. 2006). ‘Discovery of a $z = 6.1$ Radio-Loud Quasar in the NOAO Deep Wide Field Survey’. In: ApJ 652.1, pp. 157–162. doi: [10.1086/507767](https://doi.org/10.1086/507767).
- McHardy, I. M., Connolly, S. D., et al. (May 2016). ‘The origin of UV-optical variability in AGN and test of disc models: XMM-Newton and ground-based observations of NGC 4395’. In: *Astronomische Nachrichten* 337.4-5, p. 500. doi: [10.1002/asna.201612337](https://doi.org/10.1002/asna.201612337).
- McKinney, W. (2010). ‘Data Structures for Statistical Computing in Python’. In: *Proceedings of the 9th Python in Science Conference*. Ed. by S. van der Walt and J. Millman, pp. 56–61. doi: [10.25080/Majora-92bf1922-00a](https://doi.org/10.25080/Majora-92bf1922-00a).
- Meiksin, A. (Jan. 2005). ‘Constraints on the ionization sources of the high-redshift intergalactic medium’. In: MNRAS 356.2, pp. 596–606. doi: [10.1111/j.1365-2966.2004.08481.x](https://doi.org/10.1111/j.1365-2966.2004.08481.x).
- Meisner, A. M., Lang, D., et al. (Dec. 2019). ‘unWISE Coadds: The Five-year Data Set’. In: PASP 131.1006, p. 124504. doi: [10.1088/1538-3873/ab3df4](https://doi.org/10.1088/1538-3873/ab3df4).
- Meisner, A. M., Lang, D., et al. (Sept. 2022). ‘9-yr Deep Sky unWISE Coadds’. In: *Research Notes of the American Astronomical Society* 6.9, 188, p. 188. doi: [10.3847/2515-5172/ac913e](https://doi.org/10.3847/2515-5172/ac913e).
- Menzel, M. .-, Merloni, A., et al. (Mar. 2016). ‘A spectroscopic survey of X-ray-selected AGNs in the northern XMM-XXL field’. In: MNRAS 457.1, pp. 110–132. doi: [10.1093/mnras/stv2749](https://doi.org/10.1093/mnras/stv2749).
- Merlin, E., Castellano, M., et al. (May 2021). ‘The ASTRODEEP-GS43 catalogue: New photometry and redshifts for the CANDELS GOODS-South field’. In: A&A 649, A22, A22. doi: [10.1051/0004-6361/202140310](https://doi.org/10.1051/0004-6361/202140310).
- Messias, H., Afonso, J., et al. (Aug. 2012). ‘A New Infrared Color Criterion for the Selection of $0 < z < 7$ AGNs: Application to Deep Fields and Implications for JWST Surveys’. In: ApJ 754.2, 120, p. 120. doi: [10.1088/0004-637X/754/2/120](https://doi.org/10.1088/0004-637X/754/2/120).
- Michailidis, M. (2017). ‘Investigating machine learning methods in recommender systems’. PhD thesis. University College London, UK. url: <https://discovery.ucl.ac.uk/id/eprint/10031000>.
- Michelucci, U. and Venturini, F. (2023). ‘New metric formulas that include measurement errors in machine learning for natural sciences’. In: *Expert Systems with Applications* 224, p. 120013. issn: 0957-4174. doi: <https://doi.org/10.1016/j.eswa.2023.120013>.
- Mickaelian, A. M. (Dec. 2020). ‘Big Data in Astronomy: Surveys, Catalogs, Databases and Archives’. In: *Communications of the Byurakan Astrophysical Observatory* 67, pp. 159–180. doi: [10.52526/25792776-2020.67.2-159](https://doi.org/10.52526/25792776-2020.67.2-159).

- Miley, G. and De Breuck, C. (Feb. 2008). ‘Distant radio galaxies and their environments’. In: A&A Rev. 15.2, pp. 67–144. doi: [10.1007/s00159-007-0008-z](https://doi.org/10.1007/s00159-007-0008-z).
- Mingo, B., Watson, M. G., et al. (Nov. 2016). ‘The MIXR sample: AGN activity versus star formation across the cross-correlation of WISE, 3XMM, and FIRST/NVSS’. In: MNRAS 462.3, pp. 2631–2667. doi: [10.1093/mnras/stw1826](https://doi.org/10.1093/mnras/stw1826).
- Mitra, S., Choudhury, T. R., and Ferrara, A. (Jan. 2018). ‘Cosmic reionization after Planck II: contribution from quasars’. In: MNRAS 473.1, pp. 1416–1425. doi: [10.1093/mnras/stx2443](https://doi.org/10.1093/mnras/stx2443).
- Miyaji, T., Hasinger, G., and Schmidt, M. (Apr. 2001). ‘Soft X-ray AGN luminosity function from ROSAT surveys. II. Table of the binned soft X-ray luminosity function’. In: A&A 369, pp. 49–56. doi: [10.1051/0004-6361:20010102](https://doi.org/10.1051/0004-6361:20010102).
- Mo, W., Gonzalez, A., et al. (Oct. 2020). ‘The Massive and Distant Clusters of WISE Survey. VIII. Radio Activity in Massive Galaxy Clusters’. In: ApJ 901.2, 131, p. 131. doi: [10.3847/1538-4357/abb08d](https://doi.org/10.3847/1538-4357/abb08d).
- Mohan, N. and Rafferty, D. (Feb. 2015). *PyBDSF: Python Blob Detection and Source Finder*. Astrophysics Source Code Library, record ascl:1502.007.
- Morabito, L. K., Sweijen, F., et al. (Oct. 2022). ‘Identifying active galactic nuclei via brightness temperature with sub-arcsecond international LOFAR telescope observations’. In: MNRAS 515.4, pp. 5758–5774. doi: [10.1093/mnras/stac2129](https://doi.org/10.1093/mnras/stac2129).
- Morrissey, P., Conrow, T., et al. (Dec. 2007). ‘The Calibration and Data Products of GALEX’. In: ApJS 173.2, pp. 682–697. doi: [10.1086/520512](https://doi.org/10.1086/520512).
- Mostert, R. I. J., Duncan, K. J., et al. (Jan. 2021). ‘Unveiling the rarest morphologies of the LOFAR Two-metre Sky Survey radio source population with self-organised maps’. In: A&A 645, A89, A89. doi: [10.1051/0004-6361/202038500](https://doi.org/10.1051/0004-6361/202038500).
- Moya, A. and López-Sastre, R. J. (July 2022). ‘Stellar mass and radius estimation using artificial intelligence’. In: A&A 663, A112, A112. doi: [10.1051/0004-6361/202142930](https://doi.org/10.1051/0004-6361/202142930).
- Naidoo, K., Johnston, H., et al. (Feb. 2023). ‘Euclid: Calibrating photometric redshifts with spectroscopic cross-correlations’. In: A&A 670, A149, A149. doi: [10.1051/0004-6361/202244795](https://doi.org/10.1051/0004-6361/202244795).
- Nakoneczny, S. J., Bilicki, M., et al. (May 2021). ‘Photometric selection and redshifts for quasars in the Kilo-Degree Survey Data Release 4’. In: A&A 649, A81, A81. doi: [10.1051/0004-6361/202039684](https://doi.org/10.1051/0004-6361/202039684).
- Netzer, H. (Aug. 2015). ‘Revisiting the Unified Model of Active Galactic Nuclei’. In: ARA&A 53, pp. 365–408. doi: [10.1146/annurev-astro-082214-122302](https://doi.org/10.1146/annurev-astro-082214-122302).
- Newman, J. A., Abate, A., et al. (Mar. 2015). ‘Spectroscopic needs for imaging dark energy experiments’. In: *Astroparticle Physics* 63, pp. 81–100. doi: [10.1016/j.astropartphys.2014.06.007](https://doi.org/10.1016/j.astropartphys.2014.06.007).
- Newman, J. A. and Gruen, D. (Aug. 2022). ‘Photometric Redshifts for Next-Generation Surveys’. In: ARA&A 60, pp. 363–414. doi: [10.1146/annurev-astro-032122-014611](https://doi.org/10.1146/annurev-astro-032122-014611).
- Nicastro, F., Kaastra, J., et al. (June 2018). ‘Observations of the missing baryons in the warm-hot intergalactic medium’. In: Nature 558.7710, pp. 406–409. doi: [10.1038/s41586-018-0204-1](https://doi.org/10.1038/s41586-018-0204-1).
- Nicastro, F., Krongold, Y., et al. (Mar. 2017). ‘A decade of warm hot intergalactic medium searches: Where do we stand and where do we go?’ In: *Astronomische Nachrichten* 338.281, pp. 281–286. doi: [10.1002/asna.201713343](https://doi.org/10.1002/asna.201713343).

REFERENCES

- Niculescu-Mizil, A. and Caruana, R. (2005). ‘Predicting Good Probabilities with Supervised Learning’. In: *Proceedings of the 22nd International Conference on Machine Learning*. ICML ’05. Bonn, Germany: Association for Computing Machinery, pp. 625–632. ISBN: 1595931805. doi: [10.1145/1102351.1102430](https://doi.org/10.1145/1102351.1102430).
- Norris, R. P. (June 2017). ‘Astroinformatics Challenges from Next-generation Radio Continuum Surveys’. In: *Astroinformatics*. Ed. by M. Brescia, S. G. Djorgovski, et al. Vol. 325, pp. 103–113. doi: [10.1017/S1743921316012825](https://doi.org/10.1017/S1743921316012825).
- Norris, R. P., Hopkins, A. M., et al. (Aug. 2011). ‘EMU: Evolutionary Map of the Universe’. In: PASA 28.3, pp. 215–248. doi: [10.1071/AS11021](https://doi.org/10.1071/AS11021).
- Norris, R. P., Marvil, J., et al. (Sept. 2021). ‘The Evolutionary Map of the Universe pilot survey’. In: PASA 38, e046, e046. doi: [10.1017/pasa.2021.42](https://doi.org/10.1017/pasa.2021.42).
- Norris, R. P., Salvato, M., et al. (Oct. 2019). ‘A Comparison of Photometric Redshift Techniques for Large Radio Surveys’. In: PASP 131.1004, p. 108004. doi: [10.1088/1538-3873/ab0f7b](https://doi.org/10.1088/1538-3873/ab0f7b).
- Nour, D. and Sriram, K. (Jan. 2023). ‘Association of optical, ultraviolet, and soft X-ray excess emissions in AGNs’. In: MNRAS 518.4, pp. 5705–5717. doi: [10.1093/mnras/stac3505](https://doi.org/10.1093/mnras/stac3505).
- Ochsenbein, F., Bauer, P., and Marcout, J. (Apr. 2000). ‘The VizieR database of astronomical catalogues’. In: A&AS 143, pp. 23–32. doi: [10.1051/aas:2000169](https://doi.org/10.1051/aas:2000169).
- Oke, J. B. and Sandage, A. (Oct. 1968). ‘Energy Distributions, K Corrections, and the Stebbins-Whitford Effect for Giant Elliptical Galaxies’. In: ApJ 154, p. 21. doi: [10.1086/149737](https://doi.org/10.1086/149737).
- Oliver, S., Rowan-Robinson, M., et al. (Aug. 2000). ‘The European Large Area ISO Survey - I. Goals, definition and observations’. In: MNRAS 316.4, pp. 749–767. doi: [10.1046/j.1365-8711.2000.03550.x](https://doi.org/10.1046/j.1365-8711.2000.03550.x).
- Opitz, D. and Maclin, R. (July 1999). ‘Popular Ensemble Methods: An Empirical Study’. In: *J. Artif. Int. Res.* 11.1, pp. 169–198. issn: 1076-9757.
- Osorio-Clavijo, N., Gonzalez-Martín, O., et al. (July 2023). ‘AGNs in the CALIFA survey: X-ray detection of nuclear sources’. In: MNRAS 522.4, pp. 5788–5804. doi: [10.1093/mnras/stad1262](https://doi.org/10.1093/mnras/stad1262).
- Osterbrock, D. E. (Oct. 1981). ‘Seyfert galaxies with weak broad H alpha emission lines’. In: ApJ 249, pp. 462–470. doi: [10.1086/159306](https://doi.org/10.1086/159306).
- Pacifici, C., Iyer, K. G., et al. (Feb. 2023). ‘The Art of Measuring Physical Parameters in Galaxies: A Critical Assessment of Spectral Energy Distribution Fitting Techniques’. In: ApJ 944.2, 141, p. 141. doi: [10.3847/1538-4357/acacff](https://doi.org/10.3847/1538-4357/acacff).
- Padovani, P., Alexander, D. M., et al. (Aug. 2017). ‘Active galactic nuclei: what’s in a name?’ In: A&A Rev. 25.1, 2, p. 2. doi: [10.1007/s00159-017-0102-9](https://doi.org/10.1007/s00159-017-0102-9).
- Padovani, P. (Sept. 2016). ‘The faint radio sky: radio astronomy becomes mainstream’. In: A&A Rev. 24.1, 13, p. 13. doi: [10.1007/s00159-016-0098-6](https://doi.org/10.1007/s00159-016-0098-6).
- (Nov. 2017). ‘Active Galactic Nuclei at all wavelengths and from all angles’. In: *Frontiers in Astronomy and Space Sciences* 4, 35, p. 35. doi: [10.3389/fspas.2017.00035](https://doi.org/10.3389/fspas.2017.00035).
- Page, M. J. and Carrera, F. J. (Jan. 2000). ‘An improved method of constructing binned luminosity functions’. In: MNRAS 311.2, pp. 433–440. doi: [10.1046/j.1365-8711.2000.03105.x](https://doi.org/10.1046/j.1365-8711.2000.03105.x).

- Palanque-Delabrouille, N., Magneville, C., et al. (Mar. 2016). ‘The extended Baryon Oscillation Spectroscopic Survey: Variability selection and quasar luminosity function’. In: A&A 587, A41, A41. doi: [10.1051/0004-6361/201527392](https://doi.org/10.1051/0004-6361/201527392).
- Pedregosa, F., Varoquaux, G., et al. (2011). ‘Scikit-learn: Machine Learning in Python’. In: *Journal of Machine Learning Research* 12, pp. 2825–2830.
- Pepinsky, T. B. (2018). ‘A Note on Listwise Deletion versus Multiple Imputation’. In: *Political Analysis* 26.4, pp. 480–488. doi: [10.1017/pan.2018.18](https://doi.org/10.1017/pan.2018.18).
- Pérez-Torres, M., Mattila, S., et al. (Dec. 2021). ‘Star formation and nuclear activity in luminous infrared galaxies: an infrared through radio review’. In: A&A Rev. 29.1, 2, p. 2. doi: [10.1007/s00159-020-00128-x](https://doi.org/10.1007/s00159-020-00128-x).
- Perger, K., Frey, S., et al. (Aug. 2017). ‘A catalogue of active galactic nuclei from the first 1.5 Gyr of the Universe’. In: *Frontiers in Astronomy and Space Sciences* 4, 9, p. 9. doi: [10.3389/fspas.2017.00009](https://doi.org/10.3389/fspas.2017.00009).
- Planck Collaboration, Aghanim, N., et al. (Sept. 2020). ‘Planck 2018 results. VI. Cosmological parameters’. In: A&A 641, A6, A6. doi: [10.1051/0004-6361/201833910](https://doi.org/10.1051/0004-6361/201833910).
- Poisot, T. (2023). ‘Guidelines for the prediction of species interactions through binary classification’. In: *Methods in Ecology and Evolution* 14.5, pp. 1333–1345. doi: <https://doi.org/10.1111/2041-210X.14071>.
- Poliszczuk, A., Pollo, A., et al. (July 2021). ‘Active galactic nuclei catalog from the AKARI NEP-Wide field’. In: A&A 651, A108, A108. doi: [10.1051/0004-6361/202040219](https://doi.org/10.1051/0004-6361/202040219).
- Porqueres, N., Jasche, J., et al. (Apr. 2018). ‘Imprints of the large-scale structure on AGN formation and evolution’. In: A&A 612, A31, A31. doi: [10.1051/0004-6361/201732141](https://doi.org/10.1051/0004-6361/201732141).
- Portegies Zwart, S. (Sept. 2020). ‘The ecological impact of high-performance computing in astrophysics’. In: *Nature Astronomy* 4, pp. 819–822. doi: [10.1038/s41550-020-1208-y](https://doi.org/10.1038/s41550-020-1208-y).
- Pouliasis, E. (Feb. 2020). ‘Identification of Active Galactic Nuclei through different selection techniques’. PhD thesis. IAASARS, National Observatory of Athens.
- Pracy, M. B., Ching, J. H. Y., et al. (July 2016). ‘GAMA/WiggleZ: the 1.4 GHz radio luminosity functions of high- and low-excitation radio galaxies and their redshift evolution to $z = 0.75$ ’. In: MNRAS 460.1, pp. 2–17. doi: [10.1093/mnras/stw910](https://doi.org/10.1093/mnras/stw910).
- Prandoni, I., Gregorini, L., et al. (Jan. 2001). ‘The ATESP radio survey. III. Source counts’. In: A&A 365, pp. 392–399. doi: [10.1051/0004-6361:20000142](https://doi.org/10.1051/0004-6361:20000142).
- Prandoni, I., Guglielmino, G., et al. (Dec. 2018). ‘The Lockman Hole Project: new constraints on the sub-mJy source counts from a wide-area 1.4 GHz mosaic’. In: MNRAS 481.4, pp. 4548–4565. doi: [10.1093/mnras/sty2521](https://doi.org/10.1093/mnras/sty2521).
- Prandoni, I. and Seymour, N. (Apr. 2015). ‘Revealing the Physics and Evolution of Galaxies and Galaxy Clusters with SKA Continuum Surveys’. In: *Advancing Astrophysics with the Square Kilometre Array (AASKA14)*, 67, p. 67.
- Predehl, P., Andritschke, R., et al. (Mar. 2021). ‘The eROSITA X-ray telescope on SRG’. In: A&A 647, A1, A1. doi: [10.1051/0004-6361/202039313](https://doi.org/10.1051/0004-6361/202039313).
- Prestage, R. M. and Peacock, J. A. (July 1983). ‘Optical identifications of Parkes radio sources using UK Schmidt plates.’ In: MNRAS 204, pp. 355–364. doi: [10.1093/mnras/204.2.355](https://doi.org/10.1093/mnras/204.2.355).

REFERENCES

- Prokhorenkova, L., Gusev, G., et al. (2018). ‘CatBoost: unbiased boosting with categorical features’. In: *Advances in Neural Information Processing Systems*. Ed. by S. Bengio, H. Wallach, et al. Vol. 31. Curran Associates, Inc. URL: https://proceedings.neurips.cc/paper_files/paper/2018/file/14491b756b3a51daac41c24863285549-Paper.pdf.
- Radcliffe, J. F., Barthel, P. D., et al. (May 2021a). ‘Nowhere to hide: Radio-faint AGN in the GOODS-N field. II. Multi-wavelength AGN selection techniques and host galaxy properties’. In: A&A 649, A27, A27. doi: [10.1051/0004-6361/202038591](https://doi.org/10.1051/0004-6361/202038591).
- Radcliffe, J. F., Barthel, P. D., et al. (May 2021b). ‘The radio emission from active galactic nuclei’. In: A&A 649, L9, p. L9. doi: [10.1051/0004-6361/202140791](https://doi.org/10.1051/0004-6361/202140791).
- Radcliffe, J. F., Garrett, M. A., et al. (Nov. 2018). ‘Nowhere to Hide: Radio-faint AGN in GOODS-N field. I. Initial catalogue and radio properties’. In: A&A 619, A48, A48. doi: [10.1051/0004-6361/201833399](https://doi.org/10.1051/0004-6361/201833399).
- Rajagopal, M., Marchesi, S., et al. (June 2021). ‘Identifying the 3FHL Catalog. V. Results of the CTIO-COSMOS Optical Spectroscopy Campaign 2019’. In: ApJS 254.2, 26, p. 26. doi: [10.3847/1538-4365/abf656](https://doi.org/10.3847/1538-4365/abf656).
- Rasmussen, C. E. and Williams, C. K. I. (Nov. 2005). *Gaussian Processes for Machine Learning*. The MIT Press. ISBN: 9780262256834. doi: [10.7551/mitpress/3206.001.0001](https://doi.org/10.7551/mitpress/3206.001.0001).
- Ratner, B. (June 2009). ‘The correlation coefficient: Its values range between +1/-1, or do they?’ In: *Journal of Targeting, Measurement and Analysis for Marketing* 17.2, pp. 139–142. ISSN: 1479-1862. doi: [10.1057/jt.2009.5](https://doi.org/10.1057/jt.2009.5).
- Rawlings, S. (Sept. 2003). ‘High-redshift radio galaxies: at the crossroads’. In: New A Rev. 47.4-5, pp. 397–404. doi: [10.1016/S1387-6473\(03\)00056-3](https://doi.org/10.1016/S1387-6473(03)00056-3).
- Reis, I., Baron, D., and Shahaf, S. (Jan. 2019). ‘Probabilistic Random Forest: A Machine Learning Algorithm for Noisy Data Sets’. In: AJ 157.1, 16, p. 16. doi: [10.3847/1538-3881/aaf101](https://doi.org/10.3847/1538-3881/aaf101).
- Ricci, C., Trakhtenbrot, B., et al. (Dec. 2017). ‘BAT AGN Spectroscopic Survey. V. X-Ray Properties of the Swift/BAT 70-month AGN Catalog’. In: ApJS 233.2, 17, p. 17. doi: [10.3847/1538-4365/aa96ad](https://doi.org/10.3847/1538-4365/aa96ad).
- Richter, G. A. (Jan. 1975). ‘Search for Optical Identifications in the 5C3 Radio Survey. II. Statistical Treatment and Results’. In: *Astronomische Nachrichten* 296.2, p. 65. doi: [10.1002/asna.19752960203](https://doi.org/10.1002/asna.19752960203).
- Robertson, B. E. (Aug. 2022). ‘Galaxy Formation and Reionization: Key Unknowns and Expected Breakthroughs by the James Webb Space Telescope’. In: ARA&A 60, pp. 121–158. doi: [10.1146/annurev-astro-120221-044656](https://doi.org/10.1146/annurev-astro-120221-044656).
- Rodrigo, C. and Solano, E. (July 2020). ‘The SVO Filter Profile Service’. In: *XIV.0 Scientific Meeting (virtual) of the Spanish Astronomical Society*, 182, p. 182.
- Rodrigo, C., Solano, E., and Bayo, A. (Oct. 2012). *SVO Filter Profile Service Version 1.0*. IVOA Working Draft 15 October 2012. doi: [10.5479/ADS/bib/2012ivoa.rept.1015R](https://doi.org/10.5479/ADS/bib/2012ivoa.rept.1015R).
- Rohde, D. J., Drinkwater, M. J., et al. (June 2005). ‘Applying machine learning to catalogue matching in astrophysics’. In: MNRAS 360.1, pp. 69–75. doi: [10.1111/j.1365-2966.2005.08930.x](https://doi.org/10.1111/j.1365-2966.2005.08930.x).
- Rohde, D. J., Gallagher, M. R., et al. (June 2006). ‘Matching of catalogues by probabilistic pattern classification’. In: MNRAS 369.1, pp. 2–14. doi: [10.1111/j.1365-2966.2006.10304.x](https://doi.org/10.1111/j.1365-2966.2006.10304.x).
- Roscher, R., Bohn, B., et al. (2020). ‘Explainable Machine Learning for Scientific Insights and Discoveries’. In: *IEEE Access* 8, pp. 42200–42216. doi: [10.1109/ACCESS.2020.2976199](https://doi.org/10.1109/ACCESS.2020.2976199).

- Ross, N. P. and Cross, N. J. G. (May 2020). ‘The near and mid-infrared photometric properties of known redshift $z \geq 5$ quasars’. In: MNRAS 494.1, pp. 789–803. doi: [10.1093/mnras/staa544](https://doi.org/10.1093/mnras/staa544).
- Ross, N. P., McGreer, I. D., et al. (Aug. 2013). ‘The SDSS-III Baryon Oscillation Spectroscopic Survey: The Quasar Luminosity Function from Data Release Nine’. In: ApJ 773.1, 14, p. 14. doi: [10.1088/0004-637X/773/1/14](https://doi.org/10.1088/0004-637X/773/1/14).
- Rubin, D. (1987). *Multiple Imputation for Nonresponse in Surveys*. Wiley Series in Probability and Statistics. Wiley. ISBN: 9780471087052. URL: <https://books.google.com/books?id=0KruAAAAMAAJ>.
- Rubin, D. B. (Dec. 1976). ‘Inference and missing data’. In: Biometrika 63.3, pp. 581–592. ISSN: 0006-3444. doi: [10.1093/biomet/63.3.581](https://doi.org/10.1093/biomet/63.3.581).
- Rybicki, G. and Lightman, A. (2008). *Radiative Processes in Astrophysics*. Physics textbook. Wiley. ISBN: 9783527618187. URL: <https://books.google.pt/books?id=eswe2StAspsC>.
- Saarela, M. and Jauhainen, S. (Feb. 2021). ‘Comparison of feature importance measures as explanations for classification models’. In: SN Applied Sciences 3.2, p. 272. ISSN: 2523-3971. doi: [10.1007/s42452-021-04148-9](https://doi.org/10.1007/s42452-021-04148-9).
- Sabater, J., Best, P. N., et al. (Feb. 2019). ‘The LoTSS view of radio AGN in the local Universe. The most massive galaxies are always switched on’. In: A&A 622, A17, A17. doi: [10.1051/0004-6361/201833883](https://doi.org/10.1051/0004-6361/201833883).
- Sajina, A., Lacy, M., and Pope, A. (June 2022). ‘The Past and Future of Mid-Infrared Studies of AGN’. In: Universe 8.7, p. 356. doi: [10.3390/universe8070356](https://doi.org/10.3390/universe8070356).
- Salpeter, E. E. (Jan. 1955). ‘The Luminosity Function and Stellar Evolution.’ In: ApJ 121, p. 161. doi: [10.1086/145971](https://doi.org/10.1086/145971).
- Salvato, M., Buchner, J., et al. (Feb. 2018). ‘Finding counterparts for all-sky X-ray surveys with NWAY: a Bayesian algorithm for cross-matching multiple catalogues’. In: MNRAS 473.4, pp. 4937–4955. doi: [10.1093/mnras/stx2651](https://doi.org/10.1093/mnras/stx2651).
- Salvato, M., Ilbert, O., et al. (Dec. 2011). ‘Dissecting Photometric Redshift for Active Galactic Nucleus Using XMM- and Chandra-COSMOS Samples’. In: ApJ 742.2, 61, p. 61. doi: [10.1088/0004-637X/742/2/61](https://doi.org/10.1088/0004-637X/742/2/61).
- Salvato, M., Ilbert, O., and Hoyle, B. (June 2019). ‘The many flavours of photometric redshifts’. In: Nature Astronomy 3, pp. 212–222. doi: [10.1038/s41550-018-0478-0](https://doi.org/10.1038/s41550-018-0478-0).
- Samuel, A. L. (1959). ‘Some Studies in Machine Learning Using the Game of Checkers’. In: IBM Journal of Research and Development 3.3, pp. 210–229. doi: [10.1147/rd.33.0210](https://doi.org/10.1147/rd.33.0210).
- Sánchez, S. F., Avila-Reese, V., et al. (Apr. 2018). ‘SDSS IV MaNGA - Properties of AGN Host Galaxies’. In: Rev. Mexicana Astron. Astrofis. 54, pp. 217–260. doi: [10.48550/arXiv.1709.05438](https://doi.org/10.48550/arXiv.1709.05438).
- Sánchez-Sáez, P., Reyes, I., et al. (Mar. 2021). ‘Alert Classification for the ALeRCE Broker System: The Light Curve Classifier’. In: AJ 161.3, 141, p. 141. doi: [10.3847/1538-3881/abd5c1](https://doi.org/10.3847/1538-3881/abd5c1).
- Sandage, A. (Sept. 1962). ‘The Change of Redshift and Apparent Luminosity of Galaxies due to the Deceleration of Selected Expanding Universes.’ In: ApJ 136, p. 319. doi: [10.1086/147385](https://doi.org/10.1086/147385).
- Santos, M. S., Abreu, P. H., et al. (Dec. 2022). ‘On the joint-effect of class imbalance and overlap: a critical review’. In: Artificial Intelligence Review 55.8, pp. 6207–6275. ISSN: 1573-7462. doi: [10.1007/s10462-022-10150-3](https://doi.org/10.1007/s10462-022-10150-3).

REFERENCES

- Sartori, L. F., Schawinski, K., et al. (Dec. 2015). ‘The search for active black holes in nearby low-mass galaxies using optical and mid-IR data’. In: MNRAS 454.4, pp. 3722–3742. doi: [10.1093/mnras/stv2238](https://doi.org/10.1093/mnras/stv2238).
- Schapire, R. E. (June 1990). ‘The strength of weak learnability’. In: *Machine Learning* 5.2, pp. 197–227. issn: 1573-0565. doi: [10.1007/BF00116037](https://doi.org/10.1007/BF00116037).
- Schapire, R. E., Freund, Y., et al. (1998). ‘Boosting the Margin: A New Explanation for the Effectiveness of Voting Methods’. In: *The Annals of Statistics* 26.5, pp. 1651–1686. issn: 00905364. url: <http://www.jstor.org/stable/120016> (visited on 05/12/2023).
- Schawinski, K., Thomas, D., et al. (Dec. 2007). ‘Observational evidence for AGN feedback in early-type galaxies’. In: MNRAS 382.4, pp. 1415–1431. doi: [10.1111/j.1365-2966.2007.12487.x](https://doi.org/10.1111/j.1365-2966.2007.12487.x).
- Schechter, P. (Jan. 1976). ‘An analytic expression for the luminosity function for galaxies.’ In: ApJ 203, pp. 297–306. doi: [10.1086/154079](https://doi.org/10.1086/154079).
- Schmidt, M. (Feb. 1968). ‘Space Distribution and Luminosity Functions of Quasi-Stellar Radio Sources’. In: ApJ 151, p. 393. doi: [10.1086/149446](https://doi.org/10.1086/149446).
- Schneider, P. C., Freund, S., et al. (May 2022). ‘The eROSITA Final Equatorial-Depth Survey (eFEDS). The Stellar Counterparts of eROSITA sources identified by machine learning and Bayesian algorithms’. In: A&A 661, A6, A6. doi: [10.1051/0004-6361/202141133](https://doi.org/10.1051/0004-6361/202141133).
- Schuecker, P. (Jan. 1993). ‘Automated Galaxy Redshift Measurements from Very Low Dispersion Objective Prism Schmidt Plates’. In: ApJS 84, p. 39. doi: [10.1086/191744](https://doi.org/10.1086/191744).
- Scoville, N., Aussel, H., et al. (Sept. 2007). ‘The Cosmic Evolution Survey (COSMOS): Overview’. In: ApJS 172.1, pp. 1–8. doi: [10.1086/516585](https://doi.org/10.1086/516585).
- Selina, R. J., Murphy, E. J., et al. (Dec. 2018). ‘The ngVLA Reference Design’. In: *Science with a Next Generation Very Large Array*. Ed. by E. Murphy. Vol. 517. Astronomical Society of the Pacific Conference Series, p. 15. doi: [10.48550/arXiv.1810.08197](https://doi.org/10.48550/arXiv.1810.08197).
- Selina, R., Murphy, E., and Beasley, A. (Jan. 2023). ‘The ngVLA: A Technical Overview’. In: *American Astronomical Society Meeting Abstracts*. Vol. 55. American Astronomical Society Meeting Abstracts, 357.02, p. 357.02.
- Sen, S., Agarwal, S., et al. (Feb. 2022). ‘Astronomical big data processing using machine learning: A comprehensive review’. In: *Experimental Astronomy* 53.1, pp. 1–43. doi: [10.1007/s10686-021-09827-4](https://doi.org/10.1007/s10686-021-09827-4).
- Shakura, N. I. and Sunyaev, R. A. (Jan. 1973). ‘Black holes in binary systems. Observational appearance.’ In: A&A 24, pp. 337–355.
- Shapley, L. S. (1953). ‘A Value for n-Person Games’. In: *Contributions to the Theory of Games (AM-28), Volume II*. Vol. 1. Princeton University Press, pp. 307–318. doi: [10.1515/9781400881970-018](https://doi.org/10.1515/9781400881970-018).
- Shen, X., Hopkins, P. F., et al. (Jan. 2020). ‘The bolometric quasar luminosity function at z = 0–7’. In: MNRAS 495.3, pp. 3252–3275. doi: [10.1093/mnras/staa1381](https://doi.org/10.1093/mnras/staa1381).
- Shimwell, T. W., Tasse, C., et al. (Feb. 2019). ‘The LOFAR Two-metre Sky Survey. II. First data release’. In: A&A 622, A1, A1. doi: [10.1051/0004-6361/201833559](https://doi.org/10.1051/0004-6361/201833559).
- Shy, S., Tak, H., et al. (July 2022). ‘Incorporating Measurement Error in Astronomical Object Classification’. In: AJ 164.1, 6, p. 6. doi: [10.3847/1538-3881/ac6e64](https://doi.org/10.3847/1538-3881/ac6e64).

- Silva, L., Schurer, A., et al. (Jan. 2011). ‘Modelling the spectral energy distribution of galaxies: introducing the artificial neural network’. In: MNRAS 410.3, pp. 2043–2056. doi: [10.1111/j.1365-2966.2010.17580.x](https://doi.org/10.1111/j.1365-2966.2010.17580.x).
- Silva Filho, T., Song, H., et al. (Sept. 2023). ‘Classifier calibration: a survey on how to assess and improve predicted class probabilities’. In: *Machine Learning* 112.9, pp. 3211–3260. ISSN: 1573-0565. doi: [10.1007/s10994-023-06336-7](https://doi.org/10.1007/s10994-023-06336-7).
- Simpson, C., Rawlings, S., et al. (Apr. 2012). ‘Radio imaging of the Subaru/XMM-Newton Deep Field- III. Evolution of the radio luminosity function beyond z= 1’. In: MNRAS 421.4, pp. 3060–3083. doi: [10.1111/j.1365-2966.2012.20529.x](https://doi.org/10.1111/j.1365-2966.2012.20529.x).
- Singh, V., Beelen, A., et al. (Sept. 2014). ‘Multiwavelength characterization of faint ultra steep spectrum radio sources: A search for high-redshift radio galaxies’. In: A&A 569, A52, A52. doi: [10.1051/0004-6361/201423644](https://doi.org/10.1051/0004-6361/201423644).
- Sipple, J. and Lidz, A. (Jan. 2024). ‘The Star Formation Efficiency during Reionization as Inferred from the Hubble Frontier Fields’. In: ApJ 961.1, 50, p. 50. doi: [10.3847/1538-4357/ad06a7](https://doi.org/10.3847/1538-4357/ad06a7).
- Skrutskie, M. F., Cutri, R. M., et al. (Feb. 2006). ‘The Two Micron All Sky Survey (2MASS)’. In: AJ 131.2, pp. 1163–1183. doi: [10.1086/498708](https://doi.org/10.1086/498708).
- Šlaus, B., Smolčić, V., et al. (June 2020). ‘The XXL Survey. XLI. Radio AGN luminosity functions based on the GMRT 610 MHz continuum observations’. In: A&A 638, A46, A46. doi: [10.1051/0004-6361/201937258](https://doi.org/10.1051/0004-6361/201937258).
- Snyder, J. (1987). *Map Projections—a Working Manual*. Professional paper. U.S. Government Printing Office. ISBN: 9780318235622.
- (1997). *Flattening the Earth: Two Thousand Years of Map Projections*. University of Chicago Press. ISBN: 9780226767475.
- Sola, J. and Sevilla, J. (1997). ‘Importance of input data normalization for the application of neural networks to complex industrial problems’. In: *IEEE Transactions on Nuclear Science* 44.3, pp. 1464–1468. doi: [10.1109/23.589532](https://doi.org/10.1109/23.589532).
- Sollich, P. and Krogh, A. (1995). ‘Learning with ensembles: How overfitting can be useful’. In: *Advances in Neural Information Processing Systems*. Ed. by D. Touretzky, M. Mozer, and M. Hasselmo. Vol. 8. MIT Press. URL: https://proceedings.neurips.cc/paper_files/paper/1995/file/1019c8091693ef5c5f55970346633f92-Paper.pdf.
- Sommer, M. W., Basu, K., et al. (May 2011). ‘Redshift evolution of the 1.4 GHz volume averaged radio luminosity function in clusters of galaxies’. In: A&A 529, A124, A124. doi: [10.1051/0004-6361/201016150](https://doi.org/10.1051/0004-6361/201016150).
- Sørensen, T. (1948). *A Method of Establishing Groups of Equal Amplitude in Plant Sociology Based on Similarity of Species Content*. Biologiske skrifter. I kommission hos E. Munksgaard. URL: <https://books.google.pt/books?id=rpS8GAAACAAJ>.
- Spinello, C. and Agnello, A. (Oct. 2019). ‘VEXAS: VISTA EXtension to Auxiliary Surveys. Data Release 1. The southern Galactic hemisphere’. In: A&A 630, A146, A146. doi: [10.1051/0004-6361/201936311](https://doi.org/10.1051/0004-6361/201936311).
- Sravan, N., Graham, M. J., et al. (July 2023). ‘Machine-directed gravitational-wave counterpart discovery’. In: *arXiv e-prints*, arXiv:2307.09213, arXiv:2307.09213. doi: [10.48550/arXiv.2307.09213](https://doi.org/10.48550/arXiv.2307.09213).

REFERENCES

- Steidel, C. C., Adelberger, K. L., et al. (July 1999). ‘Lyman-Break Galaxies at $z > \sim 4$ and the Evolution of the Ultraviolet Luminosity Density at High Redshift’. In: *ApJ* 519.1, pp. 1–17. doi: [10.1086/307363](https://doi.org/10.1086/307363).
- Steidel, C. C., Giavalisco, M., et al. (May 1996a). ‘Spectroscopic Confirmation of a Population of Normal Star-forming Galaxies at Redshifts $Z > 3$ ’. In: *ApJ* 462, p. L17. doi: [10.1086/310029](https://doi.org/10.1086/310029).
- Steidel, C. C., Giavalisco, M., et al. (Aug. 1996b). ‘Spectroscopy of Lyman Break Galaxies in the Hubble Deep Field’. In: *AJ* 112, p. 352. doi: [10.1086/118019](https://doi.org/10.1086/118019).
- Steidel, C. C. and Hamilton, D. (Sept. 1992). ‘Deep Imaging of redshift QSO Fields Below the Lyman Limit. I. The Field of Q0000-263 and galaxies at $Z = 3.4$ ’. In: *AJ* 104, p. 941. doi: [10.1086/116287](https://doi.org/10.1086/116287).
- Stern, D. (July 2015). ‘The X-Ray to Mid-infrared Relation of AGNs at High Luminosity’. In: *ApJ* 807.2, 129, p. 129. doi: [10.1088/0004-637X/807/2/129](https://doi.org/10.1088/0004-637X/807/2/129).
- Stern, D., Assef, R. J., et al. (July 2012). ‘Mid-infrared Selection of Active Galactic Nuclei with the Wide-Field Infrared Survey Explorer. I. Characterizing WISE-selected Active Galactic Nuclei in COSMOS’. In: *ApJ* 753.1, 30, p. 30. doi: [10.1088/0004-637X/753/1/30](https://doi.org/10.1088/0004-637X/753/1/30).
- Stern, D., Eisenhardt, P., et al. (Sept. 2005). ‘Mid-Infrared Selection of Active Galaxies’. In: *ApJ* 631.1, pp. 163–168. doi: [10.1086/432523](https://doi.org/10.1086/432523).
- Stone, M. (1974). ‘Cross-Validatory Choice and Assessment of Statistical Predictions’. In: *Journal of the Royal Statistical Society: Series B (Methodological)* 36.2, pp. 111–133. doi: <https://doi.org/10.1111/j.2517-6161.1974.tb00994.x>.
- Storey-Fisher, K., Hogg, D. W., et al. (June 2023). ‘Quaia, the Gaia-unWISE Quasar Catalog: An All-Sky Spectroscopic Quasar Sample’. In: *arXiv e-prints*, arXiv:2306.17749, arXiv:2306.17749. doi: [10.48550/arXiv.2306.17749](https://doi.org/10.48550/arXiv.2306.17749).
- Storey-Fisher, K., Huertas-Company, M., et al. (Dec. 2021). ‘Anomaly detection in Hyper Suprime-Cam galaxy images with generative adversarial networks’. In: *MNRAS* 508.2, pp. 2946–2963. doi: [10.1093/mnras/stab2589](https://doi.org/10.1093/mnras/stab2589).
- Stoughton, C., Lupton, R. H., et al. (Jan. 2002). ‘Sloan Digital Sky Survey: Early Data Release’. In: *AJ* 123.1, pp. 485–548. doi: [10.1086/324741](https://doi.org/10.1086/324741).
- Suganuma, M., Yoshiii, Y., et al. (Mar. 2006). ‘Reverberation Measurements of the Inner Radius of the Dust Torus in Nearby Seyfert 1 Galaxies’. In: *ApJ* 639.1, pp. 46–63. doi: [10.1086/499326](https://doi.org/10.1086/499326).
- Sutherland, W. and Saunders, W. (Dec. 1992). ‘On the likelihood ratio for source identification.’ In: *MNRAS* 259, pp. 413–420. doi: [10.1093/mnras/259.3.413](https://doi.org/10.1093/mnras/259.3.413).
- Sweijen, F., van Weeren, R. J., et al. (Jan. 2022). ‘Deep sub-arcsecond wide-field imaging of the Lockman Hole field at 144 MHz’. In: *Nature Astronomy* 6, pp. 350–356. doi: [10.1038/s41550-021-01573-z](https://doi.org/10.1038/s41550-021-01573-z).
- Tanaka, M., Coupon, J., et al. (Jan. 2018). ‘Photometric redshifts for Hyper Suprime-Cam Subaru Strategic Program Data Release 1’. In: *PASJ* 70, S9, S9. doi: [10.1093/pasj/psx077](https://doi.org/10.1093/pasj/psx077).
- Taylor, M. B. (Dec. 2005). ‘TOPCAT & STIL: Starlink Table/VOTable Processing Software’. In: *Astronomical Data Analysis Software and Systems XIV*. Ed. by P. Shopbell, M. Britton, and R. Ebert. Vol. 347. Astronomical Society of the Pacific Conference Series, p. 29.
- Thomas, N., Davé, R., et al. (May 2021). ‘The radio galaxy population in the SIMBA simulations’. In: *MNRAS* 503.3, pp. 3492–3509. doi: [10.1093/mnras/stab654](https://doi.org/10.1093/mnras/stab654).

- Thorne, J., Robotham, A., et al. (Mar. 2022a). *AGN Unification Diagram*. doi: [10.5281/zenodo.6381013](https://doi.org/10.5281/zenodo.6381013).
- Thorne, J. E., Robotham, A. S. G., et al. (Feb. 2022b). ‘Deep Extragalactic VIisible Legacy Survey (DEVILS): identification of AGN through SED fitting and the evolution of the bolometric AGN luminosity function’. In: MNRAS 509.4, pp. 4940–4961. doi: [10.1093/mnras/stab3208](https://doi.org/10.1093/mnras/stab3208).
- Toba, Y., Oyabu, S., et al. (June 2014). ‘Luminosity and Redshift Dependence of the Covering Factor of Active Galactic Nuclei viewed with WISE and Sloan Digital Sky Survey’. In: ApJ 788.1, 45, p. 45. doi: [10.1088/0004-637X/788/1/45](https://doi.org/10.1088/0004-637X/788/1/45).
- Tonry, J. and Davis, M. (Oct. 1979). ‘A survey of galaxy redshifts. I. Data reduction techniques.’ In: AJ 84, pp. 1511–1525. doi: [10.1086/112569](https://doi.org/10.1086/112569).
- Toth, M. J., Goran, M. I., et al. (1993). ‘Examination of data normalization procedures for expressing peak VO2 data’. In: *Journal of applied physiology* 75.5, pp. 2288–2292.
- Tripodi, R., Feruglio, C., et al. (Sept. 2022). ‘Black hole and host galaxy growth in an isolated $z \sim 6$ QSO observed with ALMA’. In: A&A 665, A107, A107. doi: [10.1051/0004-6361/202243920](https://doi.org/10.1051/0004-6361/202243920).
- Troyer, J., Starkey, D., et al. (Mar. 2016). ‘Correlated X-ray/ultraviolet/optical variability in NGC 6814’. In: MNRAS 456.4, pp. 4040–4050. doi: [10.1093/mnras/stv2862](https://doi.org/10.1093/mnras/stv2862).
- Urry, C. (June 2004). ‘AGN Unification: An Update’. In: *AGN Physics with the Sloan Digital Sky Survey*. Ed. by G. T. Richards and P. B. Hall. Vol. 311. Astronomical Society of the Pacific Conference Series, p. 49. doi: [10.48550/arXiv.astro-ph/0312545](https://doi.org/10.48550/arXiv.astro-ph/0312545).
- Urry, C. M. and Padovani, P. (Sept. 1995). ‘Unified Schemes for Radio-Loud Active Galactic Nuclei’. In: PASP 107, p. 803. doi: [10.1086/133630](https://doi.org/10.1086/133630).
- Uttley, P., Edelson, R., et al. (Feb. 2003). ‘Correlated Long-Term Optical and X-Ray Variations in NGC 5548’. In: ApJ 584.2, pp. L53–L56. doi: [10.1086/373887](https://doi.org/10.1086/373887).
- Uzgil, B. D., Oesch, P. A., et al. (May 2021). ‘The ALMA Spectroscopic Survey in the HUDF: A Search for [C II] Emitters at $6 \leq z \leq 8$ ’. In: ApJ 912.1, 67, p. 67. doi: [10.3847/1538-4357/abe86b](https://doi.org/10.3847/1538-4357/abe86b).
- Van Calster, B., McLernon, D. J., et al. (Dec. 2019). ‘Calibration: the Achilles heel of predictive analytics’. In: BMC Medicine 17.1, p. 230. ISSN: 1741-7015. doi: [10.1186/s12916-019-1466-7](https://doi.org/10.1186/s12916-019-1466-7).
- van den Busch, J. L., Hildebrandt, H., et al. (Oct. 2020). ‘Testing KiDS cross-correlation redshifts with simulations’. In: A&A 642, A200, A200. doi: [10.1051/0004-6361/202038835](https://doi.org/10.1051/0004-6361/202038835).
- van der Velden, E. (Feb. 2020). ‘CMasher: Scientific colormaps for making accessible, informative and ‘cmashing’ plots’. In: *The Journal of Open Source Software* 5.46, 2004, p. 2004. doi: [10.21105/joss.02004](https://doi.org/10.21105/joss.02004).
- van der Vlugt, D., Hodge, J. A., et al. (Dec. 2022). ‘An Ultra-deep Multiband Very Large Array (VLA) Survey of the Faint Radio Sky (COSMOS-XS): New Constraints on the Cosmic Star Formation History’. In: ApJ 941.1, 10, p. 10. doi: [10.3847/1538-4357/ac99db](https://doi.org/10.3847/1538-4357/ac99db).
- van Haarlem, M. P., Wise, M. W., et al. (July 2013). ‘LOFAR: The LOw-Frequency ARray’. In: A&A 556, A2, A2. doi: [10.1051/0004-6361/201220873](https://doi.org/10.1051/0004-6361/201220873).
- van Rijsbergen, C. J. (1979). *Information Retrieval*. 2nd. USA: Butterworth-Heinemann. ISBN: 0408709294.
- Vanden Berk, D. E., Wilhite, B. C., et al. (Feb. 2004). ‘The Ensemble Photometric Variability of $\sim 25,000$ Quasars in the Sloan Digital Sky Survey’. In: ApJ 601.2, pp. 692–714. doi: [10.1086/380563](https://doi.org/10.1086/380563).

REFERENCES

- Vanschoren, J. (2019). ‘Meta-Learning’. In: *Automated Machine Learning: Methods, Systems, Challenges*. Ed. by F. Hutter, L. Kotthoff, and J. Vanschoren. Cham: Springer International Publishing, pp. 35–61. ISBN: 978-3-030-05318-5. doi: [10.1007/978-3-030-05318-5_2](https://doi.org/10.1007/978-3-030-05318-5_2).
- Vapnik, V. (1995). *The Nature of Statistical Learning Theory*. Springer. ISBN: 9780387945590. URL: https://books.google.pt/books?id=r_ayQgAACAAJ.
- Vardoulaki, E., Jiménez Andrade, E. F., et al. (Apr. 2021). ‘FR-type radio sources at 3 GHz VLA-COSMOS: Relation to physical properties and large-scale environment’. In: A&A 648, A102, A102. doi: [10.1051/0004-6361/202039488](https://doi.org/10.1051/0004-6361/202039488).
- Veilleux, S. and Osterbrock, D. E. (Feb. 1987). ‘Spectral Classification of Emission-Line Galaxies’. In: ApJS 63, p. 295. doi: [10.1086/191166](https://doi.org/10.1086/191166).
- Véron-Cetty, M. .- and Véron, P. (July 2010). ‘A catalogue of quasars and active nuclei: 13th edition’. In: A&A 518, A10, A10. doi: [10.1051/0004-6361/201014188](https://doi.org/10.1051/0004-6361/201014188).
- Villaescusa-Navarro, F., Anglés-Alcázar, D., et al. (July 2021). ‘The CAMELS Project: Cosmology and Astrophysics with Machine-learning Simulations’. In: ApJ 915.1, 71, p. 71. doi: [10.3847/1538-4357/abf7ba](https://doi.org/10.3847/1538-4357/abf7ba).
- Vuttipittayamongkol, P., Elyan, E., and Petrovski, A. (2021). ‘On the class overlap problem in imbalanced data classification’. In: *Knowledge-Based Systems* 212, p. 106631. ISSN: 0950-7051. doi: <https://doi.org/10.1016/j.knosys.2020.106631>.
- Wagstaff, K. L., Huff, E., and Rebba-pragada, U. (July 2022). ‘Machine-Assisted Discovery Through Identification and Explanation of Anomalies in Astronomical Surveys’. In: *Astronomical Society of the Pacific Conference Series*. Ed. by J. E. Ruiz, F. Pierfedereci, and P. Teuben. Vol. 532. Astronomical Society of the Pacific Conference Series, p. 183.
- Walcher, J., Groves, B., et al. (Jan. 2011). ‘Fitting the integrated spectral energy distributions of galaxies’. In: Ap&SS 331, pp. 1–52. doi: [10.1007/s10509-010-0458-z](https://doi.org/10.1007/s10509-010-0458-z).
- Wasleske, E. J. and Baldassare, V. F. (Aug. 2023). ‘X-Ray Emission of Ultraviolet Variable Active Galactic Nucleus Candidates’. In: AJ 166.2, 64, p. 64. doi: [10.3847/1538-3881/ace16b](https://doi.org/10.3847/1538-3881/ace16b).
- Wenzl, L., Schindler, J.-T., et al. (Aug. 2021). ‘Random Forests as a Viable Method to Select and Discover High-redshift Quasars’. In: AJ 162.2, 72, p. 72. doi: [10.3847/1538-3881/ac0254](https://doi.org/10.3847/1538-3881/ac0254).
- Werner, M. W., Roellig, T. L., et al. (Sept. 2004). ‘The Spitzer Space Telescope Mission’. In: ApJS 154.1, pp. 1–9. doi: [10.1086/422992](https://doi.org/10.1086/422992).
- Whittam, I. H., Prescott, M., et al. (Jan. 2024). ‘MIGHTEE: Multi-wavelength counterparts in the COSMOS field’. In: MNRAS 527.2, pp. 3231–3245. doi: [10.1093/mnras/stad3307](https://doi.org/10.1093/mnras/stad3307).
- Wilber, A. G., Dabbech, A., et al. (July 2023). ‘Scalable precision wide-field imaging in radio interferometry - II. AIRI validated on ASKAP data’. In: MNRAS 522.4, pp. 5576–5587. doi: [10.1093/mnras/stad1353](https://doi.org/10.1093/mnras/stad1353).
- Williams, W. L., Calistro Rivera, G., et al. (Apr. 2018). ‘LOFAR-Boötes: properties of high- and low-excitation radio galaxies at $0.5 < z < 2.0$ ’. In: MNRAS 475.3, pp. 3429–3452. doi: [10.1093/mnras/sty026](https://doi.org/10.1093/mnras/sty026).
- Williams, W. L. and Röttgering, H. J. A. (June 2015). ‘Radio-AGN feedback: when the little ones were monsters’. In: MNRAS 450.2, pp. 1538–1545. doi: [10.1093/mnras/stv692](https://doi.org/10.1093/mnras/stv692).
- Wolpert, D. H. (1992). ‘Stacked generalization’. In: *Neural Networks* 5.2, pp. 241–259. ISSN: 0893-6080. doi: [https://doi.org/10.1016/S0893-6080\(05\)80023-1](https://doi.org/10.1016/S0893-6080(05)80023-1).

- Wolstencroft, R. D., Savage, A., et al. (Nov. 1986). ‘The identification of IRAS point sources- I. A 304 deg² field centred on the South Galactic Pole.’ In: MNRAS 223, pp. 279–302. doi: [10.1093/mnras/223.2.279](https://doi.org/10.1093/mnras/223.2.279).
- Wright, E. L., Eisenhardt, P. R. M., et al. (Dec. 2010). ‘The Wide-field Infrared Survey Explorer (WISE): Mission Description and Initial On-orbit Performance’. In: AJ 140.6, pp. 1868–1881. doi: [10.1088/0004-6256/140/6/1868](https://doi.org/10.1088/0004-6256/140/6/1868).
- Wu, C., Wong, O. I., et al. (Jan. 2019). ‘Radio Galaxy Zoo: CLARAN - a deep learning classifier for radio morphologies’. In: MNRAS 482.1, pp. 1211–1230. doi: [10.1093/mnras/sty2646](https://doi.org/10.1093/mnras/sty2646).
- Xue, Y. Q., Luo, B., et al. (July 2011). ‘The Chandra Deep Field-South Survey: 4 Ms Source Catalogs’. In: ApJS 195.1, 10, p. 10. doi: [10.1088/0067-0049/195/1/10](https://doi.org/10.1088/0067-0049/195/1/10).
- Yan, W., Brandt, W. N., et al. (July 2023). ‘The Most Obscured AGNs in the XMM-SERVS Fields’. In: ApJ 951.1, 27, p. 27. doi: [10.3847/1538-4357/accea6](https://doi.org/10.3847/1538-4357/accea6).
- Yang, J. (Sept. 2021). ‘Fast TreeSHAP: Accelerating SHAP Value Computation for Trees’. In: *arXiv e-prints*, arXiv:2109.09847, arXiv:2109.09847. doi: [10.48550/arXiv.2109.09847](https://doi.org/10.48550/arXiv.2109.09847).
- Yang, Q. and Shen, Y. (Jan. 2023). ‘A Southern Photometric Quasar Catalog from the Dark Energy Survey Data Release 2’. In: ApJS 264.1, 9, p. 9. doi: [10.3847/1538-4365/ac9ea8](https://doi.org/10.3847/1538-4365/ac9ea8).
- Ye, H., Sweijen, F., et al. (Sept. 2023). ‘1-arcsecond imaging strategy for the LoTSS survey using the International LOFAR Telescope’. In: *arXiv e-prints*, arXiv:2309.16560, arXiv:2309.16560. doi: [10.48550/arXiv.2309.16560](https://doi.org/10.48550/arXiv.2309.16560).
- Yeo, I.-K. and Johnson, R. A. (Dec. 2000). ‘A new family of power transformations to improve normality or symmetry’. In: *Biometrika* 87.4, pp. 954–959. issn: 0006-3444. doi: [10.1093/biomet/87.4.954](https://doi.org/10.1093/biomet/87.4.954).
- Yerushalmy, J. (1947). ‘Statistical Problems in Assessing Methods of Medical Diagnosis, with Special Reference to X-Ray Techniques’. In: *Public Health Reports (1896-1970)* 62.40, pp. 1432–1449. issn: 00946214. URL: <http://www.jstor.org/stable/4586294> (visited on 10/08/2022).
- York, D. G., Adelman, J., et al. (Sept. 2000). ‘The Sloan Digital Sky Survey: Technical Summary’. In: AJ 120.3, pp. 1579–1587. doi: [10.1086/301513](https://doi.org/10.1086/301513).
- Yuan, Z., Jarvis, M. J., and Wang, J. (May 2020). ‘A Flexible Method for Estimating Luminosity Functions via Kernel Density Estimation’. In: ApJS 248.1, 1, p. 1. doi: [10.3847/1538-4365/ab855b](https://doi.org/10.3847/1538-4365/ab855b).
- Yuan, Z., Zhang, X., et al. (May 2022). ‘A Flexible Method for Estimating Luminosity Functions via Kernel Density Estimation. II. Generalization and Python Implementation’. In: ApJS 260.1, 10, p. 10. doi: [10.3847/1538-4365/ac596a](https://doi.org/10.3847/1538-4365/ac596a).
- Yule, G. U. (1912). ‘On the Methods of Measuring Association Between Two Attributes’. In: *Journal of the Royal Statistical Society* 75.6, pp. 579–652. issn: 09528385. URL: <http://www.jstor.org/stable/2340126>.
- Zajaček, M., Busch, G., et al. (Oct. 2019). ‘Radio spectral index distribution of SDSS-FIRST sources across optical diagnostic diagrams’. In: A&A 630, A83, A83. doi: [10.1051/0004-6361/201833388](https://doi.org/10.1051/0004-6361/201833388).
- Zammit, M. A. and Adami, K. Z. (Nov. 2023). ‘Machine Learning Applications in Jupiter-host Star Classification using Stellar Spectra’. In: MNRAS. doi: [10.1093/mnras/stad3668](https://doi.org/10.1093/mnras/stad3668).
- Zhang, Y. and Zhao, Y. (May 2015). ‘Astronomy in the Big Data Era’. In: *Data Science Journal* 14, p. 11. doi: [10.5334/dsj-2015-011](https://doi.org/10.5334/dsj-2015-011).

REFERENCES

- Zheng, A. and Casari, A. (2018). *Feature Engineering for Machine Learning: Principles and Techniques for Data Scientists*. O'Reilly. ISBN: 9781491953242. URL: <https://books.google.pt/books?id=Ho0UvgAACAAJ>.
- Zitzlau, R., Hoyle, B., et al. (Aug. 2016). ‘Stacking for machine learning redshifts applied to SDSS galaxies’. In: MNRAS 460.3, pp. 3152–3162. doi: [10.1093/mnras/stw1454](https://doi.org/10.1093/mnras/stw1454).
- Zou, H., Gao, J., et al. (May 2019). ‘Photometric Redshifts and Stellar Masses for Galaxies from the DESI Legacy Imaging Surveys’. In: ApJS 242.1, 8, p. 8. doi: [10.3847/1538-4365/ab1847](https://doi.org/10.3847/1538-4365/ab1847).

Appendices

This page intentionally left blank.

A

Sample of predicted radio-detectable AGN

The columns shown in the prediction results for sources in both **HETDEX** and **S82** fields are described in Table A.1. Full datasets and models from prediction pipeline can be obtained from Carvajal et al. (2023b) at <https://zenodo.org/doi/10.5281/zenodo.10220008>.

APPENDIX A. PREDICTED RADIO-DETECTABLE AGN

Table A.1: Table columns descriptions.

ID	Internal identification number
RA_ICRS	Right Ascension (in degrees) of source in CW
DE_ICRS	Declination (in degrees) of source in CW
Name	Name of source as it appears in CW catalogue
band_num	Number of non-radio bands with valid measurement per source (cf. Sect. 2.5)
class	1 if source is a confirmed AGN by MQC . 0 if has been spectroscopically confirmed as SFG in SDSS-DR16 . Sources with no value do not have a spectroscopic classification in this catalogue
Sint_LOFAR (or Fint_VLAS82) ^a	Imputed integrated flux (in mJy) of source from LOFAR or VLAS82
Sint_LOFAR_non_imp (or Fint_VLAS82_non_imp) ^a	Non imputed integrated flux (in mJy) of source from LOFAR or VLAS82
W1mproPM	Imputed W1 magnitude of source
W2mproPM	Imputed W2 magnitude of source
gmag	Imputed g magnitude of source
rmag	Imputed r magnitude of source
imag	Imputed i magnitude of source
zmag	Imputed z magnitude of source
ymag	Imputed y magnitude of source
W3mag	Imputed W3 magnitude of source
W4mag	Imputed W4 magnitude of source
Jmag	Imputed J magnitude of source
Hmag	Imputed H magnitude of source
Kmag	Imputed Ks magnitude of source
Score_AGN	Score from meta AGN-SFG classifier for prediction to be an AGN
Prob_AGN	Probability from calibrated meta AGN-SFG classifier for prediction to be AGN
LOFAR_detect	1 if source has been detected on LoTSS survey or in their analogue surveys for fields different to HETDEX (see Sects. 2.1 and 2.2). 0 otherwise
Score_radio_AGN	Score from meta radio detection model for prediction to be detected in radio
Prob_radio_AGN	Probability from calibrated radio detection model for prediction to be detected in radio
radio_AGN	<code>class</code> × LOFAR_detect. 1 if source is AGN and has been detected in radio. 0 otherwise
Score_rAGN	<code>Score_AGN</code> × Score_radio. Score of source for it to be AGN detected in radio
Prob_rAGN	<code>Prob_AGN</code> × Prob_radio. Probability of source for it to be AGN detected in radio
Z	Spectroscopic redshift as listed by the MQC (if available)
pred_Z	Redshift value predicted by our model

^a Sources from [HETDEX](#) field have columns with LOFAR suffix. Sources from [VLAS82](#) have VLAS82 suffix.

Table A.2: Predicted and original properties for 20 sources in testing subset with highest redshift predicted radio AGN. Sources sorted by decreasing predicted redshift.

ID	RA	ICRS DE	ICRS band	num class	Score_AGN	Prob_AGN	LOFAR_detect	Score_radio	Prob_radio	Score_rAGN	Prob_rAGN	z	pred_z
	(deg)	(deg)	(deg)										
9898717	203.016113	55.518097	9	1.0	0.500082	0.954114	0	0.390861	0.375122	0.195462	0.357909	4.738	4.3679
168686	164.769135	45.806320	8	1.0	0.500048	0.858157	0	0.450279	0.418719	0.225161	0.359326	4.893	4.1733
14437074	213.226517	54.236343	9	1.0	0.500090	0.965187	0	0.251632	0.263746	0.125839	0.254564	4.326	4.0475
10408176	188.163651	52.880898	9	1.0	0.500012	0.622448	0	0.604838	0.526003	0.302426	0.327410	4.340	3.9553
12612753	227.216370	51.941029	9	1.0	0.500055	0.887909	0	0.364423	0.355080	0.182231	0.315278	3.795	3.8797
5283988	210.532974	49.500351	9	1.0	0.500095	0.971223	0	0.188993	0.207802	0.094514	0.201822	3.800	3.8733
6005721	188.469818	47.834412	9	1.0	0.500045	0.845762	0	0.221281	0.237188	0.110651	0.200604	3.795	3.7482
13284852	218.364182	48.398373	9	1.0	0.500086	0.961052	0	0.340675	0.336683	0.170367	0.323570	3.892	3.7222
12308398	222.563293	49.665272	8	1.0	0.500061	0.906658	1	0.385996	0.371466	0.193021	0.336793	3.059	3.7173
8147562	200.292435	50.367386	9	1.0	0.500090	0.965431	1	0.406555	0.386820	0.203314	0.373448	3.711	3.6748
4433144	215.540436	46.992298	9	1.0	0.500085	0.958811	1	0.363854	0.354644	0.181958	0.340036	3.812	3.6541
12285636	221.428192	49.046921	12	1.0	0.500037	0.803828	1	0.254536	0.266237	0.127277	0.214009	3.880	3.5737
8170701	200.040466	50.849586	9	1.0	0.500040	0.818872	0	0.232864	0.247439	0.116441	0.202620	3.827	3.5436
12118249	223.858124	48.950409	9	1.0	0.500049	0.862100	1	0.280344	0.288020	0.140186	0.248302	3.501	3.5381
1537357	177.051697	52.934574	9	1.0	0.500015	0.645263	0	0.240127	0.253793	0.120067	0.163763	3.885	3.5037
10731551	190.228714	54.614464	9	1.0	0.500055	0.887182	1	0.277223	0.285418	0.138627	0.253218	3.938	3.4858
8721103	203.096924	50.575378	9	1.0	0.500093	0.969007	0	0.2677817	0.277525	0.133933	0.268924	3.832	3.4604
10679277	190.777359	53.089466	9	1.0	0.500104	0.978721	1	0.323977	0.323506	0.162022	0.316622	3.575	3.3764
8434867	194.881256	52.609665	9	1.0	0.500066	0.920703	0	0.811700	0.672552	0.405903	0.619221	3.374	3.1584
10314475	188.218765	51.662666	9	1.0	0.500109	0.982703	0	0.545364	0.485399	0.272741	0.477003	2.157	3.0701

DRAFT - Eddaly 21, 2024 - DRAFT

APPENDIX A. PREDICTED RADIO-DETECTABLE AGN

Table A.3: Predicted and original properties for the 20 sources in S82 with highest predicted redshift on labelled sources predicted to be radio AGN. Sources sorted by decreasing predicted redshift.

ID	RA_ICRS	DE_ICRS	band_num	class	Score_AGN	Prob_AGN	radio_detect	Score_radio	Prob_radio	Score_rAGN	Prob_rAGN	z_{pred}	z
	(deg)	(deg)											
1 406323	32.679794	-0.305035	6	1.0	0.500050	0.866373	1	0.185842	0.204867	0.092930	0.177491	4.650	4.4986
326139	33.580879	-1.121398	8	1.0	0.500040	0.822622	0	0.208769	0.225946	0.104393	0.185868	4.600	4.3785
633752	12.526446	-0.888660	9	1.0	0.500035	0.793882	0	0.206182	0.223600	0.103098	0.177512	4.310	4.2946
2 834844	344.101440	0.789000	7	1.0	0.500062	0.909395	0	0.375735	0.363709	0.187891	0.330756	4.099	4.0635
3 191865	31.881712	1.063655	9	1.0	0.500087	0.962260	0	0.264210	0.274477	0.132128	0.264118	3.841	4.0509
834857	21.023815	-0.735512	9	1.0	0.500080	0.951495	0	0.270463	0.279754	0.135253	0.266185	4.073	4.0476
927403	30.860348	-0.664943	9	1.0	0.500086	0.960503	0	0.237843	0.251800	0.118942	0.241855	4.158	3.9690
1 760668	343.580109	-0.031951	9	1.0	0.500088	0.962655	0	0.262341	0.272891	0.131193	0.262700	3.710	3.9594
1 539341	35.058613	-0.202904	5	1.0	0.500028	0.746304	0	0.243109	0.256385	0.121561	0.191341	3.712	3.9175
794288	21.752874	-0.766390	12	1.0	0.500044	0.838993	0	0.830699	0.687772	0.415386	0.577036	4.105	3.8631
201543	18.192499	-1.218799	9	1.0	0.500062	0.909994	0	0.383420	0.369525	0.191734	0.336265	3.589	3.7324
2 705463	27.703466	0.690627	12	1.0	0.500092	0.968344	0	0.284506	0.291475	0.142279	0.282248	3.685	3.6814
567008	13.804744	-0.939195	9	1.0	0.500114	0.985173	0	0.473856	0.435550	0.236982	0.429092	3.622	3.5531
2 610655	334.937775	0.618921	9	1.0	0.500107	0.981287	0	0.201475	0.219309	0.100759	0.215205	3.531	3.5031
2 972720	341.585175	0.894723	9	1.0	0.500087	0.961458	0	0.752861	0.628400	0.376496	0.604180	3.676	3.4776
3 15550	342.345581	-1.129457	9	1.0	0.500070	0.930942	0	0.485239	0.443596	0.242653	0.412962	3.989	3.4724
2 774066	21.015764	0.742418	12	1.0	0.500045	0.843852	0	0.642026	0.551288	0.321042	0.465205	3.836	3.4492
3 301527	346.665192	1.148655	9	1.0	0.500045	0.846709	0	0.305069	0.308323	0.152548	0.261060	3.648	3.4407
1 926483	22.206123	0.095463	9	1.0	0.500117	0.986782	0	0.427273	0.402055	0.213687	0.396741	3.746	3.4282
211079	31.115847	-1.211047	9	1.0	0.500106	0.980813	0	0.455339	0.422351	0.227718	0.414247	3.940	3.3345

Table A.4: Predicted and original properties for the 20 sources in `HETDEX` field with highest predicted redshift on the unlabelled sources predicted to be radio AGN.

ID	RA_ICRS	DE_ICRS	band_num	Score_AGN	Prob_AGN	radio_detect	Score_radio	Prob_radio	Score_rAGN	Prob_rAGN	pred_z
	(deg)	(deg)									
9544254	201.309235	53.746429	6	0.500007	0.578804	0	0.351672	0.345250	0.175838	0.199832	4.7114
12355845	220.838120	50.319016	5	0.500007	0.578804	0	0.937123	0.794128	0.468568	0.459644	4.6064
13814216	219.839142	52.660328	7	0.500015	0.650248	0	0.213846	0.230529	0.106926	0.149901	4.5622
6698239	184.694901	49.063766	5	0.499995	0.467527	0	0.799085	0.662753	0.399538	0.309855	4.5483
2951011	175.882446	55.497799	5	0.500008	0.589419	0	0.823295	0.681768	0.411654	0.401847	4.5320
7281571	202.589035	47.134212	9	0.500032	0.773522	0	0.567045	0.500257	0.283541	0.386960	4.5220
8634951	206.688446	51.339924	7	0.499981	0.349392	0	0.289692	0.295758	0.144841	0.103336	4.5111
5075789	207.003540	48.740067	7	0.499998	0.492974	0	0.400019	0.381966	0.200009	0.188299	4.5087
12750738	222.945663	52.196320	7	0.500009	0.593819	0	0.238322	0.252219	0.119163	0.149772	4.5064
1775496	163.331070	47.809532	7	0.500032	0.772884	0	0.764361	0.636758	0.382205	0.492140	4.4930
14577806	213.842804	56.349747	8	0.500047	0.856822	0	0.615253	0.533082	0.307656	0.456756	4.4663
9817016	198.035965	55.984398	5	0.500010	0.603443	0	0.466084	0.430028	0.233047	0.259497	4.4438
12429128	226.345795	49.744789	7	0.500007	0.581465	0	0.485468	0.443757	0.242737	0.258029	4.4438
14500121	211.942429	55.213791	7	0.500008	0.587655	0	0.809995	0.671214	0.405004	0.394443	4.4355
2166668	163.079010	53.084713	7	0.500010	0.605185	0	0.743381	0.621584	0.371698	0.376173	4.4353
7077234	181.246124	53.378967	7	0.500012	0.623304	0	0.264222	0.274486	0.132114	0.171088	4.4209
14074782	218.186417	54.400047	7	0.500019	0.681823	0	0.396363	0.379240	0.198189	0.258574	4.4065
5789667	187.343811	47.441658	8	0.500023	0.706552	0	0.725299	0.608743	0.362666	0.430109	4.4027
11070539	183.812180	54.915974	7	0.500012	0.621592	0	0.202662	0.220393	0.101333	0.136995	4.3959
8943186	202.578445	53.892410	7	0.499983	0.362751	0	0.331269	0.329286	0.165629	0.119449	4.3951

APPENDIX A. PREDICTED RADIO-DETECTABLE AGN

Table A.5: Predicted and original properties for the 20 sources in S82 with highest predicted redshift on the unlabelled sources predicted to be radio AGN.

ID	RA_ICRS	DE_ICRS	band_num	Score_AGN	Prob_AGN	radio_detect	Score_radio	Prob_radio	Score_rAGN	Prob_rAGN	pred_z
	(deg)	(deg)									
3 244 450	26.276423	1.104065	7	0.500002	0.531172	0	0.542061	0.483128	0.271031	0.256624	4.3938
1 062 270	11.744675	-0.562642	7	0.499982	0.356043	0	0.196326	0.214586	0.098159	0.076402	4.3563
3 261 269	28.882526	1.117103	7	0.500011	0.608660	0	0.354936	0.347777	0.177472	0.211678	4.3153
1 466 227	18.157259	-0.258997	5	0.500013	0.630968	0	0.456207	0.422973	0.228110	0.266882	4.3146
1 134 866	11.304936	-0.507943	7	0.500011	0.616439	0	0.226178	0.241539	0.113091	0.148894	4.3140
1 726 140	29.144888	-0.058600	7	0.499984	0.369512	0	0.261730	0.272373	0.130861	0.100645	4.3125
220011	331.973877	-1.203849	7	0.500016	0.656024	0	0.734737	0.615421	0.367380	0.403731	4.3098
2 005 587	30.130974	0.155751	7	0.500017	0.665006	0	0.828544	0.686014	0.414286	0.456203	4.2972
1 058 229	344.614166	-0.565701	5	0.500015	0.645263	0	0.394774	0.378052	0.197393	0.243943	4.2899
2 914 632	344.342316	0.850049	7	0.500009	0.594697	0	0.601936	0.524030	0.300973	0.311639	4.2767
1 255 517	20.319715	-0.418364	7	0.500012	0.625012	0	0.210549	0.227556	0.105277	0.142226	4.2711
762 162	340.426544	-0.790798	7	0.500014	0.638566	0	0.671060	0.571113	0.335539	0.364693	4.2687
1 167 955	21.433058	-0.483463	8	0.500016	0.659303	0	0.776046	0.645368	0.388036	0.425493	4.2652
1 160 900	35.526070	-0.488795	7	0.500013	0.630119	0	0.614667	0.532684	0.307341	0.335654	4.2516
706 252	332.367462	-0.833645	5	0.500013	0.630119	0	0.517853	0.466400	0.258933	0.293888	4.2481
5 10569	10.896913	-0.981369	7	0.500016	0.651903	0	0.192197	0.210775	0.096102	0.137405	4.2472
2 512 910	333.612640	0.544506	5	0.500014	0.636883	0	0.388904	0.373653	0.194457	0.237974	4.2471
840 809	341.886383	-0.730991	7	0.500042	0.827874	0	0.212097	0.228954	0.106057	0.189545	4.2433
2 932 746	35.531948	0.863913	8	0.500013	0.631815	0	0.917725	0.770169	0.458874	0.486604	4.2421
325 442	344.384644	-1.121920	7	0.500035	0.793285	0	0.624086	0.539086	0.312065	0.427649	4.2353

Extended prediction pipeline

For the calculations of Chapter 6, a new instance of the prediction pipeline was trained and implemented. Its steps were kept similar to its original definition (Sect. 1.4) with some relevant differences. The first difference is in the overall structure of the pipeline. The prediction for radio-detected AGN works as presented in Fig. 1.8, but a new branch has been added for the treatment of radio-detected galaxies (i.e. extragalactic sources without indications of AGN emission). The new branch replicates the steps of the original process. Its stages are presented, graphically, in the flowchart of Fig. B.1.

The difference in the processing of the candidates start when sources are predicted to be SFGs (i.e. not AGN). Instead of being discarded, they are subject to a series of models that replicate the process for predicted AGN. Thus, a new step that predicts their likelihood of being radio detectable is applied. The predicted radio-detectable SFGs have, then, their photometric redshifts predicted. Finally, the results from both branches, AGN and SFGs, are compiled into one single catalogue.

The internal processing of each model remains the same as described in Chapter 5 and Fig. 2.7. The only difference can be found in the data collection. In particular the cross-match of the CW-detected sources with the radio detections (for the training stages, from HETDEX). Instead of using a search radius of $1\text{''}1$ (as it is maintained for all the remaining ancillary catalogues), sources are cross-matched with a radius of $6''$. This increase of more than five times in distance (and close to 30 times in area) can be explained by the need of obtaining a larger fraction of sources with a radio counterpart (as the results of the cross-match itself would be assessed, Sect. 6.3). A modified version of Table 2.3, with the new search radius for radio counterparts, is shown in Table B.1.

As expected, the number of non-radio counterparts remains the same. In contrast, the number of radio cross-matches has grown by more than a 100 % from the use of a $1\text{''}1$ search radius. This change can, in turn, change the metrics for the radio detection models and those of the redshift predictions as well given the modification of the distribution of values of the feature

APPENDIX B. EXTENDED PREDICTION PIPELINE

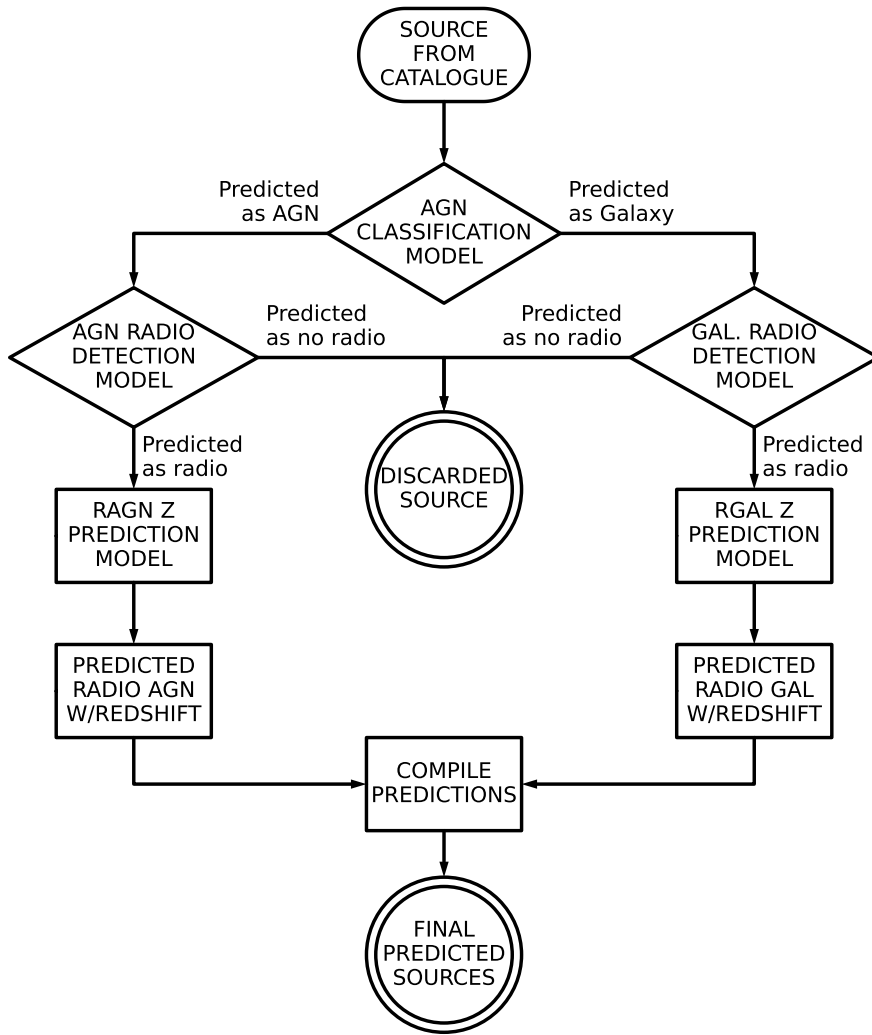


Figure B.1: Flowchart representing the proposed extended prediction pipeline used to predict the presence of radio-detected AGN and SFGs and their redshift values from IR-detected sources.

`radio_detect`. For our purposes, the differences in the metrics for this new set of models do not imply a degradation of the results they provide.

B.1 AGN-SFG classifier

Results and metrics of the `AGN-SFG` classification model have not changed with the extension of the prediction pipeline and the inclusion of a larger number of radio counterparts. This prediction stage does not use any form of radio information for its training and predictions. We refer, then, the reader to Chapter 6 and Sect. 4.1 for the analysis of its results.

Table B.1: Composition of initial catalogue and number of cross matches with additional surveys and catalogues for training of updated pipeline

Survey	HETDEX	Stripe82
CatWISE2020	15 136 878	3 590 306
AllWISE	5 955 123	1 424 576
Pan-STARRS	4 837 580	1 346 915
2MASS	566 273	214 445
LoTSS (6'')	382 431	...
VLAS82 (6'')	...	17 706
MQC (AGN)	50 538	17 743
SDSS (SFG)	68 196	4085

Table B.2: Best performing modified models the radio detection classification for [AGN](#)

Model	F_β ($\times 100$)	MCC ($\times 100$)	Precision ($\times 100$)	Recall ($\times 100$)	Rank
XGBoost	36.41 ± 1.82	34.47 ± 2.16	61.93 ± 3.18	27.18 ± 1.53	3.25
GBC	36.98 ± 2.20	36.39 ± 2.26	66.47 ± 3.39	27.10 ± 1.99	1.25
RF	36.74 ± 1.99	35.90 ± 1.90	65.48 ± 1.91	26.98 ± 1.78	2.25
CatBoost	36.18 ± 1.64	35.21 ± 1.68	64.60 ± 2.46	26.55 ± 1.48	3.50
ET	35.08 ± 1.09	34.32 ± 1.48	64.22 ± 2.48	25.52 ± 0.83	4.75
No-skill	15.29 ± 0.76	0.00 ± 0.91	15.29 ± 0.76	15.29 ± 0.76	6.00

^a Values and uncertainties as in Table 3.1.

B.2 Radio detection classifiers

The model for the classification of radio-detectable [AGN](#) is modified by the change in the distribution of values in its target feature, `radio_detect`. Nevertheless, the features selected for training remain the same as with the original model (i.e. `band_num`, `W4mag`, `g_r`, `g_i`, `r_i`, `r_z`, `i_z`, `z_y`, `z_W1`, `y_J`, `y_W1`, `J_H`, `H_K`, `K_W3`, `K_W4`, `W1_W2`, and `W2_W3`). For the selection of the meta and base models, [XGBoost](#) was adopted as the meta learner while [GBC](#), [RF](#), [CatBoost](#), and [ET](#) have been used as base learners. The results of such selection are displayed in Table B.2.

The training of the model for the prediction of radio detectability in predicted [SFGs](#) led to the use of 18 features (`W4mag`, `Kmag`, `g_r`, `g_W2`, `r_i`, `r_y`, `i_z`, `i_y`, `z_y`, `z_W2`, `y_J`, `y_W2`, `J_H`, `H_K`, `H_W3`, `W1_W2`, `W1_W3`, and `W3_W4`) together with its target, `radio_detect`. Additionally, and as seen in Table B.3, [RF](#) was selected as meta learner and [CatBoost](#), [XGBoost](#), [ET](#), and [GBC](#), as base models.

APPENDIX B. EXTENDED PREDICTION PIPELINE

Table B.3: Best performing modified models the radio detection classification for [SFGs](#)

Model	F_β ($\times 100$)	MCC ($\times 100$)	Precision ($\times 100$)	Recall ($\times 100$)	Rank
RF	39.39 ± 2.49	41.69 ± 2.36	76.09 ± 2.42	28.19 ± 2.12	1.25
CatBoost	39.24 ± 2.36	41.53 ± 2.39	75.90 ± 2.69	28.06 ± 1.97	2.25
XGBoost	38.64 ± 1.98	40.38 ± 2.23	73.55 ± 2.87	27.76 ± 1.57	4.00
ET	38.35 ± 2.57	40.69 ± 2.50	75.28 ± 2.78	27.31 ± 2.17	4.00
GBC	37.69 ± 2.32	40.83 ± 2.40	77.39 ± 3.01	26.49 ± 1.89	3.50
No-skill	14.22 ± 1.13	0.00 ± 1.32	14.22 ± 1.14	14.22 ± 1.12	6.00

^a Values and uncertainties as in Table 3.1.

Table B.4: Results of initial fit for redshift value prediction on predicted radio detectable [AGN](#)

Model	σ_{MAD} ($\times 100$)	σ_{NMAD} ($\times 100$)	σ_z ($\times 100$)	σ_z^N ($\times 100$)	η ($\times 100$)	Rank
RF	17.54 ± 1.24	7.70 ± 0.34	41.55 ± 4.38	19.63 ± 2.57	18.30 ± 1.60	2.0
ET	18.79 ± 1.22	8.32 ± 0.39	40.81 ± 3.25	18.29 ± 1.86	19.56 ± 1.78	2.0
CatBoost	21.07 ± 1.15	9.97 ± 0.25	39.65 ± 2.52	18.06 ± 1.57	21.14 ± 2.17	2.2
XGBoost	22.92 ± 1.20	10.49 ± 0.54	42.16 ± 3.85	19.36 ± 2.16	23.53 ± 1.62	3.8
GBR	28.33 ± 1.48	13.24 ± 0.73	44.77 ± 3.59	20.21 ± 1.93	29.90 ± 1.82	5.0
No-skill	97.06 ± 4.52	39.95 ± 1.89	86.78 ± 1.92	48.17 ± 1.10	72.49 ± 1.96	6.0

^a Algorithms sorted by increasing σ_{MAD} values.

^b Uncertainties as in Table 3.1.

B.3 Redshift predictors

The model for the prediction of photometric redshifts of radio-detectable [AGN](#) is also modified but, in this case, by the change in number of sources in the training set, which is increased (by the larger search radius for radio-detected sources). Thus, the features selected for training are 17 (i.e. `band_num`, `W4mag`, `g_r`, `g_W1`, `r_i`, `r_z`, `i_z`, `i_y`, `z_y`, `y_J`, `y_W1`, `J_H`, `H_K`, `K_W3`, `K_W4`, `W1_W2`, and `W1_W3`). Despite three algorithms having the same mean rank, the algorithm selected to be meta learner is [RF](#) given that it presents the best value of σ_{NMAD} , which is the metric to be optimised during training. Its metrics (together with those from the base models) are presented in Table B.4.

The model for the prediction of photometric redshifts of radio-detectable [SFGs](#) is also modified and selects 14 features for its training: `W4mag`, `g_r`, `r_i`, `r_z`, `i_z`, `i_y`, `z_y`, `y_J`, `y_W2`, `J_H`, `H_K`, `K_W3`, `W1_W2`, and `W1_W3`. The selected algorithm to be meta learner is [ET](#) (again, because it presents the best value of σ_{NMAD}) and its metrics (together with those from the base models and an no-skill prediction) are presented in Table B.5.

Table B.5: Results of initial fit for redshift value prediction on predicted radio detectable SFGs

Model	σ_{MAD} ($\times 100$)	σ_{NMAD} ($\times 100$)	σ_z ($\times 100$)	σ_z^N ($\times 100$)	η ($\times 100$)	Rank
ET	3.85 ± 0.25	2.81 ± 0.18	9.89 ± 0.81	7.03 ± 1.06	2.91 ± 0.77	2.0
RF	3.89 ± 0.12	2.86 ± 0.12	9.78 ± 0.88	6.98 ± 1.10	3.08 ± 0.88	2.0
CatBoost	4.01 ± 0.20	2.96 ± 0.12	9.75 ± 0.72	6.99 ± 1.01	2.78 ± 0.56	2.0
XGBoost	4.31 ± 0.27	3.16 ± 0.17	9.98 ± 0.90	7.05 ± 1.05	3.13 ± 0.73	4.2
GBR	4.81 ± 0.16	3.54 ± 0.08	9.96 ± 0.76	7.05 ± 0.99	3.45 ± 1.05	4.6
No-skill	33.51 ± 1.86	21.70 ± 1.31	26.74 ± 0.67	20.94 ± 0.42	49.08 ± 1.93	6.0

^a Algorithms sorted by increasing σ_{MAD} values.^b Uncertainties as in Table 3.1.

B.4 Pipeline prediction

Table B.6: Hyper-parameters values for meta-learners in modified pipeline after tuning.

AGN-SFG model (CatBoost)			
Parameter	Value	Parameter	Value
<code>learning_rate</code>	0.0075	<code>random_strength</code>	0.1
<code>depth</code>	6	<code>l2_leaf_reg</code>	10
Radio detection model for AGN (GradientBoosting)			
Parameter	Value	Parameter	Value
<code>n_estimators</code>	187	<code>min_samples_leaf</code>	2
<code>learning_rate</code>	0.0560	<code>max_depth</code>	9
<code>subsample</code>	0.3387	<code>max_features</code>	0.5248
<code>min_samples_split</code>	5		
Radio detection model for SFGs (RF)			
Parameter	Value	Parameter	Value
<code>n_estimators</code>	17	<code>max_depth</code>	6
<code>min_impurity_decrease</code>	0.0000	<code>max_features</code>	0.4280
<code>bootstrap</code>	False	<code>criterion</code>	<code>gini</code>
<code>class_weight</code>	<code>balanced_subsample</code>	<code>min_samples_split</code>	10
<code>min_samples_leaf</code>	3		
Redshift prediction model for rAGN (RF)			
Parameter	Value	Parameter	Value
<code>n_estimators</code>	187	<code>max_depth</code>	9
<code>min_impurity_decrease</code>	0.0000	<code>max_features</code>	0.6346
<code>bootstrap</code>	False	<code>criterion</code>	<code>mae</code>
<code>min_samples_split</code>	3	<code>min_samples_leaf</code>	5
Redshift prediction model for rGal (ET)			
Parameter	Value	Parameter	Value
<code>n_estimators</code>	100	<code>criterion</code>	<code>mse</code>
<code>max_depth</code>	None	<code>min_impurity_decrease</code>	0.0000
<code>max_features</code>	<code>auto</code>	<code>bootstrap</code>	False
<code>min_samples_split</code>	2	<code>min_samples_leaf</code>	1

^a This table shows the parameters which were subject to tuning.^b Remaining hyper-parameters used their default values as defined by their developers.